Design and Control of Fuel Cell management system with distributed supercapacitors storage element

Apinya Siangsanoh

UNIVERSITÉ DE LORRAINE

King Mongkut's University of Technology North Bangkok

École Doctorale "Sciences et Ingénierie des Molécules, des Produits, des Procédés, et de l'Énergie "

THÈSE

présentée à
L'UNIVERSITÉ DE LORRAINE
En vue de l'obtention du
DOCTORAT DE L'UNIVERSITÉ DE LORRAINE
Spécialité : Energie et mécanique
par

Apinya SIANGSANOH

Design and control of fuel cell management system with distributed supercapacitors storage element

Conception et contrôle d'un système de gestion de piles à combustible Avec des éléments de stockage distribués à supercondensateurs

---

Soutenue publiquement le 12 juillet 2022 devant le jury composé de :

Directeur de thèse :	Sophie Didierjean	Professeur - Université de Lorraine, France
Président de jury :	Babak Nahidmobarakeh	Professeur - Université de Lorraine, France
Rapporteurs :	Jean-Paul Gaubert	Professeur - Université de Poitiers, France
	Yuttana Kumsuwan	Professeur - Chiang Mai University, Thaïlande
Examinateurs :	Matheepot Phattanasak	Professeur - King Mongkut's University of Technology North Bangkok, Thaïlande
	Jean-Philippe Martin	Maître de conférences - Université de Lorraine
	Wattana Kaewmanee	Assistant Professeur - King Mongkut's University of Technology North Bangkok, Thaïlande
	Panarit Sethakul	Welding Institute of Thailand, Thaïlande
Membres Invité :	Serge Pierfederici	Professeur - Université de Lorraine, France

Acknowledgement

The work presented in this thesis was carried out between the Laboratoire d'Energie et de Mécanique Théorique et Appliquée (LEMTA) at the University of Lorraine in France and "renewable energy research centre" (RERC) laboratory at King Mongkut's University of Technology North Bangkok in Thailand.

First of all, I would like to appreciate to my supervisors Prof. Sophie Didierjean, Prof. Matheepot Phattanasak, Asst. Prof. Dr. Jean-Philippe Martin and Asst. Prof. Dr. Wattana Kaewmanee to support my Ph.D. and related research, motivation and give me knowledge. Their guidance helped me in all the time of research and writing of this thesis. I could not have imagined having better advisors and mentors for my Ph.D. study. It was a great privilege and honor to work and study under their guidance.

Moreover, I would like to thank my thesis committee Prof. Serge Weber, Prof. Nadia Steiner for their insightful comments and encouragement, but also for the hard question that incented me to widen my research from various perspectives.

My sincere thanks also go to Prof. Pascal Boulet, Prof. Serge Pierfederici, and Ing. Mathieu Weber, who provided me an opportunity to join their team, and who gave access to the laboratory and research facilities. Without their precious support, it would not be possible to conduct this research.

I am grateful to Dr. Roghayeh Gavagsaz-Ghoachani for helping me to present my work and follow my dreams. In particular, I thank my fellow lab mates for stimulating discussions, and for all the fun we have had in the last five years.

Last but not least, I am extremely grateful to my parents for their love, prayers, caring, and sacrifices for educating and preparing me for my future. I am very much thankful to my husband for his love, understanding, prayers, and continuing support to complete this research work.

I would like to thank all of Thai friends in Nancy. Especially, The Poolphaka family helped me with both my studies and as a mentor when I faced problems in my life. I also thank my friends in LEMTA, GREEN and CRAN laboratory (too many to list here but you know who you are!) for providing support and friendship that I needed.

Table of Contents

List of figures

List of Table

General introduction

The continuous economic expansion of all countries around the world is one of the factors that will drive the world's demand for energy increase dramatically. The Energy Information Administration (*EIA*) reported global energy consumption will continue to increase over the next three decades. While concerns about global warming, the production of electricity and transports are two of the causes of greenhouse gas emissions into the atmosphere. Many countries plan to reduce the use of fossil energy and to increase electricity generation from renewable energy even more. EIA said in its report published in 2016 (IEO 2016) that by 2040, renewable energy use will be on par with coal and natural gas, which are currently the main energy sources, accounting for 40 and 22 percent of the world's electricity generation, respectively. EIA predicts that from now until 2040, the world's use of renewable energy will increase by an average of 2.6 percent per year. Photovoltaic and wind powers will be the two main sources of energy that contribute to the proportion of electricity generation from renewable energy and account for two-thirds of the increase in renewable power generation.

However, the intermittency of wind and photovoltaic sources is a problem for the management of the electrical grid. Hydrogen production by water electrolysis fed by the renewable sources can participate to energy storage and in the same time it allows to reduce the use of fossil fuel for hydrogen production used for several industrial applications. Moreover, fuel cells fed by hydrogen are promising solutions as pollution-free energy sources for mobility applications, but their cost is still high. The ongoing research, development, and use of these technologies around the world will promote a fall of their cost over the next few years.

Polymer Electrolyte Membrane Fuel Cell (PEMFC) is an electrochemical system which converts hydrogen into electricity by producing only water. As a single fuel cell provides low voltage. cells are connected in series to increase the output voltage thus forming a fuel cells stack. The performance of the fuel cells depends on their electrochemical behavior which also depends on the operating conditions such as temperature, gas flow rates, relative humidity, pressure, ... In order to increase the reliability and efficiency, the fuel cell system usually works with a storage device. Supercapacitors used in this study can respond to the rapid power variations of the load which can't be supported by the fuel cell due to the long response time of the system providing hydrogen and air.

The essential challenge in using PEMFC is its lifespan. The management system improves the durability of the stacks when the operating conditions change, which is particularly the case for automotive applications. One of the objectives of this thesis is the development of a management system for a hybrid multi fuel cell stack energy source.

This Ph.D. has been led in "Laboratoire Energies et Mécanique Théorique et Appliquée" (LEMTA) laboratory, part of the University of Lorraine, Nancy, France, and "renewable energy research centre" (RERC) laboratory, part of *King Mongkut's University of Technology North Bangkok*, Bangkok, Thailand. This research aims to propose the novel architecture of hybridization between fuel cell and supercapacitor

This thesis is represented in four chapter as follows:

- The purpose of Chapter 1 is to carry out a literature survey about the working principle of fuel cells, main components of PEMFC, degradations including management methods related to fuel cells in order to reduce deterioration and increase lifetime. In addition, this chapter presents storage elements mainly principles and model of supercapacitors.

- Chapter 2 starts with a literature review of several architectures for FC system hybridization with supercapacitor (SC). Then, a novel converter structure for FC/SC application which is hybridized in series is proposed. The operation and modeling of the converter are presented. Closed-loop control using an indirect-sliding mode technique for the inner current loop and energy control are provided. The simulation and the experimental results are given to validate the proposed system.

- Modular Three-level (MTL) converter and its operation are proposed in the Chapter 3. The main advantage of this converter is to increase the output voltage because the voltage of fuel cell stack that produce low voltage. Moreover, a new configuration of series connected capacitors between them is proposed in this section. This method shares output capacitor in three-level converter. The unbalance output voltage can be solved by indirect sliding mode control. This structure allows to keep output capacitors voltages balance even if the input powers are not balanced.

- The energy managements are proposed in the last Chapter of the thesis. The series hybridization system is connected as each input of the modular three-level converter and several capacitors is connected in series to supply energy to the load. The behavior of global system and its control is simulated with MATLAB/Simulink program.

Finally, the conclusion and future prospect are given.

Chapter I

Electrical source and storage review

1.1. Introduction

Energy is an important factor in the basic needs of people. It is also the main factor for development in the business sector and industries sector. In addition, the rapid increase of the world population and economic growth contributes to the increase in global energy consumption [1]. At the same time, the conventional energy sources which are presented in a limited quantity and are being used for a long time tend to decline steadily around the world. These so-called non-renewable sources, for example, fossil fuels, coal, oil, and natural gas, were formed from decaying organic matter over hundreds of millions of years. Moreover, they have strong impacts on our environment, including air, water pollution, damage to public health, wildlife, and global warming problem. As a result, renewable energy, which is clean energy, is proposed to be used in place of conventional energy sources [2]. The benefits of renewable energy led many countries to invest in it. Researchers around the world are developing technology for more efficient renewable energy systems to save costs, save energy, reduce pollution, and solve the environmental problem of the world.

Although renewable energy is the promise solution to global warming, there are still many limits. For instance, renewable sources, such as solar or wind, are intermittent between a day, so that the equilibrium between supply and demand is not fulfilled.

In this context, the use of hydrogen as an energy carrier appears as a good solution. Green hydrogen would be produced by using the excess energy from renewable sources, stored or transported, and finally be used in chemical industries or to produce electrical energy. This

could solve simultaneously the problem of CO_2 emissions related to both natural gas reforming for hydrogen production and to mobility applications, mainly heavy vehicles. Indeed, while the development of small electric vehicles has taken off, electric propulsion still poses problems for trucks and trains due to the energy amount that must be taken on board. While waiting for further progress in the energy capacity of batteries, the combination of hydrogen and Fuel Cell (FC) could be a solution.

Among the different fuel cell types, the Proton Exchange Membrane Fuel Cell (PEMFC) is well suited for mobile applications. However, using PEMFC for commercial applications still has many challenges. For example, PEMFC starvation is a well-known problem in an application that the load has heavy transient demand. This problem is due to the slow response of the PEMFC, related gas flow from the source to the reaction site. The shortage of the reaction gas results in the voltage drop and may induce degradations. To mitigate this problem, fuel cell management is essential.

Many factors affect the fuel cell performance such as materials, design, and operating conditions. Gas supply to the electrodes is one of the main operating parameters, and it is strongly linked to fuel management. Water and heat, which are the products of chemical reactions, are handled by water management and thermal management. Humidity management controls the humidity inside fuel cells. Finally, the power transfer to the load or energy storage is taken care of by the power management system.

FCs are generally incorporated with other electrical energy storage devices such as batteries and supercapacitors (SC). The system which has the interaction of more than one energy source is called a "Hybrid system". As the SC supplies energy to the load faster than FC and batteries, the collaboration between FC and SC handles the load at different periods for avoiding the high stress of the fuel cell when the system is exposed to a transient load. Thus, FC-hybrid systems are wildly used in electric vehicles.

This chapter discusses the following topics. Section 1.2 is related to the FCs, especially the PEMFC. The general principle, the function of the main components, various degradations including the management methods related to fuel cells in order to reduce deterioration and increase lifetime of FC are discussed. Section 1.3 is focused on the storage device. The mechanism of the supercapacitor is presented. The advantages and disadvantages of the supercapacitor compared to the battery are also provided in this section.

1.2. Energy source based on fuel cells

The fuel cell was discovered more than 100 years ago by Sir William Robert Grove [3], and a high-power density fuel cell was first developed by Sir Francis Bacon in 1933. However, technological developments at that time mainly focus on the combustion engine instead of FC. Therefore, FC developed slowly in the early stages, but due to the present energy transition trend, researchers turned their attention to FC development again.

A FC is an electrochemical device allowing to convert the chemical energy of fuel (such as hydrogen) to electrical energy [4]- [5]. There are made with two electrodes called anode and cathode separated by the electrolyte. The two electrochemical reactions, named oxidation and

reduction, generate electricity. FC can operate as long as fuel is supplied. The voltage of a single cell is about 1 Volt or less, and to produce high power, several cells are assembled in series to form a stack. Since FCs do not produce greenhouse gases, the resulting electrical energy is considered as clean energy that helps to reduce the global warming problem.

1.2.1. Type of fuel cell

There are many types of fuel cells and each one has advantages and disadvantages. Each type is characterized by its typical behavior and materials. The classification is also separated by the working temperature and the ion transported through the electrolyte. The main FC technologies are Proton exchange membrane fuel cell (PEMFC), Phosphoric acid fuel cell (PAFC), Solid oxide fuel cell (SOFC), Alkaline fuel cell (AFC), Direct methanol fuel cell (DMFC), and Molten carbonate (MCFC).

Fuel cell	Electrolyte	Operating temperature (°C)	Electrical efficiency (%)
Proton exchange membrane fuel cell (PEMFC)	Proton exchange membrane	~80	40-70
Direct methanol fuel cell (DMFC)	Proton exchange membrane	15-130	20-40
Alkaline fuel cell (AFC)	Potassium hydroxide solution	50-100	60
Phosphoric acid fuel cell (PAFC)	Phosphoric acid	150-200	40-50
Solid oxide fuel cell (SOFC)	Oxidant ion conducting ceramic	550-1000	60-65
Molten carbonate fuel cell (MCFC)	Molten mixture of alkali metal carbonates	650	55

Table 1-1 Common fuel cell technologies.

The characteristics of different types of fuel cells are summarized in Table 1-1. It gives the electrolyte material, the operating temperature range, and the average efficiency of each FC. PAFC, MOFC, and SOFC use low-cost fuels such as natural gas, methanol, and gasoline. However, they have high operating temperatures and also emit CO_2 which is not environmentally friendly. Although, AFC, DMFC, and PEMFC operate at low temperatures, the AFC type which has been used in several spacecraft, has low operating efficiency and needs a large container for its electrolyte. The DMFC type produces electricity by reaction between methanol and oxygen. Methanol is easy to produce, to store, and has high energy density but

DMFC tends to have lower efficiency than PEMFC, longer start-up time, and produce CO_2. Considering the efficiency of each category, the technology of PEMFC which uses hydrogen and oxygen is quite interesting. It is particularly attractive and suitable for transportation applications. PEMFC is described in details in the next section.

1.2.2. Proton exchange membrane fuel cell (PEMFC)

A Proton Exchange Membrane Fuel Cell (PEMFC) has the advantages of high efficiency, high power density, quick response, and operating temperature of approximately 80°C [6]. The energy conversion efficiency, i.e., conversion of the hydrogen energy to electricity is in the order of 40-70%, the complement to 100% of energy is the heat. This is the FC type being promoted and introduced as the power source for vehicles as it presents quick startup, low-temperature operation, load following capabilities [7]- [8], high efficiency, and modularity. It also has good start-up behavior at low temperatures and it is small and compact. It is also considered as the power source in portable units as well as in large stationary power plants. An advantage is that the electrolyte is a solid phase in the form of a thin membrane of a polymer.

Consider the basic structure of PEMFC fed by hydrogen and oxygen as shown in Figure . There are two inlets for gases. The hydrogen inlet is on the anode side and the oxygen is on the cathode side. The excess gases and by-products (water) leave the cell through the outlets. The anode and cathode sides are separated by an electrolyte.

For a PEMFC operating with pure hydrogen and oxygen the electrochemical reactions are:

$$H_2 \rightarrow 2H^+ + 2e^- \tag{1-1}$$

$$\frac{1}{2}O_2 + 2H^+ + 2e^- \rightarrow H_2O \tag{1-2}$$

$$H_2 + \frac{1}{2}O_2 \rightarrow H_2O + \Delta H \tag{1-3}$$

At the anode, the hydrogen is split into protons and electrons (Equation 1-1). Protons can pass through the membrane while electrons move through the external circuit to feed the electric load. Oxygen feeds the cathode side and combines with protons and electrons to produce water (Equation 1-2). Equation (1-3) represented the overall reaction of PEMFC and ΔH is the reaction's enthalpy.

The main components of a PEMFC are shown in Figure 1-1. There are two electrodes isolated from each other with a membrane. The combination of membrane and catalyst layers is called the membrane electrode assembly (MEA). They are sandwiched between two porous materials called gas diffusion layer (GDL), and two bipolar plates. Both are used for hydrogen and oxygen supply, charge transfer, and exhaust of gas in excess, water and heat.

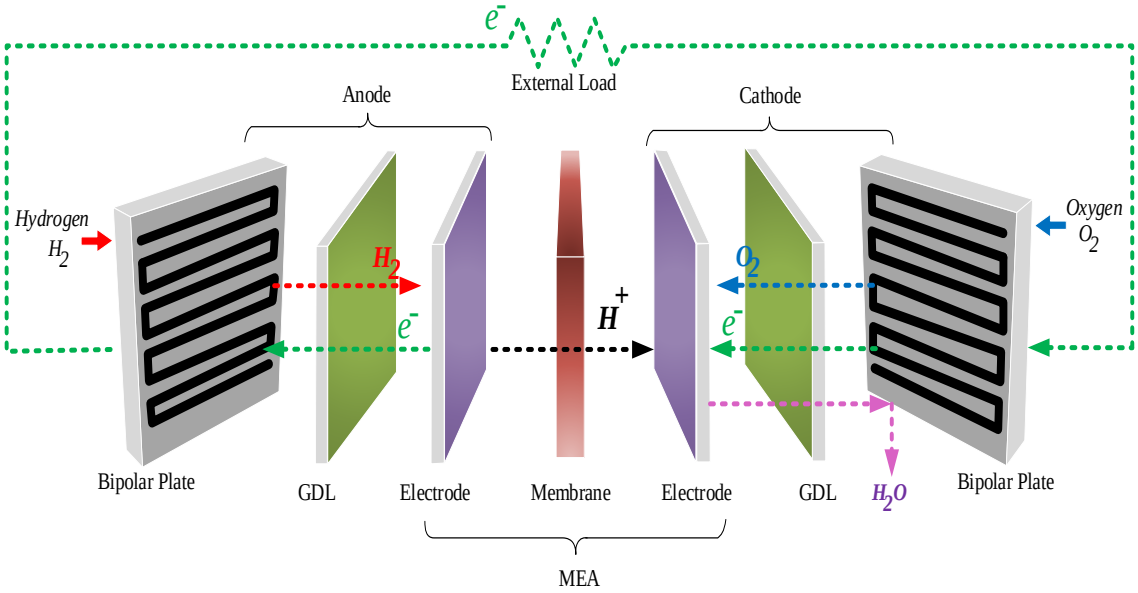

Figure 1-1 Component and operating principle of PEM fuel cell.

1.2.2.1. Membrane

The main function of the membrane is protonic conduction from the anode to the cathode. It must also prevent reactive gases permeation while allowing water transport. Typically, the membranes for PEM fuel cells are made of perfluorocarbon-sulfonic acid ionomer (PSA). This is essentially a copolymer of tetrafluorethylene (TFE) and various perfluorosulfonate monomers. The most popular material for membrane is Nafion®. The advantage of this polymer is very high proton conductivity even at room temperature. The membrane's conductivity is closely related to its water content which must always be kept high, making water management in the fuel cell a crucial issue [9]. To reduce the ionic resistance, the membrane should also be as thin as possible. Moreover, the membrane must be chemically stable.

1.2.2.2. Electrodes

In a fuel cell, the electrochemical reactions take place in the electrodes which are thin catalyst layers pressed between the membrane and the porous GDL. Each electrode is composed with carbon particles, catalyst material and small amount of ionomer. Platinum is the most common catalyst used in PEMFC for both oxygen reduction and hydrogen oxidation [10]- [11]- [12]. It is important to have small platinum particles (4 nm or smaller) to have a large surface of catalyst. The cell potential loss relates to the rate of proton transport and reactant gas transport in the electrocatalyst layer. Normally, the higher platinum loading the higher the voltage gain [13]. However, the key to improve the PEMFC performance is to increase the platinum utilization in the catalyst layer, while reducing the loading. Platinum is sensitive to the purity of hydrogen.

1.2.2.3. Gas diffusion layer (GDL)

The gas diffusion layer (GDL) is located between the electrode and the bipolar plate. There are several properties of the gas diffusion layer. Firstly, it has to be sufficiently porous to allow transport of both reactant gases and water produced by the electrochemical reaction in the catalyst layer. Secondly, it must be both electrically and thermally conductive [14]. Thirdly, it has to be strong enough to strengthen the MEA which is flimsy. The most used material for making the GDL is carbon-fiber paper. A small amount of PTFE (Teflon®) is spread into the material to make it hydrophobic to prevent water flooding. A thin layer of graphite particles mixed with PTFE forming the Micro Porous Layer (MPL) is often presented at the interface with the electrode. The size of pores in the MPL is approximately 0.1 to 0.5 μm that smaller than the pore size of carbon fiber paper (20-50 μm) [15]- [16]- [17].

1.2.2.4. Bipolar plates

The bipolar plates are used for the reactive gases supply, to remove heat, water, gases in excess and Nitrogen (PEMFC being generally fed by air), to separate the individual cells in a stack, and to carry the current from one cell to its neighboring cell until reaching the end plate. Generally, graphitic-polymer and metallic are two popular types of materials that are used for PEM fuel cell bipolar plate fabrication [18]. However, materials such as aluminum, steel, … may corrode in the fuel cell environment and a corrosion layer on the bipolar plate surface would rise electrical resistance [19]- [20]. This problem is solved by coating the plate with non-corrosive material. An important characteristic of bipolar plates is their electrical conductivity that must be high to limit the electrical resistance [21]- [22].

1.2.3. Fuel cell current-voltage characteristic

The polarization curve which gives the cell voltage variation with the current density, allows a quick assessment of the fuel cell's performance. Many factors affect the fuel cell voltage such as materials (described in the preceding sections), design, and operating conditions such as temperature, pressure, gas composition, and fuel properties. These factors have an influence on the voltage drop observed when the current flows through the cell. The theoretical potential of the hydrogen-oxygen fuel cell is between 1.18 and 1.23 Volts with respect to the hydrogen reference electrode. However, the cell potential is less because the polarization of the electrodes results in a potential loss in the system.

The maximum amount of energy produces by the fuel cell corresponds to Gibbs free energy ΔG [23] in the form of electrical work can be written as:

$$W_{el} = -\Delta G \tag{1-4}$$

Where $\Delta G = \Delta H - T\Delta S$. Then, the theoretical potential of the fuel cell can be calculated as:

$$E = \frac{-\Delta G}{nF} \tag{1-5}$$

Where n is the number of electrons per molecule of H_2 (2 electrons per molecule) and F is Faraday's constant (96485 C).

In the standard conditions ($T_{ref} = 25°C$ and 1 bar), $\Delta G = -237.34$ kJ mol^{-1}.

$$E_{cell}^{0} = \frac{-\Delta G}{nF} = \frac{237.34 \times 10^{3}}{2 \times 96485} = 1.23\ V \tag{1-6}$$

This theoretical cell voltage corresponds to water produced in liquid phase, and it is reduced to 1.18 Volts when the water is produced as vapor.

The cell voltage variation with the temperature and the pressure is given by the Nernst equation:

$$E_{cell} = E_{cell}^{0} - k_e(T - T_{ref}) - \frac{RT}{2F} \ln\left(\frac{p_{H_2O}}{p_{O_2}^{0.5} p_{H_2}}\right) \tag{1-7}$$

Where k_e stands for the reaction entropy assumed constant, T is the absolute temperature of the fuel cell (K), R is the universal gas constant (J mol^{-1}K^{-1}) and p_{H_2O}, p_{O_2}, p_{H_2} are the water, oxygen and hydrogen partial pressure, respectively.

The polarization curve is represented schematically in Figure 1-2. There are three main overpotentials in the cell. Firstly, the activation polarization is the overvoltage that needs to overcome the activation energy of the electrochemical reaction on the catalytic surface. The activation loss is given by the Butler-Volmer's law which is usually approximated by the Tafel's law as:

$$V_{act} = \frac{RT}{\alpha nF} ln\left(\frac{I_{FC}}{j_o}\right) \tag{1-8}$$

α is the charge transfer coefficient ($\alpha = 0.5$), I_{FC} is the current density of the FC (A cm^{-2}), and j_o is the exchange current density (A cm^{-2}).

Due to the logarithm form of this polarization, the voltage dropped by approximately 0.1 to 0.2 volts at low current density, and then it varies linearly and slowly for higher current [24]. Secondly, the ohmic polarization is voltage loss caused by charge transport. It included the conductor's intrinsic electronic or ionic resistance and the electrical contact resistances at the interface between the different layers and at the terminal connections of components. This leads to:

$$V_{ohm} = R_{ohm} I_{FC} \tag{1-9}$$

R_{ohm} being the sum of all the resistances in (Ω cm^2), the protonic membrane resistance being the main contributor, closely linked to humidity condition inside the cell.

Lastly, the concentration polarization is the voltage loss due to mass transport limitation. Fuel cell is continuously supplied with gases which are transported by diffusion through the GDL from the channels in the bipolar plates to the catalytic layers. Furthermore, according to the equations (1-1) and (1-2), the hydrogen and oxygen fluxes are proportional to the current density, so that at high current density, the reactant concentration in the catalyst layer can be very low even fall to zero. The concentration losses are deduced from the Butler-Volmer's law and are given by:

$$V_{conc} = \frac{RT}{2nF} ln\left(1 - \frac{I_{FC}}{j_{lim}}\right) \quad (1\text{-}10)$$

The limiting current density j_{lim} (A cm^{-2}) is the higher current density which corresponds to the reactant concentration equal to zero. The cell voltage is zero when $I_{FC} = j_{lim}$.

Therefore, the cell voltage $V_{FC_{cell}}$ can be modeled as:

$$V_{FC_{cell}} = E_{cell} - V_{act} - V_{ohm} - V_{conc} \quad (1\text{-}11)$$

The general shape of the polarization curve of a PEMFC is given in Figure 1-2, as a function of the current density:

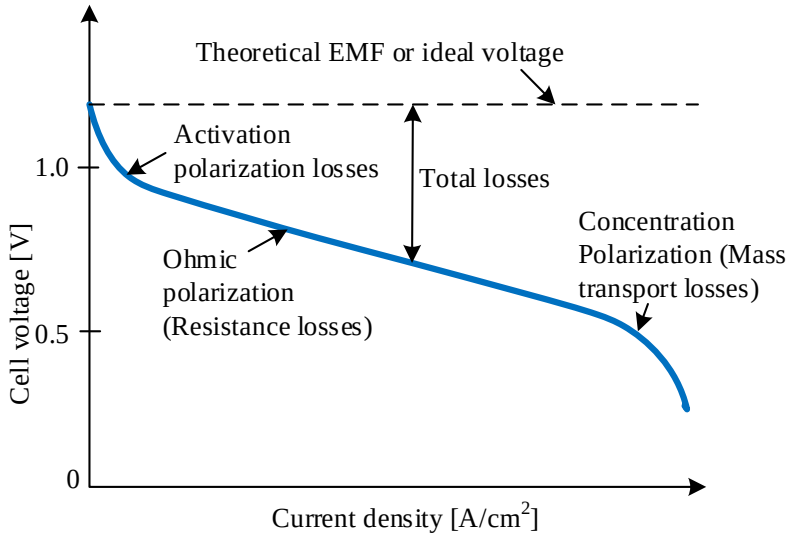

Figure 1-2 Typical fuel cell polarization curve.

The actual output voltage of the fuel cell (blue line) is less than the ideal voltage as shown in the figure. The red line in Figure 1-3 gives the power density delivered by a fuel cell as a function of the current density; it was deduced from the information in a fuel cell I-V curve.

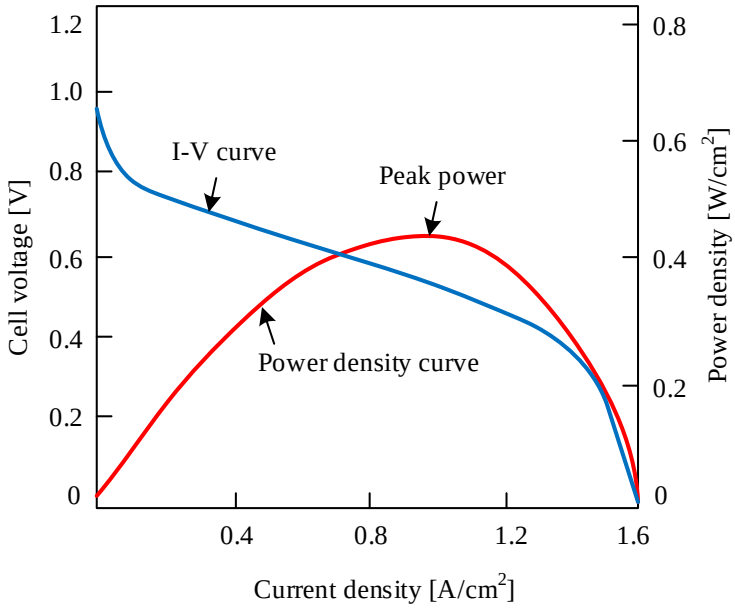

Figure 1-3 power output as a function of current density.

Fuel cell power density increases with increasing current density, reaches a maximum, and then falls at still higher current densities. Fuel cells are designed to operate at or below the power density maximum. At current densities below the power density maximum, voltage efficiency improves but power density falls. At current densities above the power density maximum, both voltage efficiency and power density fall.

1.2.4. PEM fuel cell degradations

Fuel cell degradation is an important factor in the design of fuel cell power supply. The degradation is impacted by the operating voltage, temperature, humidity, and by current oscillations if they exist. Maintaining the precise balance of liquid and vapors water inside the cell cause optimal performance of stack, whereas insufficient balance like membrane drying, electrodes flooding, fuel starvation, and impurities, affect the performance and can have an influence on the durability. To improve reliability and durability, appropriate management must be carried out to eliminate the faults and prevent possible damage. Some degradations of the PEMFC performances are reversible because they are linked to operating conditions that can be adapted, others are irreversible because they are related to physical modifications of the materials which composed the cells.

1.2.4.1. Drying and flooding

In an PEMFC, the water comes from the electrochemical reaction and from the gases (generally air) which are humidified before entering in the cells. Drying and flooding are mainly related to the water transport inside the cell, the transport mechanisms described below are presented in Figure 1-4.

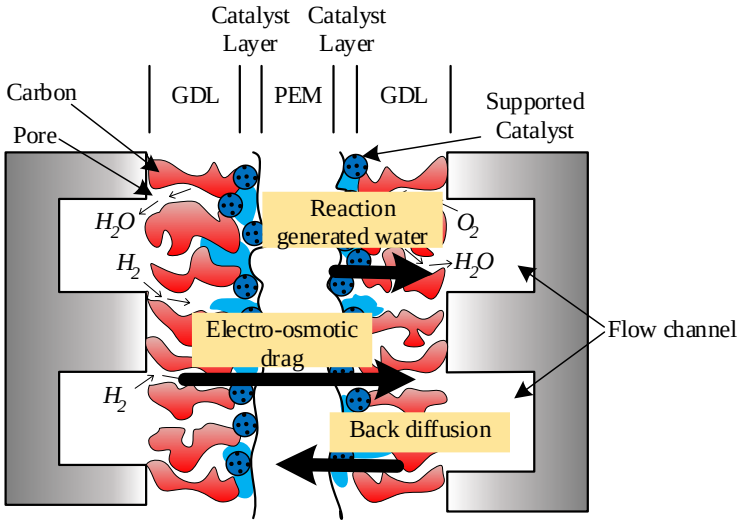

Figure 1-4 The water transport mechanism inside a PEMFC.

- Through the membrane, water is transported by electro-osmotic drag with protons from the anode to the cathode. The electro-osmotic water flow N^{EO} (mol m^{-2} s^{-1}) is proportional to the protons flux:

$$N^{EO} = \xi \frac{I_{FC}}{F} \tag{1-12}$$

with ξ the electro-osmotic drag coefficient.

In addition to the water produced by the electrochemical reaction, this electro-osmotic flux increases the amount of the water at the cathode and then the water content of the membrane may be higher at the cathode side than at the anode side which induces water diffusion in the opposite direction (back diffusion in the figure above).

- In the GDLs, the water vapor is transported by diffusion. As the diffusive flux of vapor depends on the concentration of water in the gas, it is influenced by the temperature field in the cell: The saturated vapor pressure gradient resulting from temperature gradient drives vapor diffusion through the GDLs and consequently, the water preferentially flows to the cold side of the cell [25]. Also, for thermal reasons, or because the amount of vapor is so that the partial pressure reached the saturated value, water may condense in the GDL. In porous materials, liquid water transport is mainly related to its capillary pressure. Liquid water can then be observed in the catalyst layer, in the GDL and in the channels.

- In the channel, the vapor flows with the gases, and under normal conditions, the liquid water is continuously drained out from the cell by the gases. However, liquid can accumulate leading to channel flooding which may block the gas flow.

Associated with water supply (humid gases) and evacuation of the water outside the cell, these mechanisms can cause drying of the polymer used for proton conduction in the catalyst layers and in the membrane, or flooding of the catalyst layers, the GDL, and the channels.

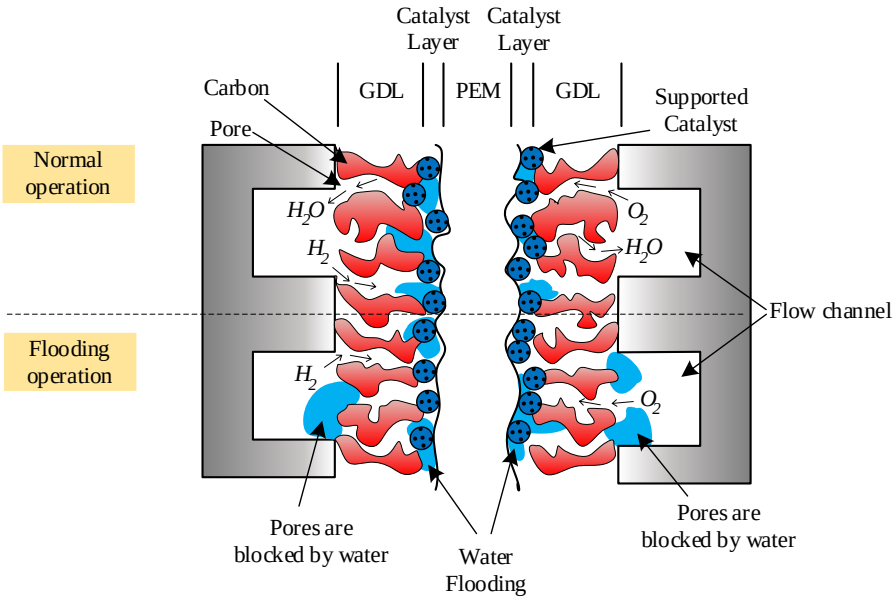

Figure 1-5 Mass transport processes in normal and flooding operations.

Insufficient moisture of the membrane reduces the proton conductivity and therefore increases its ionic resistance. This leads to an increase of the heat production rate, then to an increase of the MEA temperature which may amplify the membrane drying and may degrade it until an FC failure. There are many origins for drying. For instance, high current densities amplified water transport by electroosmosis that may induce membrane drying at the anode side. Furthermore, a temperature difference between the anode and the cathode plates can modify the water transfer (as shown in [25]). This temperature difference may be a consequence of premature aging of one cell which will then produce more heat than the others, it can also result from poor thermal insulation of the end-plates or an imperfect dimensioned cooling system.

Flooding occurs when the rate of drainage is lower than the water production rate. Water is produced from an oxygen reduction reaction (ORR) in the catalyst layer at the cathode (equation 1-2). Under normal operation, water is effectively removed, and enough gas can be passed through the GDL to reach the catalyst. It is important that water must be continually removed from the channel. This is presented in the upper part of Figure 1-5. If liquid water fills the pores in the catalyst layer and in the gas diffusion layer, oxygen and/or hydrogen transport is blocked. This effect which reduces the performance in the FC is presented in the bottom part of Figure 1-5. Flooding may propagate from the catalyst layer to the channels, depending on the gas flow rate.

Therefore, a suitable equilibrium between maintaining a high level of water to ensure high ionic conductivity, and membrane drying or cell flooding must be found to ensure optimum PEMFC efficiency [26].

1.2.4.2. Starvation

Reactant starvation may be caused by water flooding (see the previous section) or it can appear during rapid and large change of the power load because of the generally large response time of the gas supply. Failure of the reactant supply reduces the performance, and it can induce degradation. For instance, a lack of hydrogen at the anode side produces corrosion of the carbon support in the catalyst layer at the cathode. Air starvation at the cathode generally results in a lower cell potential and promotes liquid water accumulation. Remedial action to mitigate this effect requires identification and distinction of the source of fuel starvation, in order to adjust the operating parameters such as flow rate or current density.

1.2.4.3. Impurities

Various impurities may contaminate air and hydrogen and then affect FC efficiency. Some of them have an effect on the catalyst surface at the anode and the cathode sides. These lead to the reduction of the area for the oxygen reduction reaction (ORR) and the hydrogen oxidation reaction (HOR) causing overpotential loss. The issue was found when hydrogen was produced by steam reforming of methane and contained carbon monoxide (CO). CO is the poison of the platinum used as catalyst at the anode [27]. It forms strong bonds with Pt and a small amount is enough to decrease dramatically cell performance. However, it can be eliminated by methods such as air bleeding [28]. Another form of impurities in natural gas reforming hydrogen is hydrogen sulfide. The cathode side is often exposed to airborne pollutants that successfully pass through existing filters before entering the FC system. A common pollutant on this side is sulfur dioxide (SO_2) produced by the burning of fossil fuels.

1.2.4.4. Degradation of the components

PEMFC has multi-component that may degrade continuously during the time. There are three main types of degradation of FC components: mechanical, chemical, and thermal. Mechanical degradations may be due to the pressure difference between hydrogen and oxygen, to gripping force causing stress on the GDL and on the membrane, sometimes because it is a non-uniform on the whole surface of the cell. Chemical degradation generally concerns ionomer in the membrane (leading to the reduction of the membrane thickness) and in the catalyst layer, it may also concern some loss of PTFE in the GDL and in the MPL, and bipolar plate corrosion, loss of catalyst, etc. Thermal degradation is caused by too high temperature in the MEA (membrane cannot operate at temperature close to 100°C) which also induce insufficient gas humidity.

- **Gas diffusion layer (GDL) degradation**

Mechanical and chemical are the causes of degrading GDLs that affect the ability to transfer the input gasses to the anode and the cathode reaction sites. The mechanical degradation of GDL is due to the compression on the GDL which can break the carbon fibers, modify the pore

size and finally reduce or block the gas passageways. Another damage of GDL is the loss of Teflon® (PTFE) supported by the fibers: a loss of hydrophobic material promotes flooding. Although, temperature and humidity variations can slowly destroy the carbon in the GDL and the MPL.

- **Membrane degradation**

The membrane degradation led to gas crossover (gas can cross the membrane) and this issue significantly reduce the power of FC. A too high temperature degrades the membrane [29] and a structural failure has been observed after cycling the relative humidity of the gas between 30% to 80%.

- **Catalyst degradation**

There are many factors of catalyst degradation. First, platinum particles become ions and ions repeatedly accumulated on the large platinum particles or dissolve and then migrate from the catalyst layer to near areas. This issue decreases the available catalyst surface on both sides (anode and cathode). The power loss is the result of this problem. In addition, carbon corrosion is another important issue of degradation. The FC catalyst is also affected by the oxidation of platinum particles. This oxidation creates surface films of platinum oxide that reduce the available catalyst surface area which increases the loss of power [30]- [31].

1.2.5. PEMFC management

To obtain a system with high power, multiple fuel cells are needed to build a FC stack. Fuel cell control system strategies must consider of the main problem associated of energy harvesting. The purpose of the PEMFC management system is to make the electrochemical reaction more efficient and operate in suitable conditions.

Figure 1-6 illustrate general PEMFC management systems which consist of water management, thermal management, humidity management, fuel management, and power management. Most of them are linked.

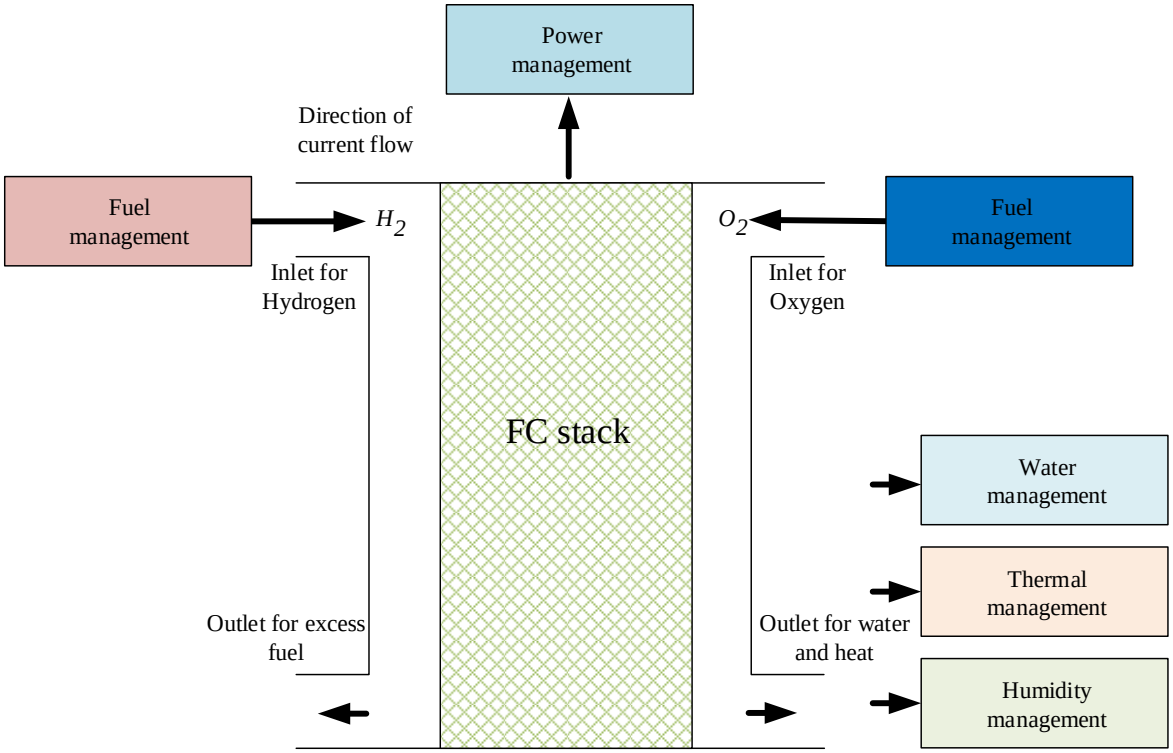

Figure 1-6 PEMFC management system.

1.2.5.1. Water management

By changing the current density, the water production and the electroosmotic water flux through the membrane are modified. As the saturation pressure also depends on the temperature, the water content into a cell is modified by a change of the temperature – for instance, a lower temperature allows to increase the relative humidity of the gases. The dry gas flow rate is an operating parameter that affects the water content, in addition to the control of the relative humidity at the inlet presented in the following section.

1.2.5.2. Gas humidity management

Maintaining proper cell humidity allows having a high protonic conductivity. It can be controlled by feeding the cell with humid gases instead of dry gases. Different types of humidifiers can be used for PEMFC: nozzle spray, gas bubbling (gas flows through a hot water tank), enthalpy wheel (limited use due to its complexity), and membrane humidifier. This last method is the most commonly used to control the humidity of the air at the inlet. Water is transferred through a membrane from the humid air at the outlet of the cathode to the dry air. Then, the humidity of the gases at the inlet can be modified to ensure efficient operation.

1.2.5.3. Thermal management

The operating temperature of PEMFC is about 60-80°C. In addition to water, the FC also produced heat due to the ohmic losses and overpotentials. Maintaining the temperature in a controlled range avoid heat build-up and drying, and then degradations [32]. Due to the strong link between the relative humidity and the temperature (by means of the saturated pressure),

and between water transport and temperature gradients, the humidity of the cell depends on the heat management.

The thermal controller operates under the setpoint temperature, based on the measurement of a temperature sensor located at the inlet or the outlet of the cooling system. Different types of the cooling system are used:

- Heat spreader is a passive cooling technique for PEMFC. Several advantages of this method are simple to design, low parasitic losses, no need for a cooling system. thereby improving the overall efficiency of the stack. This method requires good thermal conductivity of the materials [33].
- Air cooling method uses the passing air on the cathode side. It is simple, reduced in size, reduced weight, and reduced costs due to the heat dissipation channel integrated into the cathode. However, this method suits only a small system.
- Liquid cooling is mostly used for high-power PEMFC. Generally, deionized water flows in channels machined inside the bipolar plates. The heat is removed in an external heat exchanger.
- Phase Change Material (PCM) could be used as a coolant. This method which has a high cooling rate and can distribute evenly the temperature suit for large FC systems is complex.

1.2.5.4. Gases management

Hydrogen and oxygen must be supplied to the FC in sufficient quantity to generate the electrical energy required by the load.

The stoichiometric amount of hydrogen $N_{H_2}(\text{mol s}^{-1})$ needed for a current intensity I (A) produced by an FC stack composed with n_{cell} cells is:

$$N_{H_2} = n_{cell}\frac{I}{2F} \tag{1-13}$$

Hydrogen is generally provided to the cell with a small excess in the order of 1% to 5%, the higher excess is used if a recirculating system exists. The hydrogen is stored at high pressure in a tank, a pressure controller is used at the inlet. Hydrogen can be humidified or not.

The stoichiometric amount of oxygen $N_{O_2}(\text{mol s}^{-1})$ needed for a current intensity I (A) produced by an FC stack composed with n_{cell} cells is:

$$N_{O_2} = n_{cell}\frac{I}{4F} \tag{1-14}$$

PEMFC is generally fed by air in excess. Then the air molar flow rate at the inlet is:

$$N_{\text{air}} = n_{cell}\frac{I}{4F} \times 4.76 \times \gamma \tag{1-15}$$

with γ the excess coefficient in the order of 2 to 5. The air is supplied by a compressor, which must control the flow rate or the pressure of air which is also humidified before entering the FC stack. The delayed supply of oxygen to FCs is due to the long response time of all the devices use for the air system and can lead to oxygen starvation problems when the load suddenly changes [34]- [35]. Gas flow rate can be modified to solve water management issues (such as flooding).

1.2.5.5. Power management

Power management systems are used to control the flow of electrical energy from unstable sources through electrical equipment that efficiently processes, filters and distributes electricity. The voltage of a FC stack decreases when the current increases during higher load demands. Therefore, the current of FC stack must be controlled by the power management subsystem to obtain sufficient power from the FC stack to the load and to control the electricity to meet the load in terms of voltage and current.

1.2.6. Fuel cell stack and Multi-stack

A single PEM fuel cell produces a low voltage that is insufficient for practical use. Therefore, several cells are assembled in series where the cathode of one cell is connected to the anode of another cell. They formed a fuel cell stack shown in Figure 1-7. The main components of FC stack are similar to a single fuel cell, excepted the gas flow channel plates between each cell, because there are gas flow channels on both sides and they are called bipolar plate: One side of the plate guides the hydrogen into the anode of one cell, and the other side brings air into the cathode of the next cell. The number n_{cell} of cells in the stack allows to calculated the stack voltage $V_{FC_{stack}}$:

$$V_{FC_{stack}} = n_{cell} \times V_{FC_{cell}} \tag{1-16}$$

The purpose of making a fuel cell stack is to increase the total power. Two main parameters that affect the power of the fuel cell stack are the active surface area S (m²) which gives the current intensity delivered by the fuel cell (I_{FC} S). The power is given by:

$$P_{stack} = n_{cell} \times V_{FC_{cell}} \times I_{FC} \times S \tag{1-17}$$

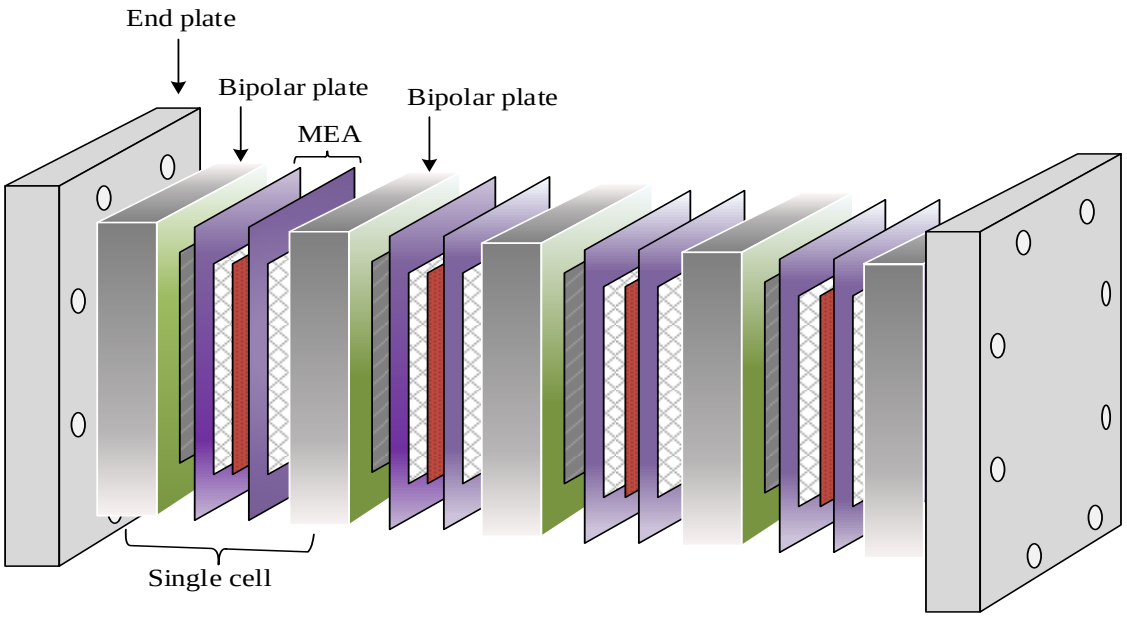

Figure 1-7 A typical fuel cells stack.

To be efficient in the design of the gas flow channel, the gas must be evenly distributed throughout the cells. Uneven distribution of gases causes unequal distribution of the cell voltage in the stack. This results in low energy efficiency and the cells may have a shorter lifespan. The objective of gas flow channel design is that the gas supply must be as efficient as possible. In addition, the design of flow channel should consider other factors such water and heat management, and pressure in the system.

To reach very high power, several stacks are associated to form a multi-stack system. The gas circuits dedicated to supply O_2 and H_2 in a multi-stack system can be categorized in three different structures: parallel distribution (Figure 1-8 (a)), series distribution (Figure 1-8 (b)), and combination series-parallel (Figure 1-8 (c)). In a parallel configuration, the common channel of O_2 and H_2 supply gas to the inlet of each stack. However, this type increase size and cost [36]. In the series configuration, the gases are fed at the inlet of the first FC stack, the outgoing gas being the incoming gas of the next stack. The commonly used gas flow channel for flat panel fuel cells is parallel flow channel. A combination of parallel and series gas supply can also be considered.

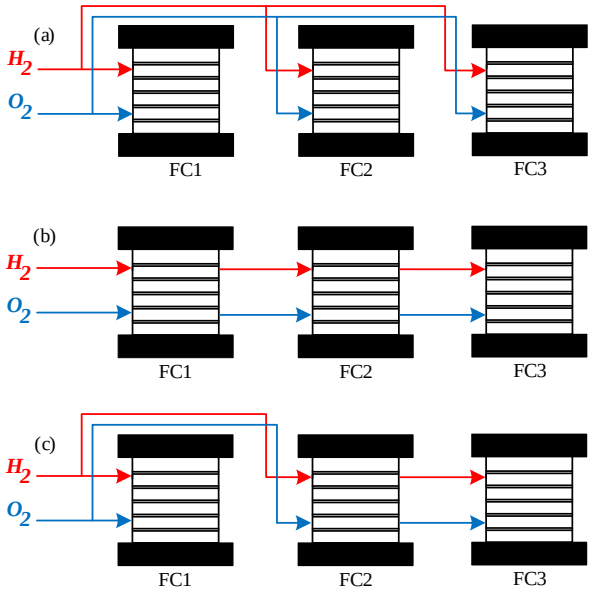

Figure 1-8 Structure of fluidic circuit, (a) parallel distribution. (b) series distribution and (c) combination series-parallel.

1.2.7. Electrical architecture of multi-stack fuel cell

The multi-stack fuel cell architecture (MFC architecture) has performance in a wider power range than a single stack fuel cell. This section is dedicated to a comparison of different MFC electrical architectures. The method of distributing the energy makes the design process easier when increasing or decreasing the number of fuel cell stacks depending on the chosen architecture. The MFC architecture allows degraded operation when some part of the system fails.

The MFC system links multiple FC stack together through architecture. The electric architecture can be used series, parallel or series-parallel systems. The fluidic architecture of MFC system was mentioned in the preceding section.

1.2.7.1. Multi-stack series architecture

Figure 1-9 shows several fuel cells stacks connected in series with one power converter. This architecture has low gain values which produce less stress on the converter. However, the output power of the stack is limited by the state of the weakest cell. When one of the series-connected stacks is underperforming, the stack power decreases leading to reduced total power of the system. Besides, the fuel cell cannot be controlled individually [37]. If the stack contains malfunctioning or defective cells, the whole system must be taken out of service until major repairs are done [38]- [39]. Although, placing a diode in an anti-parallel position with each of the FC stacks and a switch to disconnect the degraded stacks, malfunctioning FCs can be bypassed. Performing a soft restart using the diode bypass systems requires an interruption in the power delivery, which might not be acceptable [40].

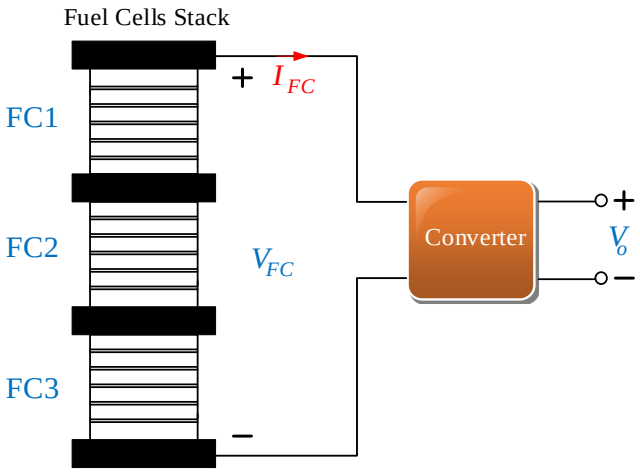

Figure 1-9 Fuel Cells are connected in series architecture.

1.2.7.2. Multi-stack parallel architecture

Figure 1-10 shows stacks connected with their own power converter through output voltage [41]. This architecture uses a redundancy power converter. Furthermore, this system can be controlled individual fuel cell stacks. The voltage gain will be higher than the series configurations and lead to higher stress on the converter too. In degradation mode, the system can be operated without any addition to the system.

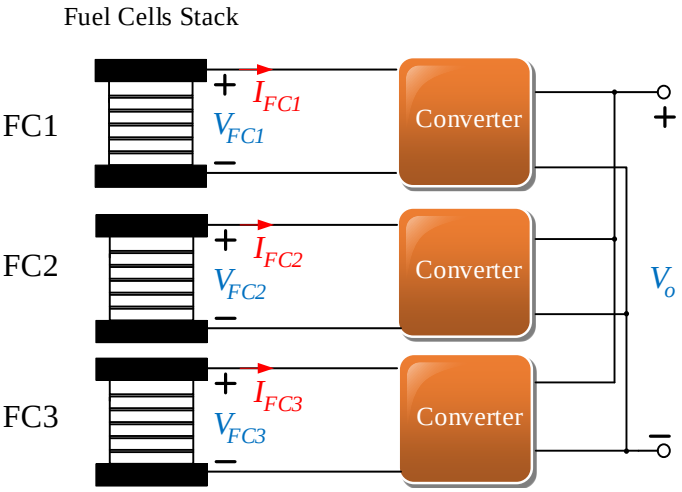

Figure 1-10 Fuel Cell Stacks are connected in a parallel architecture.

1.2.7.3. Multi-stack cascade architecture

Cascade architecture is presented in Figure 1-11. Each FC stack is connected to each converter through the output voltage. However, this system is unlike the parallel architecture due to the global output voltage being divided among the FC converters. This division leads to low stress on the power converter and could lead to lower-cost solutions. The system proposed the following advantages. Firstly, the modular fuel fell can be independently controller by each DC-DC converter. Secondly, limiting load current can reduce the internal losses in the FC.

Thirdly, the DC-DC converter can be controlled to bypass the faulty section. Finally, under fault conditions, the driver can steer the vehicle to a safe location at reduced power mode until faulty stack sections can be shut down.

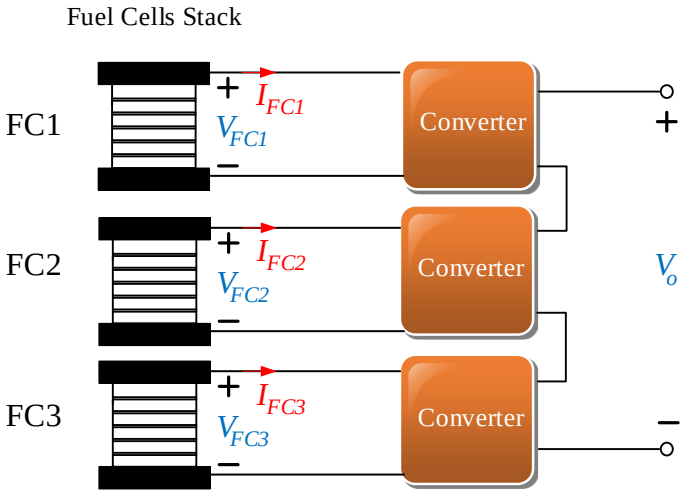

Figure 1-11 Fuel Cell Stacks are connected in cascade architecture.

1.2.7.4. Multi-stack series-parallel architecture

The series-parallel system presented in Figure 1-14 is a collaboration between series and parallel architecture. This system provides benefits and drawbacks of each configuration. The voltage ratio is less than the parallel system. Moreover, the power of the system is shared between the different series. The number of power converters is decreased and lead to reducing the stress of the converter. These capabilities endure as well. Furthermore, this architecture can be controlled individual series and use distribution methods.

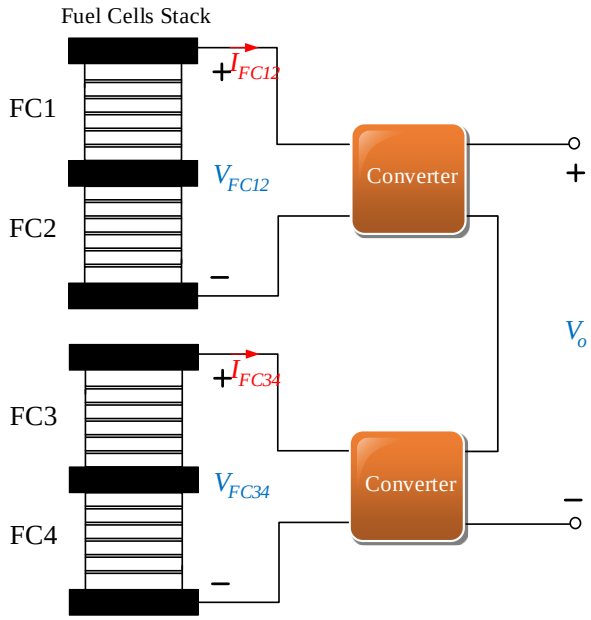

Figure 1-12 A modular fuel cell powered by a modular dc-dc converter.

1.3. Storage device

Worldwide energy consumption and environmental impacts encourage the widespread adoption of renewable energy. One of concern is the alternative to adequate energy storage from a variety of renewable energy sources. Indeed, electric power is generated for the continuous demands, and when the needed generating power is beyond its capacity, the energy storage device [ESD] system is essential [42]- [43].

The invention of storage devices was developed in the middle of the 1800s by a French physicist named Gaston Planté with the concept of storage in the form of lead-acid batteries. Since then, there have been many developments in the battery sector. In the 1950s, electrical engineers began to use porous carbon electrodes to fabricate capacitors. A low voltage capacitor using porous electrodes was proposed in 1957. After that, the first patent was filed in 1970 by Donald L Boosin. Scientists research electrochemical capacitor systems with activated carbon electrodes that is a fundamental property of supercapacitors and batteries. Since 1990, Maxwell Research Institute has introduced "Boost caps" as high-energy supercapacitors. Until now, it has been developed for demanding applications.

The Ragone plot facilitates the selection of a working area for energy storage [44]. The relation between power density and energy density is described in Figure . This figure compares the storage systems in batteries, supercapacitors (SCs), and capacitors. It can be observed that the batteries provide high energy density but low power density. They are heavy, bulky, and cannot be recycled. Conventional capacitors provide high power density and have a long lifespan. Its disadvantage is low energy density. The SCs are a bridge between batteries and capacitors, the energy density of SCs being higher than the capacitors, and the power density of SCs being higher than batteries.

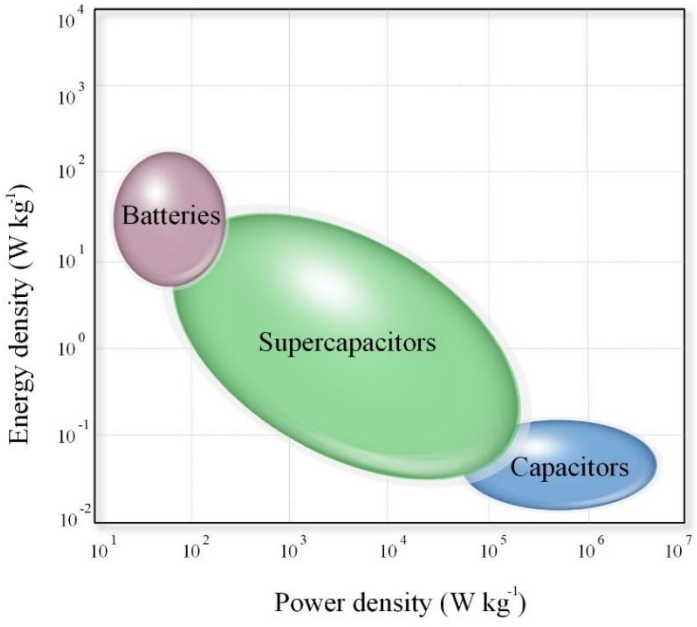

Figure 1-13 Ragone plot for different energy storage systems.

Finally, supercapacitors are developed under the dominant difference between batteries and capacitors. Thus, their advantage is its featherweight, flexible, portable, fast response, and high

robustness that leads to greater performance such as high energy density and high power density [45].

1.3.1. Supercapacitor

Developed electrochemical capacitors called "Supercapacitors (SCs)" or ultracapacitors are proposed as alternative storage for stand-alone and hybrid applications with another storage device. The storage mechanism of SC is based on the principle of charge separation. SCs can be reused with almost unlimited charge and discharge. Supercapacitors are electrical storage devices that can deliver a high amount of energy in a short time. It has excellent specific performance and is often used to manage high power peaks. Therefore, it is suitable for use in applications with high dynamic loads. This feature is good for transport applications with good acceleration.

1.3.1.1. Principle of supercapacitor

The primary structure of a supercapacitor is shown in Figure 1-15. The current collectors collect electrons and support the electrode material. Their conductivity and the contact resistance with the electrode affect directly the power density and capacitance of SC. Generally, an electrode is made out of activated carbon which is impregnated in an organic or aqueous electrolyte. The electrodes are named on their electrical polarities, the positive electrode having a higher electric potential than the negative electrode, the current flows from the anode to the cathode, and then it passes to the external circuit. A separator isolates the two electrodes to prevent a short circuit between them and allows ions to pass through.

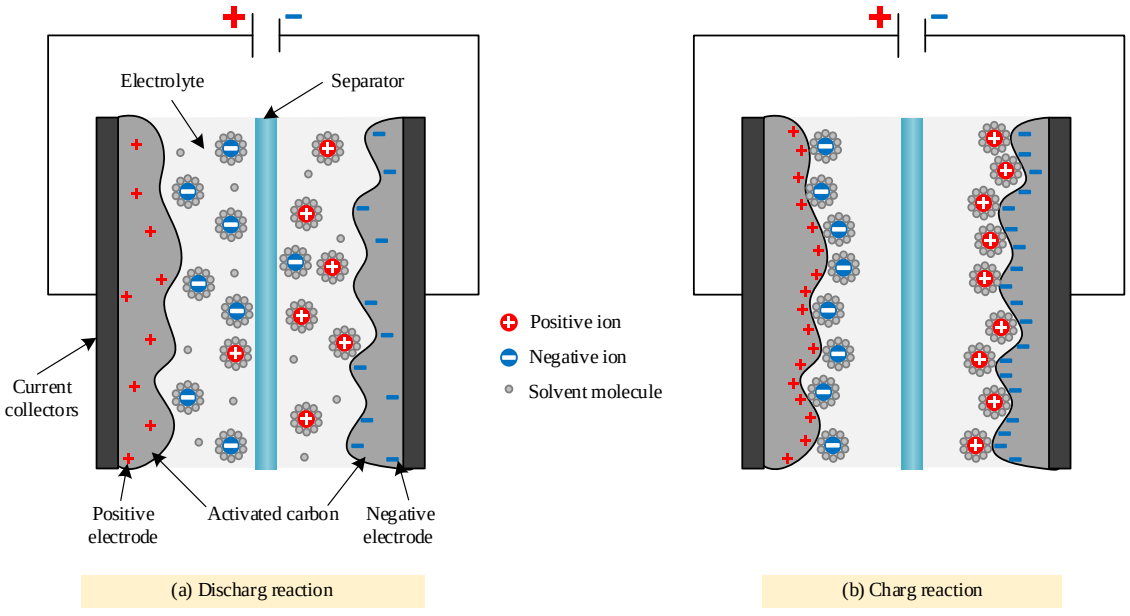

Figure 1-14 Supercapacitor structure and working principle when (a) discharge and (b) Charge.

The principle of operation of SC is based on the storage of energy via the ions which distribute from the electrolyte around the surface of the two electrodes. Three basic types of

SCs are represented in Figure 1-15. They depend on the energy storage mechanisms. SC can be divided into Electrical double-layer capacitors (EDLS) and pseudocapacitors.

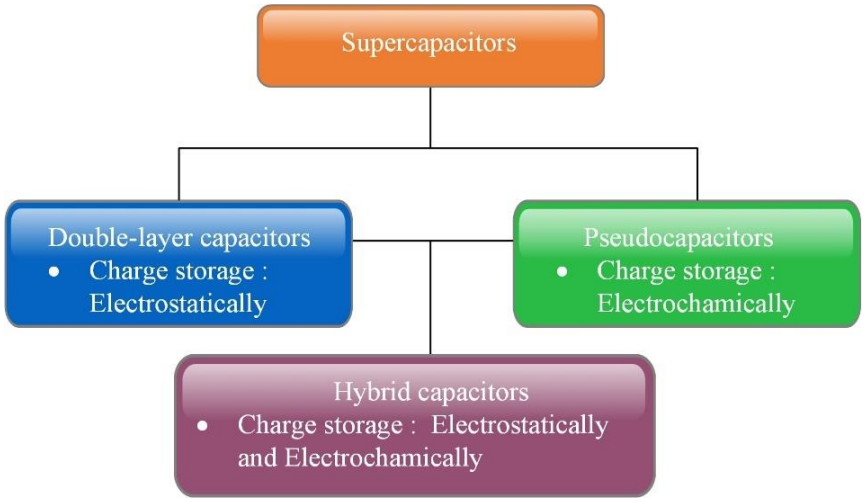

Figure 1-15 Storage mechanisms classification of supercapacitors.

- **Electric double-layer capacitors (EDLCs)**: the charge storage of this capacitor occurs at the interface between the electrode and electrolyte. Naturally, the surface of the charge is surrounded by a shell of the solvent. The active material is attached to the current collector which is connected to an external circuit. The materials for an electrode are carbon powder, fibers or felts. The energy storage principle of EDLCs is to store electrostatic charges at the electrodes interface. The charge density on electrodes surface is depended on the applied voltage.

- **Pseudocapacitor**: this type involves reversible and faradic reactions to store the charges which can be stored electrochemically between electrode and electrolyte. The oxidation takes place on the electrode surface. It is almost similar to battery operation. The reaction involves moving charges through two layers. The capacitance is the result of the specific thermodynamic relationship between the extent of charge acceptance and the change of voltage [46]. While compared with EDLC, pseudocapacitors have higher energy density and specific capacitance. Therefore, this type is suitable for applications requiring high energy density. Issues of this kind are still being debated. They found two reasons which are low power density and less circulating capacity. The main disadvantage is the irreversible reversal of the chemical reaction dynamics. The reason for this is the faster deterioration of the electrode. On the other side, energy capability is limited by reaction dynamics.

- **Hybrid capacitors**: They store charge by synergistic capacitive of the EDLCs with pseudocapacitive in order to achieve a higher energy and power density. This type offers the principle of accumulating battery electrode and capacitor type in the same cell. This leads to improvements in energy and power density. The mechanism for this type of storage depends on the electrode material, whether it is polarizable electrodes, such as carbon, or non-polarizable electrodes, such as metal or conducting polymer. In general, metal cations are intercalated and deintercalated [47]. These reactions must be coupled with redox reactions which is called Faradaic behavior. Faradaic and Non-Faradaic

processes accumulate high energy result in better cycle stability and lower cost than EDLCs.

1.3.1.2. Model of supercapacitor

Supercapacitor simulation requires a model to analyze the performance and for performance estimations. The model was analyzed in many forms, from simple models to complex models such as coulombic efficiency, self-discharge, and parasitic inductances. They are represented in the equivalent circuit instead of physical phenomena [48]- [49].

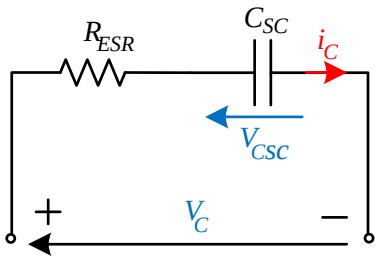

Figure 1-16 simple equivalent circuit of supercapacitor.

A simple model is shown in Figure 1-16, which consists of a capacitor and a resistor connected in series. This model is basic and has only two parameters. It is very fast when simulating on a computer. It is generally used to determine the size of the energy storage and to determine the system efficiency.

The voltage of capacitor C_{sc} can be calculated for the capacitor current i_c and its initial voltage $V_{C_{sc}}(0)$ given as:

$$V_{C_{sc}} = \frac{1}{C_{sc}} \int i_c \, dt + V_{C_{sc}}(0) \tag{1-18}$$

The voltage of the supercapacitor at its terminal V_c can be expressed as:

$$V_c = V_{C_{sc}} + R_{ESR} i_c \tag{1-19}$$

Where V_c is the voltage of supercapacitor, $V_{C_{sc}}$ is the voltage of equivalent serial capacitance C_{sc}, R_{ESR} is equivalent serial resistance and i_c is current of the supercapacitors.

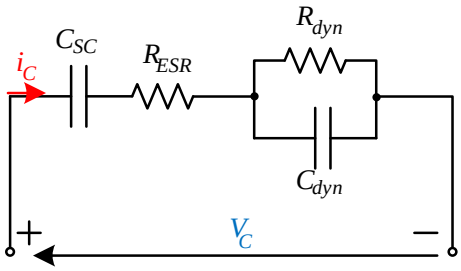

Figure 1-17 equivalent circuit dynamic model of supercapacitor

The dynamic model adds a capacitor and a resistor that are connected in parallel from the simple model. It is represented in Figure 1-17. This model improves accuracy for high-frequency circuits and suits for simulation fast charging and discharging system in supercapacitors.

1.3.1.3. Specific parameters of supercapacitors

For evaluating the SC performance, three essential parameters are capacitance, the voltage of the supercapacitor, and equivalent series resistance. They are often used to assess their energy and power performance. The capacitance is the ratio between the stored charge (q) and the voltage of the supercapacitor. It can be calculated as:

$$C_{sc} = \frac{q}{V_{csc}} \tag{1-20}$$

The current i_c is determined as:

$$i_c = C_{sc} \frac{dV_{csc}}{dt} \tag{1-21}$$

The most important characteristics of the SC are the amount of energy stored and the energy provided. The energy storage of a supercapacitor can be defined as:

$$E = \frac{1}{2} C_{sc} V_{csc}^2 \tag{1-22}$$

The electrical power is generated based on the terminal voltage and the current passing thought and electrical component. It is given by:

$$P = V_c \times i_c \tag{1-23}$$

Considering the simple model shown in Figure 1-16. The energy is converted and wasted as heat in the internal resistance (R_{ESR}) of SC. A particular level of power to be delivered to the external load and is limited by the combination of internal and external resistance. One can find maximum possible power supplies from the following as:

$$P_{max} = \frac{V_{csc}^2}{4\, R_{ESR}} \tag{1-24}$$

1.3.2. Advantages and disadvantages of supercapacitors

The comparisons between the supercapacitor are presented in Table 1-2 [50]- [51]. The terms energy density and power density should be considered for a power system. Supercapacitors have high power density and low energy density. Indeed, batteries have generally a high energy density and low power density. Although, supercapacitors cannot store as much energy as batteries. Therefore, the charge and discharge times in the case of a supercapacitor are always lower than in the case of batteries.

Advantage	Disadvantage
Virtually unlimited lifespan: the lifespan of supercapacitors is considered 1000 times greater than that of batteries.	**Low energy density**: the energy density is lower than batteries (10% at 20% of that of a battery)
Low series resistance: thanks to this property, losses during charging and discharge are lower than for batteries.	**Need for voltage balancing**: this voltage balancing is required
Fast dynamic: supercapacitors can support in charge or in discharge from rapid variations in operating speed.	**Low voltage components**: series connections are necessary to obtain voltages higher than the few volts of an elementary cell
High power density: corresponding to several times those of batteries.	**Price**: the price of supercapacitors is higher than that of batteries.

Table 1-2 Advantages and disadvantages of supercapacitors compared to batteries.

1.4. Conclusions

Fuel cells are highly efficient energy conversion device because it has a one step energy transformation process. The fuel cell power conversion process is environmentally friendly as it produces only water. Fuel cells can operate continuously as long as fuel (hydrogen) and oxidants are fed into the system. There are several types of fuel cells. The most commonly used in automotive applications is Proton Exchange Membrane Fuel Cell (PEMFC). This type of fuel cell operates at low temperatures, small size, and high current density. The main components of PEMFC are membrane, electrodes, gas diffusion layer and bipolar plates. Moreover, the combination of membrane and catalyst layers is called the membrane electrode assembly (MEA).

The essential of FC performance and functionality is polarization curve. The curve is influenced by the operating conditions such as temperature, pressure, gas composition. When these operating conditions change, they will result in the polarization curve and may lead to the degradation of FC. For instance, drying flooding starvation impurities and components degradation. To prevent all of the degradation, the PEMFC management is essential. They consist of water management, thermal management, humidity management, fuel management, and power management.

Supercapacitors are devices to store energy. It can charge and supply energy quickly. It also has a long lifespan. The types involved in this research are Electric double-layer capacitors (EDLCs).

Chapter II

Hybridization architecture

2.1. Introduction

To reduce global warming caused by pollution on Earth, fossil energy must no longer be used [52]. Instead, we need to use renewable energies that respect the environment. Increasing the use of renewable energy is needed for two main reasons: economic reasons due to an increase in fuel prices and environmental reasons due to restrictions from international organizations to reduce toxic emissions.

Hybridization systems working with electric generators and energy storage devices lead to optimal technologies for recent power sources. They are become more popular due to their advantages such as high efficiency, saved energy and low pollution. Hybridization between an energy source such as fuel cell (FC) and storage device, e.g., battery or supercapacitor (SC) has been proposed twenty years ago. The fuel cell system has to supply all the load power including the peak power. It combines two or more sources, not only to highlight the benefits but also to mitigate the disadvantages inherited from each source. It has been used in several applications, for example, vehicular and electric aircraft and standalone micro-grid.

The advantages and disadvantages of these sources can be found as follows. FC is an electrochemical device that produces electricity without any pollution from an electrochemical reaction of hydrogen and oxygen from the air [53]. Both of them need pipes; Moreover, the air supply system needs a pump [54]. Accordingly, the dynamics of FC would be slow. Fuel starvation phenomenon may happen if the supplied gazes' pressures are not sufficient. This might force FC to get a low lifespan [53]. To avoid such a problem, the power dynamics of FC needs to be controlled. Since FC provides high energy density, it is usually used as the main

energy source. In contrast, SC has a low energy density, but it has a high-power density. It can supply and absorb energy rapidly. Therefore, SC is used as an auxiliary source to deliver the different powers of the main source and the load. Moreover, SC has a long-life cycle [55].

Using a large number of DC-DC converters increases system losses and weight and decreases system reliability. Several architectures for FC systems hybridized with SC will be detailed in this chapter. The objective of this chapter is to propose a novel converter structure for a hybrid fuel cell/supercapacitor application in which the fuel cell is hybridized with a bank of supercapacitors. Its benefits include high efficiency and maximum use of supercapacitor energy. The operation and modeling of the converter are presented. Closed-loop controls are provided by using an indirect-sliding mode technique for the inner current loop and the energy control for in outer loop are provided. Finally, the simulation and the experimental results are given to validate the proposed system.

2.2. FC-SC hybridization architecture

Green energy and environmental protection rise to the concept of electric cars instead of petrol cars. Currently, proton exchange membrane fuel cells (PEMFCs) are the main source of vehicles [56]- [57]. Supercapacitors can solve the shortcomings of fuel cells as an additional source. For better performances, the power management between the fuel cell and the supercapacitor is a significant issue in hybrid electric vehicles.

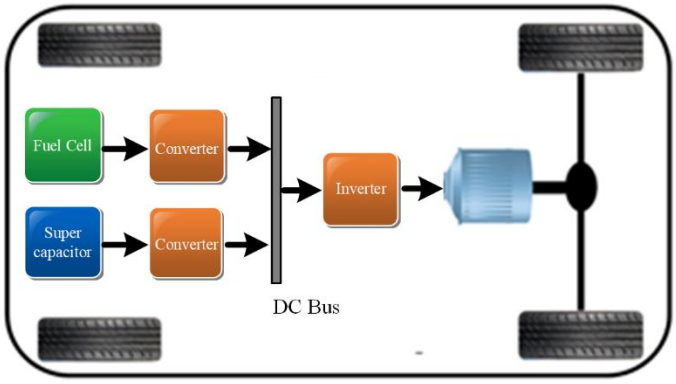

Figure 2-18 Fuel cell/Supercapacitor hybrid for electric vehicle.

In hybrid systems, shown in Figure 2-18, supercapacitors are typically used to provide fast dynamic power, while fuel cells allow to meet average power demands. After presenting the classical hybrid architecture [58]- [59]- [60], the proposed structure will be detailed. It is based on partial power architecture. Isolated DC-DC converter is connected in series between the fuel cell and supercapacitor and allow to take into account fuel cell constraints.

2.2.1. FC-SC directly connected

As Figure 2-19 shows a direct coupling between the fuel cell and SC. It is the simplest architecture and lowest cost, but it cannot directly control power distribution. The constraints of the fuel cells are taken into account according to the system design, leading oversizing of SC. The converter is used to control the DC Bus voltage.

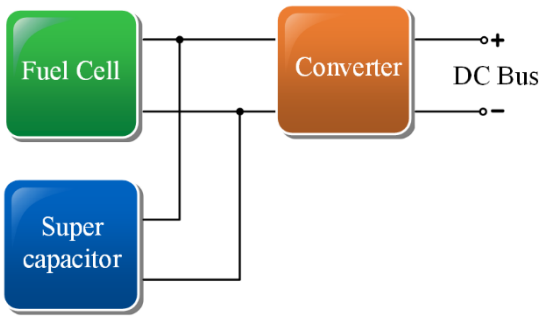

Figure 2-19 Fuel cell directly connected with supercapacitor.

2.2.2. SC connected on dc bus

As shown in Figure 2-20, a DC/DC converter is used to connect to FC to DC bus and the SC is connected directly on DC bus. The advantage of this architecture is that it can control power and protect the fuel cell. However, the structure cannot make the best use of the SC because the SC operates in a narrow range of voltage.

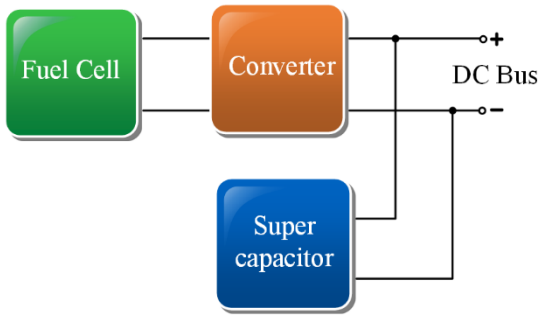

Figure 2-20 One converter connected to FC and SC directly connected to the DC bus.

2.2.3. SC connected through DC-DC converter

SC is connected to FC via a DC/DC converter, as shown in Figure 2-21, In fact, for this architecture, the constraints of FC can be meet by indirect control thanks to the SC converter. The advantage is that it can control power flow and make the most use of the SC. However, the topology requires a high-performance control algorithm to protect the fuel cell. The second converter is used to control the DC Bus voltage.

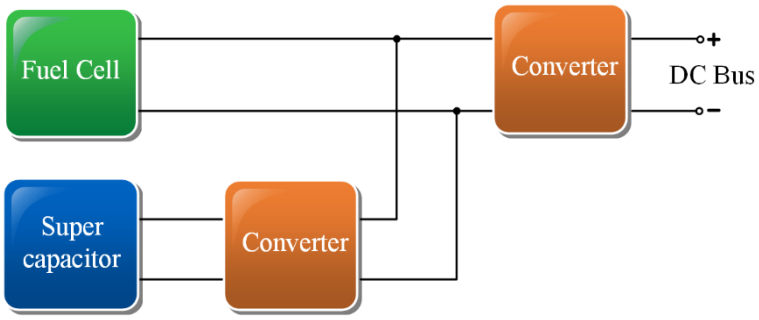

Figure 2-21 Supercapacitor connected with its converter.

2.2.4. FC and SC connected with its converter

The two converters allow controlling the instantaneous power of the SC and the FC, as represented in Figure 2-22. In this case, the constraints of the fuel cell, like the maximum value of the power and the dynamic of the current, and the constraints of SC, such as the maximum value of voltage and power, can easily be taken into account. However, the large number of DC/DC converters increases the losses and weight and reduces the system's reliability. Therefore, the reduction of the DC/DC converter number reduces the system's losses and the weight as well as volume. The third converter is used to control the DC Bus voltage if high voltage ratio is required.

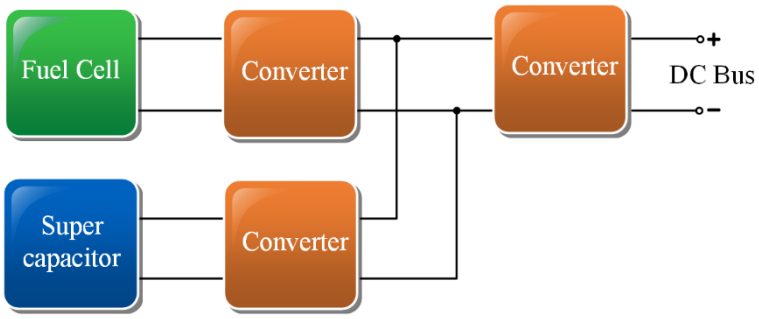

Figure 2-22 Fuel cell and supercapacitor connected with 3 converters.

2.2.5. Series converter

The novel power electronic architecture is proposed in Figure 2-23. An isolated DC-DC converter is serially connected between FC and SC. FC constraints can be meet with this converter without oversizing of SC. Theoretically, its efficiency is unity when FC and SC voltages are the same. This condition is obtained in steady state. In order to increase the use of electrostatic energy stored in SC, its voltage could decrease to half of its rated voltage value. In this case, SC provides almost 75% of the maximum stored energy.

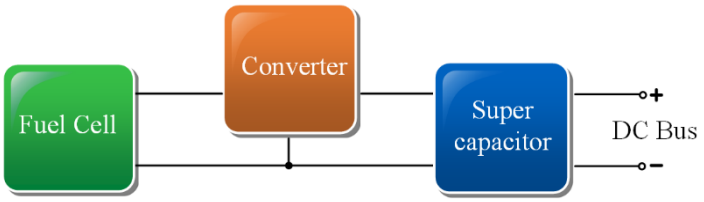

Figure 2-23 Series converter architecture.

2.3. Proposed series hybrid system and proposed power converter

This section proposes an analytical model for the series converter. This converter can be operated as a series voltage regulator. A topology is inspired by a partial power converter (PPC) shown in Figure 2-24. This topology is presented in order to increase the efficiency of the system [61]- [62]. In literature [63]- [64], the LC filter is connected to the output of the

converter. But for the proposed topology, the voltage V_{AB} is a high-frequency square wave obtained thanks to PWM strategy.

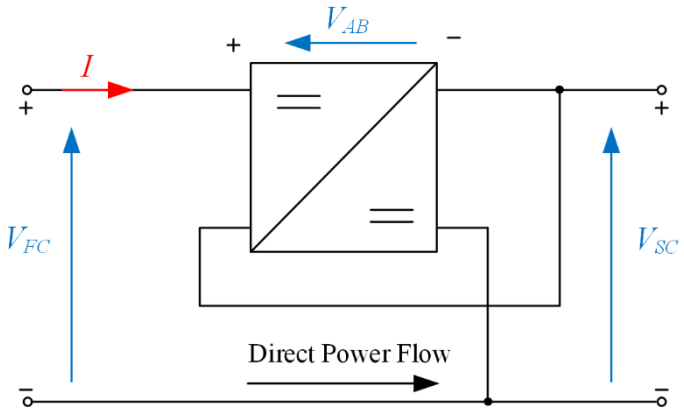

Figure 2-24 Partial power converter topology.

The proposed architecture is detailed in Figure 2-25 where the current I can be controlled. For this application, there is only positive current flows from FC to SC and to the load. There are two switches K_2 and K_3. Each switch is connected to a diode to support the negative voltage. Both switches are used to rectify the voltage fed by the multi-winding transformer to provide the voltage V_{AB}.

When the system is in a steady state, the averaged voltage can be defined by

$$V_{FC} = V_{SC} + V_{AB} \tag{2-25}$$

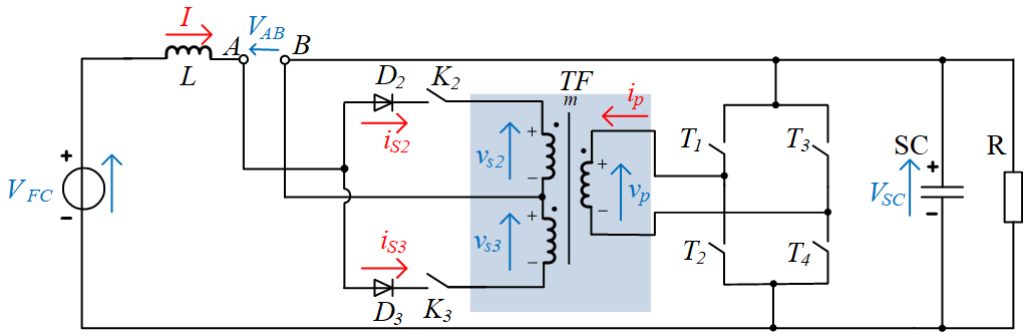

Figure 2-25 Proposed schematic of FC/SC hybrid using a series DC-DC converter.

There are two operation modes defined by the polarity of V_{AB}, which are a negative value ($V_{AB} < 0$) and positive value ($V_{AB} > 0$). Negative value of V_{AB} is obtained when $V_{FC} > V_{SC}$ and positive value of V_{AB} is obtained when $V_{FC} < V_{SC}$.

2.3.1. Modeling of series converter

To study the proposed converter, we use the multi-winding transformer model detailed in Figure 2-26. The H-bridge inverter is used to generate AC voltage of the primary side of the

transformer (v_p). The magnetic flux inside the core of the transformer is modelled through magnetizing inductance (L_m) placed in primary side. The magnetizing inductances and leakage inductances, as well as parasitic resistances, are presented on the primary side, which are $L_m, L_{f1}, L_{f2}, L_{f3}, r_{f1}, r_{f2}$ and r_{f3} respectively. Where i_{f1}, i_{f2}, i_{f3} are currents flown through the leakage inductances and i_{S2}, i_{s3} are currents on the secondary side. For this modelisation, we consider ideal switches and we neglected the core losses.

According to the model in Figure 2-26, the primary side current (i_p) is a sum of current magnetizing (i_m) and current of leakage inductances L_{f1} (i_{f1})

$$i_p = i_m + i_{f1} \tag{2-26}$$

According to Figure 2-26, the leakage inductances current (i_{f1}) can be calculated by summing the leakage inductances currents i_{f2} and i_{f3}.

$$i_{f1} = i_{f2} + i_{f3} \tag{2-27}$$

The relationship between the current at the primary side i_{f2} and i_{f3} and the secondary side i_{s2} and i_{s3} can be defined according to the ratio m of the transformer.

$$i_{f2} = -m i_{S2} \tag{2-28}$$

$$i_{f3} = m i_{S3} \tag{2-29}$$

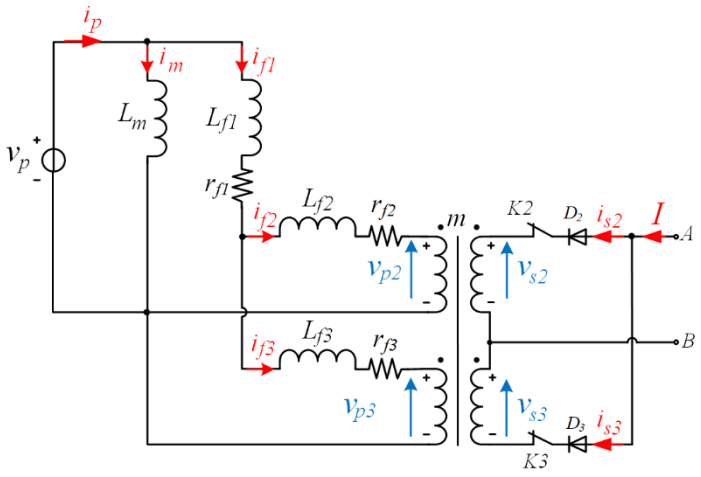

Figure 2-26 Multi-winding transformer considering parasitic parameters.

the current I is the sum of the current i_{S2} and i_{S3}.

$$I = i_{S2} + i_{S3} \tag{2-30}$$

From Figure 2-26, putting equations (2-28), (2-29) into (2-27). After that, using equation (2-30), the leakage inductances current (i_{f1}) can be rewritten as:

$$i_{f1} = m(I - 2i_{S2}) = mI + 2i_{f2}$$
$$i_{f1} = m(2i_{S3} - I) = 2i_{f3} - mI \quad (2\text{-}31)$$

From equation (2-32), since the current I is constant, the time derivative of i_{f1} can be found as:

$$\frac{di_{f1}}{dt} = \frac{d}{dt}(mI + 2i_{f2}) = 2\frac{di_{f2}}{dt} = \frac{d}{dt}(2i_{f3} - mI) = 2\frac{di_{f3}}{dt} \quad (2\text{-}32)$$

2.3.2. Operation and modeling sequence

2.3.2.1. Negative mode (Case $V_{AB} < 0$)

In this mode the voltage V_{AB} is negative. The current I flow from the fuel cell to the supercapacitor. There are six sequences to operate the series converter in negative mode. Figure 2-27 illustrates the waveform of voltage v_p, including the waveforms of command signals for switches K2 and K3.

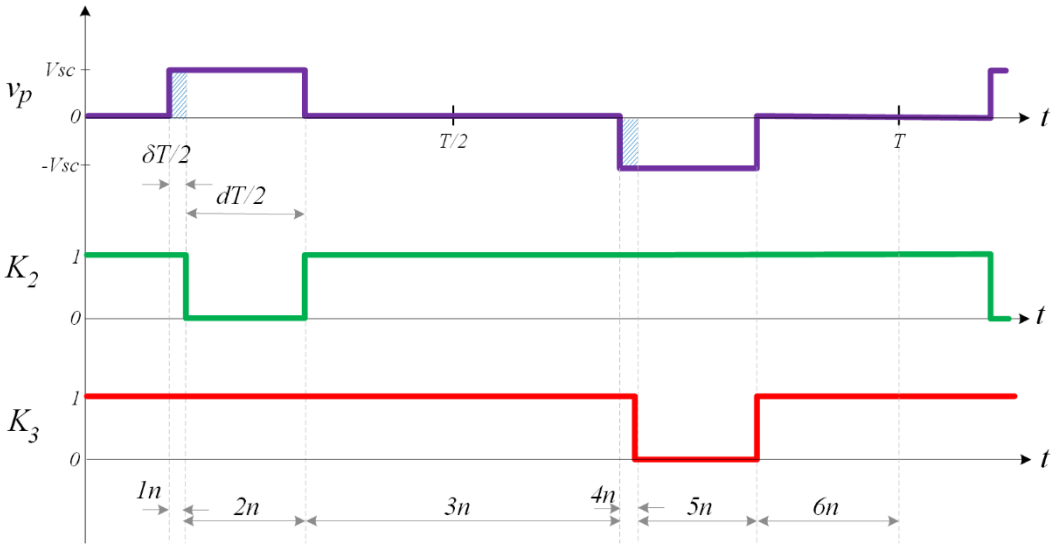

Figure 2-27 Key waveforms of the series converter for $V_{AB} < 0$.

Sequence 1n: The control signals during this sequence are defined in Figure 2-27 and the equivalent circuit is defined in Figure 2-28 sequence 1n. The control signal of the H-bridge inverter allows to have V_p positive. Its duration is $(\delta\frac{T}{2})$. Switches K2 and K3 are turned ON. The differential equation of the currents i_m is expressed as:

$$L_m\frac{di_m}{dt} = v_p \quad (2\text{-}33)$$

The differential equations on the primary side of the transformer can be defined by:

$$-v_p + L_{f1}\frac{di_{f1}}{dt} + r_{f1}i_{f1} + L_{f2}\frac{di_{f2}}{dt} + r_{f2}i_{f2} + v_{p2} = 0 \quad (2\text{-}34)$$

$$-v_p + L_{f1}\frac{di_{f1}}{dt} + r_{f1}i_{f1} + L_{f3}\frac{di_{f3}}{dt} + r_{f3}i_{f3} + v_{p3} = 0 \quad (2\text{-}35)$$

Since K2 and K3 conduct, the voltages v_{p2} and v_{p3} verifies:

$$v_{S2} + v_{S3} = 0 \text{ thus } v_{p2} + v_{p3} = 0 \quad (2\text{-}36)$$

From equation (2-34) and (2-35), we obtain

$$2v_p = L_{f2}\frac{di_{f2}}{dt} + r_{f2}i_{f2} + L_{f3}\frac{di_{f3}}{dt} + r_{f3}i_{f3} + 2L_{f1}\frac{di_{f1}}{dt} + 2(r_{f1}i_{f1}) \quad (2\text{-}37)$$

The differential equation of i_{f1}can be defined by:

$$\left(\frac{L_{f2}+L_{f3}}{2} + 2L_{f1}\right)\frac{di_{f1}}{dt} = 2v_p + \left(\frac{r_{f2}+r_{f3}}{2} + 2r_{f1}\right)i_{f1} - (r_{f3}-r_{f2})m\frac{I}{2} \quad (2\text{-}38)$$

If $r_{f2} = r_{f3} = r_{fs}$, we can obtain:

$$\frac{di_{f1}}{dt} = \frac{v_p - \left(\frac{r_{fs}}{2} + r_{f1}\right)i_{f1}}{\left(\frac{L_{f2}+L_{f3}}{4} + L_{f1}\right)} \quad (2\text{-}39)$$

Using equations (2-28), (2-29) and (2-32), the differential equation of current i_{S2} and i_{S3} can be defined:

$$\frac{di_{S2}}{dt} = -\frac{1}{2m}\frac{di_{f1}}{dt} = -\frac{1}{2m}\frac{v_p - \left(\frac{r_{fs}}{2} + r_{f1}\right)i_{f1}}{\left(\frac{L_{f2}+L_{f3}}{4} + L_{f1}\right)} \quad (2\text{-}40)$$

$$\frac{di_{S3}}{dt} = \frac{1}{2m}\frac{di_{f1}}{dt} = \frac{1}{2m}\frac{v_p - \left(\frac{r_{fs}}{2} + r_{f1}\right)i_{f1}}{\left(\frac{L_{f2}+L_{f3}}{4} + L_{f1}\right)} \quad (2\text{-}41)$$

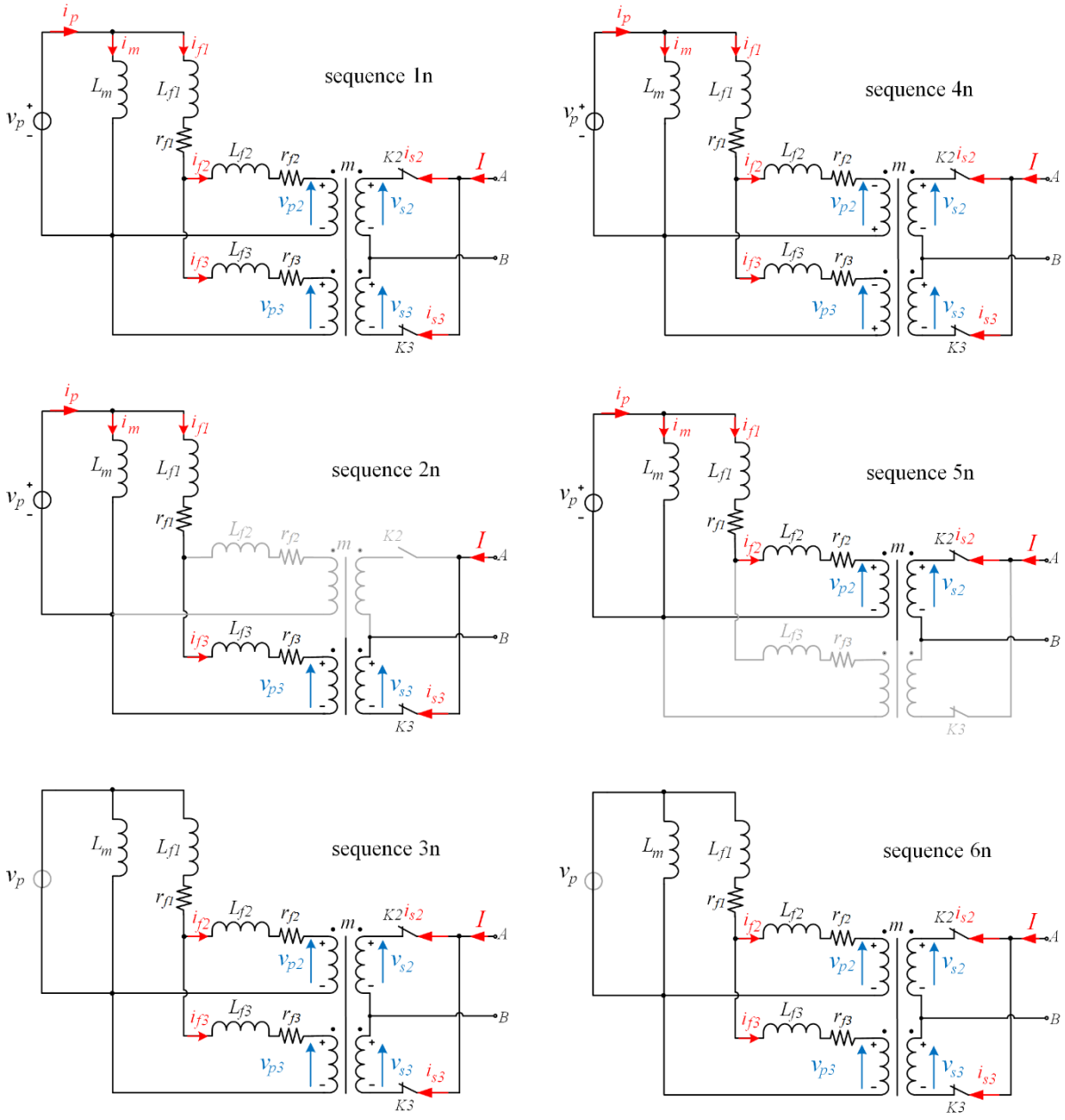

Figure 2-28 Sequence 1n-6n of case $V_{AB} < 0$.

During this sequence, when $v_p = Vsc > 0$, then i_{s2} decreases and i_{s3} increases.

Replacing equation $i_{f2} = \frac{i_{f1}-mI}{2}$ into equation (2-34) and $\frac{di_{f1}}{dt}$ are defined in equation (2-39), it can be rewritten as:

$$v_{p2} = v_p - (\frac{r_{f2}}{2} + r_{f1})i_{f1} + r_{f2}\frac{mI}{2} - \left(L_{f1} + \frac{L_{f2}}{2}\right)\frac{v_p - \left(\frac{r_{f2}}{2}+r_{f1}\right)i_{f1}}{\left(\frac{L_{f2}+L_{f3}}{4}+L_{f1}\right)} \qquad (2\text{-}42)$$

with $L_{f2} = L_{f3}$ and $r_{f2} = r_{f3} = r_{fs}$ the voltage relation can be obtained:

$$v_{p2} = \frac{1}{2} mIr_{fs} \text{ and } v_{s2} = \frac{1}{2} m^2 Ir_{fs} \quad (2\text{-}43)$$

V_{AB} can be defined by:

$$V_{AB} = v_{s2} = \frac{m^2 Ir_{fs}}{2} \approx 0 \quad (2\text{-}44)$$

This sequence ends when i_{S3} reaches I and i_{S2} reaches zero then D_2 turns off. The waveforms are shown in Figure 2-29.

Sequence 2n: The control signals during this sequence are defined in Figure 2-27 and the equivalent circuit is defined in Figure 2-28-sequence 2n. The primary voltage (v_p) is still positive voltage. K2 turn off and K3 still conducts. The time duration of the sequence is ($d\frac{T}{2}$). Where d is duty cycle.

The differential equation of current i_m is defined by:

$$L_m \frac{di_m}{dt} = v_p \quad (2\text{-}45)$$

The differential equation on the primary side can be summarized as:

$$-v_p + L_{f1} \frac{di_{f1}}{dt} + r_{f1} i_{f1} + L_{f3} \frac{di_{f3}}{dt} + r_{f3} i_{f3} + v_{p3} = 0 \quad (2\text{-}46)$$

Because the current i_{f1} and i_{f3} are the same and constant, the voltage v_{p3} can be calculated using (2-46) as:

$$v_{p3} = v_p - (r_{f3} + r_{f1}) mI \quad (2\text{-}47)$$

The voltage at v_{s3} can be defined:

$$v_{S3} = mv_{p3} = mv_p - (r_{f3} + r_{f1}) m^2 I \quad (2\text{-}48)$$

V_{AB} can be defined:

$$V_{AB} = -mv_{p3} = -m\left(v_p - mI\left(r_{f1} + r_{f3}\right)\right) \quad (2\text{-}49)$$

During this sequence, if we suppose that r_{f1} and r_{f3} are close to zero, and the primary voltage equals to the supercapacitor voltage ($v_p = v_{SC}$), so

$$V_{AB} \approx -mV_{sc} \quad (2\text{-}50)$$

The switch K2 is off in this sequence. The equivalent circuit is shown in Figure 2-28 sequence 2n. The voltage of switch K2 can be defined by:

$$v_{S3} + v_{S2} + v_{K2} = 0 \text{ Thus } v_{K2} = -2mV_{sc} \quad (2\text{-}51)$$

The diode connected in serial with K2 is reverse bias. The end of this sequence is defined by the modification of the control signal of the H-bridge inverter. We obtain $v_p = 0$. The waveforms during this sequence are shown in Figure 2-29

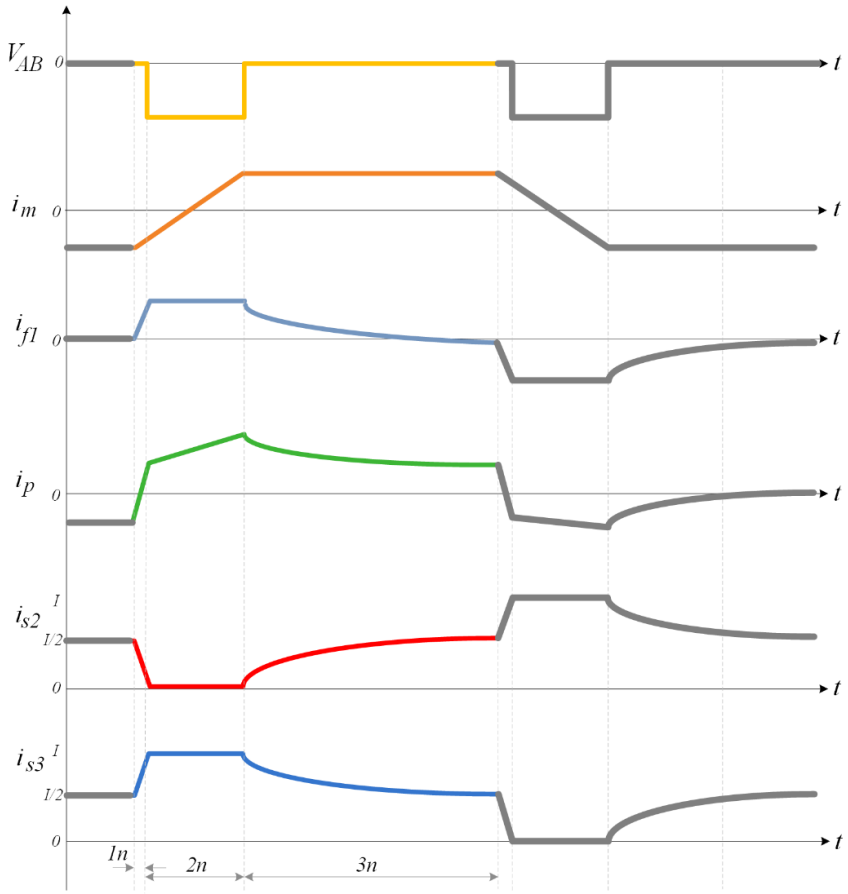

Figure 2-29 Waveform of voltage and current of the series converter when $V_{AB} < 0$. (Sequence 1n-3n)

Sequence 3n: The control signals during this sequence are defined in Figure 2-27 and the active circuit is defined in Figure 2-28 sequence 3n. The primary voltage (V_p) is equal to zero. Switches K2 and K3 are turned on.

The differential equation of the magnetizing current i_m is defined by:

$$L_m \frac{di_m}{dt} = 0 \tag{2-52}$$

The differential equations on the primary side of the transformer can be defined by:

$$-v_{p2} = L_{f1}\frac{di_{f1}}{dt} + r_{f1}i_{f1} + L_{f2}\frac{di_{f2}}{dt} + r_{f2}i_{f2} \tag{2-53}$$

$$-v_{p3} = L_{f1}\frac{di_{f1}}{dt} + r_{f1}i_{f1} + L_{f3}\frac{di_{f3}}{dt} + r_{f3}i_{f3} \tag{2-54}$$

By summing (2-53) to (2-54), with $r_{f2} = r_{f3} = r_{fs}$ and $L_{f2} = L_{f3}$, one can deduce the expression of the current i_{f1}:

$$0 = \left(2L_{f1} + L_{f2}\right)\frac{di_{f1}}{dt} + (2r_{f1} + r_{fs})i_{f1} \tag{2-55}$$

Using (2-31), the differential equations of current i_{f2} and i_{f3} can be defined by:

$$0 = \left(2L_{f1} + L_{f2}\right)2\frac{di_{f2}}{dt} + (2r_{f1} + r_{f2})(mI + 2i_{f2}) \tag{2-56}$$

$$0 = \left(2L_{f1} + L_{f2}\right)2\frac{di_{f3}}{dt} + (2r_{f1} + r_{f2})m(2i_{f3} - mI) \tag{2-57}$$

In steady state, i_{f1}=0, $\frac{di_{f2}}{dt} = 0$, and $\frac{di_{f3}}{dt} = 0$, it leads to

$$i_{S3} = \frac{I}{2}, i_{S2} = -\frac{I}{2} \tag{2-58}$$

From equations (2-53) and (2-54), With $L_{f2} = L_{f3}$ and $r_{f2} = r_{f3} = r_{fs}$ the voltage relations can be obtained:

$$v_{p2} = \frac{1}{2}mIr_{f2} \text{ and } v_{s2} = \frac{1}{2}m^2Ir_{fs} \tag{2-59}$$

$$v_{p3} = -\frac{1}{2}mIr_{f2} \text{ and } v_{s3} = -\frac{1}{2}m^2Ir_{fs} \tag{2-60}$$

In the same manner as in sequence 1n detailed in equation (2-44).

$$V_{AB} = v_{s2} = -v_{s3} = \frac{m^2}{2}Ir_{fs} \approx 0 \tag{2-61}$$

This sequence is finished when the control signals of the H-bridge are modified. The waveforms are shown in Figure 2-29.

Sequence 4n: The control signals for this sequence shown in Figure 2-27 and the circuit is shown Figure 2-30 sequence 4n. The model of the converter in this sequence is the same than for the sequence 1n. In this sequence, the primary voltage $v_p = -V_{sc}$.

The differential equation of current i_m are expressed as:

$$L_m\frac{di_m}{dt} = -V_{sc} \tag{2-62}$$

The current i_{f2} and i_{f3} are replaced by i_{f1} that following equations (2-34)-(2-11). It can be rewritten:

$$2v_p = \left(\frac{L_{f2} + L_{f3}}{2} + 2L_{f1}\right)\frac{di_{f1}}{dt} + \left(\frac{r_{f2} + r_{f3}}{2} + 2r_{f1}\right)i_{f1} + \left(r_{f3} - r_{f2}\right)m\frac{I}{2} \tag{2-63}$$

From equation (2-63), the current i_{f1} can be found as:

$$\frac{di_{f1}}{dt} = \frac{v_p - \left(\frac{r_{f2}}{2} + r_{f1}\right) i_{f1}}{\left(\frac{L_{f2} + L_{f3}}{4} + L_{f1}\right)} \tag{2-64}$$

The voltage between A and B is

$$V_{AB} = mv_{p2} = -mv_{p3} = \frac{m^2 I r_{fs}}{2} \approx 0 \tag{2-65}$$

The differential equations of current i_{S2} and i_{S3} can be defined from the relationship between i_{f1}, $i_{f2}$and i_{f3} following equations (2-28) and (2-29).

$$\frac{di_{S2}}{dt} = -\frac{1}{2m}\frac{di_{f1}}{dt} = -\frac{1}{2m}\frac{v_p - \left(\frac{r_{f2}}{2} + r_{f1}\right) i_{f1}}{\left(\frac{L_{f2} + L_{f3}}{4} + L_{f1}\right)} \tag{2-66}$$

$$\frac{di_{S3}}{dt} = \frac{1}{2m}\frac{di_{f1}}{dt} = \frac{1}{2m}\frac{v_p - \left(\frac{r_{f2}}{2} + r_{f1}\right) i_{f1}}{\left(\frac{L_{f2} + L_{f3}}{4} + L_{f1}\right)} \tag{2-67}$$

According to these equations, the current i_{S3} decrease and the current i_{s2} increase. This sequence terminates when i_{s2} reaches *I* and i_{S3} reaches zero. The waveforms are shown in Figure 2-30.

Sequence 5n: The control signal for this sequence shown in Figure 2-27 and the circuit is shown Figure 2-28 sequence 5n. The waveforms of voltage and currents are given in Figure 2-30. The input voltage is still negative. Moreover, switches K2 is on while switch K3 is turned off. The differential equation of current i_m are as sequence 4n:

$$L_m \frac{di_m}{dt} = v_p \tag{2-68}$$

One can find the differential equation for this sequence as

$$-v_p + L_{f1}\frac{di_{f1}}{dt} + r_{f1}i_{f1} + L_{f2}\frac{di_{f2}}{dt} + r_{f2}i_{f2} + v_{p2} = 0 \tag{2-69}$$

Regarding Figure 2-28 sequence 5n, and waveforms of the currents in Figure 2-30, the currents i_{f1} and i_{f2} are constant. They can be expressed as

$$i_{f1} = i_{f2} = -mi_{S2} = -mI \tag{2-70}$$

The voltage v_{p2} can be calculated as:

$$v_{p2} = v_p - (r_{f2} + r_{f1})mI \tag{2-71}$$

The relationship between voltage primary and secondary side can be found:

$$v_{S2} = mv_p - (r_{f2} + r_{f1})m^2 I \tag{2-72}$$

The voltage V_{AB} for this sequence can be determined as:

$$V_{AB} = -mv_{p2} = -m\left(v_p - mI(r_{f1} + r_{f2})\right) \approx -mV_{sc} \tag{2-73}$$

This mode terminates when $V_p = 0$ and K3 turns off. The waveforms are shown in Figure 2-30.

Sequence 6n: In this sequence, the control signal are detailed in Figure 2-27 and the circuit are shown in Figure 2-28 sequence 6n. This sequence is the same manner as sequence 3n. v_p equals zero, both switches K2 and K3 are turned on. The voltage V_{AB} can be expressed as:

$$V_{AB} = v_{s2} = -v_{s3} = \frac{m^2}{2} I r_{fs} \approx 0 \tag{2-74}$$

This mode terminates when $V_p < 0$. The waveforms are shown in Figure 2-30.

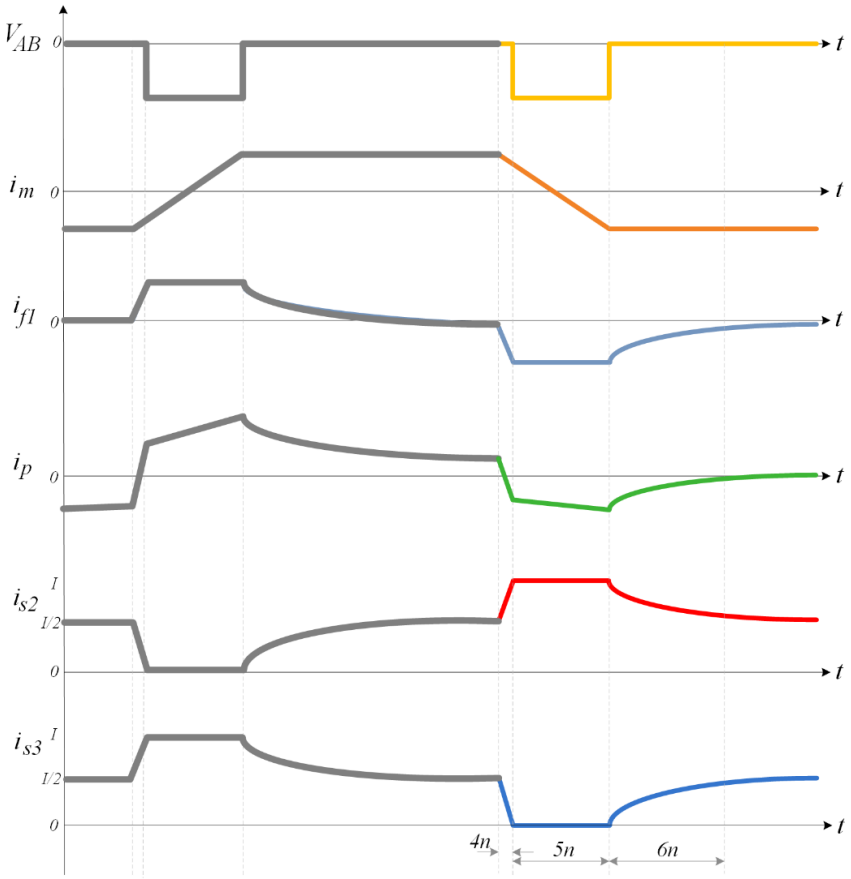

Figure 2-30 Waveform of voltage and current of seriers converter when $V_{AB} < 0$. (Sequence 4n-6n)

2.3.2.2. Positive mode (Case $V_{AB} > 0$)

There are six sequences in positive mode. Figure 2-31 and Figure 2-32 illustrated the circuit in each sequence and proposed the operation of switches K2 and K3.

Sequence 1p: the control signals of this sequence are detailed in Figure 2-31 and the equivalent circuit is shown in Figure 2-32-sequence 1p; this sequence is the same manner as sequence 4n. The control signal of the H-bridge provides the negative of v_p. Switches K2 and K3 are turned on.

In the same manner in Sequence 4n, in this sequence, V_{AB} is:

$$V_{AB} = mv_{p2} = -mv_{p3} = \frac{m^2 I r_{fs}}{2} \approx 0 \tag{2-75}$$

This sequence ends when i_{S2} reaches I and i_{S3} reaches zero then K_3 turns off with ZCS while i_{f1} equals mI. The waveforms are shown in Figure 2-33.

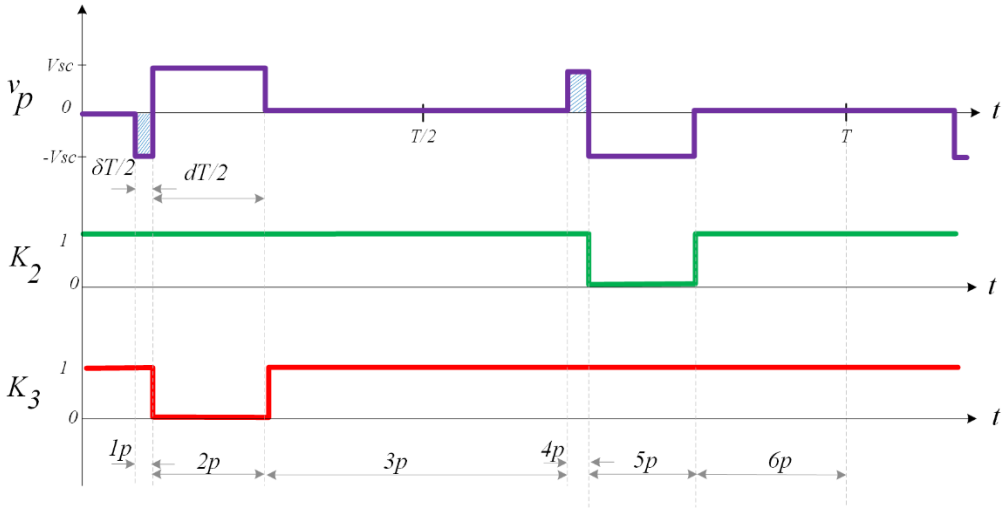

Figure 2-31 Key waveforms of the series converter for $V_{AB} > 0$.

Sequence 2p: In this sequence, the control signals of this sequence are detailed in Figure 2-31 and the equivalent circuit is shown in Figure 2-32 sequence 2p. This sequence is in the same manner as the sequence 5n. However, the primary voltage (v_p) is positive. Switch K2 is conducted while switch K3 is still off. The equations can be derived:

$$-v_p + L_{f1}\frac{di_{f1}}{dt} + r_{f1}i_{f1} + L_{f2}\frac{di_{f2}}{dt} + r_{f2}i_{f2} + v_{p2} = 0 \tag{2-76}$$

The variations of magnetizing currents are expressed as:

$$L_m \frac{di_m}{dt} = v_p \tag{2-77}$$

For this sequence can be defined the value of V_{AB} as:

$$V_{AB} = mv_{p2} = m\left(V_p - mI\left(r_{f1} + r_{f2}\right)\right) \approx mV_{sc} \tag{2-78}$$

This mode terminates with $V_p = 0$ and K3 turns off. The waveforms are shown in Figure 2-33.

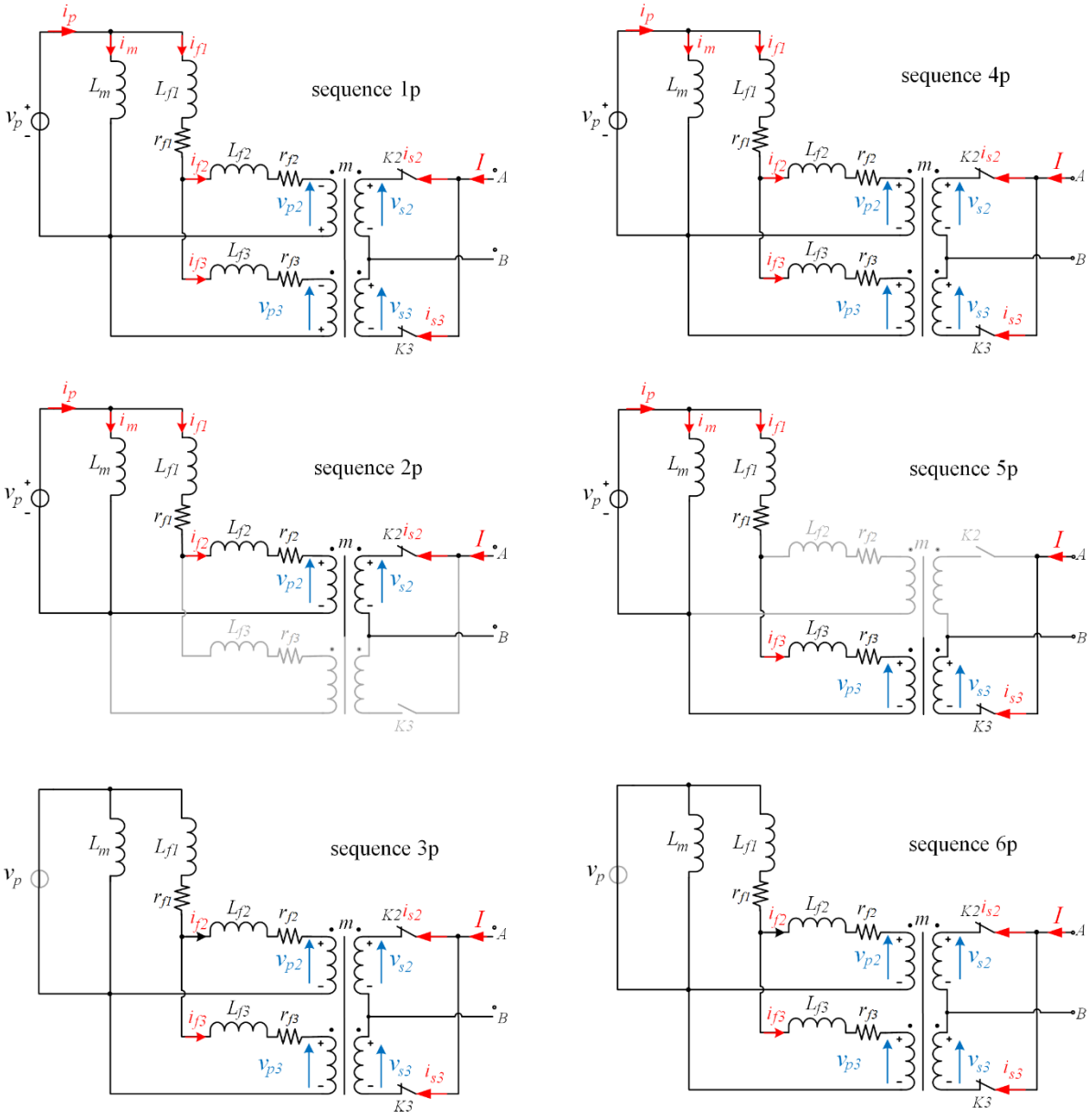

Figure 2-32 Sequence 1p-6p of case $V_{AB} > 0$.

Sequence 3p: In this sequence, the control signal for the system operates in Figure 2-31 and the circuit is shown in Figure 2-32 sequence 3p. This sequence is the same as sequences 3n and 6n. The primary voltage (v_p) is zero. K2 and K3 are conducted. The voltage V_{AB} can be defined as:

$$V_{AB} = v_{s2} = -v_{s3} = \frac{m^2}{2} I r_{fs} \approx 0 \tag{2-79}$$

This mode terminates with $v_p > 0$. K2 and K3 still turned on. The waveforms are shown in Figure 2-33.

Sequence 4p: In this sequence, the control signals of the system are shown inFigure 2-31 and the circuit is shown in Figure 2-32 sequence 4p. The primary voltage v_p of this sequence is positive, switch K2 and switch K3 are turned on. This sequence is in the same manner as sequence 1n.

The voltage V_{AB} is

$$V_{AB} = mv_{s2} = \frac{m^2 I r_{fs}}{2} \approx 0 \tag{2-80}$$

This mode terminates when i_{s2} reaches I and i_{S3} reaches zero and then K_3 turns off with $V_p < 0$. The waveforms are shown in Figure 2-34.

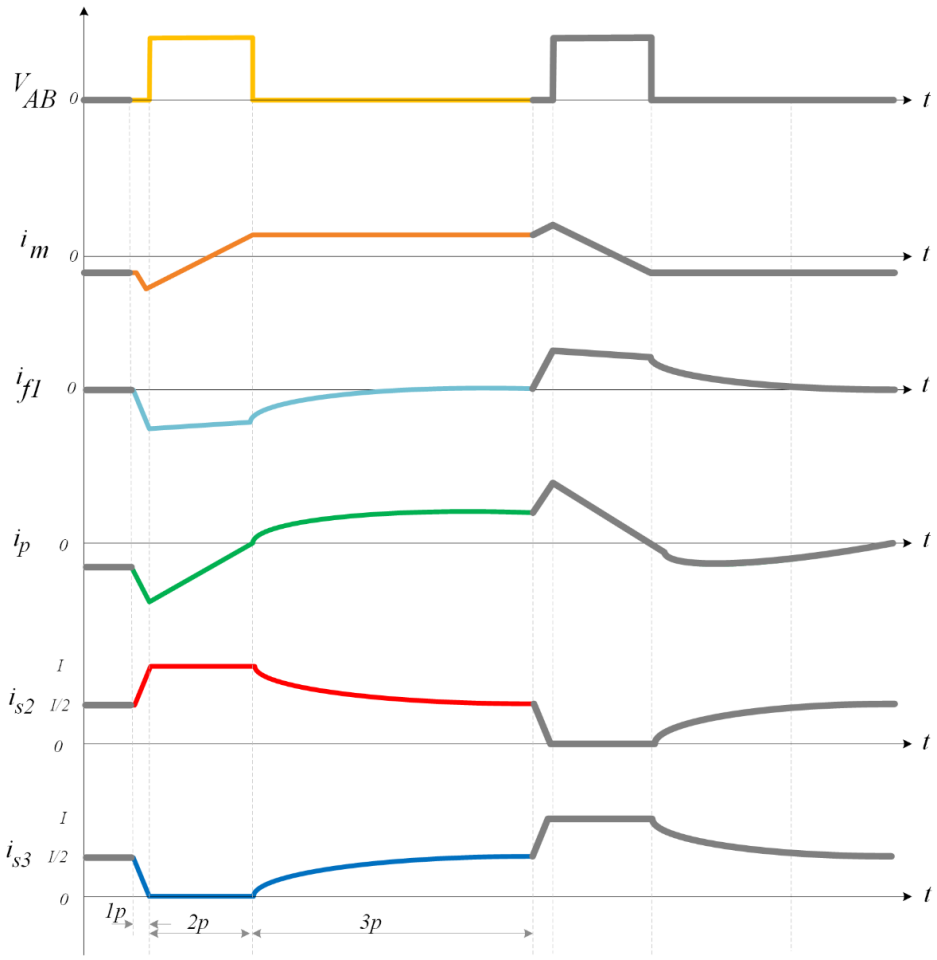

Figure 2-33 Sequence 1p-3p of case $V_{AB} > 0$.

Sequence 5p: In this sequence, the control signals of the system are shown in Figure 2-31 and Figure 2-32 sequence 5p. This sequence is similar to sequence 2n. However, the input voltage v_p is negative, switch K2 is on and K3 is turned off. The derivative equations of the system are as follows:

$$-v_p + L_{f1}\frac{di_{f1}}{dt} + r_{f1}i_{f1} + L_{f3}\frac{di_{f3}}{dt} + r_{f3}i_{f3} + v_{p3} = 0 \quad (2\text{-}81)$$

Regarding Figure 2-32 sequence 5p, the current i_{f1} equal to the current i_{f3}. The voltage v_{p3} can be calculated as:

$$v_{p3} = -v_p - (r_{f3} + r_{f1})mI \quad (2\text{-}82)$$

The relationship between the voltage on the primary and secondary sides can be found:

$$v_{S3} = -mv_p - (r_{f3} + r_{f1})m^2 I \quad (2\text{-}83)$$

V_{AB} for this sequence can be determined in the same manner as detailed in Sequence 5n as:

$$V_{AB} = mv_{p3} = m\left(v_p - mI\left(r_{f1} + r_{f3}\right)\right) \approx mV_{sc} \quad (2\text{-}84)$$

This mode terminates when $V_p = 0$ and K_2 turns on. The waveforms are shown in Figure 2-34.

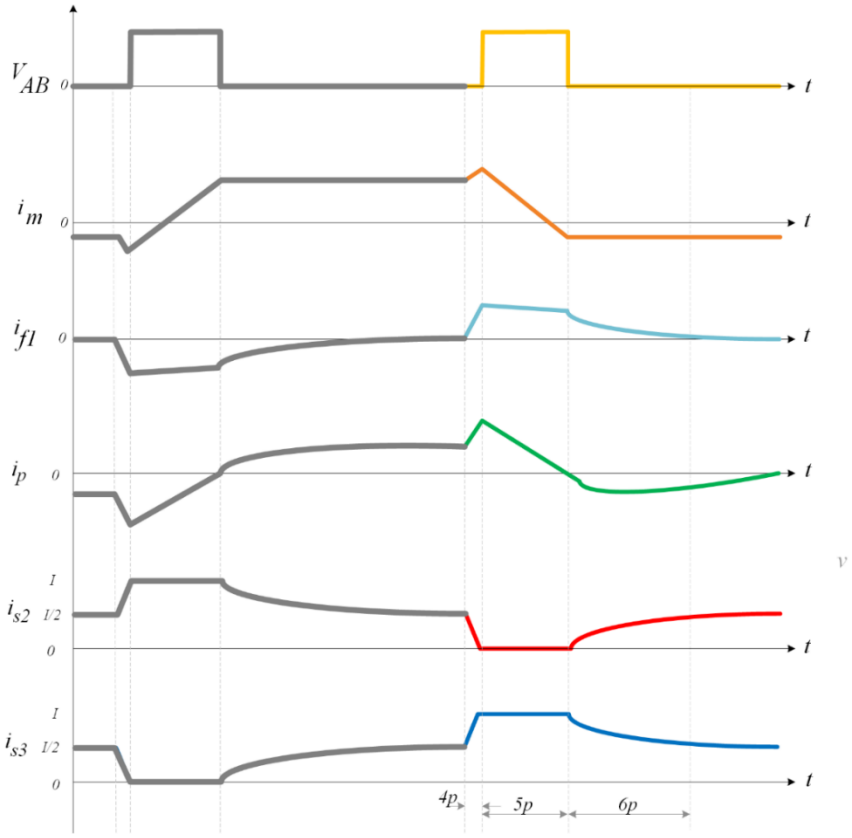

Figure 2-34 Sequence 4p-6p of case $V_{AB} > 0$.

Sequence 6p: In this sequence, the control signals of system are shown in Figure 2-31 and the equivalent circuit is shown in Figure 2-32 sequence 6p. This sequence is in the same manner as sequences 3n, 6n and 3p. The primary voltage is zero. Both switches K2 and K3 are turned on.

The voltage V_{AB} for this sequence can be determined:

$$V_{AB} = v_{s2} = -v_{s3} = \frac{m^2}{2} I r_{fs} \approx 0 \tag{2-85}$$

This mode terminates when $V_p < 0$. The waveforms are shown in Figure 2-34.

2.3.3. Calculation of duration δT

In this section, the duration δT in the primary voltage waveform generated by the inverter for the series converter is discussed. For simplicity, the assumption is made as follows:

- The transformer ratio is $m = k\frac{N2}{N1}$ where k is the coupling coefficient, turn ratio $N1 = 1$ and turn ratio $N2 = 2$.
- The coupling coefficient between the secondary windings is unitary. Thus, the transformer ratio is $m = 2$.
- The switches are proposed as the ideal devices.

The high voltage spike caused by a high current in leakage inductances can be reduced by adding the delta (δ). The zero current switching (ZCS) technique is proposed [65]- [66]. It is presented in the special waveforms (blue square) that can see in Figure 2-27 and Figure 2-31. The objective of this method is to create a zero-current condition for the switch to turn off in order to significantly decrease the switching losses and increase the reliability of the converter. The concept of the delta is adding input voltage before switches K2 and K3 turn off.

At the beginning of this sequence, we can suppose that $i_{S2} = i_{S3} = \frac{I}{2}$. The duration $\delta T/2$ depending on the leakage inductance L_k, fuel cell current I, turn ratio m and supercapacitor voltage V_{SC} can be defined δT as:

$$\frac{\Delta I/2}{\delta T/2} = \frac{V_{sc}}{L_k \cdot m} \tag{2-86}$$

The delta can be defined as:

$$\delta T = \frac{I \cdot L_k \cdot m}{V_{sc}} \tag{2-87}$$

2.4. Generation of primary voltage: V_p

Many research articles have been developed on proper converter design [67]. This section describes the design of the signals for the inverter.

The main requirement for the inverter is to produce and maintain a stable voltage waveform. MOSFET and IGBT are mainly switches used in inverters. The inverter operates at a high switching frequency to reduce the size of the passive devices, while it is often limited by equipment. IGBT has slow switching; it suits switching frequencies lower than 20 kHz [68]. This research uses MOSFET in the full-bridge inverter operating at a switching frequency of 40 kHz for the series converter.

In the series converter architecture, the primary voltage (v_p) is generated by the single-phase inverter or H-bridge inverter fed by the supercapacitor, as shown in Figure 2-35. The voltage v_p is supplied to the primary side of transformer in the series converter circuit.

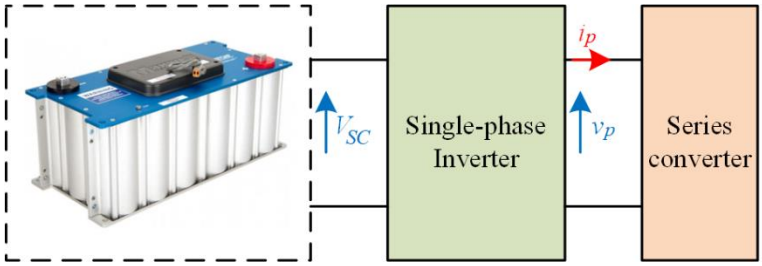

Figure 2-35 supercapacitor fed voltage for single-phase inverter.

A single-phase full-bridge inverter or H-bridge inverter is shown in Figure 2-36. There are two legs with four MOSFETs: T1, T2, T3, and T4. The inverter can generate three different voltage output levels: $+v_p$, 0, and $-v_p$. The waveform of the H-bridge inverter presents in Figure 2-37.

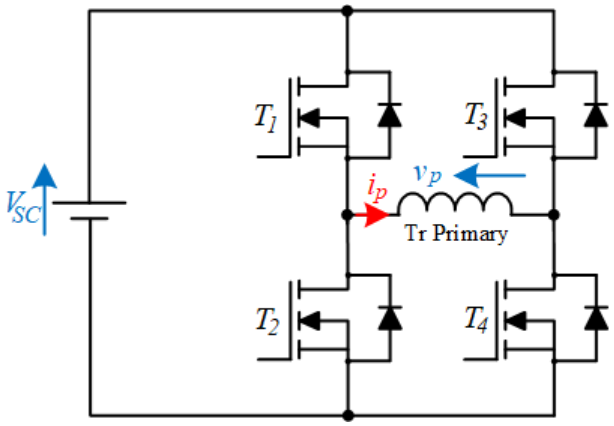

Figure 2-36 Schematic of H-bridge inverter.

The operation of the inverter can be explained using a combination of the four switches' actions presented in Figure 2-37 where the load is the primary winding of the transformer in the following stages:

- ***Stage A:*** T_1 and T_3 are turn ON which give $v_p = 0$.
- ***Stage B:*** T_1 and T_4 are turn ON which give $v_p = +V_{SC}$.
- ***Stage C:*** T_2 and T_4 are turn ON which give $v_p = 0$.
- ***Stage D:*** T_2 and T_3 are turn ON which give $v_p = -V_{SC}$.

Stage A and C provide the V_p equal to zero. T1 and T3 or T2 and T4 are shorted circuit depending on stage A or C, respectively. While the primary current i_p flows in the loop through only two switches, as in Figure 2-38, stages A and C.

Like conventional inverter, dead time should be added for the switching commands for the inverter to achieve perfect waveform of v_p. The method to add the dead time for the pulse-width modulated (PWM) signal for the first leg is presented in Figure 2-39 [69]- [70]. When d is duty cycle, tm is deadtime and T1, T2 are switch command signals for the switches in the same leg. The duty cycle and tm are compared with a triangular wave to generate two switching command signals: T1 and T2.

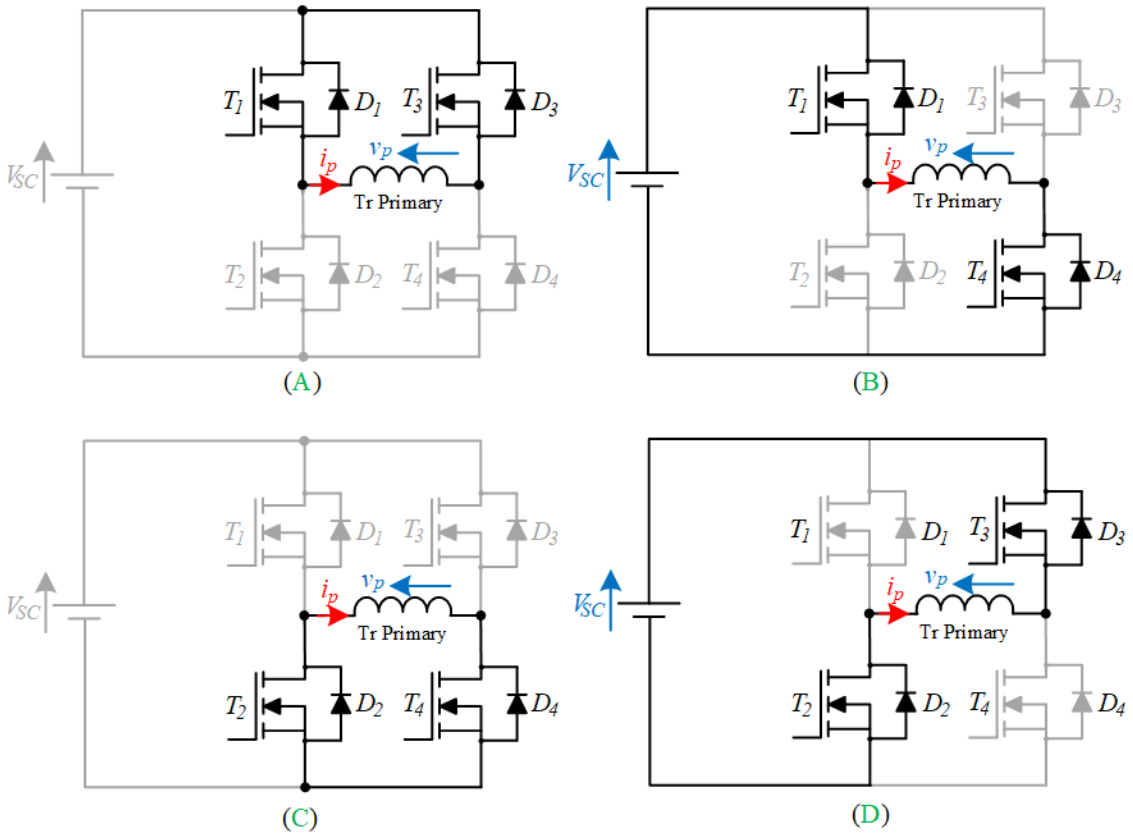

Figure 2-37 Operation of the H-bridge inverter.

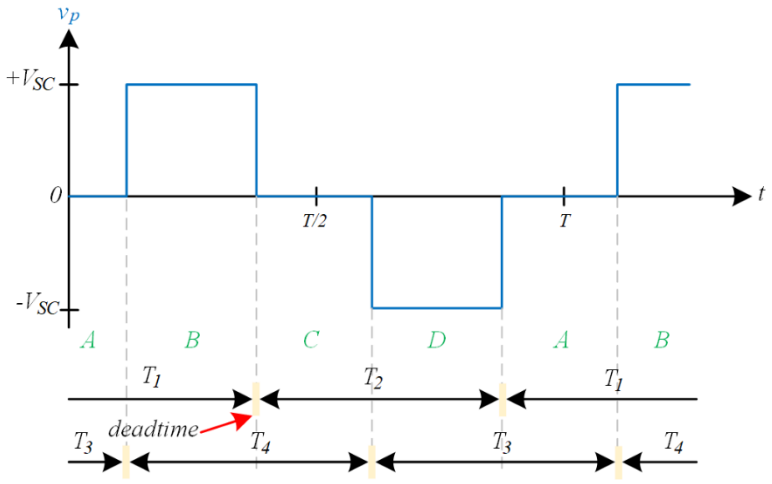

Figure 2-38 the waveform of primary voltage (V_p).

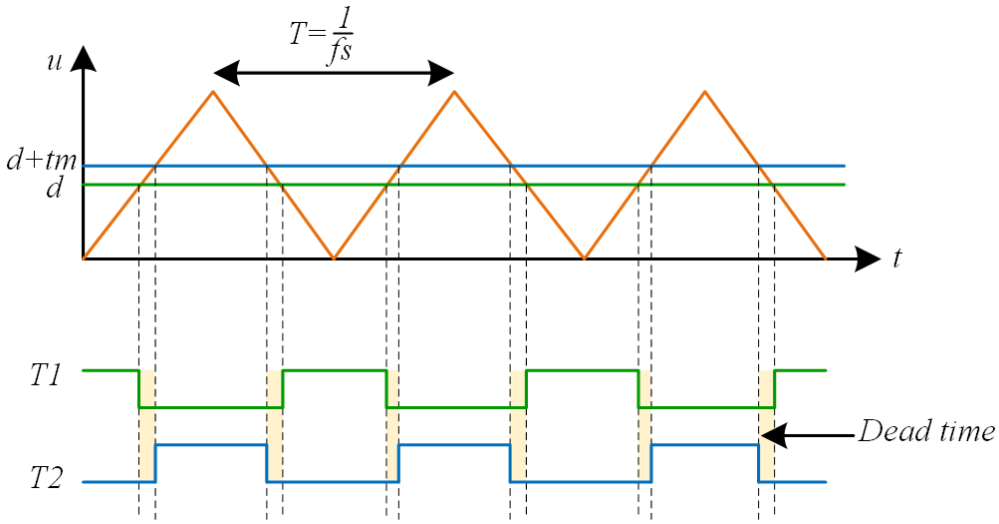

Figure 2-39 Adding dead time between switches T1 and T2.

Choosing the dead time value is very important and should be performed very carefully. The dead time should be chosen as small as possible to ensure the correct operation of the voltage source inverter.

In this work, the controlled switch signals of the inverter are generated by a field-programmable gate array (FPGA). The FPGA belongs to programmable logic devices, and very large-scaled integrated circuits. Also, FPGA is formed as a matrix of configurable logic blocks which can be connected to each other via fully programmable interconnections. The clocking rate can be multiples of 100 MHz. The Xilinx block diagram for programming the FPGA is shown in Figure 2-40. The latency of each signal must be considered to have a proper signal without any glitch. To take into account the propagation delay of Xilinx blocks, the additional blocks have to be used.

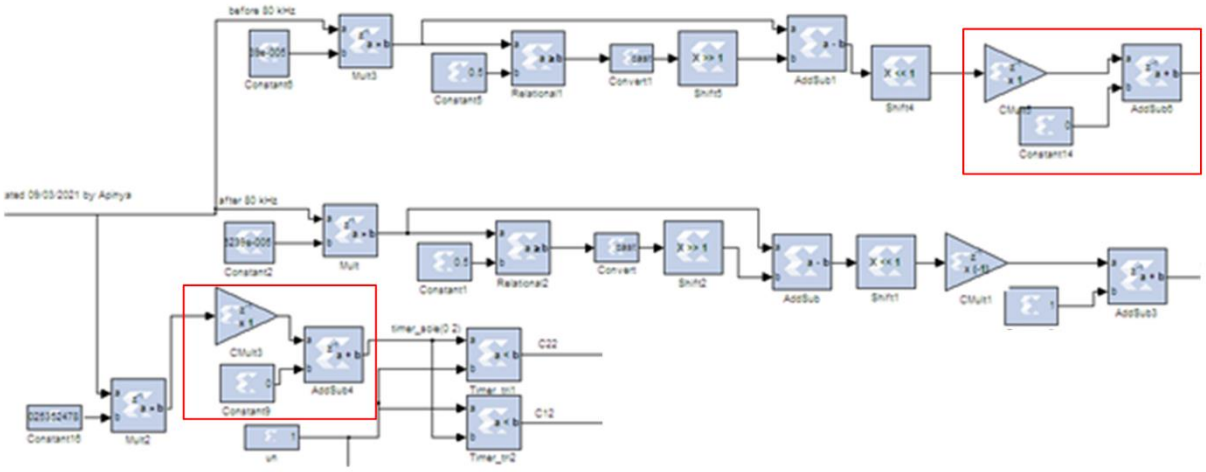

Figure 2-40 Generating triangle signal using FPGA.

The waveforms of all switches are presented in Figure 2-41. For negative mode, four switches of the H-bridge inverter operate at the same switching frequency. However, the switching frequency of T1 and T2 is twice that of T3 and T4 in positive mode when increasing the delta.

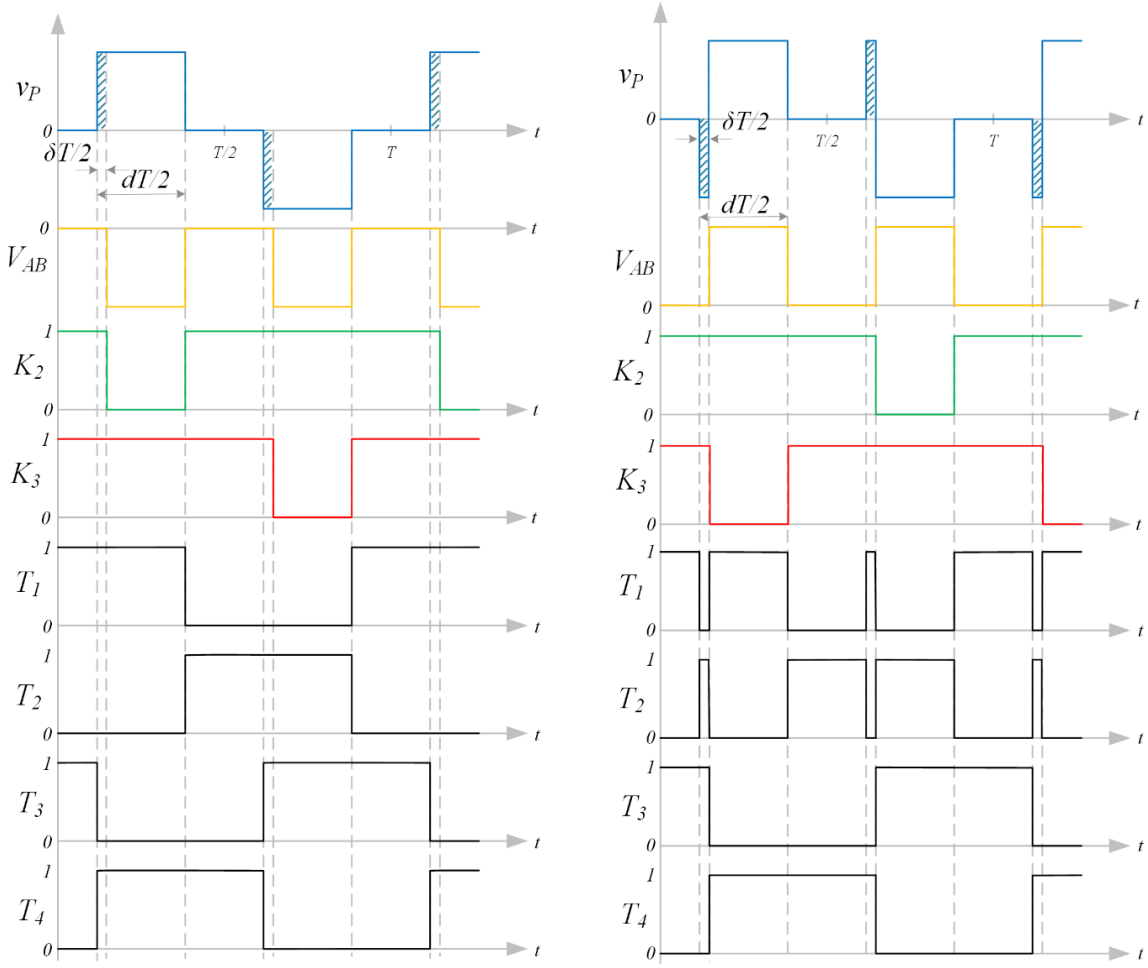

Figure 2-41 Theoretical waveform of controlled signals for (left) negative mode and (right) positive mode.

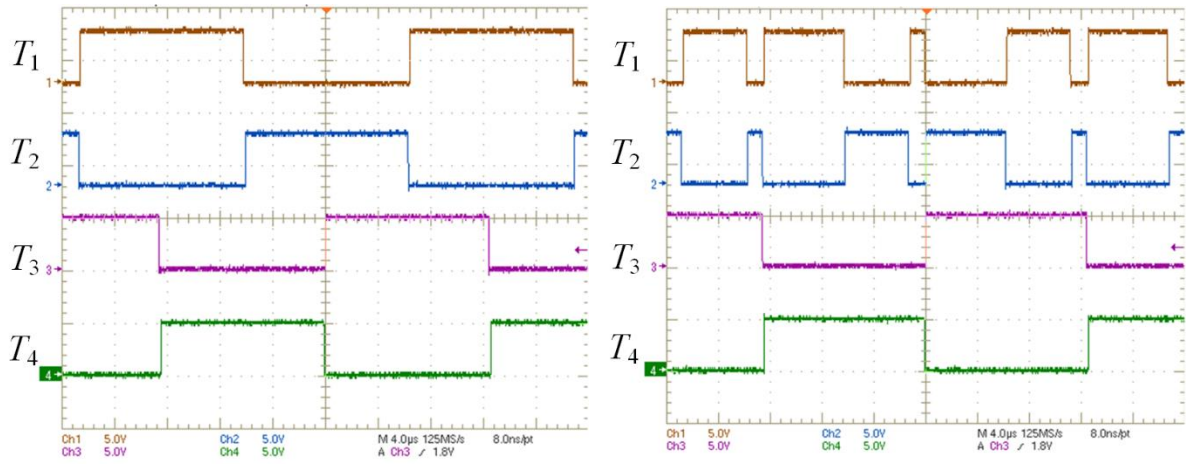

Figure 2-42 Experimental results of the primary voltage with only one deadtime. Left: negative mode (duty: 0.1, delta: 0.05 and deadtime: 0.005), right: positive mode (duty: 0.1, delta: 0.05 and deadtime: 0.005).

Figure 2-42 shows the experimental results of control signal switches of the inverter from FPGA. These results are agreed with the theoretical waveform. Different duty cycles, delta, and deadtime can be implemented.

2.5. Simulation and experimental results in open loop of the series converter

The proposed model is implemented using MATLAB/Simulink. The currents such as i_{f1}, i_{f2}, i_{f3}, i_p, i_m and voltages such as v_{p2}, v_{p3}, v_{s2}, v_{s3}, The proposed model was compared with the one using Simscape power systems blockset in MATLAB/Simulink.

The simulation of the proposed model was built following the flowchart Figure 2-43. The parameters of the system are detailed in Table 2-3. It is started to check the status of the V_p and the operation of switches K2 and K3. When the V_p equal to zero, the process have to check the current i_{S2} which is greater or lower than $\frac{I}{2}$.

Parameter	Value
Maximum FC voltage	12 V
Maximum FC current	15 A
Maximum SC voltage	12 V
Transformer turn ratio $n_p : n_{s1} : n_{s2}$	1:2:2
L_m	56.8 μH
L_{f1}	1.5 μH
$L_{f2} = L_{f3}$	0.58 μH
$r_{f1} = r_{f2} = r_{f3}$	0.2 Ω
Switching frequency	40 kHz

Table 2-3 Parameter of the simulation.

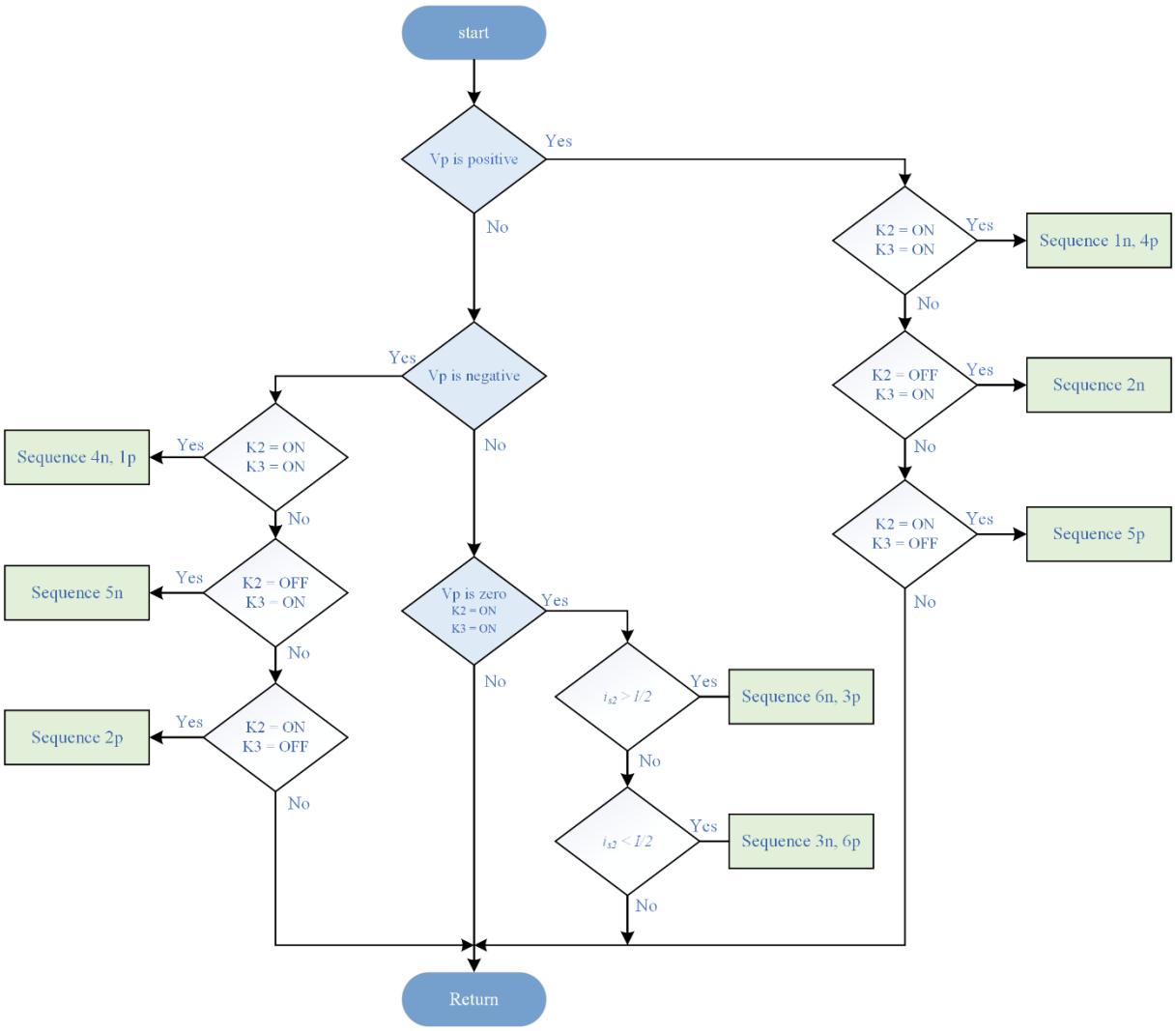

Figure 2-43 Flowchart of sequence of the series converter.

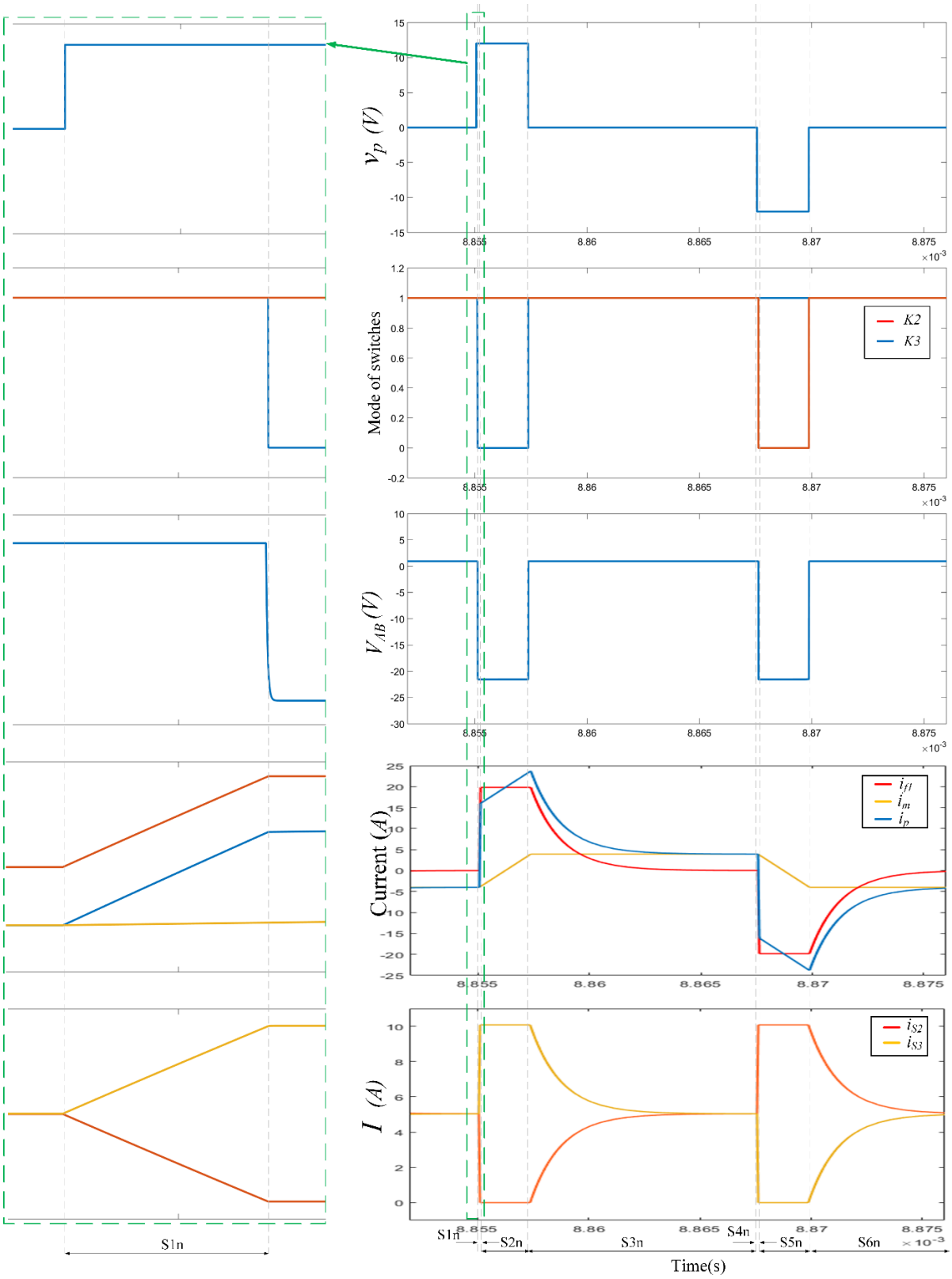

Figure 2-44 Simulation of key waveforms of the case $V_{AB} < 0$.

The simulation results of the negative mode are shown in Figure 2-44 and the positive mode is shown in Figure 2-45. Both figures are zoomed in for the first sequence because the duration time of the delta is very small. The behavior of currents should be verified. From the section

2.3.1, the current i_p is sum of the current i_{f1} and the current i_m. The slope of current i_m in Figure 2-44 (S1n and S1p) is small**.** It depends on the value of magnetizing inductances (L_m). The current i_{S2} and i_{S3} have opposite directions. All voltage and current waveforms are the same as the responses of the differential equations that are obtained in the previously section.

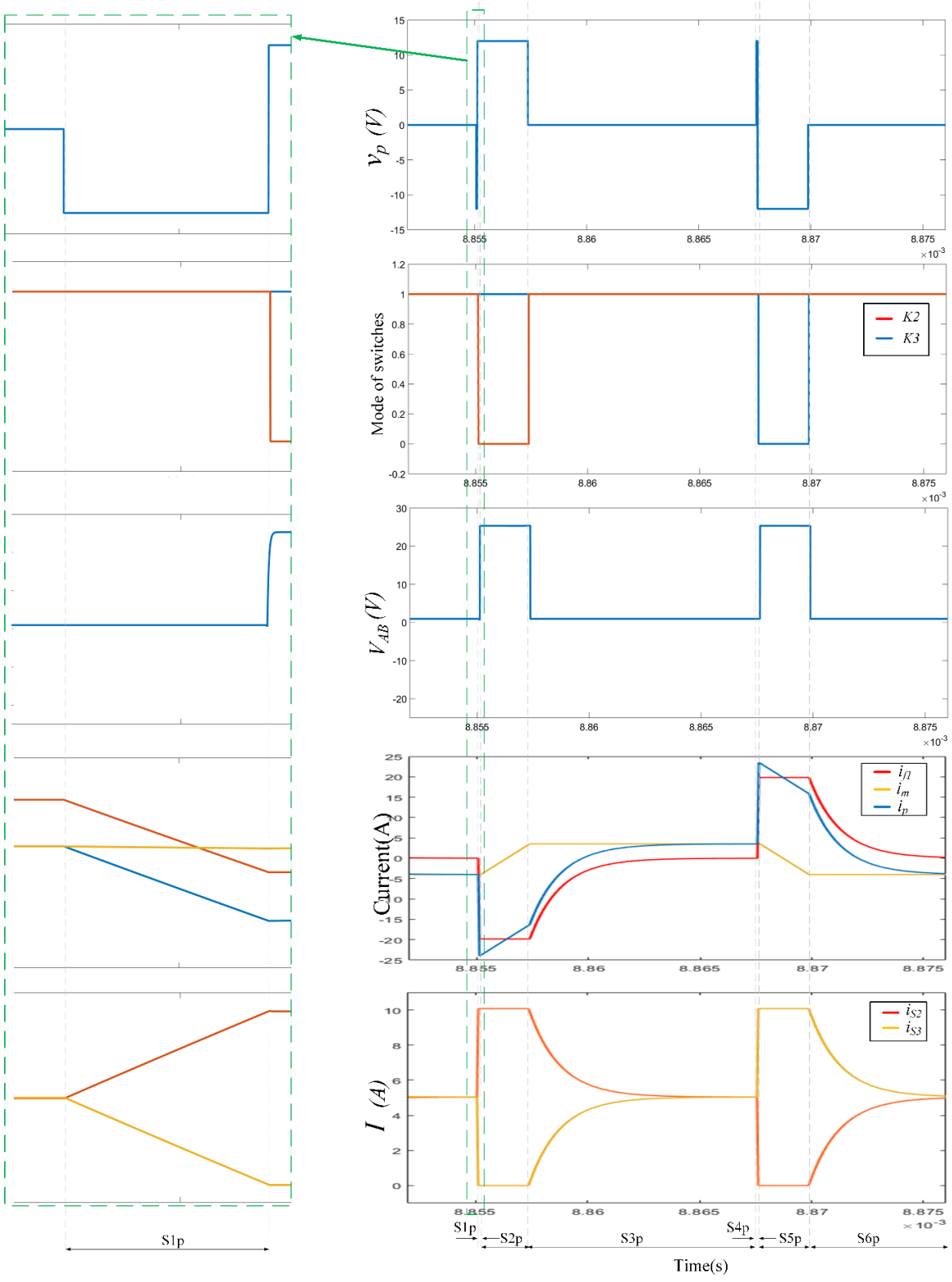

Figure 2-45 Simulation of key waveforms of the case $V_{AB} > 0$.

In addition to the methods mentioned above, the proposed model was compared with the one using Simscape power systems blockset in MATLAB/Simulink. Figure 2-46, Figure 2-47 and Figure 2-48 show the waveforms for negative mode.

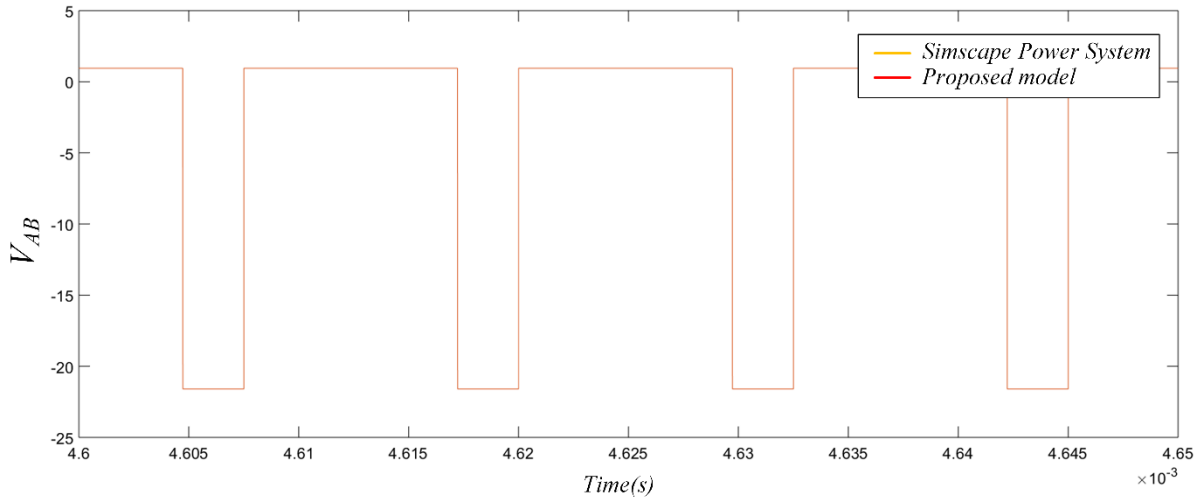

Figure 2-46 Simulation results obtained using the model with Simscape power systems blockset and the proposed model: $V_{AB} < 0$.

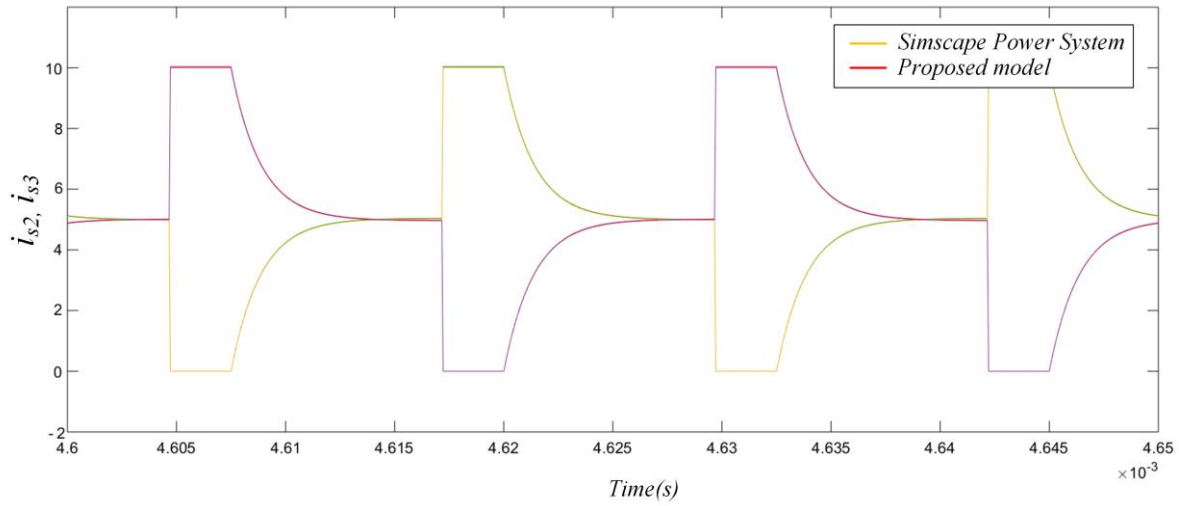

Figure 2-47 Simulation results obtained using the model with Simscape power systems block set and the proposed model: the currents i_{s2} and i_{s3}.

The voltage V_{AB} determines the dynamics of the current I, which is related to the voltage of the supercapacitor. If V_{AB} is in a negative mode. It means that the voltage V_{AB} is less than 0 shown in Figure 2-46.

The current of both switches (K_2 and K_3) are presented in Figure 2-47. They start with the half of maximum current $\frac{I}{2}$. Both switches K2, K3 are turned on in sequences 1, 3, 4, and 6. Especially, they will not operate in the same mode (turn on-turn off) in sequences 2 and 5 at the same time. The primary current is presented in Figure 2-48. It is the sum of magnetizing current and inductor current i_{f1}. According to the simulation results, the proposed model is validated.

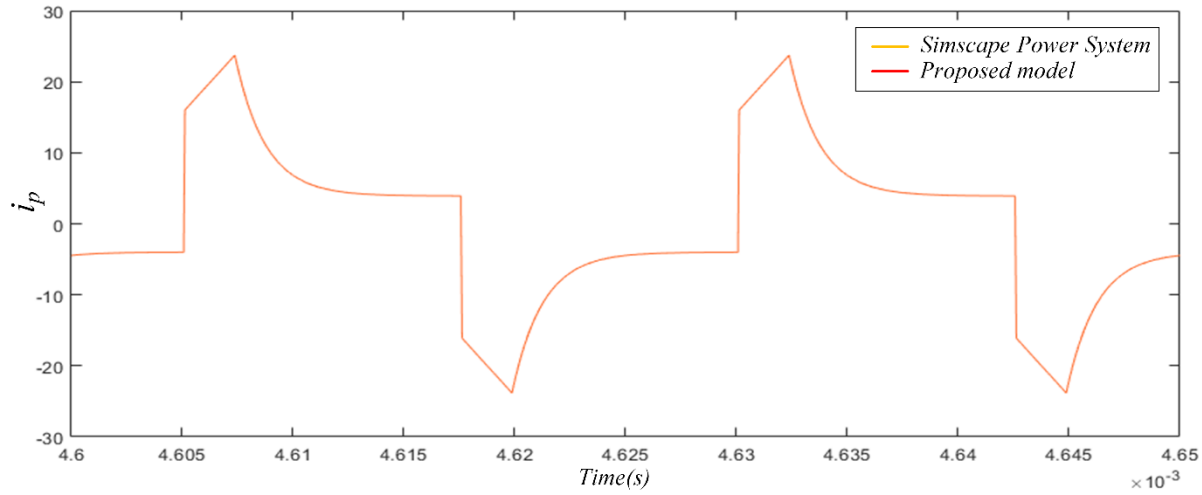

Figure 2-48 Simulation results obtained using the model with Simscape power systems block set and the proposed model: the current i_p when $V_{AB} < 0$.

The test bench was built as shown in Figure 2-49. The full-bridge inverter is implemented using MOSFETs. The switches K_2- K_3 and diode D_2 - $D_3$was realized with MOSFETS and Schottky Barrier diode, respectively. A planar transformer was used. The switching command signals were generated using DS5203 FPGA Base Board in dSPACE system. A programmable DC power supply was used to emulate the fuel cell. The parameters of the system are detailed in Table 2-4.

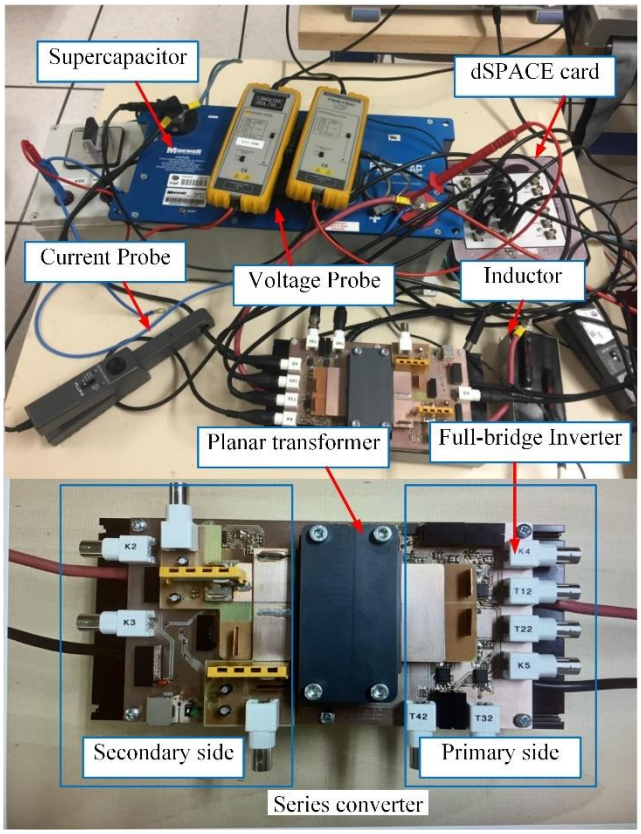

Figure 2-49 Test bench.

The main experimental waveforms $v_p, i_p, V_{AB}, i_{s2}, i_{s3}$ of the proposed converter are presented in Figure 2-50 - Figure 2-51 for two values of duty cycle and for both cases where $V_{AB} < 0$ and $V_{AB} > 0$. It should be noted that the experimental results are obtained using the control signal from FPGA without taking into account the latency of the FPGA components. The experimental results allow to validate the modelisation of the converter. The waveforms are similar to the waveforms obtained from simulation in Figure 2-44-Figure 2-45. The results of the experiment contain high-frequency ripples. It is due to parasitic inductance and capacitance of the switches, diodes, and printed-circuit board design.

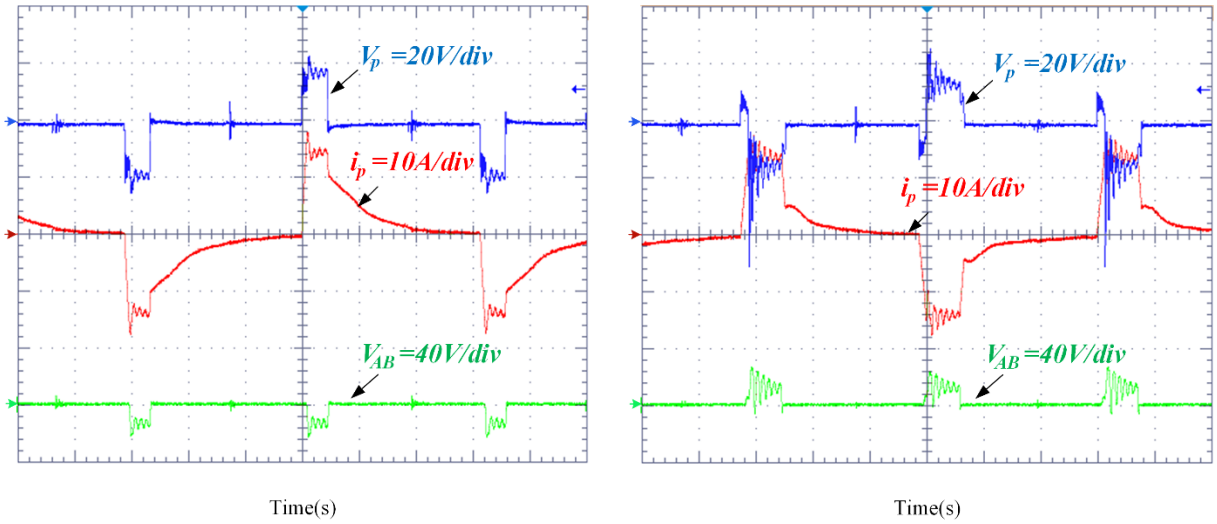

Figure 2-50 Experimental results: $v_p, i_p, V_{AB} < 0$ shown in the left and $V_{AB} > 0$ shown in the right.

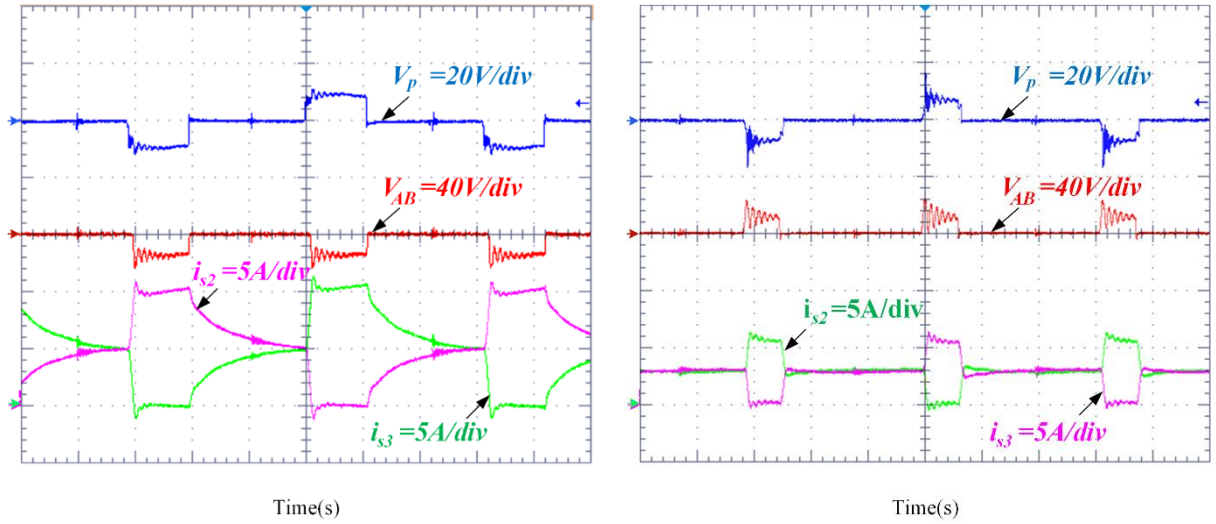

Figure 2-51 Experimental results**:** V_{AB}, secondary currents (i_{S2} and i_{S3}) of both switches**: (**left**)** $V_{AB} < 0$, **(**right**)** $V_{AB} > 0$.

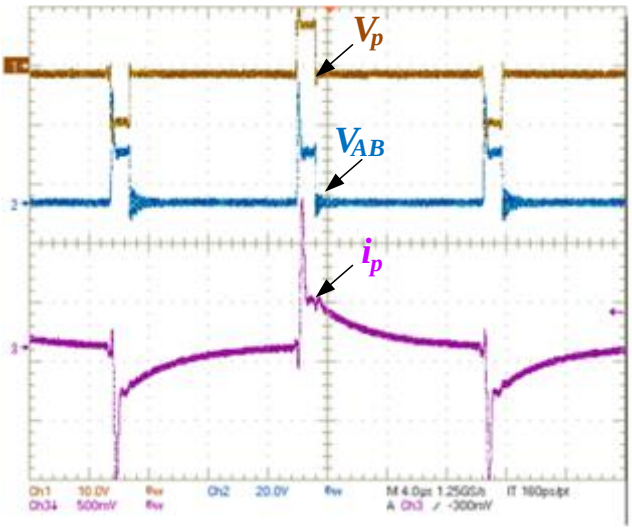

Figure 2-52 Experimental results: v_p, V_{AB}, i_p in positive mode after adding the additional blocks.

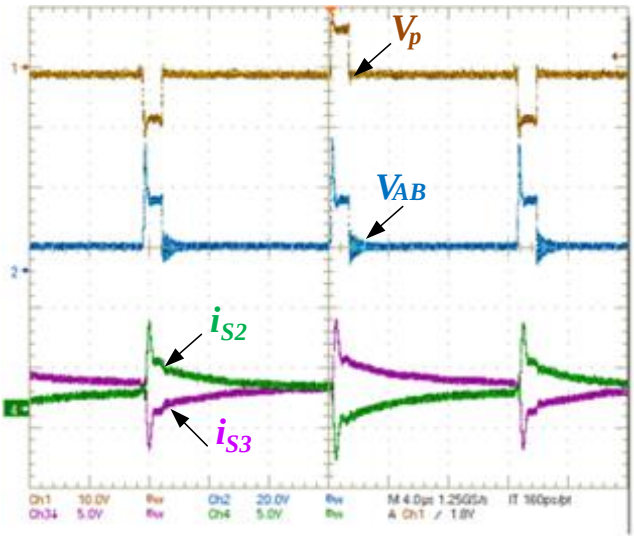

Figure 2-53 Experimental results: $v_p, V_{AB}, i_{S2}, i_{S3}$ in positive mode after adding the additional blocks.

From the Figure 2-50 and Figure 2-51 can be observed that the small spike appears every at $\frac{T}{2}$. Using the additional blocks to take into account the latency of the FPGA components, the results are shown in Figure 2-40. The results of voltages and currents waveform are shown in Figure 2-52 and Figure 2-53. The perturbations on the waveforms are suppressed. The high-frequency components of the waveform are due to using the new MOSFETs. The design of the converter have to take into account parasitic elements.

Nonetheless, the proposed modelisation of the series converter is validated by the experimental results.

2.6. Control method

To control this system, cascade control is often used to achieve smooth tracking with fast disturbance rejection. The simplest cascade architecture involves two control loops (inner and outer loops), as shown in the block diagram in Figure 2-54. The inner loop controls the current in the system, and the outer loop controls the energy stored in the supercapacitor. The inner loop is typically faster than the outer loop to reject disturbances before propagating to the outer loop.

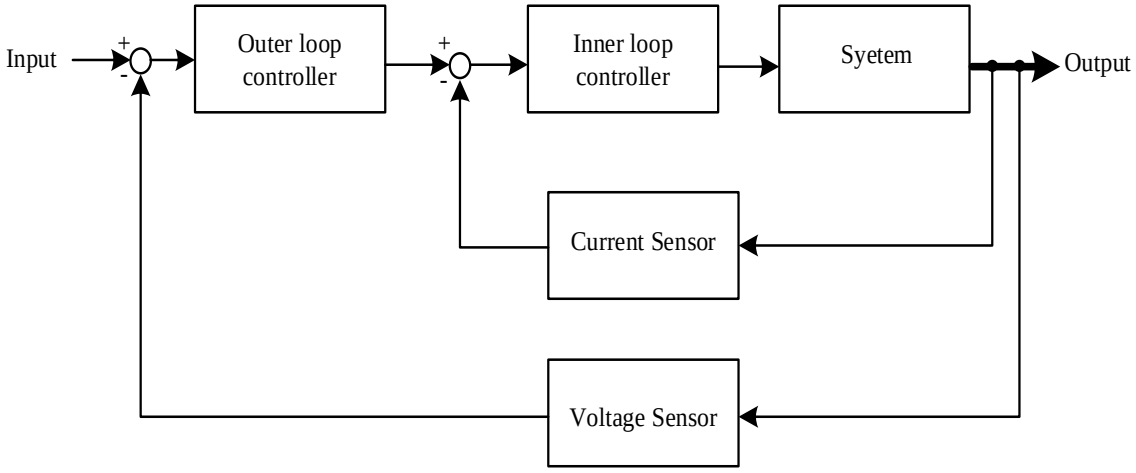

Figure 2-54 Cascade controller structure.

In steady-state, the SC voltage has to track the FC voltage while respecting the FC's constraints, which are the changing rate of the fuel current $di/dt\ max$ and the maximum value of the fuel cell power $P_{FC}max$. The outer loop is used to define the current reference I_{ref} from the definition of the reference of the SC voltage. The current loop is used to regulate the FC current from the definition mode of V_{AB}.

2.6.1. Inner loop

In this work, sliding mode control is chosen to control the FC current. There are two approaches: direct and indirect methods.

A. Direct approach

Direct SMC offers excellent advantages of robustness and ease of implementation. However, when the controlled state variable $x \in \mathbb{R}^n$ is moving away from or towards the predefined trajectory called the sliding surface $s(x) = 0$, which contains a vector of state variable $x \in \mathbb{R}^n$, the switching frequency may not be constant. A typical direct SMC structure for a system $\dot{x} = f(x, u)$ is shown in Figure 2-55. The control provides a command u in an on–off manner:

$$u = \begin{cases} u^+ \ \ if\ s(x) > 0 \\ u^- \ \ if\ s(x) < 0 \end{cases}. \tag{2-88}$$

Traditional SMC is generally based on a hysteresis modulator. Nevertheless, the performance of the SMC for a DC–DC converter is entirely limited by two significant factors, namely, the steady-state error of the control target when the switching frequency does not reach infinity, as assumed in theory, and the non-constant switching frequency. A variable switching frequency can lead to noise problems, significant losses, and electromagnetic interference problems. Therefore, the design of filters for the converter is complicated.

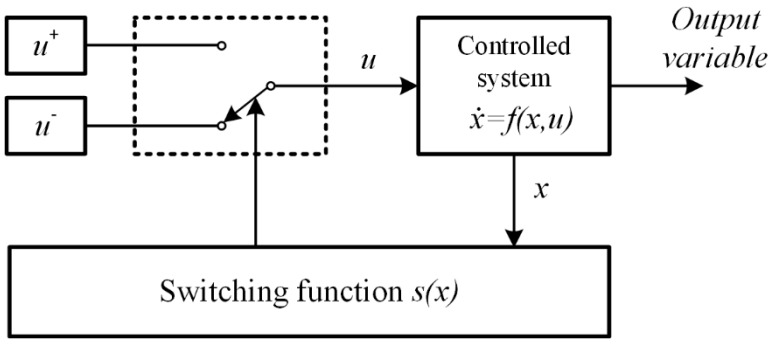

Figure 2-55. Direct sliding mode control structure.

B. Indirect approach

In this approach, the sliding mode controller gives a continuous output command signal $d \in [0,1]$. This signal is then fed to a PWM to generate the switch command $u \in \{0,1\}$ with a fixed switching frequency.

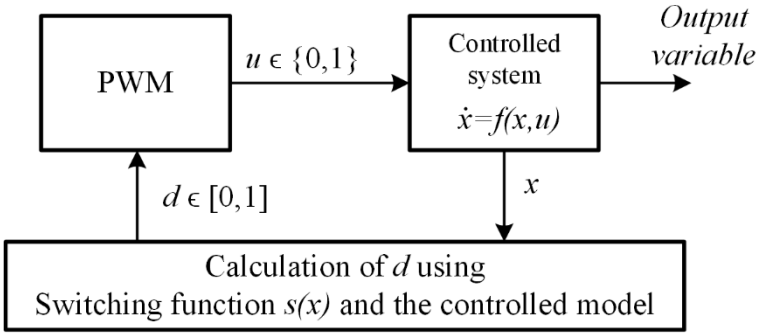

Figure 2-56 Indirect sliding mode control structure [28].

Consider a nonlinear system with perfect modeling, which all parameters are known, it can be expressed as:

$$\dot{X} = AX + BU + C \tag{2-89}$$

where $X \in \mathbb{R}^n$ is a state vector, $A \in \mathbb{R}^{n\times n}$ is a matrix, $B \in \mathbb{R}^n$ is a vector, and $U \in \mathbb{R}^n$ is the command.

The predefined trajectory, referred to as sliding surface S, can be defined to drive the control target. That is, the state variable X slides on the trajectory X_{ref}:

$$S(X) = G\left(X - X_{ref}\right) \tag{2-90}$$

where G is a constant to be set for the desired dynamics of the controlled system.

To make the dynamics of the sliding surface reach zero in an exponential manner, the reaching law may be defined as

$$\dot{S}(X) = -\lambda S. \tag{2-91}$$

The command U for the system can be found, which can drive the sliding surface from the initial point to zero:

$$U = (GB)^{-1}\left((-\lambda G - GA)X + \lambda G X_{ref} + G\dot{X}_{ref} - GC\right) \tag{2-92}$$

The dynamics of the indirect SMC-controlled system can be studied by evaluating the eigenvalues concerning the control parameters, which are λ and G. Substituting (2-92) into (2-89) yields

$$\dot{X} = \underbrace{\left(A + B(GB)^{-1}(-\lambda G - GA)\right)}_{M} X + B(GB)^{-1}\left(\lambda G X_{ref} + G\dot{X}_{ref} - GC\right) + C. \tag{2-93}$$

Thanks to the Laplace transformation, the eigenvalues of the controlled system can be found by evaluating the determinant of the following equation:

$$det(sI - M) = 0 \tag{2-94}$$

By setting λ and G equally, the eigenvalues of the controlled system are found as λ and G. It should be noted that under the matching condition, the eigenvalues of the controlled system do not depend on the system parameters, such as parasitic elements. Therefore, with the indirect-sliding mode control, the control system that can be presented above is stable.

For the inner loop in the chapter, indirect-sliding mode controller [71]- [72]- [73] is utilized as shown in equation **(**2-73**)** and **(**2-74**)** where the parameters K_i and λ are related to the controlled bandwidth, which will be chosen**.**

$$s = I - I_{ref} + K_i \int \left(I - I_{ref}\right) dt \tag{2-95}$$

The control law can be written

$$\dot{s} = -\lambda s \tag{2-96}$$

To ensure that the current I will reach its reference I_{ref}, the product of $\dot{s} \cdot s$ must be negative.

$$\dot{s} \cdot s = -\lambda \cdot s^2 \tag{2-97}$$

It can be seen that the current I will reach its reference I_{FCref}, if λ is positive.

To perform equation (2-71), the state equation for the inductor current regarding the series converter shown in Figure 2-25 governed by the command of V_{AB} is needed:

$$\frac{d}{dt}i = V_{FC} - ri - V_{AB} - V_{SC} \tag{2-98}$$

V_{ABsel} can be defined thanks to the indirect-sliding controller:

$$V_{AB_{sel}} = \left(\left(\lambda s - \frac{d}{dt}I_{ref} + K_i\left(i - I_{ref}\right)\right)L\right) - ri - V_{SC} + V_{FC} \tag{2-99}$$

Using (2-95) with (2-96) and (2-97), the control voltage V_{AB} is obtained. This voltage is now called V_{ABsel}. The sign of V_{ABsel} is utilized for generated the V_{AB} of the converter. Using V_{ABsel}, the duty cycle can be calculated regarding the supercapacitor voltage and the transformer's turn ratio m as

$$d = \frac{|V_{ABsel}|}{m \cdot V_{SC}} \tag{2-100}$$

2.6.2. Outer loop

An external controller based on the energy stored in supercapacitors will be introduced in Figure 2-57. After introducing the relationships required for the simulation, its performance in terms of tracking and regulation as well as its effect on the SC voltage reference and the SC voltage measurements, will be investigated.

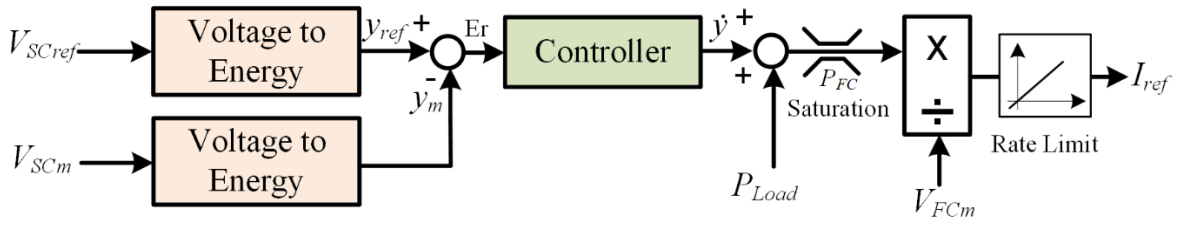

Figure 2-57 Block diagram of the outer loop.

The energy stored associated with the SC voltage is:

$$y = \frac{1}{2}C_{sc}V_{sc}^2 \tag{2-101}$$

The error (Er) can be calculated from the difference value between energy (y) and reference energy (y_{ref}). where $y_{ref} = \left(\frac{1}{2}\right) C_{SC} {V_{FC}}^2$. The equation is described in the following manner:

$$Er = y_{ref} - y \tag{2-102}$$

The dynamic of Er can be expressed by the following control law:

$$0 = \dot{y}_{ref} - \dot{y} + K_1\left(y_{_{ref}} - y\right) + K_2 \int \left(y_{ref} - y\right) d\tau \tag{2-103}$$

where $\dot{y}$ is the variation of energy stored in the SC.

$$\dot{y} = \dot{y}_{ref} + k_1\left(y_{ref} - y\right) + k_2 \int \left(y_{ref} - y\right) d\tau \tag{2-104}$$

Neglecting the losses, the FC input power can be defined as follows:

$$P_{FC} = \dot{y} + P_{Load} \tag{2-105}$$

The current reference I_{ref} can be found using the power balance when losses are neglected:

$$I_{ref} = (P_{load} + \dot{y})/V_{FC_m} \tag{2-106}$$

2.6.2.1. Estimator for V_{SCref}

To control this system, generating a voltage reference for the supercapacitor voltage is based on the use of the knowledge of the polarization curve of the fuel cell. Moreover, an estimator is added to track the non- matching parameters or uncertain parameters such as the voltage across the diode and unmodeled resistances. This converter keeps the control voltage v_{AB} zero to make highest converter's efficiency.

Consider the circuit diagram, the FC power reference p_{FCref} is given by

$$p_{FCref} = p_{Load_{filtered}} \tag{2-107}$$

p_{load} is filtered according to frequency distribution. The fuel cell power reference p_{FCref} will be fed into a power-voltage characteristic function of the fuel cell to get the fuel cell voltage relating to the delivered power. The obtained voltage is used to generate the supercapacitor reference voltage together with the diode voltage and voltage across the resistance in the system. The block diagram of this control scheme is illustrated in Figure 2-58 As all parameters are well known, therefore, in steady-state operation, the control voltage v_{AB} equals zero. However, practically, the real fuel cell characteristic function has changed due to several conditions. Moreover, diode voltage as well as parasitic resistances are usually changed in time. To maintain v_{AB} zero, the supercapacitor reference voltage must be adapted. To do this, we propose to use v_{AB} as an indicator to estimate the compensated voltage.

Consider the circuit diagram, the supercapacitor reference voltage is given by

$$V_{SCref} = \hat{f}(p_{FCref}) - V_{AB\infty} \tag{2-108}$$

where $V_{AB\infty}$ is the steady-state final value of V_{AB} without estimator.

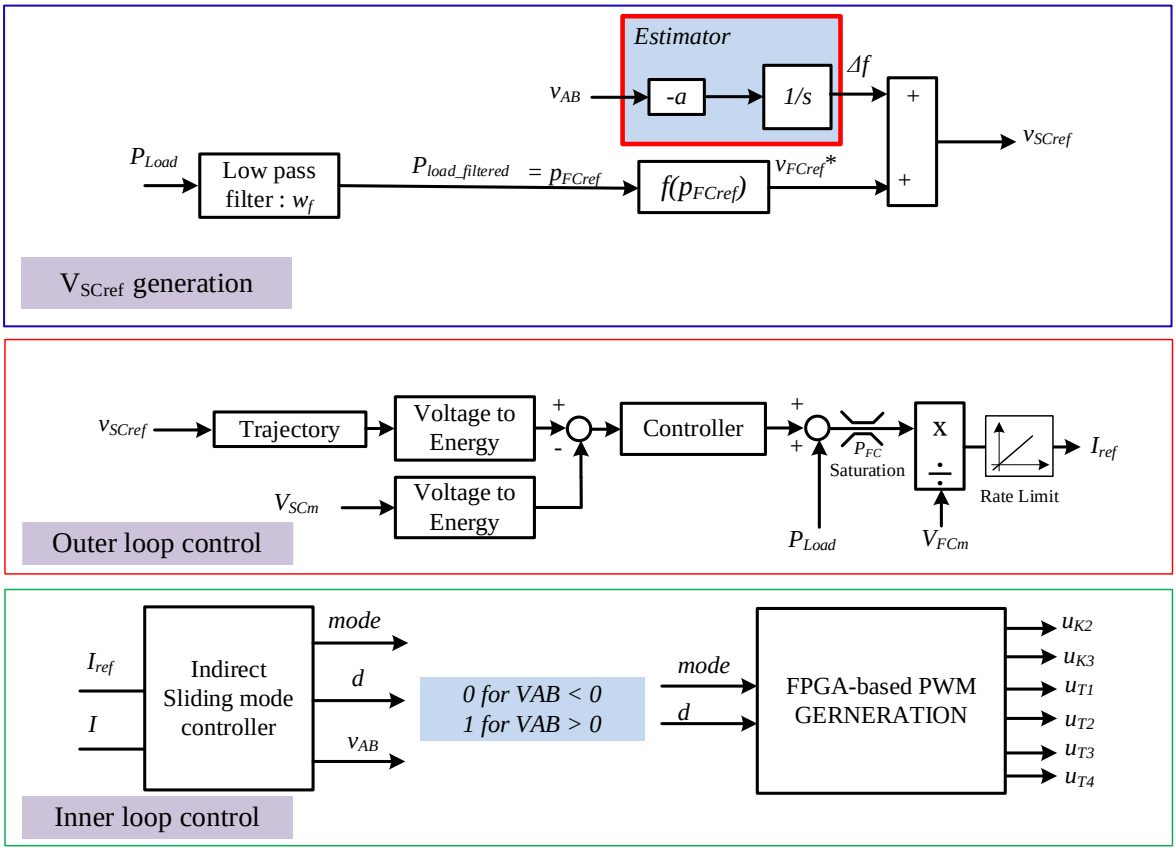

Figure 2-58 Block diagram of the closed-loop control, including estimator.

The fuel cell voltage V_{FC} can be found using a function of power-voltage characteristic equation $\hat{f}(p_{FCref})$ and it can be written as:

$$V_{FC} = \hat{f}(p_{FCref}) = f(p_{FCref}) + \Delta f \tag{2-109}$$

Which corresponds to the nominal voltage $f(p_{FCref})$ and its variation Δf.

Therefore, the supercapacitor reference voltage is given by

$$V_{SCref} = f(p_{FCref}) + \Delta f - V_{AB\infty} \tag{2-110}$$

Consider the circuit diagram, suppose that under an operation where all parameters and the fuel cell model are well known, the supercapacitor reference voltage is given by

$$V_{SCref} = f(p_{FCref}) \tag{2-111}$$

Replace v_{SCref} from (2-110) into (2-111), one gets

$$\Delta f = V_{AB\infty} \tag{2-112}$$

As can be seen, the steady-state control voltage $v_{AB\infty}$ can be used to obtain the variation of the supercapacitor reference voltage. Consequently, we propose an estimator based on the mentioned indicator V_{AB} multiplies to the positive constant value α:

$$\frac{d}{dt}\hat{f}(p_{FCref}) = \dot{\Delta}f = -\alpha V_{AB\infty} \tag{2-113}$$

To prove stability of this estimator, a Lyapunov candidate function is chosen as:

$$V = \frac{1}{2}\left(\hat{f}(p_{FCref}) - f(p_{FCref})\right)^2 = \frac{1}{2}\Delta f^2 \tag{2-114}$$

It is found that its first-time derivative is given by

$$\dot{V} = \Delta f \dot{\Delta} f = -\alpha\left(V_{AB\infty}\right)^2 \tag{2-115}$$

As the first time-derivative of V is negative except when $V_{AB\infty} = 0$, this estimator is asymptotically stable.

2.6.3. Experimental results of the series converter with controller

A test bench was built as shown in Figure 2-59. The switches $T_1 - T_4$ was implemented using IPT059N15N3ATMA1. The switches K_2, K_3 and diode D_2, D_3 was realized with IPT004N03L and diode. A planar magnetic was used for the transformer. The switching command signals were generated using FPGA Base Board in dSPACE system. A programmable DC power supply was used to emulate an FC thanks to the polarization curve: voltage-current of the fuel cell in Figure 2-60 (left), whereas the voltage-power of the fuel cell is shown in Figure 2-60 (right). The parameters of the system, controller, and the used equipment are detailed in Table. 1 and 2, respectively.

Parameter	Value
Maximum FC voltage	15 V
Maximum FC current	15 A
Maximum SC voltage	15 V
Transformer turn ratio $n_p : n_{s1} : n_{s2}$	1:2:2
L_m	56.8 µH
L_{f1}	1.5 µH
$L_{f2} = L_{f3}$	0.58 µH
$r_{f1} = r_{f2} = r_{f3}$	0.2 Ω
Switching frequency	40 kHz
Power supply	TDK lambda
Electronic load	EA-ELR 9750-22 3.5kW
Power analyzer	YOKOGAWA
Oscilloscope	Tektronix TDS5034B

Table 2-4 System parameters, devices, and equipment in the test bench

Figure 2-59 Test bench of the series converter with the controller.

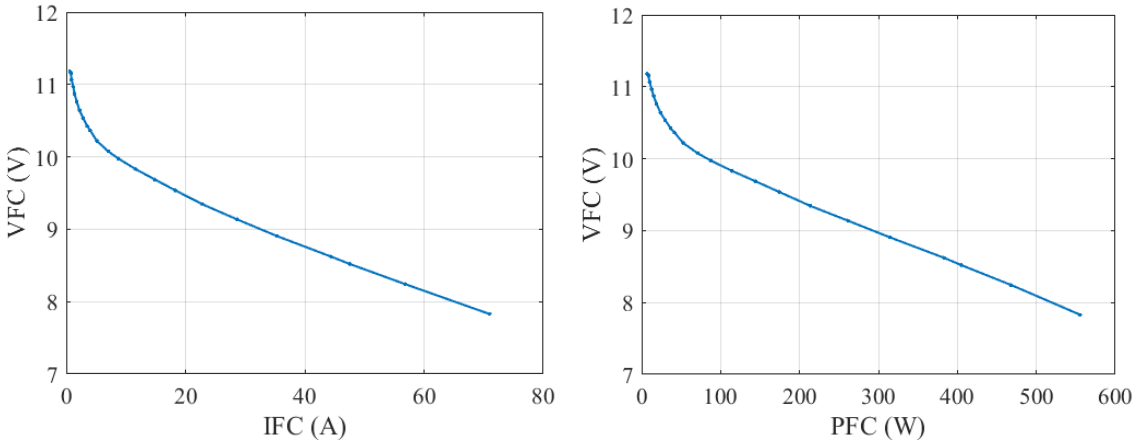

Figure 2-60 Characteristics of the used fuel cell. Left: V_{FC}-I_{FC} curve, right: V_{FC}-P_{FC} curve.

Parameter	Value
$K_i = \lambda$	1000 rad/s
Maximum FC current slope	± 10 A/s
Maximum FC power	200 W
delta	0.01
alfa	0.0001
r	0.001 Ω
V_D	0.5 V

Table 2-5 System and control parameters for estimator method.

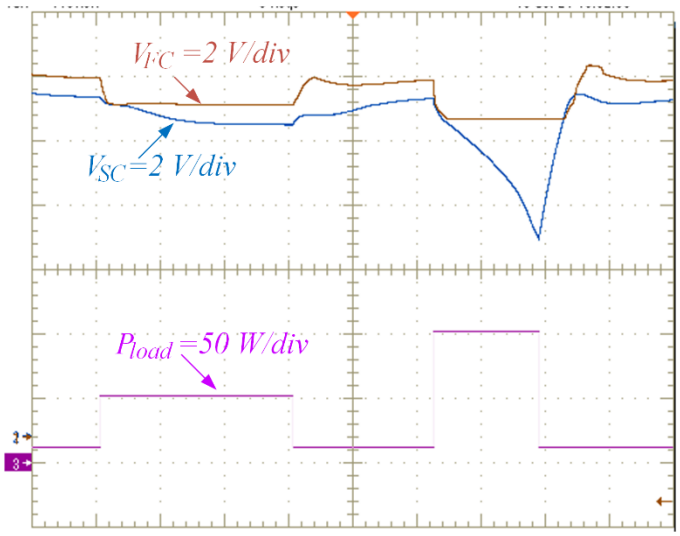

Figure 2-61 Waveform of fuel cell voltage, supercapacitor voltage, and load power.

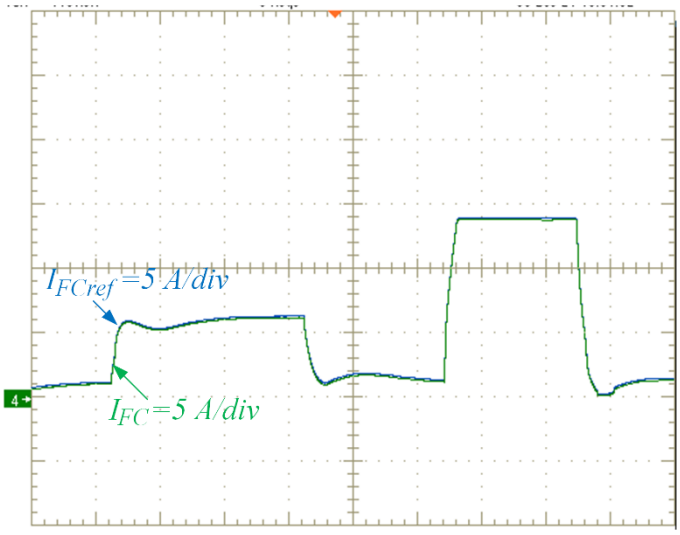

Figure 2-62 Current of fuel cell and its reference.

Figure 2-61 presents the load power profile of 10 W, 50 W, and 100 W varied in time, including the fuel cell voltage and supercapacitor. In theory, the V_{FC} and V_{SC} are equal in steady state but the V_{FC} and V_{SC} in the experiment have a gap which is equal to the losses in the system. In this test, the maximum power of the fuel cell P_{FCmax} is set at 100 W. When load power P_{load} is 100 W, the V_{FC} is limited by the limited voltage corresponding to P_{FCmax} as a consequence V_{SC} supplies energy to the power load. V_{SC} can be low to half the maximum stored energy. When the load power is very small at the end of the load profile, the voltage V_{FC} and V_{SC} will return to the same value as at the beginning.

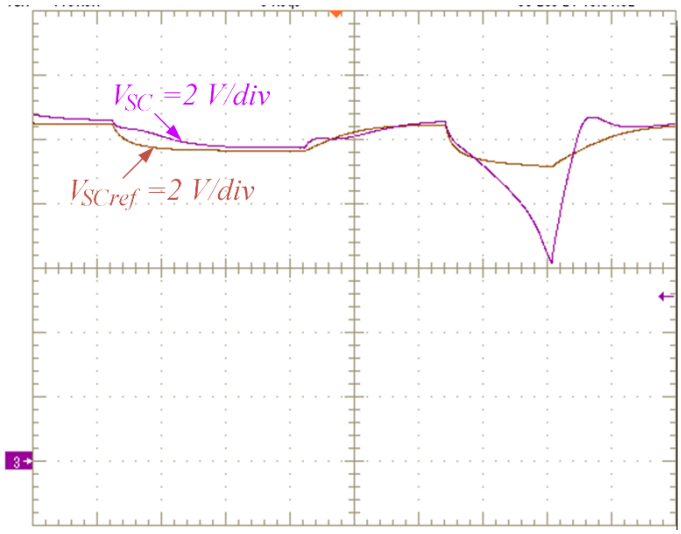

Figure 2-63 Waveform of supercapacitor voltage and reference of supercapacitor voltage.

At the same the load power profile in Figure 2-61, the current I_{FC} and its reference are shown in Figure 2-62. the current I_{FC} following their reference very well. The voltage V_{SC} and V_{SC} reference is described in Figure 2-63. The voltage V_{SC} tracking its reference. Both figures

are verified the controller that describes in the section previously. Finally, the controller can be controlled the system

2.7. Conclusions

The new power architecture of the FC/SC series hybrid has been proposed. The converter modeling, including parasitic parameters of the transformer, such as leakage inductance and resistance of the transformer, is provided and validated. The definition of the control signal of the H-bridge inverter strongly reduces the overshoot voltage without using any clamp circuit. Although the switching frequency is relatively high, zero current switching (ZCS) in some devices allows the system has high efficiency. With the help of the proposed estimator, the control algorithms allow for managing the power provided by the fuel cell and taking into account the fuel cell constraints as desired.

Chapter III

Modular Three-level converter

3.1. Introduction

Fuel cell is one of the most important alternative energy sources. They were expected to employ in several applications such as portable applications [79], transportation applications [80], and stationary power applications [81]. However, fuel cell cells produce low voltage. An appropriate solution for this problem is a boost converter which is used to increase the voltage. In literature, isolated DC-DC converters have been proposed to increase the output voltage. This type of DC-DC converter, including a transformer, might have low efficiency if it must have a high voltage ratio for this particular application [82]- [83].

As detailed in Chapter two, that the stacked fuel cell structure offers advantages. Each fuel cell stack is connected to its DC-DC switching converter, such as a DC-DC boost converter [84]. Overall, for a system consisting of several stacks, a series connection of output capacitors of the DC-DC converters is required to increase the system's output voltage. This solution will increase the degree of freedom in the management and control of fuel cells. However, the primary drawback of this structure is the probability of losing control [85] . For example, if the input power of a cell is less than the power of the other inputs, the output voltage of the related capacitor decreases. If the output voltage becomes lower than the input voltage for the boost converter, its controllability is lost. Then, some heterogeneities between the cells constituting the stack can occur while using the mentioned fuel cells with the boost converters. The voltage of one specific cell in the stack may decrease due to particular aging or local malfunctioning, such as drying. Consequently, extra heat is produced in this cell, leading to an increase in its

temperature and an additional voltage loss. This snowball effect can cause a failure of the cell. Hence, by using DC-DC converters that can balance its output voltage for different input power levels, including an energy management strategy for the stacked fuel cell, the lifetime of the fuel cell stack can be enlarged [86].

In many studies, voltage imbalances in batteries and supercapacitors banks have been investigated [87]- [88]. Voltage balancing strategies can be categorized into two types: with and without an auxiliary source, as shown in Figure 3-64. The equalizers using additional sources to compensate cells with lower voltages might not specifically suitable for transportation system applications, since they have a high weight and large volume [86]. On the other hand, Equalizers without auxiliary sources can be categorized as passive and active balancing methods. The passive balancing method is based on wasting the extra energy of high voltage cells, which is done until the cell voltage is the same as the voltage in other cells. Thus, passive equalizers have low efficiency [89]. Active equalizers can be categorized as capacitor-based [90], converter-based [91] and other equalizer methods [92].

Voltage equilibrium is achieved more rapidly in converter-based equalizers. However, precise control is also needed to balance the voltage. Converter-based method [93]- [94] can be categorized as Cûk, flyback, ramp, full-bridge, quasi-resonant, and buck or boost converters. These converters control the process of balancing. Using these converters makes voltage balancing relatively expensive and complex.

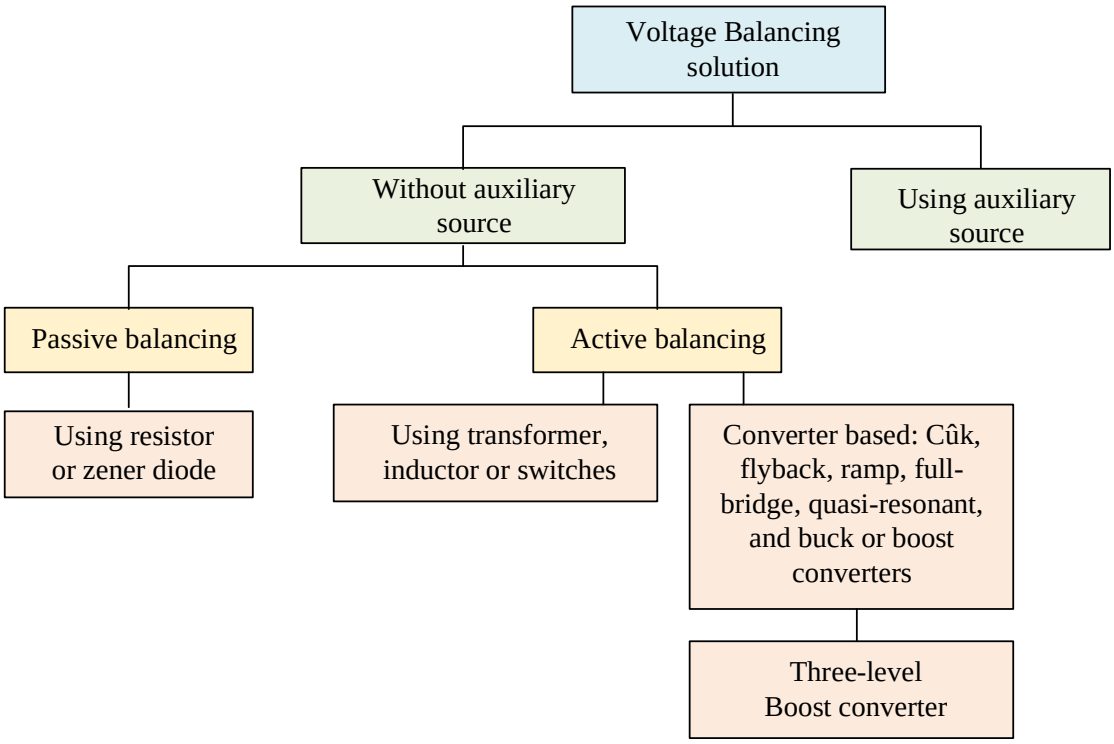

Figure 3-64 Classification of various solutions for balancing voltage [10].

Step-down (buck), step-up (boost), and buck-boost converters are widely used in balancing systems. Applying these converters as equalizers is relatively expensive and complex, but they are suitable for modular design. When needed, expanding the systems is very simple using the

modular structure [88]. Another topology is a modular three-level boost converter. It has been investigated in many pieces of research [95]- [96].

A new modularity topology based on a modular three-level converter where the output capacitors of each module are serial connected is investigated in this chapter [97]. Based on the hybridization architecture in Chapter 2, a suitable arrangement for the series converter hybridization of fuel cells and supercapacitors, this hybridization is applied to a modular system, as shown in Figure 3-65. In this arrangement, the supercapacitors are distributed modularly throughout the system. In this system, the fuel cell and supercapacitor energy are transferred to the load through a DC-DC converter. The design of this converter should be such that it can be used to manage the requirements of the fuel cell system, i.e., water and fuel management (thus addressing the snowball phenomenon), and the voltage imbalance due to differences in the power output of each cell.

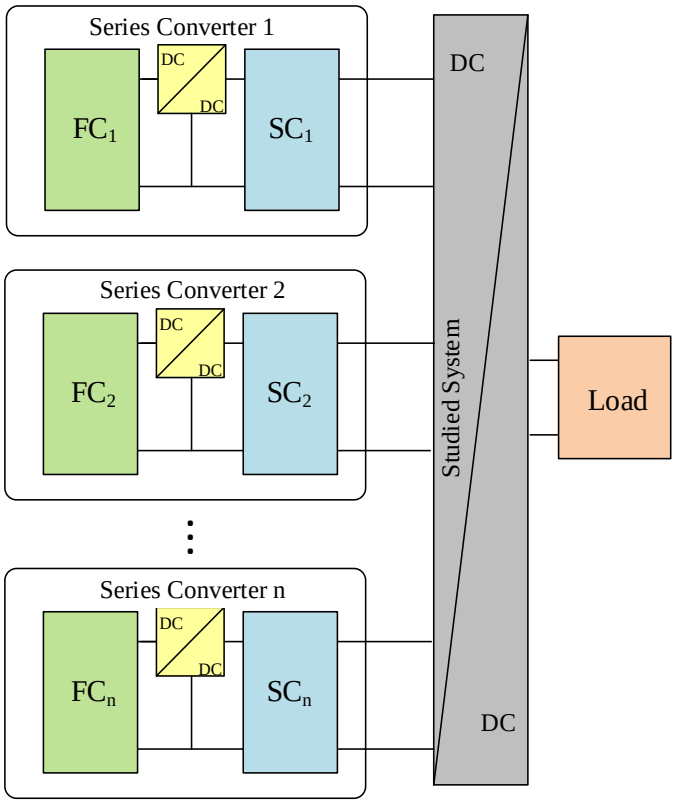

Figure 3-65 Hybridization arrangement of fuel cell and supercapacitor and their placement in the modular system.

Section 3.2 represents the operation of the three-level converter. Many modules of the three-level converter are represented in the three-level converter's N-module to increase the output voltage. Moreover, this chapter proposes a new configuration of series-connected capacitors between them. The method is to share the output capacitor. A control method for the converter

is described. The simulation results with MATLAB/Simulink software and experimental results are given.

3.2. Proposed modular three-level converter

This section investigates a modular three-level (MTL) converter modified from the three-level boost converter [98]. Three-level boost converters have a significant advantage compared to the conventional boost converter. The size of the inductor is reduced, and the switch voltage rating is half of the output voltage. This reduces the overall size and improves the efficiency of the system. However, the voltage balancing across the DC bus capacitors is required due to nonidealities in the components. It is feasible by sensing the voltages across them with corrective feedback through controllers [99].

3.2.1. MTL converter with single input

The MTL converter with single input corresponds to the three-level boost converter illustrated in Figure 3-66. This circuit consists of an inductor (L), four switches (S_1, S_2, S_3 and S_4), and two output capacitors (C_1 and C_2).

The switches control signals are obtained by pulse width modulation (PWM): u_1, $\overline{u_1}$, u_2 and $\overline{u_2}$ corresponding to the duty cycles generated by the controller of the system. The signal $\bar{u}_x$ is the complement signal of u_x for $x = \{1,2\}$. The output voltage (V_{dc}) is the voltage across the two capacitors C_1 and C_2 and it can be written as follows:

$$V_{dc} = V_{c1} + V_{c2} \tag{3-116}$$

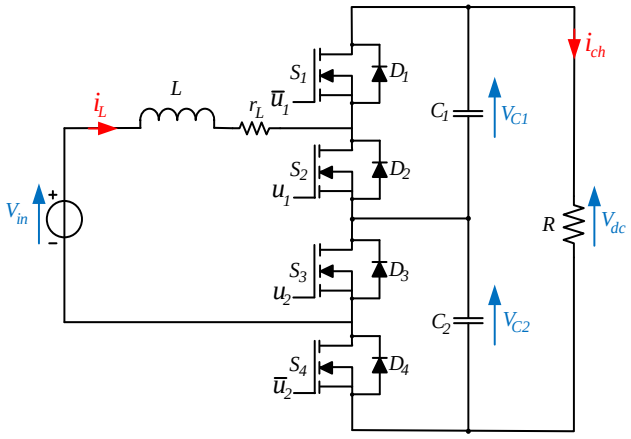

Figure 3-66 Single module of a three-level boost DC-DC converter.

The system state equations are derived thanks to the KVL and KCL equations. The current of the inductor (L) satisfies the following relation :

$$L\frac{di_L}{dt} = V_{in} - r_L \cdot i_L - (1-u_1)\cdot V_{C1} - (1-u_2)\cdot V_{C2} \tag{3-117}$$

Where r_L is the series resistance of inductor L.

The current of the capacitors C_1 and C_2 satisfies the following equation:

$$C_1\frac{dV_{C1}}{dt} = (1-u_1)\cdot i_L - i_{ch} \tag{3-118}$$

$$C_2\frac{dV_{C2}}{dt} = (1-u_2)\cdot i_L - i_{ch} \tag{3-119}$$

3.2.1.1. Pulse-width modulation

One can use the interleaved technique to generate switching commands u_1 and u_2 based on pulse-width modulation (PWM), which can be found in the literature [100]. This technique can double the frequency of the inductor current. Therefore, the inductance and capacitance can be lower than the synchronous switching technique [101]. The PWM signal generation for the converter in Figure 3-66 is shown in Figure 3-67. For ideal case, the signal duty cycles d_1 and d_2 are indentical. The parameters detailed in Table 3-6 are used for the simulation.

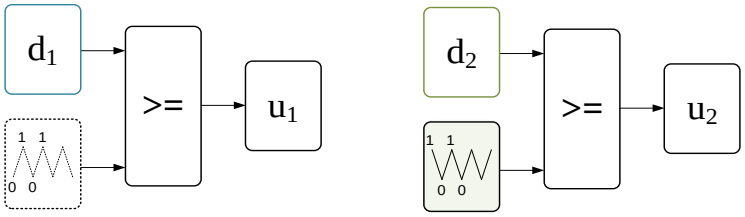

Figure 3-67 PWM generation for three-level boost DC-DC converter.

The current i_L obtained from equation (3-117) is shown in Figure 3-68. the output voltage of each capacitor and system are described in Figure 3-69, respectively. For an ideal case, the voltage of V_{c1} and V_{c2} are equal. The output voltage of converter is the sum of both voltage given in Figure 3-70.

Parameter	Value	description
V_{in}	24 V	Input voltage
d	0.5	Duty cycle
f	20 kHz	Switching frequency
L	1 mH	Inductor
r_L	0.01 Ω	Equivalent serial resistance of the inductor
$C_1 = C_2$	100 µF	Capacitor
R	12.5 Ω	Load resistance

Table 3-6 Simulation parameters for three-level converter.

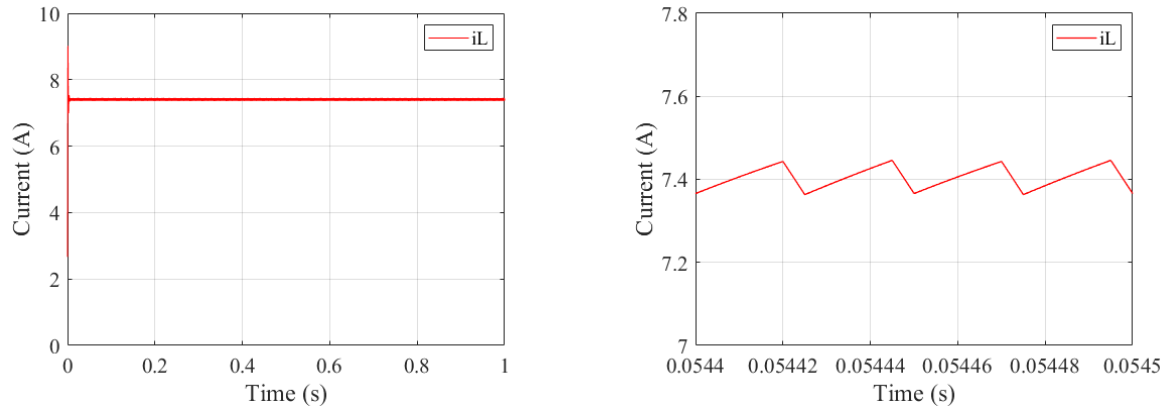

Figure 3-68 Input current of a single module of three-level. (Right) zoomed input current.

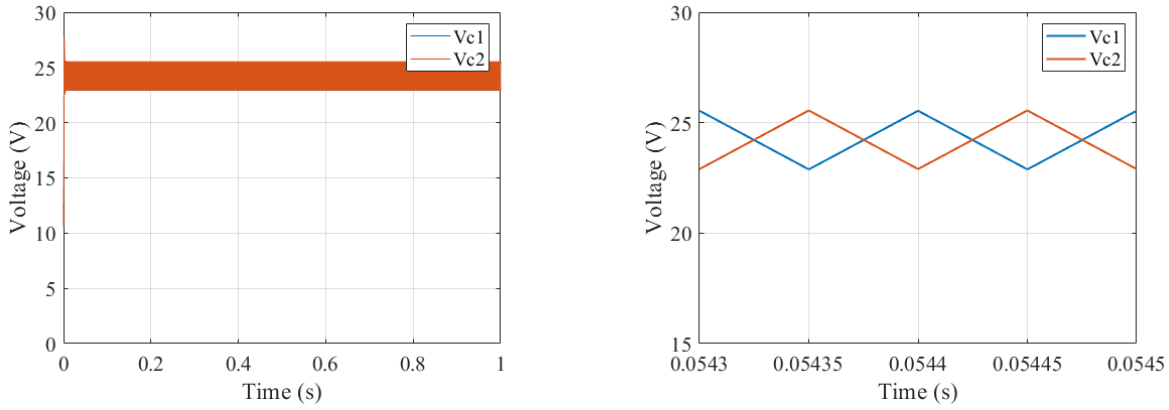

Figure 3-69 Voltage across the capacitor C_1 and C_2. (Right) zoomed capacitor voltages.

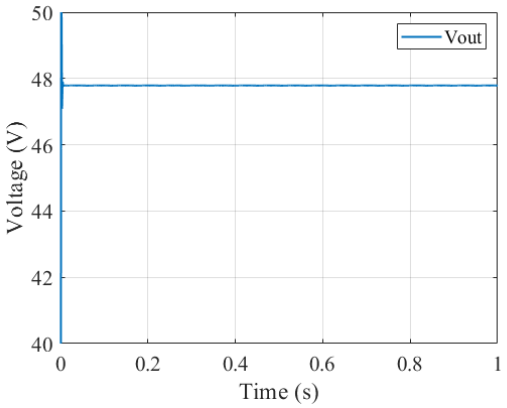

Figure 3-70 Output voltage of the system.

3.2.2. MTL converter with two inputs

A novel DC-DC converter topology is proposed based on two three-level converters. It consists of the association of two modules of the three-level converter, as shown in Figure 3-71. The capacitor C_2 is shared for both modules. The state equations for the current i_{L1} and i_{L2} can be derived as:

$$L_1 \frac{di_{L1}}{dt} = V_{in1} - r_{L1} \cdot i_{L1} - (1 - u_{11}) \cdot V_{C1} - (1 - u_{12}) \cdot V_{C2} \quad (3\text{-}120)$$

$$L_2 \frac{di_{L2}}{dt} = V_{in2} - r_{L2} \cdot i_{L2} - (1 - u_{21}) \cdot V_{C2} - (1 - u_{22}) \cdot V_{C3} \quad (3\text{-}121)$$

where the resistance r_{L1} and r_{L2} are the equivalent serial resistance of the inductor for each input.

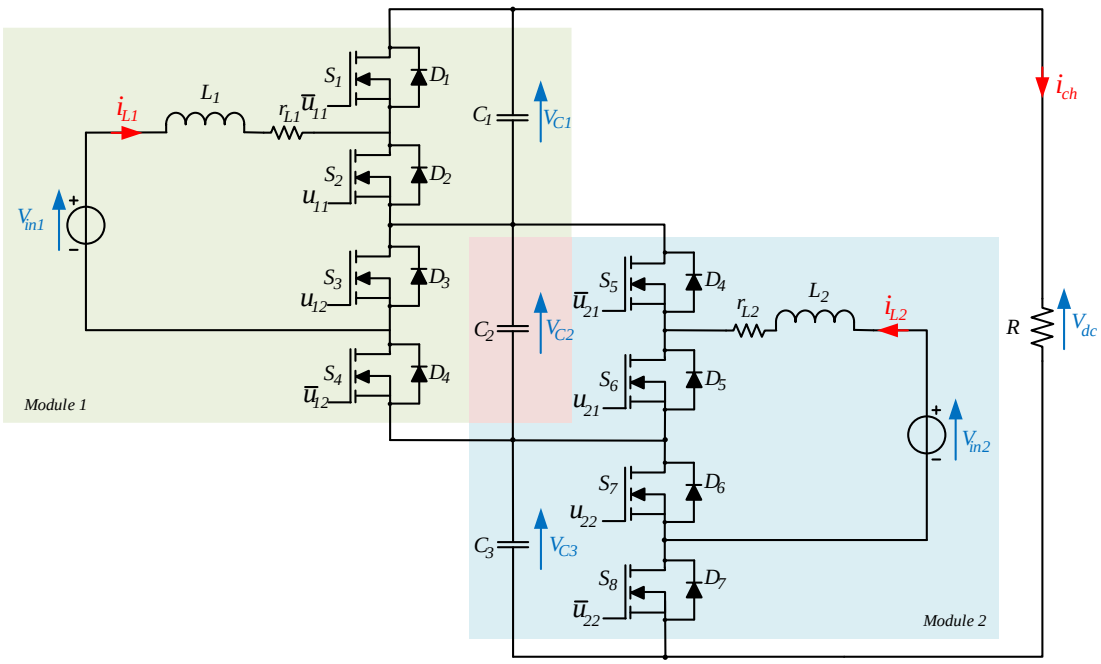

Figure 3-71 Two modules of the three-level DC-DC converter.

The state equations for the voltage across C_1 and C_3 can be written depending on the switching signal:

$$C_1 \frac{dV_{C1}}{dt} = (1 - u_{11}) \cdot i_{L1} - i_{ch} \tag{3-122}$$

$$C_3 \frac{dV_{C3}}{dt} = (1 - u_{22}) \cdot i_{L2} - i_{ch} \tag{3-123}$$

For the shared capacitor C_2, the state equation composes of the inductor currents and the load current (i_{ch}):

$$C_2 \frac{dV_{C2}}{dt} = (1 - u_{12}) \cdot i_{L1} + (1 - u_{21}) \cdot i_{L2} - i_{ch} \tag{3-124}$$

3.2.2.1. Pulse-width modulation

Interleaved PWM signals for the MTL converter with two modules are shown in Figure 3-72. The phase shift of the signal u_{11} and u_{12} is 180 degrees. Furthermore, the phase shift of the signal u_{12} and u_{21} is 180 degrees. In this way, the frequency of the current of the shared capacitor is double, which leads to the possibility of use of lower capacitance value for the same voltage ripple compared to the adjacent capacitors.

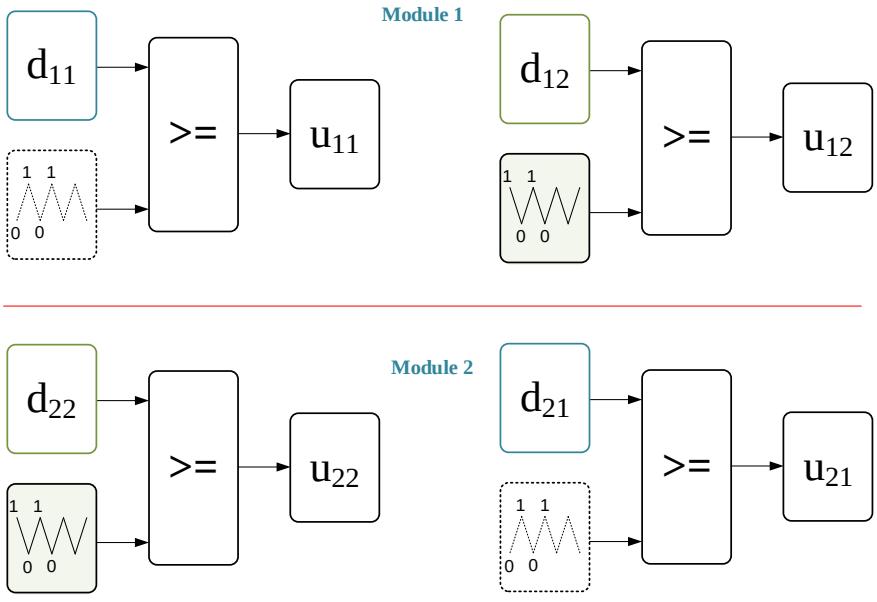

Figure 3-72 PWM generation for two module of three-level DC-DC converter.

3.2.3. N-module MTL converter

This section presents an N-module MTL converter following the two-input three-level boost converter detailed in Section 3.2.3. The proposed topology is shown in Figure 3-73. This section aims to determine the general steady-state equations of the N-module system.

The state equation for the inductor currents for the N-module three-level converter is expressed for the first four input sources as follows:

$$\begin{aligned}
L_1 \frac{di_{L1}}{dt} &= V_{i1} - r_{L1} \cdot i_{L1} - (1 - u_{11}) \cdot v_{C1} - (1 - u_{12}) \cdot v_{C2} \\
L_2 \frac{di_{L2}}{dt} &= V_{i2} - r_{L2} \cdot i_{L2} - (1 - u_{21}) \cdot v_{C2} - (1 - u_{22}) \cdot v_{C3} \\
L_3 \frac{di_{L3}}{dt} &= V_{i3} - r_{L3} \cdot i_{L3} - (1 - u_{31}) \cdot v_{C3} - (1 - u_{32}) \cdot v_{C4} \\
L_4 \frac{di_{L4}}{dt} &= V_{i4} - r_{L4} \cdot i_{L4} - (1 - u_{41}) \cdot v_{C4} - (1 - u_{42}) \cdot v_{C5}
\end{aligned} \tag{3-125}$$

For N-modules: the state equation of inductor current for the module k[th] can be rewritten as:

$$L_k \frac{di_{Lk}}{dt} = V_{ik} - r_{Lk} \cdot i_{Lk} - (1 - u_{k1}) \cdot v_{Ck} - (1 - u_{k2}) \cdot v_{C_{k+1}} \tag{3-126}$$

where k=1, 2, 3, …, N.

The state equations for the capacitor for the first five capacitors are:

$$C_1 \frac{dv_{C1}}{dt} = (1 - u_{11}) \cdot i_{L1} - i_{ch} \tag{3-127}$$

$$C_2 \frac{dv_{C2}}{dt} = (1 - u_{12}) \cdot i_{L1} + (1 - u_{21}) \cdot i_{L2} - i_{ch} \tag{3-128}$$

$$C_3 \frac{dv_{C3}}{dt} = (1 - u_{22}) \cdot i_{L2} + (1 - u_{31}) \cdot i_{L3} - i_{ch} \tag{3-129}$$

$$C_4 \frac{dv_{C4}}{dt} = (1 - u_{32}) \cdot i_{L3} + (1 - u_{41}) \cdot i_{L4} - i_{ch} \tag{3-130}$$

$$C_5 \frac{dV_{C5}}{dt} = (1 - u_{42}) \cdot i_{L4} + (1 - u_{51}) \cdot i_{L5} - i_{ch} \tag{3-131}$$

For N-modules, the state equation for the common capacitor can be defined as follows:

$$C_1 \frac{dv_{C1}}{dt} = (1 - u_{11}) \cdot i_{L1} - i_{ch} \tag{3-132}$$

$$C_k \frac{dv_{Ck}}{dt} = \left(1 - u_{k-1,2}\right) \cdot i_{L_{k-1}} + (1 - u_{k1}) \cdot i_{Lk} - i_{ch} \tag{3-133}$$

where k= 2, 3, …, N.

The equation of the lowest capacitor can be obtained:

$$C_{N+1}\frac{dV_{CN+1}}{dt} = (1 - u_{N2}) \cdot i_{LN} - i_{ch} \tag{3-134}$$

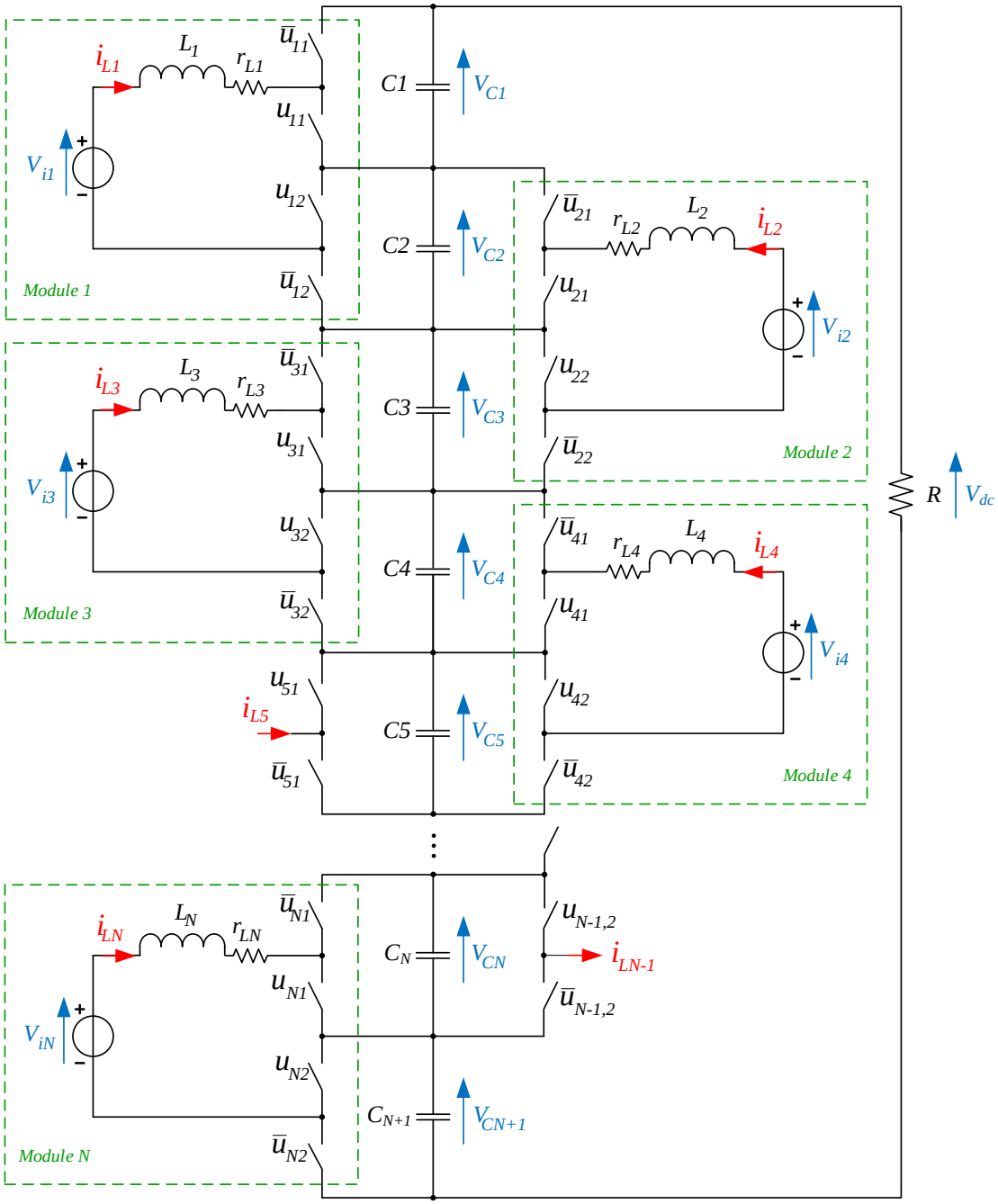

Figure 3-73 Proposed MTL converter with N module.

3.2.3.1. Pulse-width modulation

The PWM signal generation for N-module is shown in Figure 3-72. The phase shift for the k[th] module of the signal u_{k1} and u_{k2} is of 180 degrees. While the phase shift of the signal u_{k2} and $u_{k+1,1}$ is of 180 degrees.

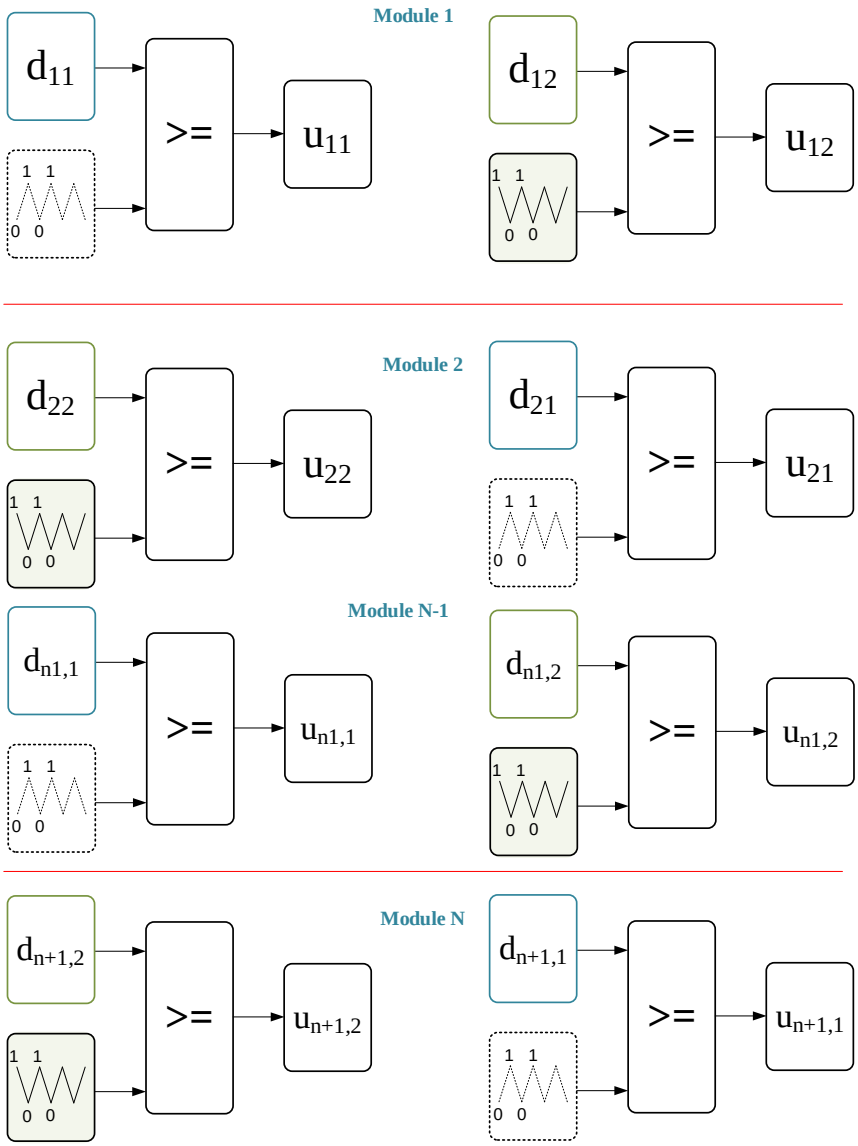

Figure 3-74 PWM generation MTL DC-DC converter with N modules.

3.3. Controller

The primary objective is to control the input current of each module. Moreover, balancing the voltage across the output capacitors is mandatory. For this purpose, the indirect-sliding mode control is used.

3.3.1. Controller for N-module

For the MTL converter with N module, the input current of each module (j[th]) is controlled thanks to the sliding function defined as:

$$s_{ij} = i_{Lj} - I_{refj} + k_{ij}\int (i_{Lj} - I_{refj})d\tau \tag{3-135}$$

where j=1, 2, 3, …, N.

The voltage balancing of the capacitors C_j and C_{j+1} is ensure thanks to the sliding function defined as:

$$s_{vj} = (v_{Cj+1} - v_{Cj}) + k_{vj}\int (v_{Cj+1} - v_{Cj})d\tau \tag{3-136}$$

where j=1, 2, 3, …, N.

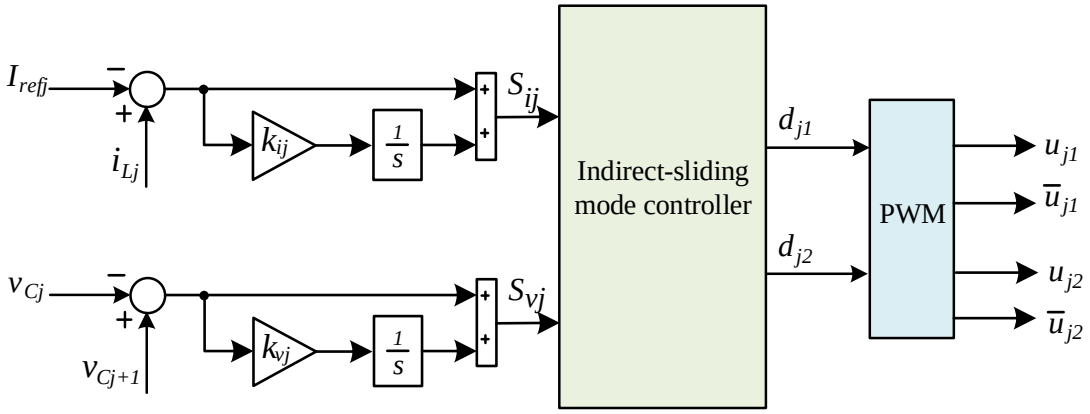

Figure 3-75 Block diagram of current and voltage balancing controls for the j[th]-module.

To force the slide functions to slide on their references exponentially, the reaching laws are used:

$$\dot{s}_{ij} = -\lambda_{ij} s_{ij} \tag{3-137}$$

$$\dot{s}_{vj} = -\lambda_{vj} s_{vj} \tag{3-138}$$

where j=1, 2, 3, … N. λ_{ij}, and λ_{vj} are positive constant values which allow to fix the dynamics of s_{ij} and s_{vj}. The block diagram for the current control and voltage balancing is given in Figure 3-75 for MTL converter with N modules.

3.3.2. Controller for two modules and four modules of MTL converter

This section presents examples where two modules and four modules of the MTL converter are implemented.

3.3.2.1. Controller for N = 2

The architecture of the studied converter is presented in Figure 3-71. According to previous section, the block diagram of the control is shown in Figure 3-76.

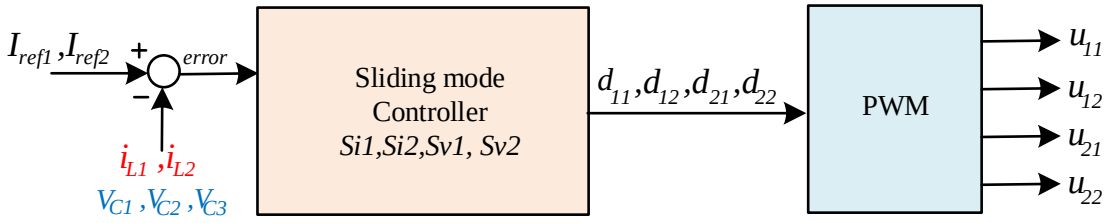

Figure 3-76 Block diagram for generating command signal of two modules.

The sliding surface for the inductor currents $i_{L1}$and i_{L2} can be defined as:

$$s_{i1} = i_{L1} - I_{ref1} + k_{i1}\int (i_{L1} - I_{ref1})d\tau \quad (3\text{-}139)$$

$$s_{i2} = i_{L2} - I_{ref2} + k_{i2}\int (i_{L2} - I_{ref2})d\tau \quad (3\text{-}140)$$

For balancing the voltage across the three capacitors, two sliding surfaces have to define:

$$s_{v1} = (V_{c2} - V_{c1}) + k_{v1}\int (V_{c2} - V_{c1})d\tau \quad (3\text{-}141)$$

$$s_{v2} = (V_{c3} - V_{c2}) + k_{i2}\int (V_{c3} - V_{c2})d\tau \quad (3\text{-}142)$$

To force the sliding functions to zero, the reaching laws are used.

$$\dot{s}_{i1} = -\lambda_{i1}s_{i1} \quad (3\text{-}143)$$

$$\dot{s}_{i2} = -\lambda_{i2}s_{i2} \quad (3\text{-}144)$$

$$\dot{s}_{v1} = -\lambda_{v1} s_{v1} \quad (3\text{-}145)$$

$$\dot{s}_{v2} = -\lambda_{v2} s_{v2} \quad (3\text{-}146)$$

The duty cycles d_{11}, d_{12}, d_{21} and d_{22} can be solved by equations (3-141) to (3-142). The control signal u is obtained by PWM strategy detailed in previous section.

To demonstrate the proposed control, a simulation of two-module architecture including its controller are implemented in MATLAB/Simulink. The parameters used for simulation are detailed in Table 3-7.

Parameter	system	Value
Input voltage	V_{i1}, V_{i2}	12 V
Inductor	L_1, L_2	1 mH
Resistance of inductor	r_{L1}, r_{L2}	0.76 Ω
Capacitor	C_1, C_2, C_3	100 µF
Switching frequency	f_s	10 kHz
	$k_{ij} = \lambda_i$	1250 rad/s
	$k_{vj} = k_{vj+1} = \lambda_v$	250 rad/s

Table 3-7 System and control parameter.

Figure 3-77 shows that the currents follow their references and the voltage of across capacitor is balancing. The frequency of the voltage across the capacitor C_2 is two times than that of C_1 or C_3. As the capacitances in this simulation are equal, the shared capacitor voltage ripple is lower than others. These figures present the switching waves of u_{11} and u_{12} and their impacts on the inductor currents.

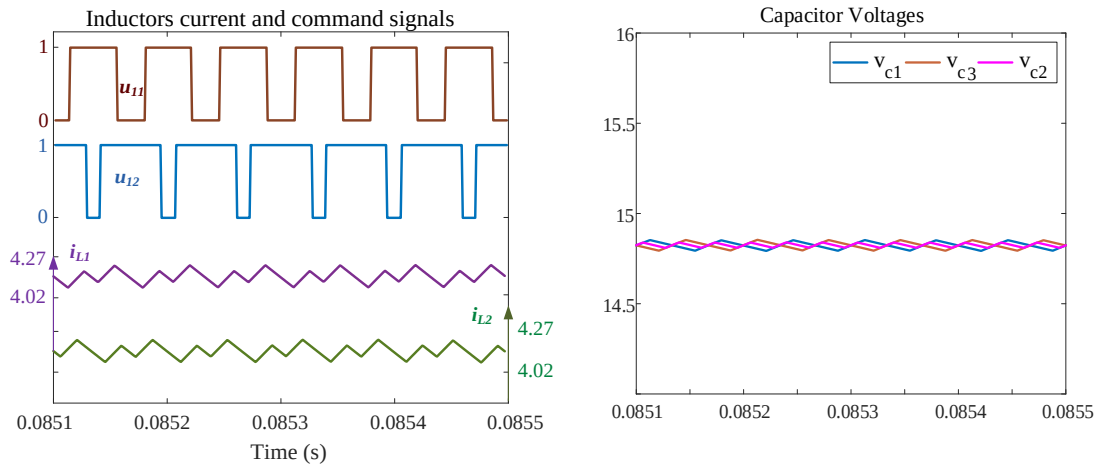

Figure 3-77 Simulation of current waveform $i(t)$, command signal u_{11}, u_{12} and capacitor voltages ($i_{ref1} = i_{ref2} = 4.16\ A$).

The Figure 3-78 show the impact of the voltage balancing control. The balancing voltage controller is activated excepted in the zone II. It can be shown that the voltage balancing is ensure when the controller is activated. Large imbalance voltage appears when the voltage controller is turned off.

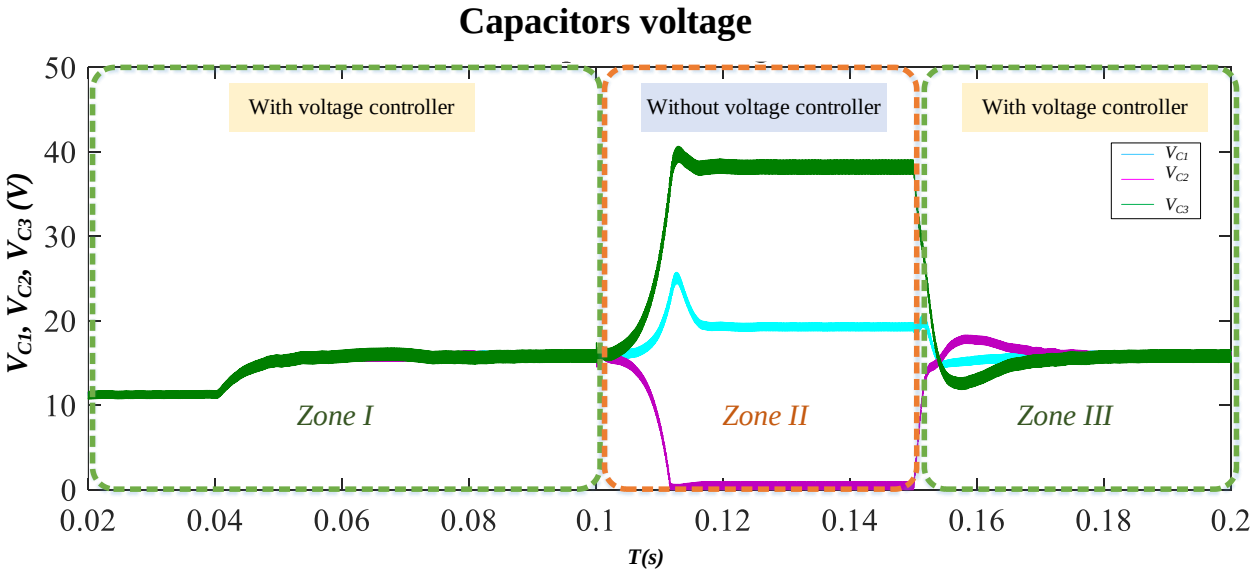

Figure 3-78 Capacitor voltage waveform with voltage controller and without voltage controller.

3.3.2.2. Controller for N = 4

In this section, the simulation for four modules highlights the possibility to extend the proposed control law. Based on the proposed control method, the control objectives are fulfilled. The inductor currents track their references well, whereas the voltage balance for the capacitor voltage is achieved as shown in Figures 3-24 and, respectively, for the system where all capacitances are identical. The voltage accross C_2, C_3, C_4 see the doubles switching frequency. Therefore, reducing the capacitance value for the capacitor corresponding to the frequency they face to have the same ripple voltage is possible. Furthermore, eventually reduce the system's overall volume, size, and cost.

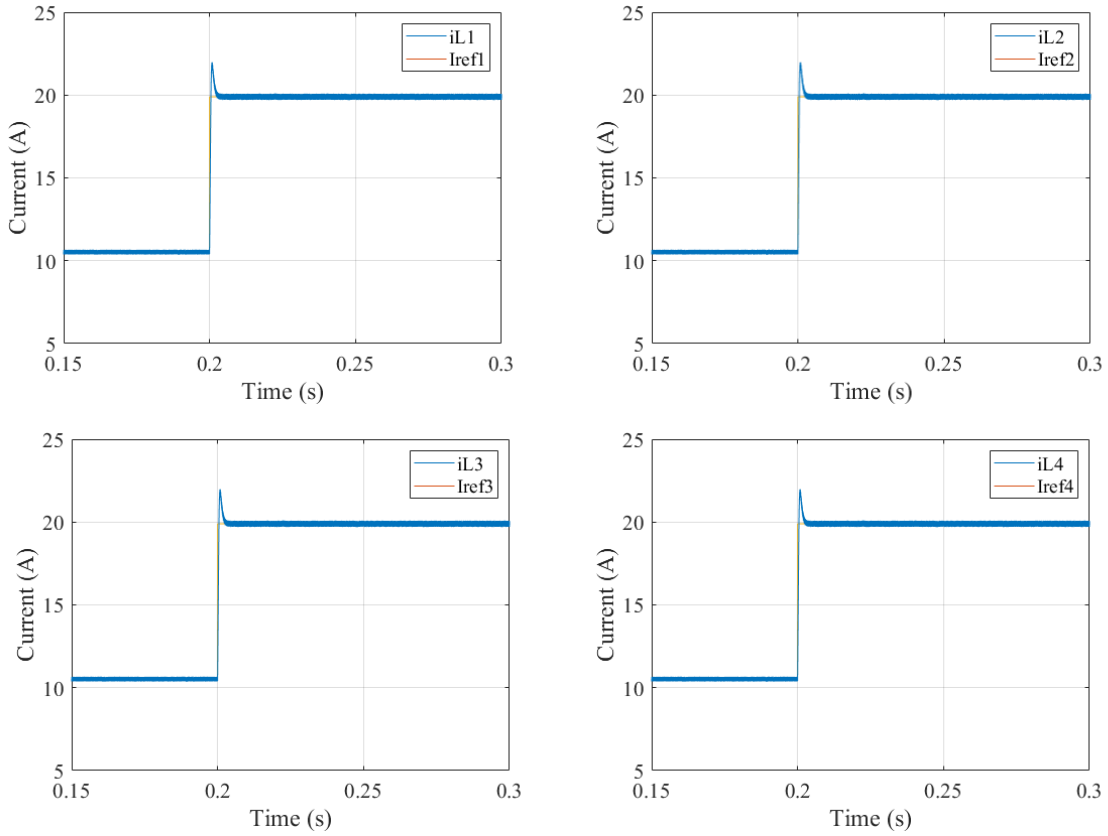

Figure 3-79 Inductor currents and their references of four modules (N = 4).

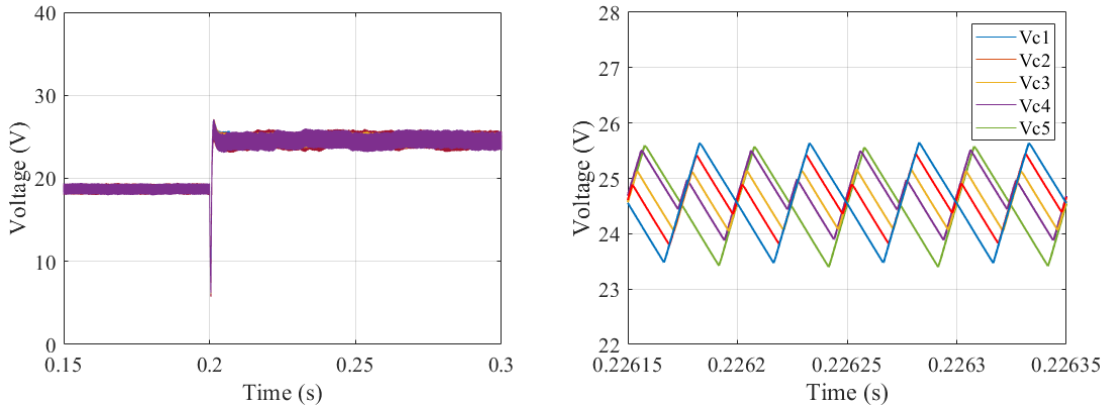

Figure 3-80 Output capacitor voltages. (Right) Zoomed waveforms.

3.4. Controllability area for N modules

To ensure the controllability according to imbalance input power, we investigate the evoluation of the duty cycle of each switches. For this study, we suppose that all the components are ideal. The controllability is ensure when each duty cycle is between 0 and 1.

3.4.1. Evaluation of duty cycles

The duty cycles of each switch related to the state equations will be given at this stage with the help of load current and output voltage [102]. For the given averaged input powers and averaged input voltages, the source currents can be calculated:

$$i_L = \frac{P}{V_i} \tag{3-147}$$

Hence, the relationship between the input power and currents of voltage sources in the steady state can be expressed as:

$$Steady\ State: \forall k \in \{1,\dots,N\} \rightarrow i_{Lk} = \frac{P_k}{V_{ik}} \tag{3-148}$$

The load current in steady-state can be defined as a function of the output power when losses are neglected:

$$i_{ch} = \frac{P_{ch}}{\sum_{k=1}^{N+1} V_{Ck}} = \frac{\sum_{k=1}^{N} P_k}{V_{dc}} = \frac{P_T}{V_{dc}} \tag{3-149}$$

The output voltage V_{out} in the steady-state can be defined under an assumption the all capacitor voltages are equal. The kth capacitor voltage can be found by dividing the DC bus voltage V_{dc} by the number of capacitors:

$$Steady\ State: \forall k \in \{1,\dots,N+1\} \rightarrow V_{Ck} = \frac{V_{dc}}{N+1} \tag{3-150}$$

To define the duty cycle in steady state, we consider N-modules converter. Using the equation (3-127) for the first capacitor, one can obtain the equation:

$$1 - d_{11} = \frac{i_{ch}}{i_1} = \frac{P_T}{V_{dc}} \cdot \frac{V_{i1}}{P_1} = d_{11}^* \tag{3-151}$$

In the same way, for the lowest capacitor, using equation (3-18) it can be written as follows:

$$1 - d_{N2} = \frac{i_{ch}}{i_N} = \frac{P_T}{V_{dc}} \cdot \frac{V_{iN}}{P_N} = d_{N2}^* \tag{3-152}$$

In equations (3-151) and (3-152), the expression $(1-d_{11})$ is taken as d_{11}^{*}, and the expression $(1-d_{N2})$ is equal to d_{N2}^{*} for simplicity.

Similarly, using the differential equation of the voltages for the shared capacitors in (3-13), it leads to

$$\forall k \in \{2,\dots,N\} \rightarrow \tag{3-153}$$

$$(1-d_{k1})i_{Lk} + \left(1-d_{k-1,2}\right)i_{Lk-1} - i_{ch} = 0$$

Replacing i_{Lk} and i_{Lk-1} in equation (3-153) by the power and input voltage detailed in equation (3-148), equation (3-154) can be obtained:

$$(I): \frac{(1-d_{k1})P_k}{V_{ik}} + \frac{\left(1-d_{k-1,2}\right)P_{k-1}}{V_{i_{k-1}}} - i_{ch} = 0 \tag{3-154}$$

From equation (3-11) in steady state, supposing that the losses are neglected, equation (3-155) is achieved.

$$V_{ik} - (1-d_{k1})V_{Ck} - (1-d_{k2})V_{C_{k+1}} = 0 \tag{3-155}$$

$V_{C_{k+1}}$ and V_{Ck} in equation (3-155) can be replaced by equation (3-150), and by respecting the condition that all capacitors' voltages are equaled, it yields:

$$(II): V_{ik} - \frac{(1-d_{k1})V_{dc}}{N+1} - \frac{(1-d_{k2})V_{dc}}{N+1} = 0 \tag{3-156}$$

By using the equations (*I*) and (*II*), the duty cycles can be computed. It can be applied by placing the different quantities of k in equations (*I*) and (*II*). By putting k=1 in equation (*II*) and using d_{11}^{*} from (3-23), the quantity of d_{12}^{*} can be obtained:

$$d_{12}^{*} = \frac{[(N+1)\cdot P_1 - P_T]}{P_1} \cdot \frac{V_{i1}}{V_{dc}} \tag{3-157}$$

When k=2 in equation (*I*), d_{21}^{*} can be found:

$$d_{21}^{*} = -\frac{[(N+1)\cdot P_1 - 2P_T]}{P_2}\cdot\frac{V_{i2}}{V_{dc}} \tag{3-158}$$

When k=2 in equation (*II*), d_{22}^{*} can be obtained.

$$d_{22}^{*} = \frac{V_{i2}(N+1)}{V_{dc}} - d_{21}^{*} \tag{3-159}$$

According to the value of, d_{21}^{*}, the value of d_{22}^{*} can be obtained.

$$d_{22}^{*} = \frac{[(N+1)\cdot(P_1+P_2) - 2P_T]}{P_2}\cdot\frac{V_{i2}}{V_{dc}} \tag{3-160}$$

By placing k=3 in equation (*I*), the following equation can be obtained.

$$d_{31}^{*} = \frac{V_{i3}}{P_3}\left[i_{ch} - d_{22}^{*}\cdot\frac{P_2}{V_{i2}}\right] \tag{3-161}$$

Given that the value of d_{22}^{*} can be obtained from equation (3-161), the value of d_{31}^{*} is calculated as equation (3-162).

$$d_{31}^{*} = -\frac{[(N+1)\cdot(P_1+P_2) - 3P_T]}{P_3}\cdot\frac{V_{i3}}{V_{dc}} \tag{3-162}$$

After replacing k=3 in equation (*II*), the following equation can be obtained.

$$d_{32}^{*} = \frac{V_{i3}(N+1)}{V_{dc}} - d_{31}^{*} \tag{3-163}$$

By inserting the value of d_{31}^{*} in equation (3-163) and simplification, the value of d_{32}^{*} can be calculated as equation (3-164).

$$d_{32}^{*} = \frac{[(N+1)\cdot(P_1+P_2+P_3) - 3P_T]}{P_3}\cdot\frac{V_{i3}}{V_{dc}} \tag{3-164}$$

Putting k=4 in (II) and using the value of d_{32}^* in equation (3-164), the value of d_{41}^* is calculated using equation (3-165).

$$d_{41}^* = -\frac{[(N+1)\cdot(P_1+P_2+P_3)-4P_T]}{P_4}\cdot\frac{V_{i4}}{V_{dc}} \tag{3-165}$$

After replacing k=4 in equation (*II*), the following equation can be obtained.

$$d_{42}^* = \frac{[(N+1)\cdot(P_1+P_2+P_3+P_4)-4P_T]}{P_4}\cdot\frac{V_{i4}}{V_{dc}} \tag{3-166}$$

From the information above, the duty cycles for different k>1 quantities can be expressed as:

$$\begin{cases} d_{k1}^* = -\dfrac{[(N+1)\sum_{j=1}^{k-1}P_j - kP_T]}{P_k}\cdot\dfrac{V_{ik}}{V_{dc}} \\ d_{k2}^* = \dfrac{[(N+1)\sum_{j=1}^{k}P_j - kP_T]}{P_k}\cdot\dfrac{V_{ik}}{V_{dc}} \end{cases} \tag{3-167}$$

To prove whether the inductive is guessed, it will be investigated from the principle of induction for (k+1). From equation (3-154), and for (k+1), it leads to

$$d_{k+1,1}^*\frac{P_{k+1}}{V_{ik+1}} + 1 - d_{k2}^*\frac{P_k}{V_{i_k}} - i_{ch} = 0 \tag{3-168}$$

After replacing i_{ch} and d_{k2}^* with (3-149), (3-167) becomes

$$d_{k+1,1}^* = \frac{V_{i,k+1}}{P_{k+1}}\left[\frac{P_T}{V_{dc}} - \frac{P_k}{V_{i,k}}\cdot\frac{(N+1)\sum_{j=1}^{k-1}P_j - kP_T}{P_k}\cdot\frac{V_{i_k}}{V_{dc}}\right] \tag{3-169}$$

By simplifiying,

$$d_{k+1,1}^* = \frac{V_{i,k+1}}{P_{k+1}}\left[\frac{P_T(k+1)}{V_{dc}} - \frac{(N+1)\sum_{j=1}^{k}P_j}{V_{dc}}\right] \tag{3-170}$$

For k+1 in (3-168), one can express

$$V_{i,k+1} - \frac{d_{k+1,1}^* V_{dc}}{N+1} + \frac{d_{k+1,2}^* V_{dc}}{N+1} = 0 \tag{3-171}$$

By inserting $d_{k+1,1}^*$ from (3-170) into (3-171), it leads to

$$d_{k+1,2}^{*} = \frac{N+1}{V_{dc}}\left[V_{i,k+1} - \frac{V_{dc}}{N+1}\cdot\frac{V_{i,k+1}}{P_{k+1}}\right]\left[\frac{P_T(k+1)}{V_{dc}} - \frac{(N+1)\sum_{j=1}^{k} P_j}{V_{dc}}\right] \quad (3\text{-}172)$$

After simplifying of (3-172), it becomes

$$d_{k+1,2}^{*} = \frac{V_{i,k+1}}{P_{k+1}\cdot V_{dc}}\left[(N+1)\sum_{j=1}^{k+1} P_j - (k+1)P_T\right] \quad (3\text{-}173)$$

Therefore, d_{k+1}^{*} holds. It means that the induction term is well selected. Since the base case and the induction step have been performed, by mathematical induction, the statement d_k^{*} holds for all natural number k. Therefore, the definition of each duty cycle for the MTL converter with N modul is defined by the equation (3-40).

3.4.2. Controllable area evaluation

The duty cycles for the converter are essential to ensure that the converter will operate safely. For this converter, when all duty cycles are inside [0,1] relating to input powers, the zone is called a commandable zone. The voltage of each output capacitor is defined by:

$$V_C = \Upsilon \cdot V_i \quad (3\text{-}174)$$

where Υ allows to set the output voltage ($V_{out} = (N+1)\cdot V_C = \Upsilon\cdot(N+1)\cdot V_i$).

3.4.2.1. 2 modules

The two-module system is shown in Figure 3-71, the system has five state variables in five equations [97]. According to previous section and using $\Upsilon = 2$, the relationships between the duty cycle and input powers can be presented in Table 3-8.

Duty cycles in steady-state
$d_{11} = \frac{5P_1 - P_2}{6P_1}$
$d_{12} = \frac{4P_1 + P_2}{6P_1}$
$d_{21} = \frac{P_1 + 4P_2}{6P_2}$
$d_{22} = \frac{-P_1 + 5P_2}{6P_2}$

Table 3-8 Duty cycle of the proposed two-module converter.

It should be noted that when the input powers of each module are equal, one can see the following relationships:

$$d_{11} = d_{22} \tag{3-175}$$

$$d_{12} = d_{21} \tag{3-176}$$

To illustrate the commandable areas according to parameters detailled in Table 3-8, we suppose that $\Upsilon = 2$ $\left(V_{i1} = V_{i2} = \frac{V_{dc}}{6}\right)$. The commandable area for the MTL converter is represented in Figure 3-81. A ratio of input power approximatively equal to two ($P_1 = 2\,P_2$ or $P_2 = 2\,P_1$) correspond to the boundary of the commandability area for MTL converter with 2 modules.

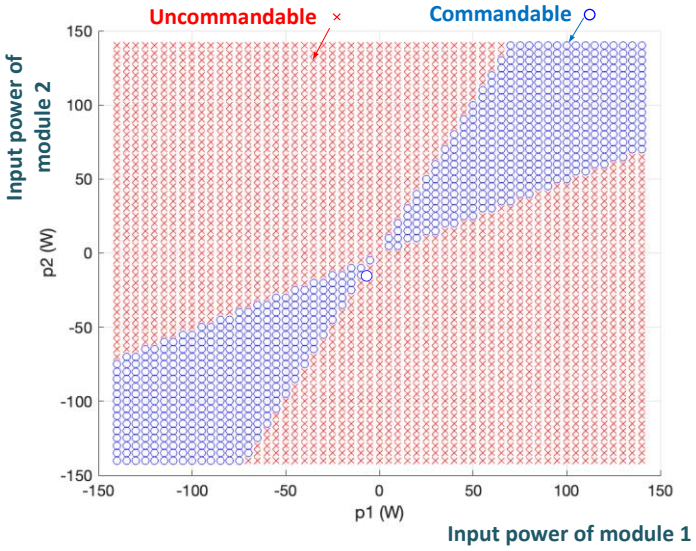

Figure 3-81 Commandable areas of the two-module system for changes in the input powers of each module.

3.4.2.2. 3, 4 and 5 modules

In this section, the case of 3, 4, and 5 module are discussed. Here, we assume that by changing (increasing or decreasing) the power of one of the sources, the power of the other sources is changed, such that the sum of powers (P_T) is constant. In an N-module MTL converter, to change one of the powers, a coefficient α is introduced, and the power P_i is defined as follows:

$$P_i = \frac{\alpha P_T}{N} \tag{3-177}$$

where α is a number greater than zero and N denotes the number of modules. Therefore, the power of other sources can be found as

$$P_j = \frac{P_T - P_i}{N - 1} \tag{3-178}$$

By changing α to the desired value, the duty cycles can be obtained. Considering N=3 and $\gamma = 2$, the values of the duty cycles are shown in Table 3-9 where the values of α varying from 0.4 to 1.3.

Note that for α ranging from α = 0.4 to 0.75, the value of duty cycle d_{12} is greater than one. These values are listed in red in Table 3-9. Therefore, this system is not commandable for α values below 0.75. The commandable area of the system in this case is 0.76 <α <1.3.

α	$\frac{P_1}{P_T}$	$\frac{P_2}{P_T}, \frac{P_3}{P_T}$	$\frac{P_1}{P_2}$	Duty cycles					
				d_{11}	d_{12}	d_{21}	d_{22}	d_{31}	d_{32}
0.4	0.13	0.43	0.307	0.062	**1.437**	0.57	0.92	0.78	0.711
0.6	0.2	0.4	0.5	0.375	**1.125**	0.625	0.875	0.812	0.687
0.7	0.23	0.38	0.608	0.464	**1.035**	0.652	0.847	0.826	0.673
0.75	0.253	0.375	0.66	0.5	**1**	0.66	0.83	0.83	0.66
0.76	0.256	0.373	0.67	0.506	0.99	0.669	0.8303	0.834	0.665
0.8	0.26	0.366	0.727	0.53	0.96	0.68	0.81	0.84	0.659
0.9	0.3	0.35	0.85	0.58	0.916	0.714	0.78	0.85	0.642
1.0	0.33	0.33	1	0.625	0.875	0.75	0.75	0.875	0.625
1.1	0.36	0.316	1.15	0.65	0.84	0.78	0.71	0.89	0.605
1.2	0.4	0.3	1.33	0.68	0.81	0.83	0.66	0.91	0.58
1.3	0.43	0.28	1.52	0.71	0.78	0.88	0.61	0.94	0.55

Table 3-9 Duty cycles in a 3-module three-level boost converter with variation of α.

Similarly, for a 4-module three-level boost converter, the results are presented in Table 3-10. Note that for the coefficient α ranging between 0.8 and 1.6, the system is in its commandable region.

α	$\frac{P_1}{P_T}$	$\frac{P_2}{P_T}, \frac{P_3}{P_T}, \frac{P_4}{P_T}$	$\frac{P_1}{P_2}$	Duty cycles							
				d_{11}	d_{12}	d_{21}	d_{22}	d_{31}	d_{32}	d_{41}	d_{42}
0.5	0.125	0.29	0.42	0.2	**1.3**	0.52	0.97	0.68	0.81	0.84	0.65
0.6	0.15	0.283	0.52	0.33	**1.16**	0.558	0.94	0.705	0.794	0.852	0.647
0.7	0.175	0.275	0.63	0.42	**1.07**	0.59	0.9	0.72	0.77	0.86	0.63
0.75	0.18	0.27	0.69	0.46	**1.03**	0.607	0.89	0.73	0.76	0.869	0.63
0.8	0.2	0.26	0.75	0.5	**1**	0.62	0.87	0.75	0.75	0.875	0.625
0.81	0.202	0.265	0.76	0.506	0.993	0.628	0.871	0.752	0.74	0.87	0.62
0.9	0.225	0.25	0.87	0.55	0.94	0.66	0.83	0.77	0.72	0.88	0.61
1	0.25	0.25	1	0.6	0.9	0.7	0.8	0.8	0.7	0.9	0.6
1.2	0.3	0.23	1.28	0.66	0.83	0.78	0.71	0.85	0.64	0.92	0.57
1.3	0.32	0.22	1.44	0.69	0.8	0.83	0.66	0.88	0.61	0.94	0.55
1.4	0.35	0.21	1.61	0.71	0.78	0.88	0.61	0.92	0.57	0.96	0.53
1.5	0.37	0.2	1.8	0.73	0.76	0.94	0.56	0.96	0.54	0.98	0.52
1.6	0.4	0.2	2	0.75	0.75	**1**	0.5	**1**	0.5	**1**	0.5
1.7	0.42	0.19	2.21	0.76	0.73	**1.06**	0.43	**1.04**	0.45	**1.02**	0.47

Table 3-10 Duty cycles in a 4-module three-level boost converter with variation of α.

The commandable intervals of the 3-module, 4-module, and 5-module systems are summarized in Table 3-11. In these cases, the voltage ratio ($\Upsilon = 2$) and variations in the coefficient α are the same. At this point, the number of modules that leads to the optimal range for the commandable area can be explored.

System	V_i	α	Zone commandable
3-module	$\frac{V_{dc}}{8}$	0.5 - 1.7	0.76< α <1.3
4-module	$\frac{V_{dc}}{10}$		0.8< α <1.6
5-module	$\frac{V_{dc}}{12}$		0.835< α <1.7

Table 3-11 Commandable intervals of three to five modules

As it can be seen in this table, the increase of the module number reduce the ratio of power between the source number.

3.5. Capacitor sizing

Voltage ripple reduction is a significant challenge for converter topology design. This section details the capacitance design for the proposed topology compared to the topology with a conventional boost converter, as shown in Figure 3-82. For simplicity, the system for N =2 is considered. Both topologies are fed by two power sources while supplying only one resistive load with the same DC bus voltage. Because both topologies use the same number of inductors, but a different number of output capacitors, the size, volume, and cost of such capacitors result in a good index.

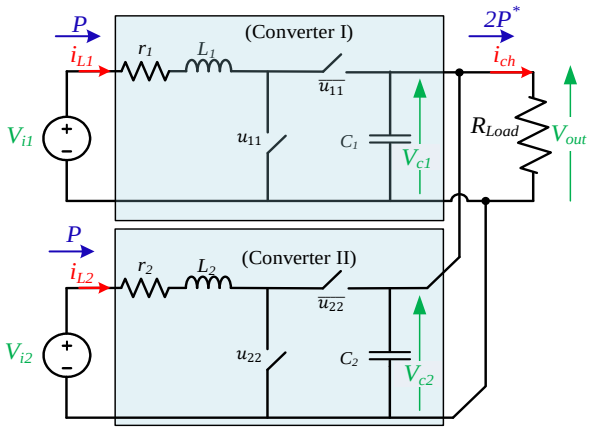

Figure 3-82 Topology based on the two-boost converters.

3.5.1. Capacitor sizing for MTL converter

The following assumptions are made to investigate the system in steady state, which is a MTL converter with two modules. The input voltages are similar as $V_i = V_{i1} = V_{i2}$. The input power of each module is identified as $P_1 = P_2 = P = V_i \cdot I$. The input currents are the same as $= i_{L1} = i_{L2}$. The inductor resistances for the two modules are similar, as detailed in $r_1 = r_2 = r$.

Considering the loss in the inductor resistances, the output power $2P^*$ for a 2-module three-level converter (Figure 3-82), each input power P is

$$P^* = P - r\left(\frac{P}{V_i}\right)^2 \tag{3-179}$$

Therefore, the output voltage for the 2-module three-level converter can be calculated:

$$2P^* = \frac{{V_{out}}^2}{R_{out}} \Rightarrow V_{out} = \sqrt{2P^* R_{out}} \tag{3-180}$$

In steady state, consideing $2P^* = P_{out} = V_{out} \cdot I_{ch}$, I_{ch} is the average value of the load current, and the duty cycles of switches s_{11}, s_{22} are $d_{11} = d_{22} = d$, it leads to:

$$(1-d)\frac{P}{V_i} = \frac{2P^*}{V_{out}} = \frac{P_{out}}{V_{out}} \tag{3-181}$$

Using equations (3-180) and (3-181), we obtain:

$$d = 1 - \frac{2P^*}{P}\frac{V_i}{V_{out}} = 1 - 2(1 - r\frac{P}{{V_i}^2}) \cdot \frac{V_i}{\sqrt{2P^* R_{out}}} \tag{3-182}$$

Similarly, using the shared capacitor equation (3-124), the duty cycles d_{12} and d_{21} can be found:

$$d_{12} = d_{21} = 1 - \frac{P^*}{P}\frac{V_i}{V_{out}} \Rightarrow d_{12} = d_{21} = 1 - (1 - r\frac{P}{{V_i}^2}) \cdot \frac{V_i}{\sqrt{2P^* R_{out}}} \tag{3-183}$$

where $d_{12} = d_{21}$ are the duty cycles of switches s_{12}, s_{21}.

Calculation of $C_1 = C_2 = C$, the ripple of voltage ΔV for C_1 and C_2 in this structure can be obtained:

$$C_1 \frac{\Delta v_{C_1}}{d_{11} T} = I_{ch} = \frac{P_{out}}{V_{out}} \Longrightarrow \Delta v_{C_1} = \frac{d_{11}}{C_1 f_s}\frac{P_{out}}{V_{out}} = \Delta V \tag{3-184}$$

By replacing $d_{11}$from equation (3-181), the capacitance C_1 can be determined as follows:

$$C_1 = \frac{\left(1 - 2(1 - r\frac{P}{{V_i}^2}) \cdot \frac{V_i}{V_{out}}\right)}{\Delta V f_s}\frac{P_{out}}{V_{out}} = C \tag{3-185}$$

The shared capacitor is defined C_x. Owing to the interleaved PWM modulation technique, capacitor C_x sees its current containing a double switching frequency $f_{sCx} = 2f_s = \frac{2}{T}$. Therefore, the capacitance C_x necessary to maintain the ripple voltage $\Delta v_{C_x} = \Delta V$ is

$$C_x = \frac{1 - (1 - r\frac{P}{{V_i}^2}) \cdot \frac{V_i}{\sqrt{2P^* R_{out}}}}{2\Delta V f_s} \frac{P_{out}}{V_{out}} = \frac{C}{2} \tag{3-186}$$

It can be seen in Figure 3-83 that when the capacitance values for C_2 is one-fourth of those for C_1 or C_3, the ripple voltage across the output capictors is identical.

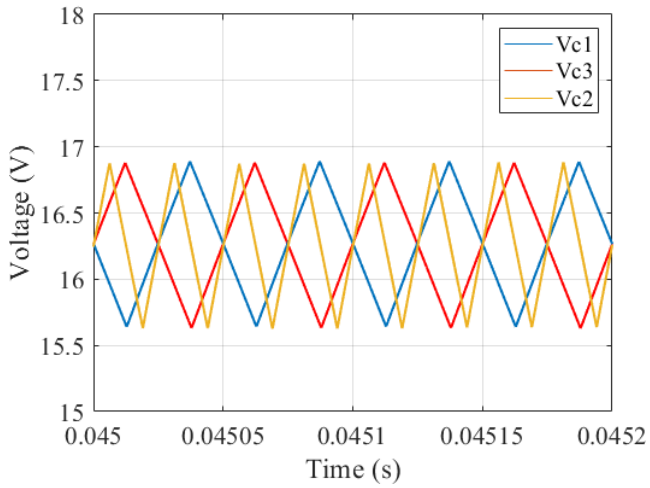

Figure 3-83 The frequency of output capacitor voltages of 2-module of three-level when the capacitor C_2 is two times of C_1 or C_3.

3.5.2. Capacitor sizing for topology using two classical boost converters

To compare with the system using two classical boost converters shown in Figure 3-82 where the switching commands for both switches are synchronized, we made the same assumptions as done for the three-level converter.

Considering the loss in the inductor resistances, the output power P^* for a 2-module three-level converter, each input power is

$$P_{out} = 2\left(P - r\left(\frac{P}{V_i}\right)^2\right) = 2P^* \tag{3-187}$$

Therefore, the output voltage is:

$$V_{out} = \sqrt{2P^* R_{out}} \tag{3-188}$$

The duty cycles, $d = d_{11} = d_{22}$ can be calculated as

$$d = 1 - (1 - r\frac{P}{{V_i}^2}) \cdot \frac{V_i}{V_{out}} \tag{3-189}$$

The total capacitance $C_{tot} = C_1 + C_2$ for the given ripple voltage can be put in the following form:

$$C_{tot} = \frac{\left(1 - (1 - r\frac{P}{{V_i}^2}) \cdot \frac{V_i}{V_{out}}\right)}{\Delta V f_s} \frac{P_{out}}{V_{out}} \tag{3-190}$$

3.5.3. Comparison of stored energy in the output capacitor

The energy stored in the output capacitors for both topologies can be calculated for the same operating point. There are three capacitors for two modules of a MTL boost converter, each capacitance is *C*, and the voltage across all capacitors is identical. The energy stored W_T in all capacitors are:

$$W_T = \frac{1}{2}\left(C + \frac{C}{2} + C\right)\frac{V_{out}^2}{9} = \frac{5}{36} C V_{out}^2 \tag{3-191}$$

For the topology with two boost converters, the energy stored in the capacitor C_{tot} is

$$W_B = \frac{1}{2} C_{tot} V_{out}^2 \tag{3-192}$$

The ratio of the stored energy for both topologies can be in the following equation:

$$\frac{W_T}{W_B} = \frac{5}{18} \frac{\sqrt{2P^* R_{out}} - 2V_i\left(1 - r\frac{P}{V_i^2}\right)}{\sqrt{2P^* R_{out}} - V_i\left(1 - r\frac{P}{V_i^2}\right)} \tag{3-193}$$

where the input power P is expressed in terms of the input current reference $P = V_i I_{ref}$ and $P^* = V_i I_{ref} - r I_{ref}^2$.

The evolution of the ratio is plotted in Figure 3-84. As can be seen, when the current reference I_{ref} higher than 40 A, the stored energy $W_T = 0.28 \cdot W_B$. It shows that the stored energy of capacitors in the topology based on the MTL converter is significantly less than the topology with the two-boost converter. The relation between the stored energy in the converters and the cost and volume has been studied in [103]- [104]- [26]. As detailed in these studies, a decrease in the stored energy decreases the converter cost. Therefore, the MTL topology has a lower cost and volume than the topology using the two-boost converters.

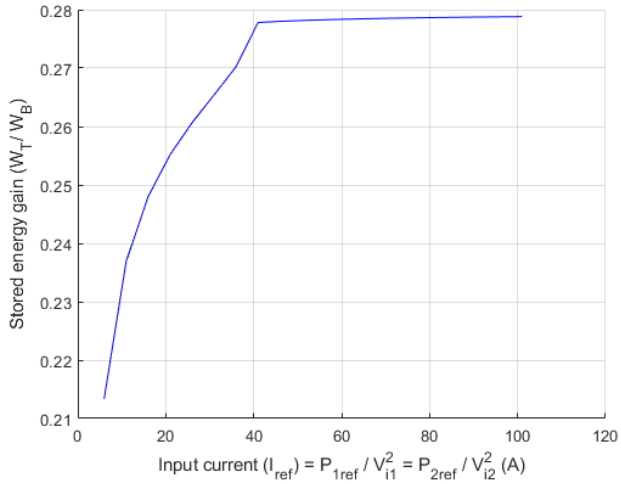

Figure 3-84 Comparison of the stored energy in the capacitors, where $I_{ref} = \frac{P_{1ref}}{{V_{i1}}^2} = \frac{P_{2ref}}{{V_{i2}}^2}$.

3.6. Experimental results

In this section, the MTL converter with two module will be validated. A test bench was developed, as shown in Figure 3-85. Two programmable power supplies (TDK-Lambda GEN1500 W) are used.

The controllers were implemented with MATLAB/Simulink-RTW software and implanted into a dSPACE-DS1202 real-time controller. All needed signals were sampled in each switching period of $T = \frac{1}{f_s}$ with $f_s = 10\ kHz$. The parameters of the system and the controllers are given in Table 3-7.

Figure 3-86 shows the waveforms of current and voltage in the steady-state when the input voltage was $V_{i1} = V_{i2} = 12V$ and $R_{ch} = 24\ \Omega$ when both input powers references are 50 W. It is confirmed theoretical analysis is given along with the simulation results.

For transient operation, Figure 3-87 shows the system's response when both input current references have changed from 2 A to 5 A. It is shown that the system's behavior exposes the controller's effectiveness in dealing with the input currents control and capacitor voltages balancing.

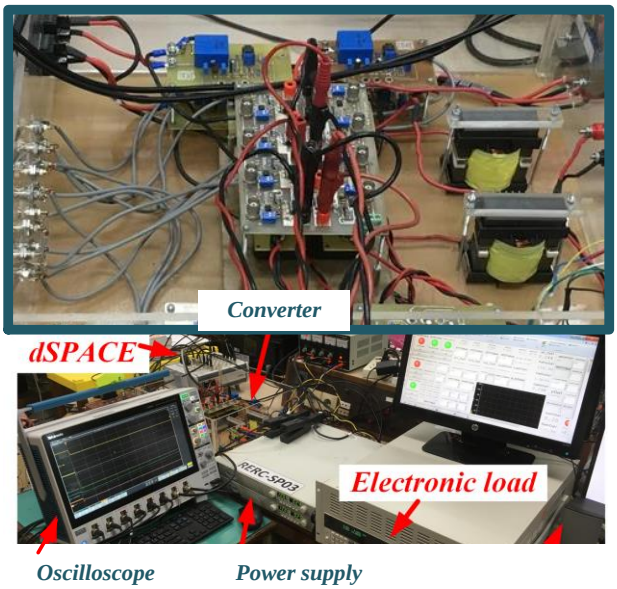

Figure 3-85 Test bench system.

When the input current references for both modules are constant at 5 A, a step load resistance from 24 Ω to 8.6 Ω is introduced. In this test, a variation in capacitor voltages occurs, as shown in Figure 3-30 where the balancing of the capacitor voltages is done as expected.

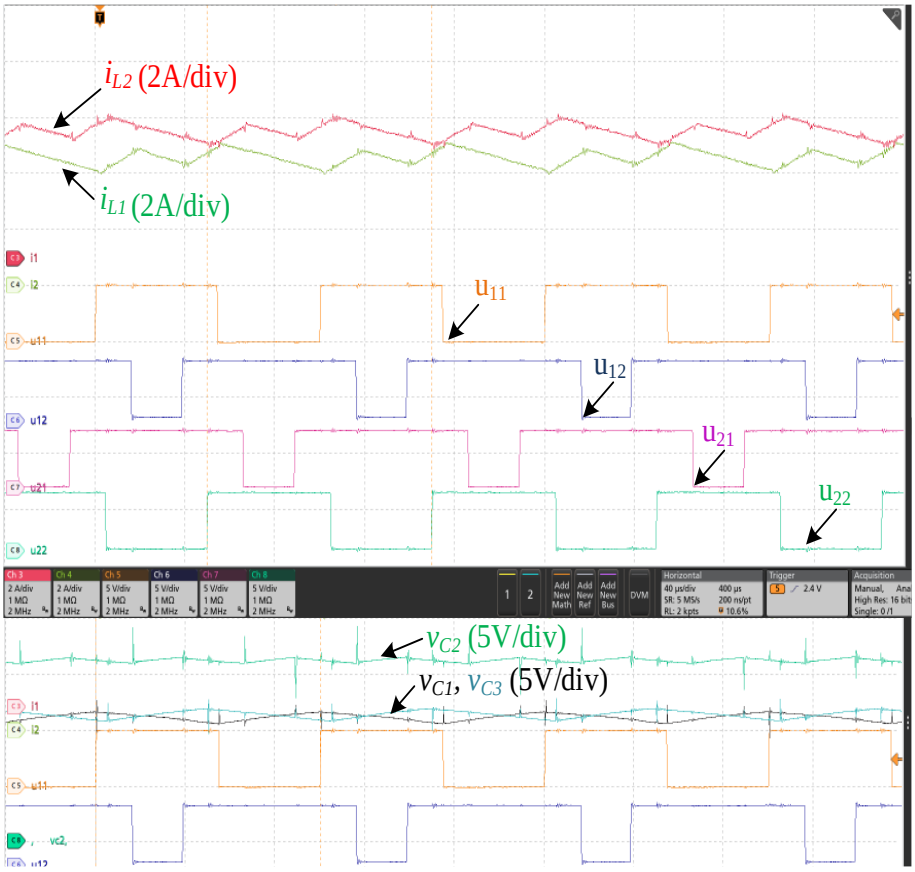

Figure 3-86 Steady-state waveforms currents and capacitor voltages with an input power reference of 50 W for both modules.

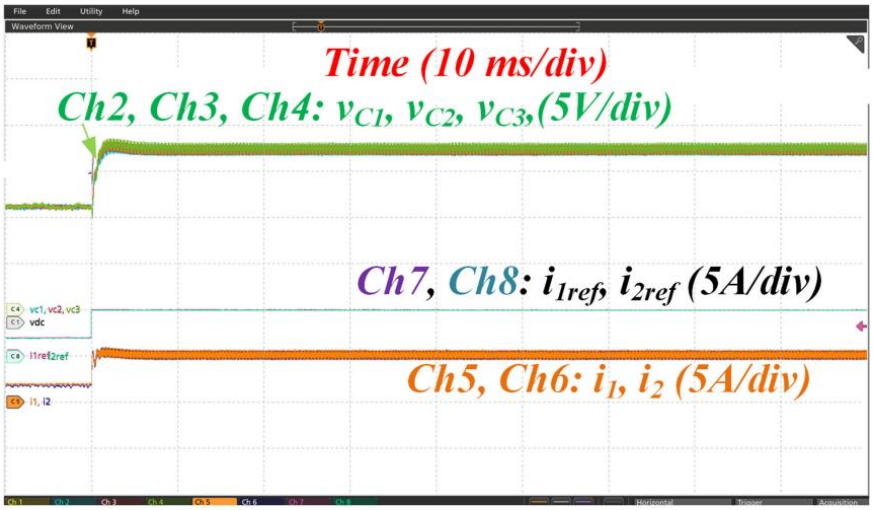

Figure 3-87 Waveforms currents and capacitor voltages with an input current reference spped from 2 A to 5 A.

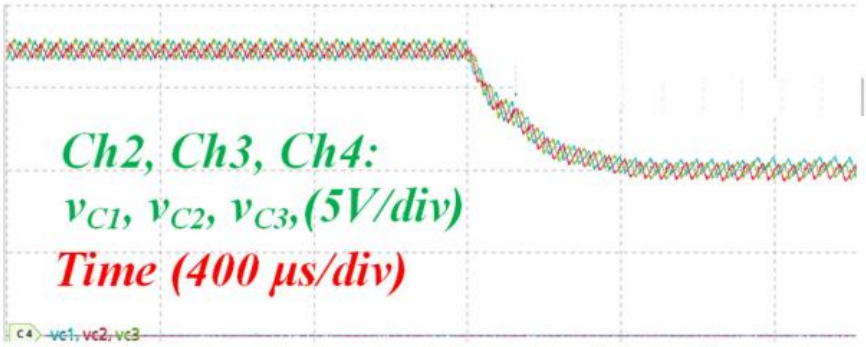

Figure 3-88 Capacitor voltages for a resistance load change from 24 Ω to 8.6 Ω.

3.7. Conclusion

This chapter presents a new multi-input MTL converter. It can use with several energy sources and be applied to a fuel cell system, or the hybrid system presented in Chapter 2. The fuel cell can be separated into several stacks to augment the degree of freedom to manage the fuel cell system and may increase overall efficiency and its lifespan.

This novel configuration based on a three-level DC-DC boost converter was investigated. Sharing one of the capacitors of the N-module of three-level makes voltage balancing the output capacitor voltages. The controller based on the indirect-sliding mode control is applied to control both the input current for each input and the capacitor voltage balancing to ensure that the converter can be operated under a suitable zone. The studied topology was validated by experimental results.

Chapter IV

Energy management

4.1. Introduction

Currently, the combination of various renewable energy sources has been presented in several publications [105] [106]. In particular, fuel cells work in conjunction with the energy storage source (ESS). In application that requires a fast power supply, we usually use supercapacitor. Moreover, to increase the voltage from the hybrid system, they must connect with a converter, such as boost converter. For this thesis, the converter based on the three-level converter detailed in Chapter 3 are chosen to connect the SC to the DC Bus.

As explained in the first chapter, the instability of fuel cells has been linked to various physical degradation phenomena. They affect the state of health of each fuel cell stack [107]-[108]. The state of health models and the decision to cure the defected cells are discussed in [109].

Polarization curves (V-I curves) are a popular approach for assessing the PEMFC deterioration process. Different losses, including activation, ohmic, and mass transfer, may be studied by analyzing fluctuations in V-I model parameters during PEMFC operation. Several researches have been conducted to analyze and enhance PEMFCs operation utilizing V-I curves. In [110], [111], [112], the impacts on the V-I curves are studied according to fuel cell parameters, geometric parameters, and material characteristics. It concludes that using multi-stack configuration instead of using one stack offers possibility to manage the fuel cell system

and allowing prolong its lifetimes. Each fuel cell stack with its DC-DC converter can be used to adapt the power of each stack according to the state operation.

This chapter aims to explain the energy management strategy. The fuel cell management system (FCMS) can be used as a supervisor which can counteract the electrochemical instability of cells to cure it. The supervisor can be based on data-driven [113] [114] or model-based [8], [115], [10]. There are at least two possibilities to cure the instability of cells either modifying the operating point of the auxiliary unit or electrical power of each stack. In this thesis, we suppose that the supervisor can define the reference power for each stack due to the operating condition. This operating condition will be used to control the power of each stack, thanks to the DC/DC converter.

The entire system is composed by distributed SC unit connected to FC stack thanks to the series converter illustrated in Chapter 2. Each SC unit is considered as input source for the multi-input converter based on modular three-level boost converter illustrated in Chapter 3.

In this chapter, we present the modification of the polarization curves according to the modification of the operating point leading to drying or flooding of the fuel cell. Then, the global structure will be detailed for three stacks. Finally, the global control structure including output of the supervisor will be presented and validate by simulation results.

4.2. Analysis of polarization change curves

The performance of PEMFC degrades with prolonged use [116] or because of some heterogeneity propagate from cell to cell in the stack [117]. Many studies have analyzed the causes and mechanisms of degradation. Detection of symptoms at the beginning degradation or as soon as possible is realized by the supervisor. The structure of the supervisor is beyond this thesis.

The loss of potential is the most visible indicator of fuel cell deterioration since its performance is simply assessed by its potential vs current density. In most fuel cells, there are four basic causes of potential losses: 1) activation polarization (kinetic losses), 2) ohmic losses, 3) concentration polarization, and 4) internal currents and/or crossover losses. Generally, it is not quite straightforward to establish which type of polarization has risen over time using basic performance diagnostics, but some phenomena such as drying, or flooding can be detected. One should be able to define the contribution of different polarization changes on the cell's performance by charting the polarization-change over time curves. [118].

For a whole range of current densities, the polarization-change curve is generated by subtracting the actual cell potential from the potential at the beginning of use. We consider that the operational condition for each cell of stack is the same.

As detailed in Chapter 1, the cell voltage $V_{FC_{cell}}$ can be modeled as:

$$V_{FC_{cell}} = E_{cell} - V_{act} - V_{ohm} - V_{conc} \tag{4-194}$$

The total current in the cell can be calculated from the temperature and the pressure of gases. The theoretical cell voltage is given by the Nernst equation:

$$E_{cell} = E^0_{cell} - k_e(T - T_{ref}) - \frac{RT}{2F}\ln\left(\frac{p_{H_2O}}{p^{0.5}_{O_2} p_{H_2}}\right) \quad (4\text{-}195)$$

The activation losses are given by Butler-Volmer's law. The law can be approximated by Tafel's law as:

$$V_{act} = \frac{RT}{\alpha nF} ln\left(\frac{I_{FC}}{j_o}\right) \quad (4\text{-}196)$$

With:
$$j_0 = 10^{-5} exp\left(-\frac{53990}{R}\left(\frac{1}{T} - \frac{1}{298}\right)\right) \quad (4\text{-}197)$$

Ohmic polarization is voltage losses caused by charge transport. This leads to:

$$V_{ohm} = R_{ohm} I_{FC} \quad (4\text{-}198)$$

In this study, the electronic and contact resistances are neglected compare to the ionic resistance of the membrane given by:

$$R_{ohm} = \frac{e_m}{\sigma_m} \quad (4\text{-}199)$$

$$\sigma_m = 5.14\ 10^{-3} \times \lambda \times exp\left(1268\ \left(\frac{1}{303} - \frac{1}{7}\right)\right) \quad (4\text{-}200)$$

e_m is the membrane thickness, and λ the water content of the membrane which depends on the relative humidity of the gas in the fuel cell.

Concentration polarization is voltage losses due to mass transport limitation. Concentration losses are:

$$V_{conc} = \frac{RT}{nF} ln\left(1 - \frac{I_{FC}}{j_{lim}}\right) \quad (4\text{-}201)$$

To simulate the behavior of fuel cells, the V-I curve can use the equations mentioned in (4-194). Polarization curves make easier understanding the underlying physical principles at work in the assembly.

Many factors can influence the performance of a PEMFC. The factors include the load current, temperature, relative humidity, membrane thickness, membrane-active area, electrode active area, corrosion, purity, pressure, and concentration of hydrogen fuel, maintenance of water inside the cell, and pressure in the electrode particularly on both sides of the membrane [119].

In this section, several V-I curves are presented in normal and degraded operating conditions. This thesis interested in flooding and drying in a simplified way.

The standard parameters used are given in Table 4-1.

Parameter	Value	description
R	8.134 J/mol/K	The universal gas constant
F	96485 C/mol	Faraday's constant
n	2	The number of electrons per molecule of H_2
α	0.5	The charge transfer coefficient
k_e	0.9 10^{-3} V/K	Parameter related to the Reaction entropy assumed constant
R_{ohm}	Ω cm²	The sum of all the resistances
I_{FC}	A cm^{-2}	The current density of the FC
j_o	A cm^{-2}	The exchange current density
e_m	80 10^{-6} m	Thickness of the membrane
N_{cell}	16	Number of cells in the stack
	100 cm²	The area of cell.

Table 4-12 The parameter for simulation V-I curve.

Flooding and drying are considered in this part, and all the 16 cells in the stack are supposed to follow the same variations in their operating conditions

Flooding can occur when some water droplets appear in the gas channels or accumulate in the porous layers into the cell. The main effect of the presence of liquid water is to degrade gases transfer in the cell from the channels to the catalyst layer which may lead to starvation. As the 0D model used in this study doesn't allow to simulate the local effect of flooding, it was considered by varying the limiting current density. Indeed, the limiting current density is related to the diffusive transport limitations of the gases and corresponds to the conditions where the reactant concentration falls to zero in the catalyst layers. Its value was reduced as stronger flooding occurs. The effect of the value of the limiting current on the polarization curve is given in Figure 4-89. The decrease of j_{lim} leads to a decrease of the stack voltage mainly at high current density (where the gas fluxes are the higher).

Drying can occur when some overpotential appear in the stack leading to an increase of the temperature of membrane electrodes assembly (MEA) of one or more cells in the stack, or if the external gas humidification is defective [120] [121]. As it mostly depends on its water content, the main effect of drying conditions is an increase of the membrane ionic resistance, and then of the total ohmic resistance R_{ohm}. The effect of the total ohmic resistance on the polarization curve is presented in Figure 4-90. The values of the resistance correspond respectively to water content of the membrane respectively set to $\lambda = 15$, 10 and 5 in the equation (4-199), 15 being the highest value in humid gas conditions.

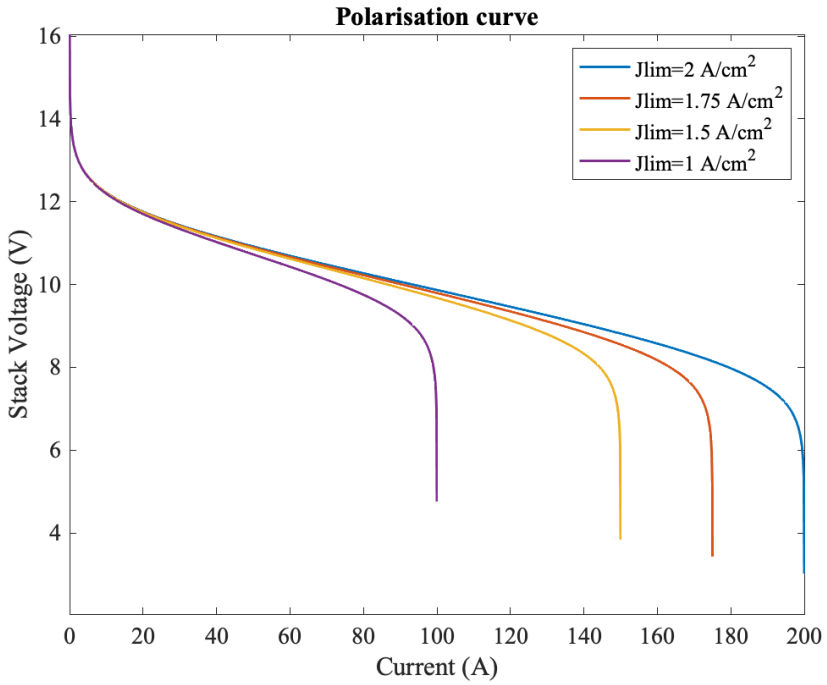

Figure 4-89 Effect of flooding (limiting current density) for T = 70 °C, R_{ohm} = 0.22 Ω cm^2

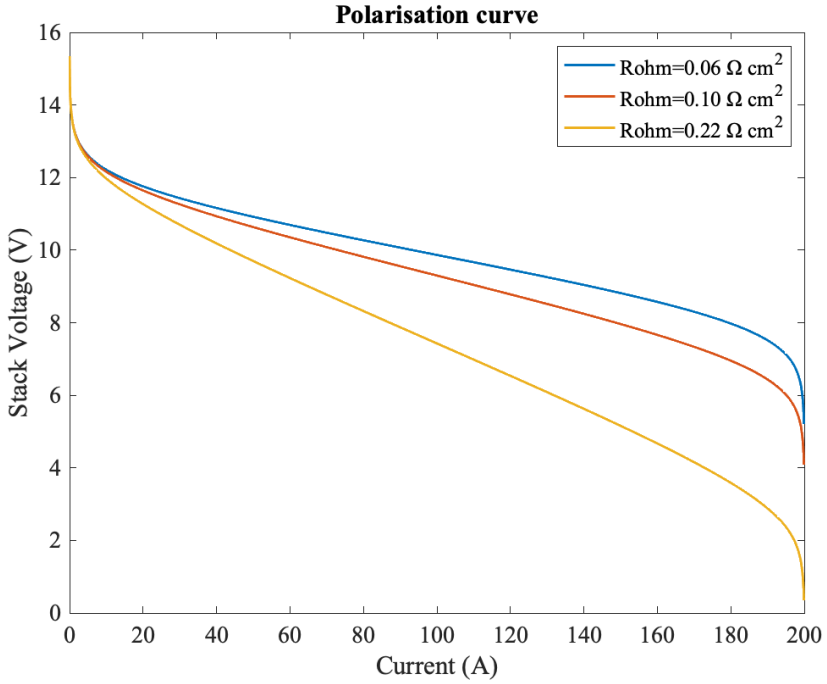

Figure 4-90 Effect of drying. When T=70 °C, j_{lim}=2 A/cm^2.

First one can observed that the effect of the resistance on the polarization is clearly different than the effect of the value of the limiting current density observed previously. In dry operating condition, as the ohmic resistance of the membrane increases, the stack voltage decreases at all current densities. Therefore, heat generation increases and then the MEA temperature which

makes the membrane even more dry and resistive. If this condition is not modified, it can go to a membrane irreversible degradation.

4.3. System description

For a single stack fuel cell, the hybrid system including a series converter and a three-level DC-DC converter is shown in Figure 4-91. The concept of the hybrid system using a series converter allowing control the dynamics of the fuel cell power while the supercapacitor supplies power to the three-level converter then to load. Thanks to the three-level converter, the output voltage will be controlled being constant.

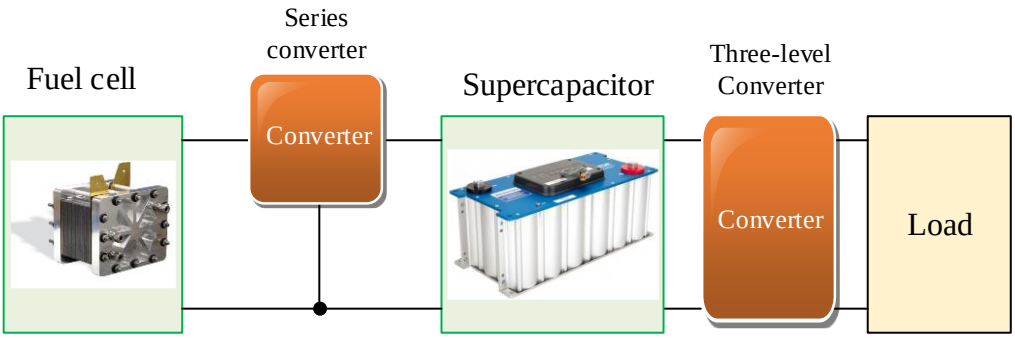

Figure 4-91 General diagram of single fuel cell stack system.

The generalization of this architecture can be realized for N fuel cell stack system. There are N-series converter connects with N-input modular three-level converter. The architecture for N = 3 is shown in Figure 4-92.

The voltage of supercapacitor is the input voltage of the modular three-level boost converter, which for the k^{th} stack is:

$$V_{SC_k} = V_{i_k} \tag{4-202}$$

The differential equation of the modular three-level converter can be rewritten in the following form:

$$L_k \frac{di_{Lk}}{dt} = V_{SC_k} - r_{Lk} \cdot i_{Lk} - (1 - d_{k1}) \cdot V_{Ck} - (1 - d_{k2}) \cdot V_{C(k+1)} \tag{4-203}$$

where k=1, 2, 3…, N.

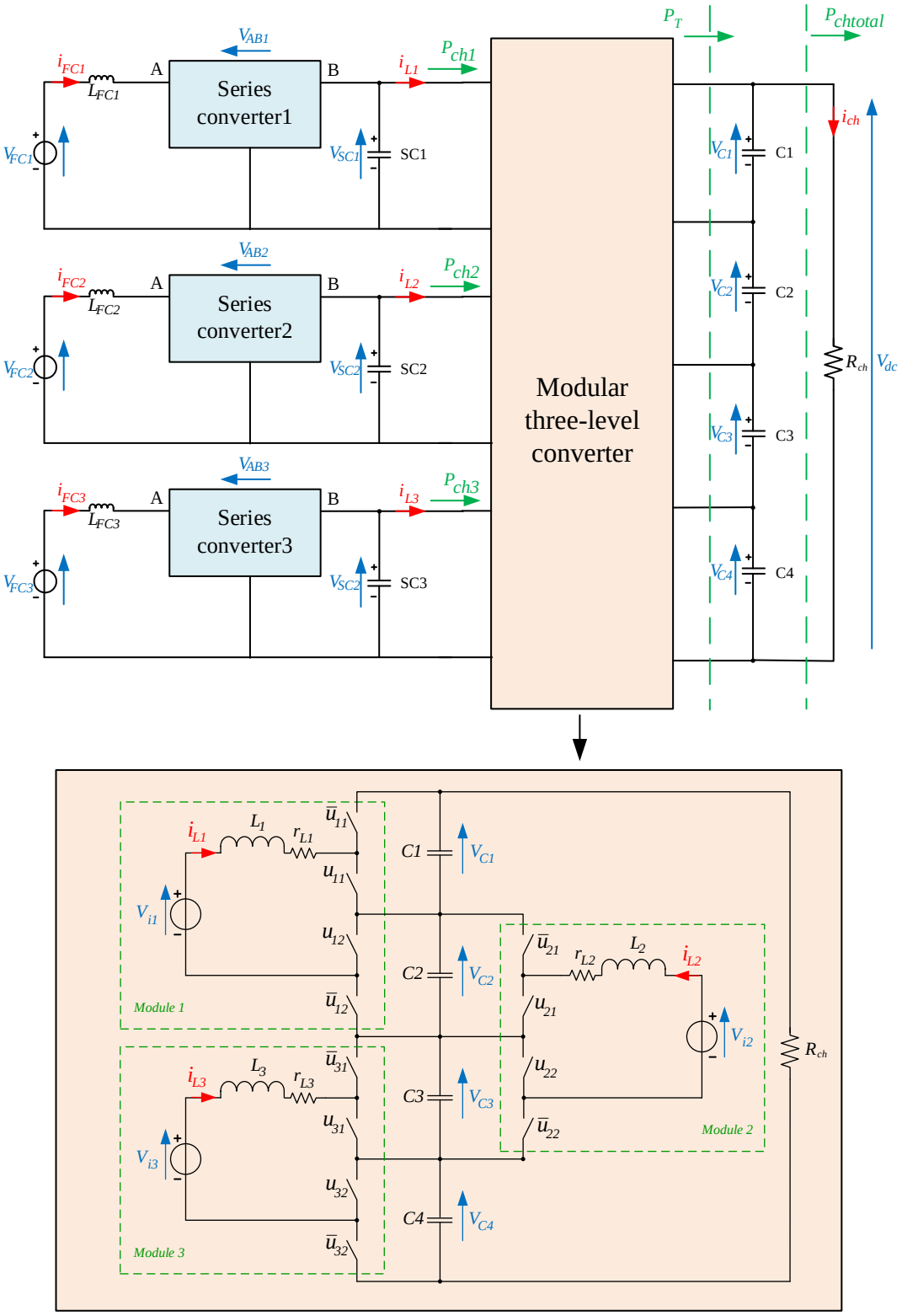

Figure 4-92 Proposed architecture.

4.4. Control strategy description

The main objective of this thesis is to prevent the system failures from changing the power of each stack. While the output voltage of the system must be guaranteed to be constant, independently of load power. The control strategy for the proposed topology is based on cascaded control where the outer-control loop is the output voltage, and the inner-control loop is the fuel cell current.

In the first part, a control strategy to regulate the output voltage is introduced, based on the control law detailed in Chapter 3. The fuel cell current is controlled based on the indirect-sliding mode control as detailed in Chapter 2.

4.4.1. Output voltage control

To control the output voltage V_{out}, we propose to control the energy y stored in the equivalent output capacitors C_{eq}:

$$y = \frac{1}{2} C_{eq} V_{dc}^2 \tag{4-204}$$

where the equivalent output capacitors C_{eq} can be found for the N stack system if the voltages across each capacitor are the same as:

$$C_{eq} = \frac{1}{N} \sum_{k=1}^{N} C_k \tag{4-205}$$

The output voltage must track its reference V_{outref} therefore, the energy reference y_{ref} is defined as:

$$y_{ref} = \frac{1}{2} C_{eq} V_{dcref}^2 \tag{4-206}$$

The error can be calculated from the difference value between energy (y) and reference energy (y_{ref}). The control law for outer loop can be defined by:

$$\dot{\varepsilon} + K_1 \varepsilon + K_2 \int \varepsilon(\tau) d\tau = 0 \tag{4-207}$$

where $\varepsilon = y_{ref} - y$

The parameter K_1 and K_2 can be chosen to make the error dynamics as the second-order system's response, such as $K_1 = 2\xi\omega_n$ and $K_2 = \omega_n^2$ with a desired damping factor ξ and a chosen angular frequency ω_n.

Considering the variation over time of the energy $\dot{y}$ stored in the equivalent output capacitors, which is

$$\dot{y} = P_T - Pch_{total} \tag{4-208}$$

Using (4-7), $\dot{y}$ is given by:

$$\dot{y} = \dot{y}_{ref} + K_1\left(y_{ref} - y\right) + K_2 \int \varepsilon(\tau) d\tau = \nu \tag{4-209}$$

From equation (4-206), the reference power required to maintain the output voltage constant and equal to its reference is:

$$P_T = \nu + Pch_{total} \tag{4-210}$$

For lossless system, this power P_T will be used to generate the power reference signals for both the modular three-level boost converter and the series converter.

From supervisor proposed in [115], it is possible to generate an adaption signal for the power required for each stack according to operating conditions of each stack. For example, one of the FC stacks must decrease or increase its power because of its own problem.

Supposing that the algorithm of the supervisor gives information about output power for each fuel cell stack associated with Alpha (α). It can be ranged from zero to a positive value. The Alpha can be defined following the equation (4-187).

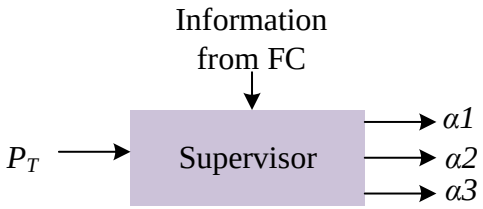

Figure 4-93 Block diagram of management power of system.

For lossless system, the input power of the k[th] module of the MTL converter is defined by:

$$P_{Chk} = \frac{P_T}{N} \alpha_k \tag{4-211}$$

The current reference for the k[th] converter I_{FCref_k} can be found using the obtained power and the supercapacitor voltage V_{SC_k}:

$$I_{ref_k} = \frac{P_{ch_k}}{V_{SC_k}} \tag{4-212}$$

The modified control block diagram of the system for the k[th] input is presented in Figure 4-94.

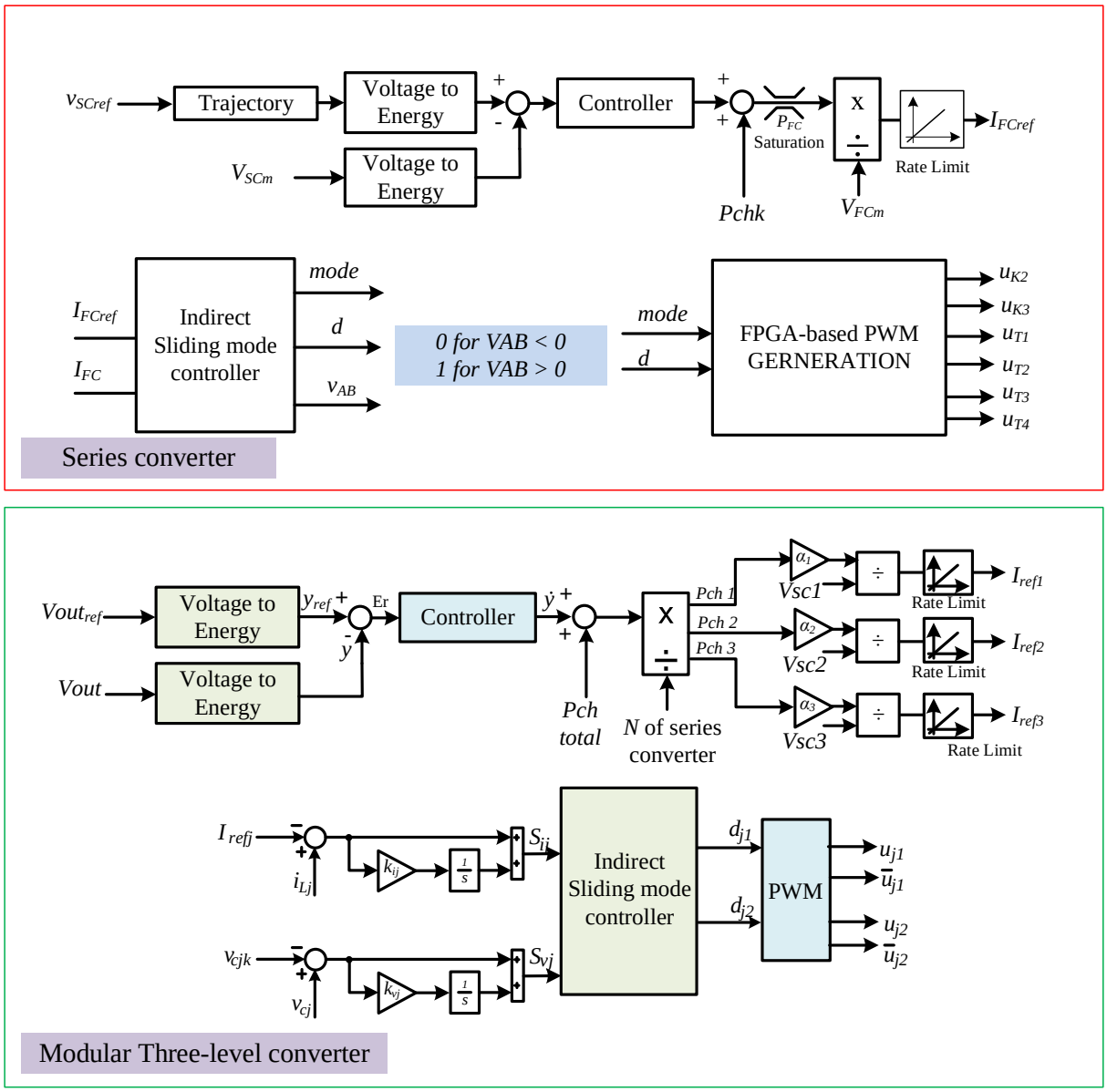

Figure 4-94 Block diagram to control the system.

4.5. Simulation results

To validate the proposed topology and the proposed control method, several simulations have been done in several scenarios using three fuel cell stacks. In this section, three scenarios are presented: normal operation, drying and flooding operations. To simulate the fuel cell stacks, the polarization curves presented above are used. The load profile (Figure 4-95) comprises three operation modes of hybrid system [122], which are normal mode, overload mode, and recovery mode. Normal mode is when the load power is lower than the maximum power of FC, overload mode is when the load power is higher than the maximum FC power and recovery mode when the load power is negative.

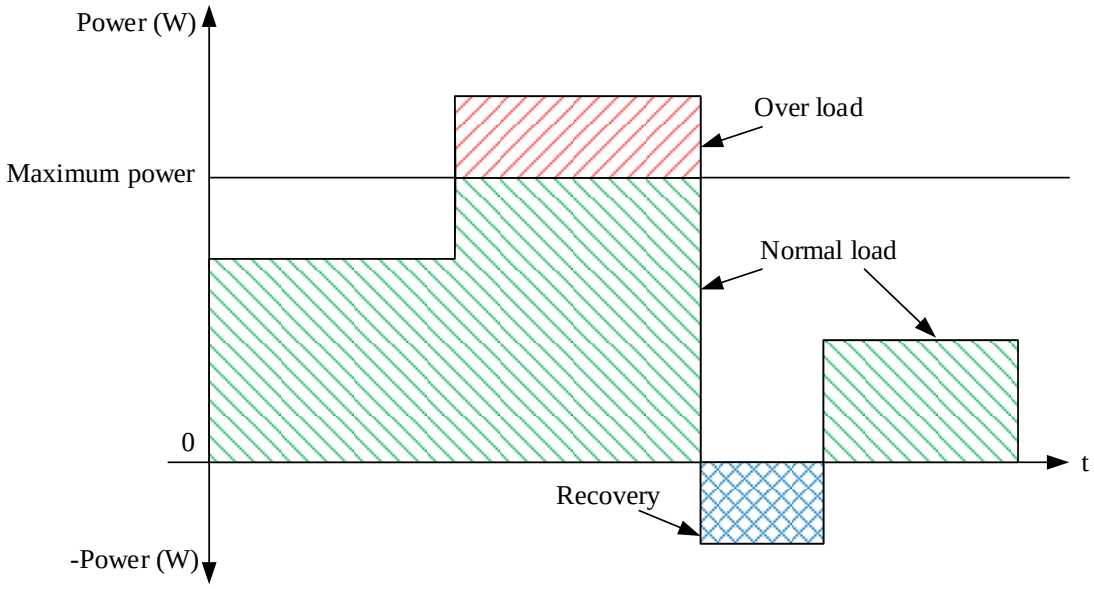

Figure 4-95 Load profile for normal, overload, and recovery modes.

4.5.1. Normal conditions

In this case, the three fuel cell stacks are considered in normal condition. The signal α1= α2= α3 = 1 (Figure 4-96), all power references are the same. The results are given in Figure 4-97 to Figure 4-103.

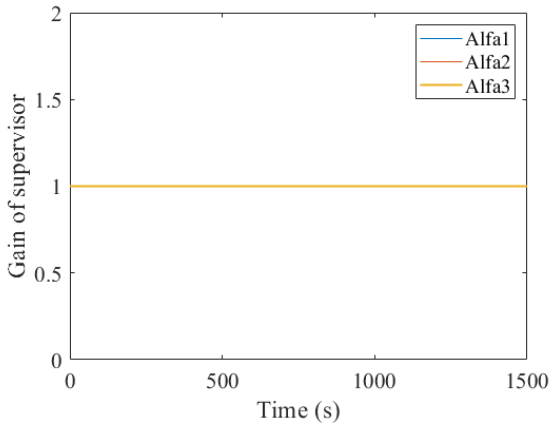

Figure 4-96 Supervisor output α for each input of the modular three-level converter.

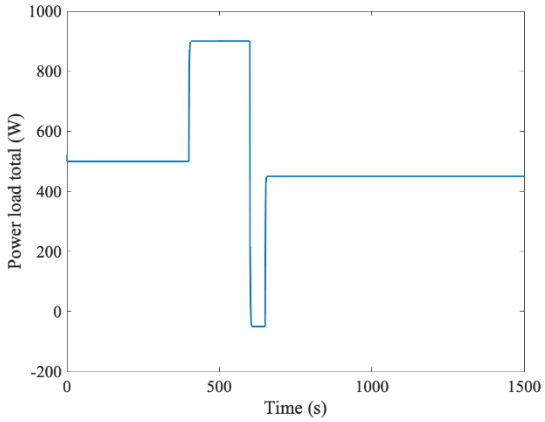

Figure 4-97 Total load power profile for the system.

The load profile is presented in Figure 4-97. At $t = 0$, the load absorbs 500 W. At $t = 400\ s$, the load power steps up from 500 W to 900 W. After that, the load power steps down to -50 W and then the load power is back to 450 W at $t = 1000\ s$.

Figure 4-98 (left) illustrates that each SC provides the same power to the modular three-level boost converter. Figure 4-98 (right) shows the power of fuel cell stacks is the same for each stack.

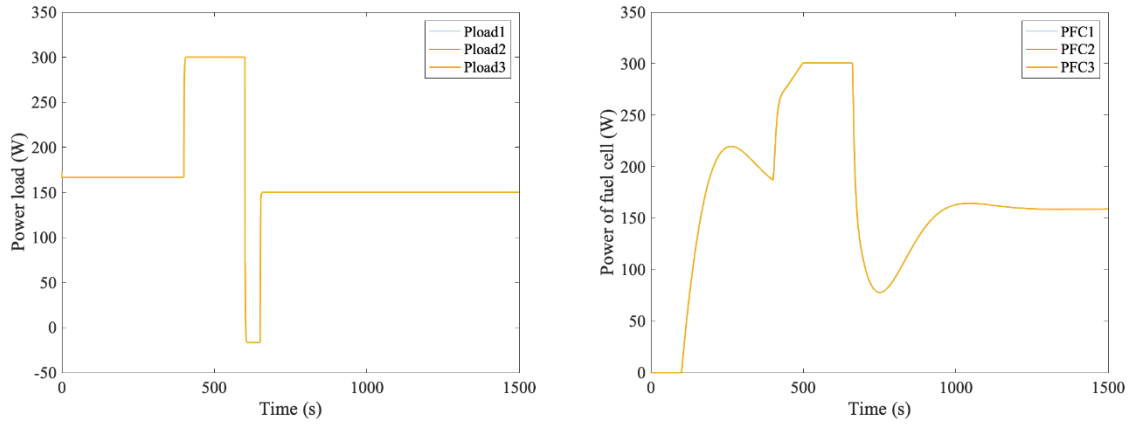

Figure 4-98 (Left): Load power. (Right): Delivered power of each FC stack.

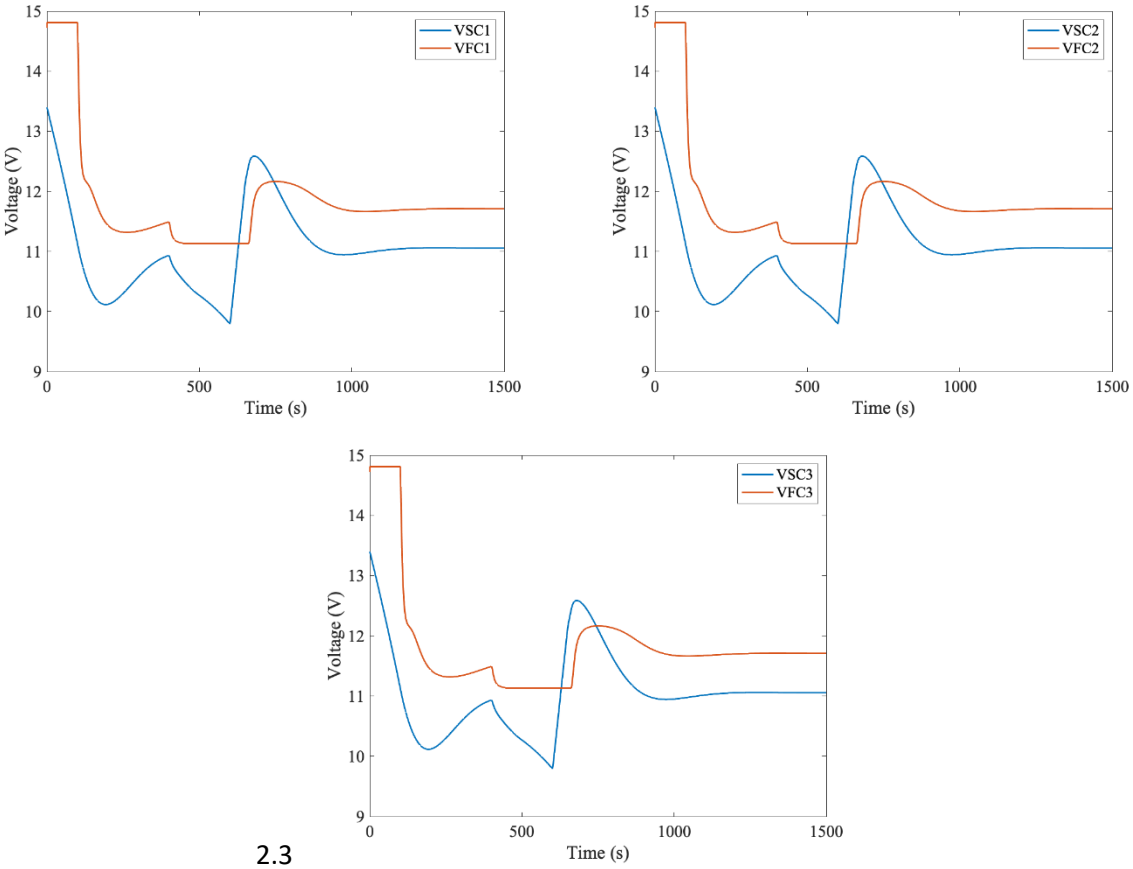

2.3

Figure 4-99 Voltage of FC and SC of each series converter.

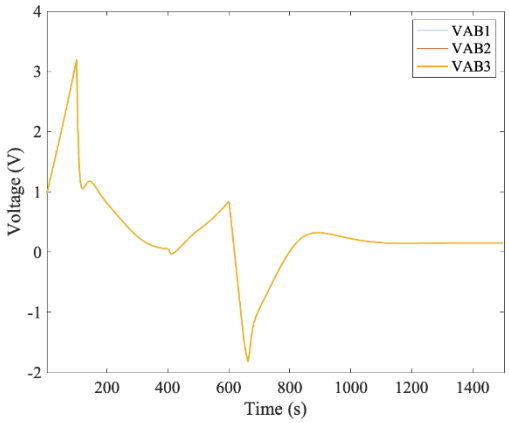

Figure 4-100 VAB of each series converter.

The voltage of FC stacks and SCs are shown in Figure 4-99. At normal load, the FC supply the energy to the load. At $t = 400\ s$, the load steps up to overload mode. The maximum FC power for all stacks is limited at 300 W, corresponding to the fuel cell voltage of 12.5 volts while the SCs provide the overload power. When the load step down to normal mode, the FCs provide energy to the load and the SCs are recharged. At $t = 900\ s$, the load power is negative. It is a recovery mode and lead to increasing of the SC voltage.

The voltage V_{AB} for each module of series converter is drawn in Figure 4-100. It will change more or less depending on the behavior of V_{FC} and $V_{SC.}$ For normal and overload modes, V_{AB} is positive and for overload mode, V_{AB} is negative. V_{AB} leads to zero in the steady state.

The duty cycles of the modular three-level converter for this case shows in Figure 4-101. As can be seen, since the modular three-level converter operates in a commandable zone, the duty cycles are between 0 to 1. The input currents for the modular three-level converter are given in Figure 4-102. Thanks to the control method, the input currents, which are the inductor currents track well their references for both positive and negative values.

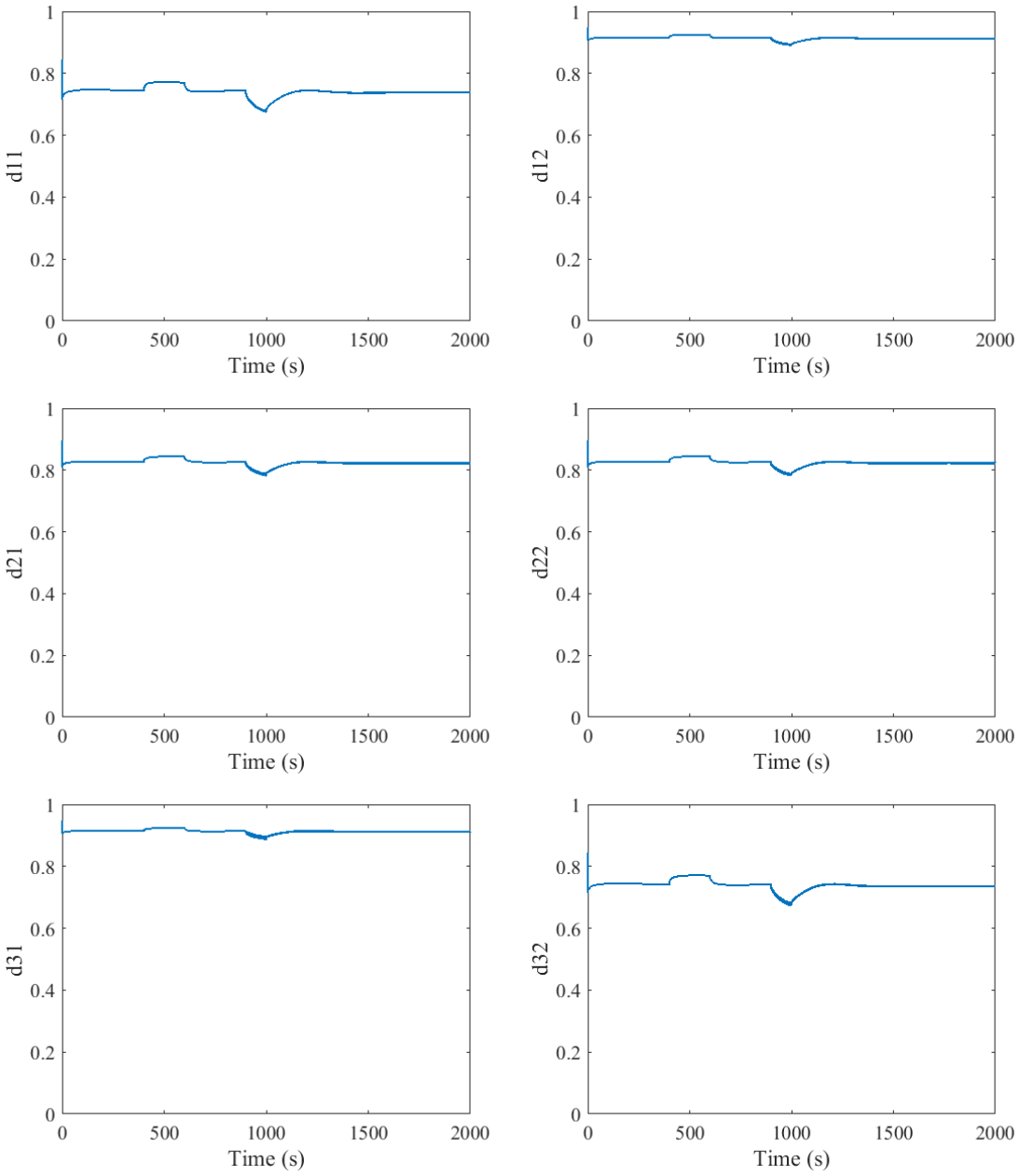

Figure 4-101 Duty cycle.

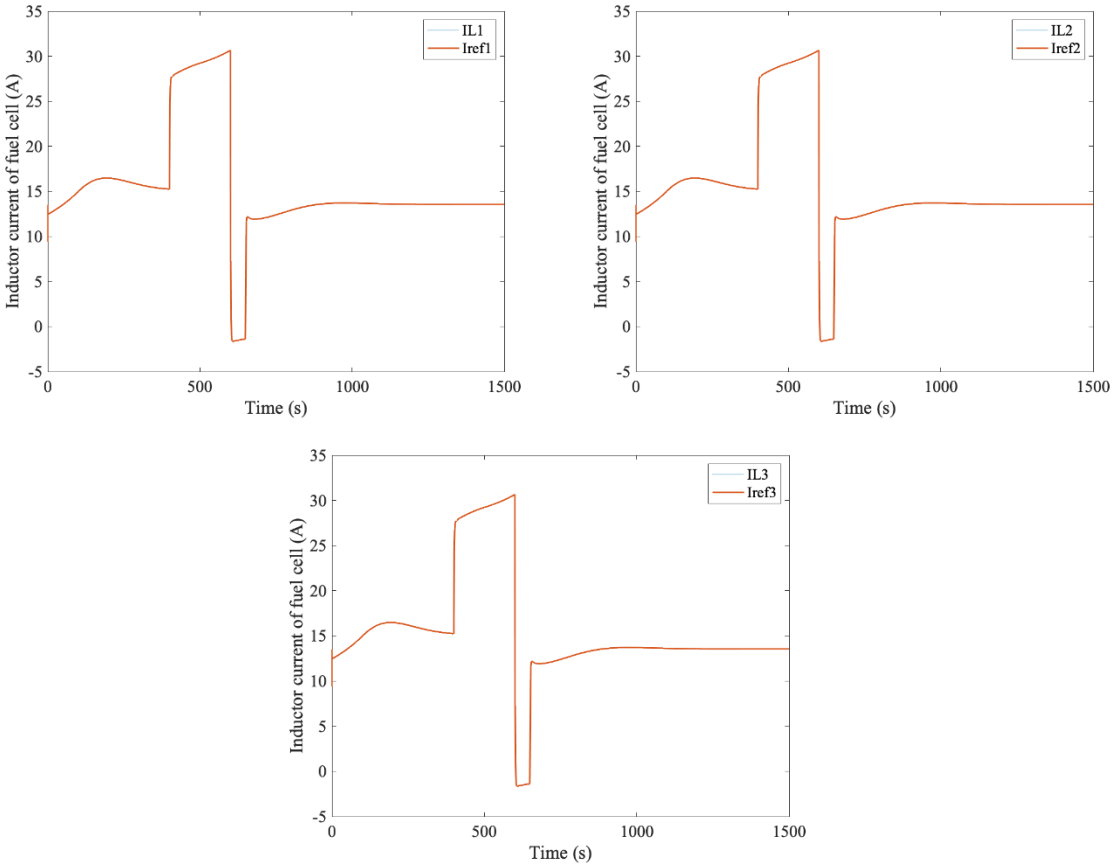

Figure 4-102 Inductor currents and their references for the modular three-level boost converter.

The output capacitor voltages are shown in Figure 4-103 (left). The voltage for each capacitor is equal. The output voltage for system is illustrated in Figure 4-103 (right). Thanks to the energy control law, the output voltage track well with the reference.

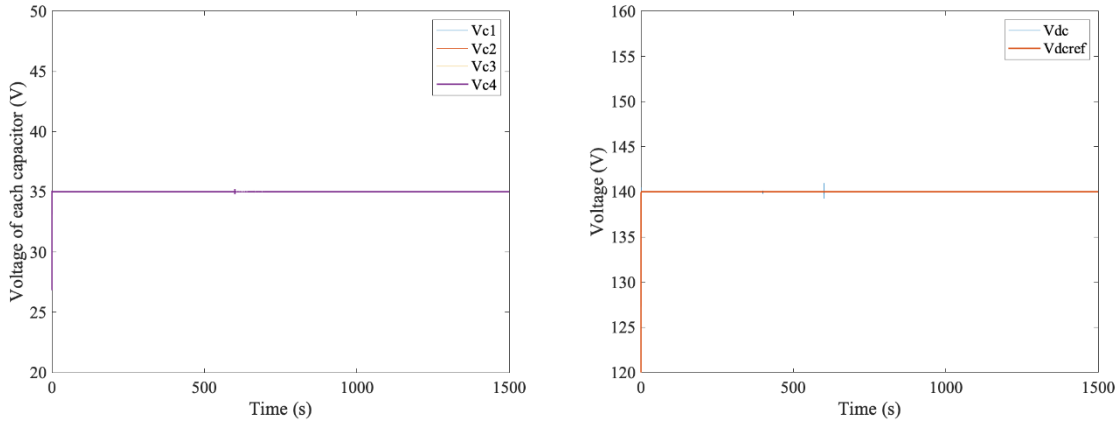

Figure 4-103 (Left): Each output capacitor voltages are equal for the modular three-level boost converter. (Right): Output voltage V_{dc} and its reference.

4.5.2. Operation points in Flooding (limiting current density) condition

Supposing that the first stack is in flooding condition while other stacks are in normal conditon. In this case, the V-I curve of the first FC stack is lower than that of other stacks as shown in Figure 4-89. The power or current drawn from the first stack must be reduced [109]. The supervisor serves to allocate the lack of power α to other FC stack to supply load (Figure 4-104).

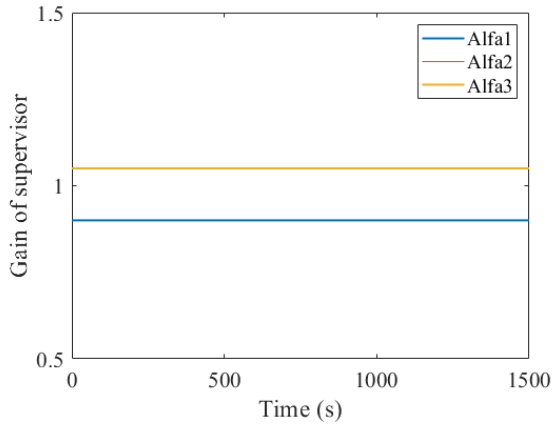

Figure 4-104 Supervisor output α for each input of the modular three-level converter.

The simulation results for these scenarios are given in Figure 4-105 to Figure 4-109, for the same load power profile given in in Figure 4-97. While the first stack has to reduce its power, with constant total power, the first stack delivers less power than other stacks as shown Figure 4-105. In this test, the second and third stacks deliver the same powers.

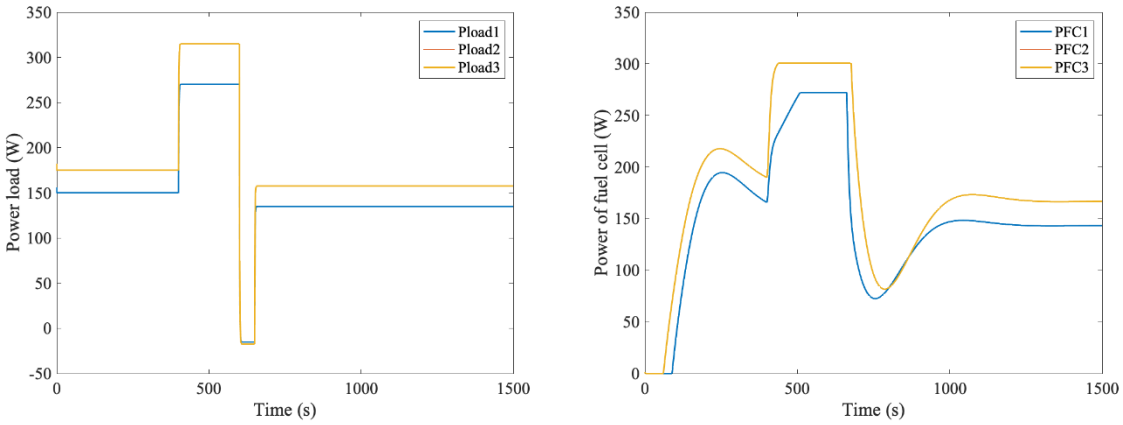

Figure 4-105 (Left): the power load of each series converter (Right): the power of fuel cell for each series converter.

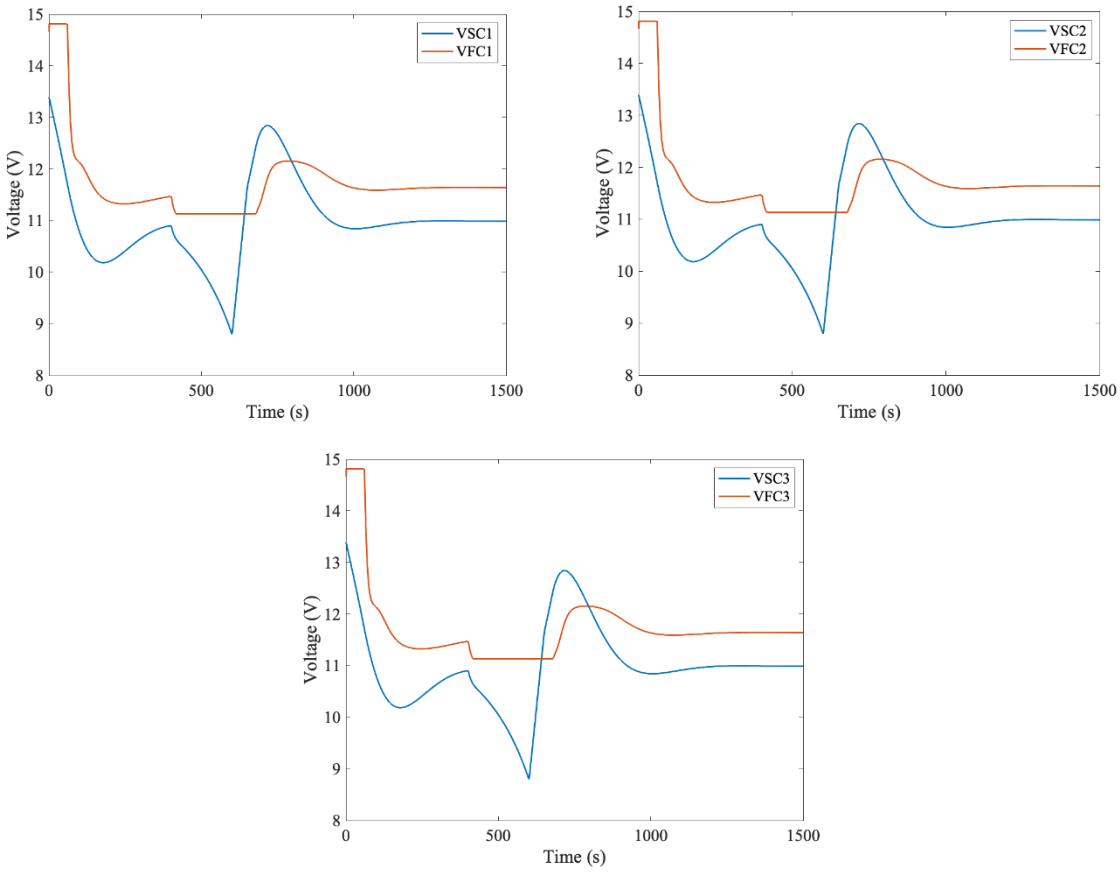

Figure 4-106 Voltage of FC and SC for each series converter.

The voltage of FC and SC of the series converter are shown in Figure 4-106. The voltages for the first converter are slightly different from the other one. The first stack has lower voltage, delivery less power than those.

In the same manner, the voltage V_{AB1} is different from others because the modification of the V-I curve of the first FC stack. Nonetheless, all the voltages V_{AB} lead to zero in steady state.

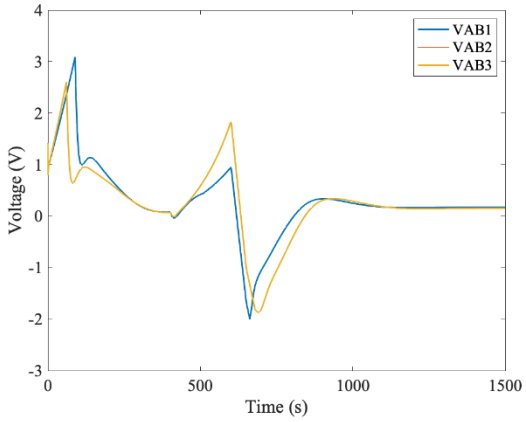

Figure 4-107 Voltage V_{AB} of each series converter.

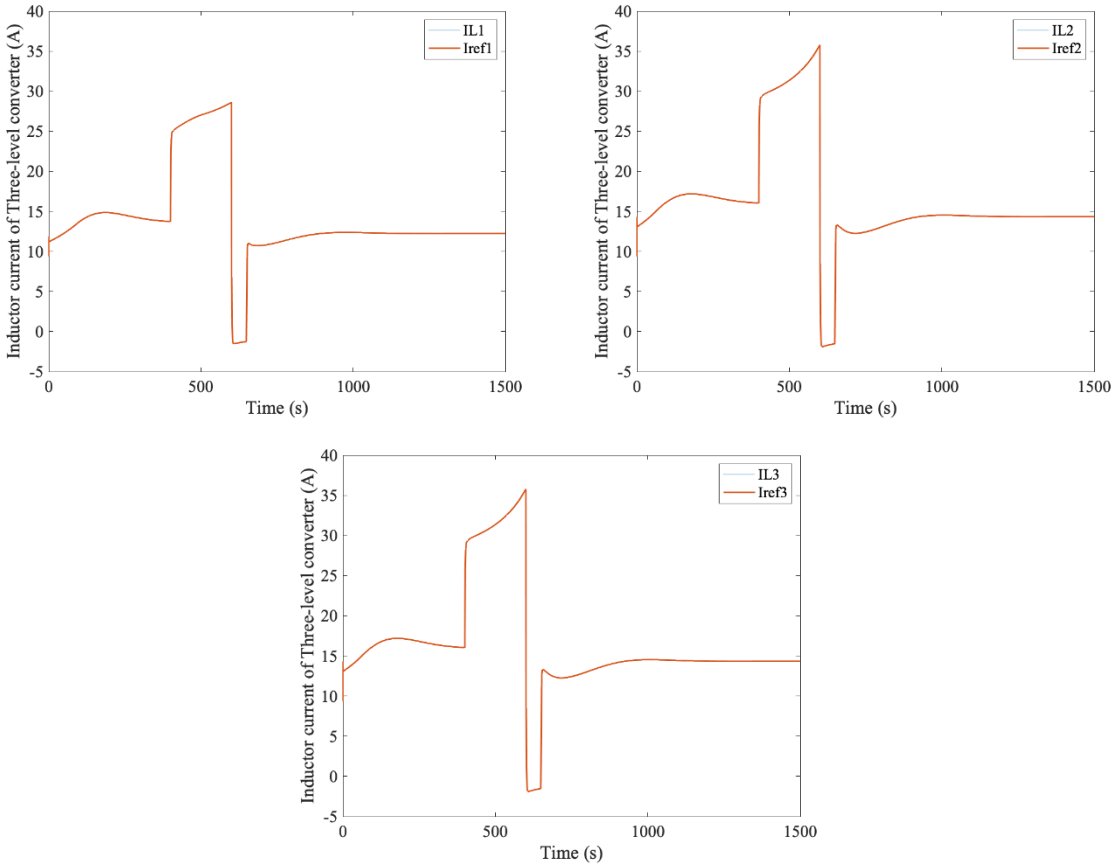

Figure 4-108 Inductor currents and their references for the modular three-level converter.

The inductor currents are depicted in Figure 4-108. The current of the first stack is lower than the currents of the other stack corresponding to the lower power of the first stack.

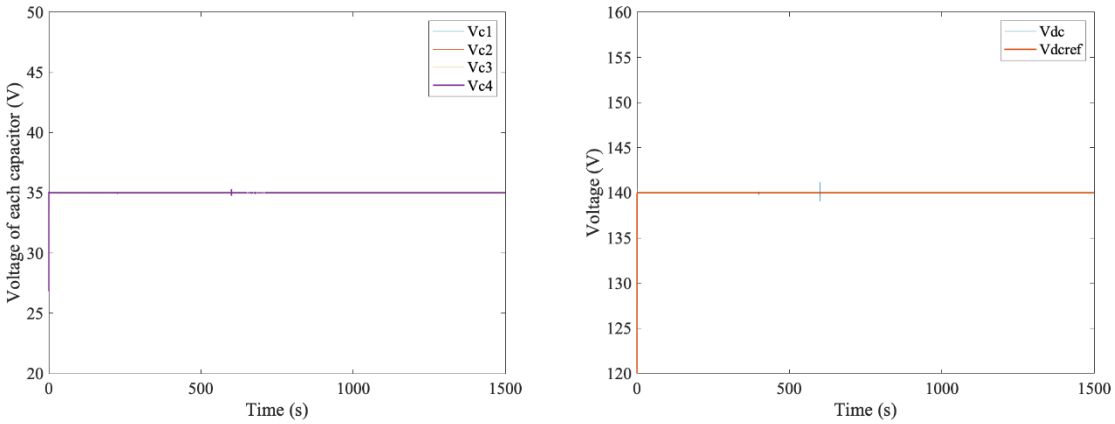

Figure 4-109 (left): Capacitor voltages. (Right): Output voltage.

The first FC stack has different conditions from the rest, but the output capacitor voltages still balance and are equal to 35 V as in Figure 4-109 (Left). In addition, Figure 4-109 (Right) shows that the output voltage respects its reference.

4.5.3. Operation points: Drying case

In this case, we consider that the first FC stack is in the drying condition while the other stacks are in the normal operation condition. To obtain more water in the first stack, its power or current must be increased as much as possible [115]. The supervisor gives the output α as shown in Figure 4-110.

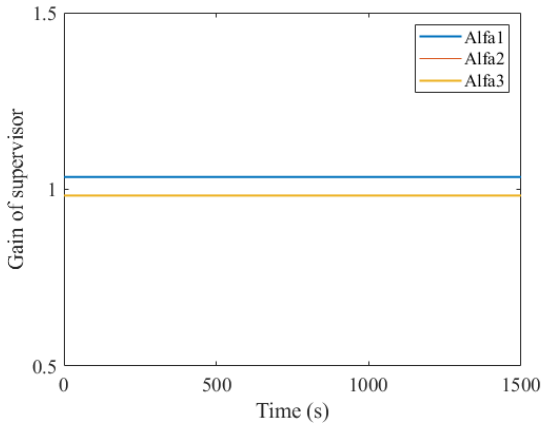

Figure 4-110 Supervisor output α for each input of the modular three-level converter.

For the given load power profile, the FC powers are presented in Figure 4-111 (Left) where the first stack power provides more power than that provided by other stacks. The input powers of the modular three-level converter are shown in Figure 4-111 (Right). The P_{load1} is higher than those of the other modules. In Figure 4-112, the V_{SC1} is less than that of the other modules. The current i_{FC1} limited between t=400 s to t=600 s to meet the maximum value of the FC current for the first stack.

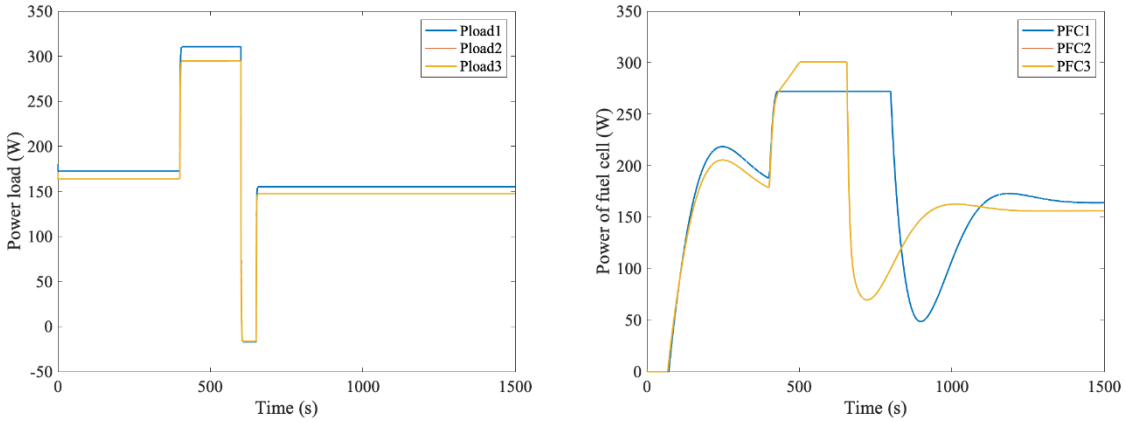

Figure 4-111 (Left): Power load supply from each series converter. (Right): FC power for each stack.

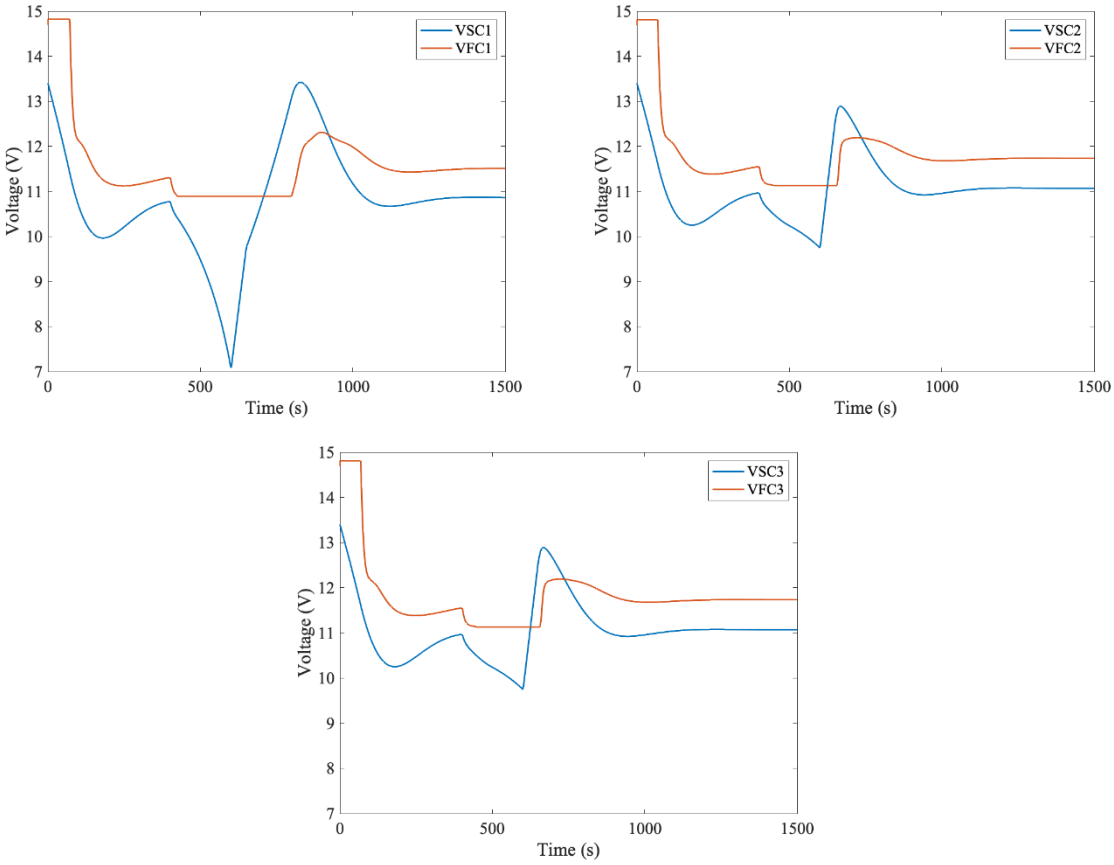

Figure 4-112 Voltage of FC and SC of each series converter.

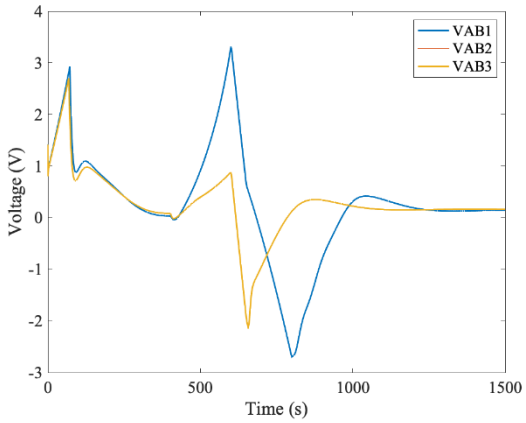

Figure 4-113 V_{AB} voltage of each series converter.

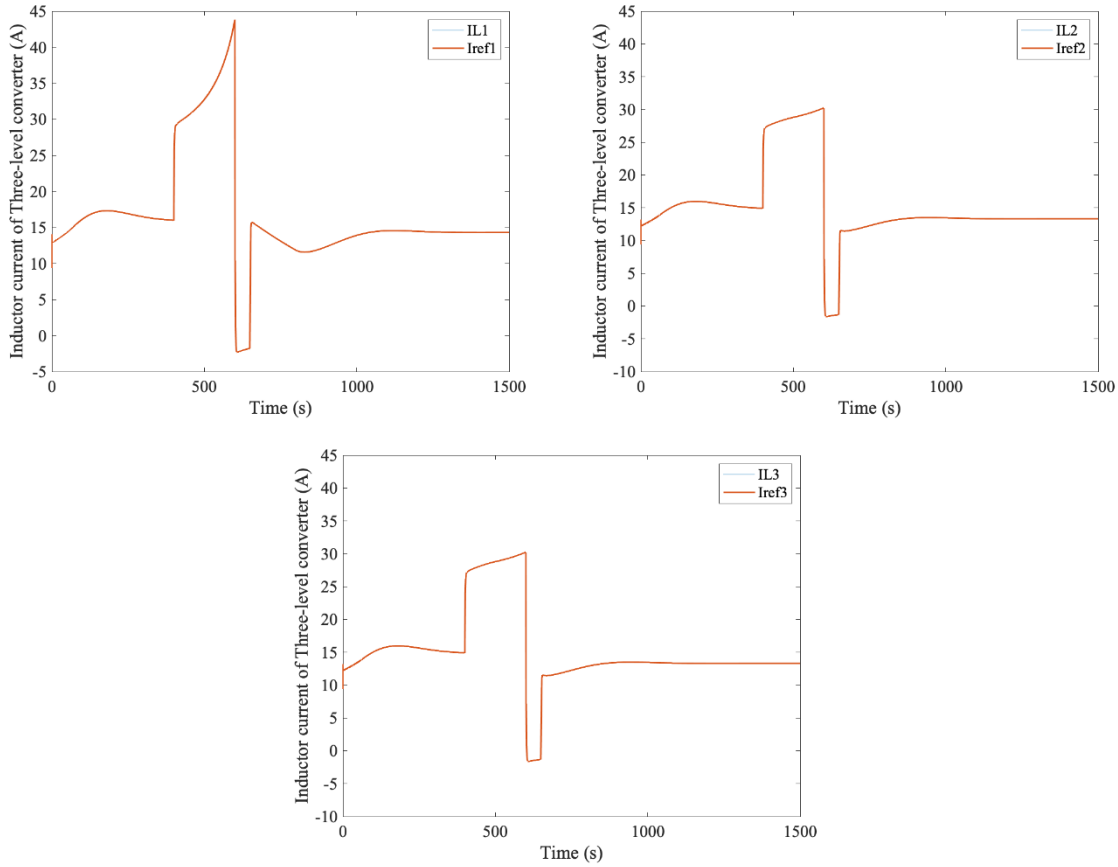

Figure 4-114 Inductor current and their references of the modular three-level converter.

The voltage V_{AB} for each series converter are shown in Figure 4-113. The V_{AB1} for the first stack is difference according to the voltage difference between V_{FC1} and V_{SC1}. The inductor currents of modular three-level converter are followed well their references as shown in Figure 4-114. Figure 4-115 (Left) shows the output voltage of each capacitor. They are equal to 35 V. The output voltage follows its reference at 140 V.

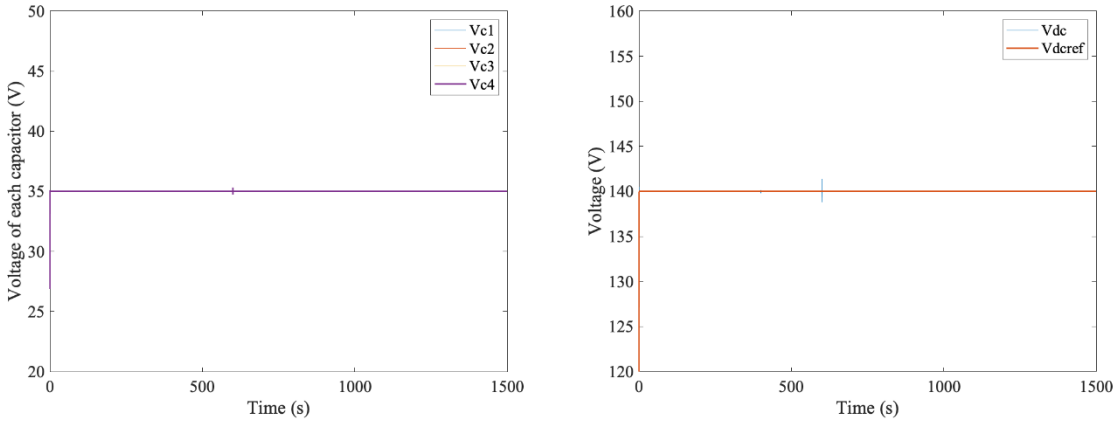

Figure 4-115 (Left): The output capacitors for three-level converter. (Right): The output voltage and its reference.

4.6. Conclusion

The management system for the proposed architecture, based on series converter and the modular three-level converter, was presented in this chapter. The FC stacks' operation conditions (normal, flooding, and drying) are considered.

The FC stacks power can be managed independently concerning their operation conditions following information given by the supervisor. They may lead to solving the problem of the drying and flooding problem of FCs. The simulation results show the behavior of the system and validate the proposed management system.

General conclusion

The thesis focuses on the development of hybrid system architecture associating fuel cell and supercapacitor. The literature review is detailed in the first chapter. The principle of the fuel cell and supercapacitor behavior was presented. The fuel cell in this thesis focuses on Proton Exchange Membrane Fuel Cell (PEMFC) type. The FC voltage-current characteristic is presented to observe the performance of FC. Moreover, their degradations of PEMFC were illustrated. The model of supercapacitor was represented

The novel hybridization architecture is based on the series converter placed in series between the FC and SC. This topology is inspired from partial power converter architectures (PPC) in order to increase the efficiency of the system. The concept of PPC is that a large amount of power flows directly from the input to the output. The proposed architecture is described in the second chapter. The operation of two modes which are negative and positive mode according to the voltage of the FC and SC was presented. For simulation and experimentation, the FC polarization curve presented in Chapter 1 was used. The current control based on indirect-sliding mode control was designed and implemented. The constraints of FC, which are the maximum FC power and transition rate of FC current, were considered. In order to maximize the system efficiency, thanks to the control law, the supercapacitor voltage reference is defined to ensure that the output voltage of the series converter V_{AB} leads to zero in steady state. The design of the control signals and the modelisation of the proposed converter was detailed and validated by experimental results.

In order to increase the FC voltage, the output of the series converter from the chapter 2 was connected with multi-input MTL converter presented in chapter 3. This novel configuration based on a three-level DC-DC boost converter was investigated. Sharing one capacitors of the N-module MTL converter allows the balancing voltage at the output capacitor voltages. The controller based on the indirect-sliding mode control was applied to control both input current for each input and capacitor voltage balancing to ensure that the converter can be operated under a suitable zone. The duty cycle and controllable zone for the MTL converter were presented. The calculation of capacitor sizing was compared with the converter based on the classical boost converter to define the stored energy in the output capacitor. It leads to reduction of the capacitance for MTL converter. The studied topology was validated using simulation and experimental results.

Finally, the global management system was proposed in chapter 4. The FC characteristic curve under normal condition and drying as well as flooding conditions were presented. The supervisor, which is beyond to this thesis was chosen to provide the value of the reference power for the MTL converter and series converter concerning FC operating condition. The simulation results were obtained supposing that the first FC stack is in the drying or flooding condition. These results showed the ability of system for the given load profile to adapt the FC power following the reference from the supervisor.

Following perspective are conceivable:

- In chapter 2, the new power electronic architecture for hybridization system was validated. To reduce oscillating current and voltage waveforms of V_{AB}. The device for the circuit should be chosen in an optimized manner. Moreover, the mathematical model of PEMFC with parameters for flooding and drying mechanisms allowing to simulate PEMFC in real-time should be included.
- In chapter 3, there is a limitation of commandable zone which have to study and extend the zone for supporting large number of modules. Moreover, working on modifying the topology allows to have identical duty cycles to ensure thermal distribution for all devices should be investigated.
- In chapter 4, simulation results of the whole architecture with global energy management were presented. There are three module of series converter connected to MTL converter. Increasing the power of whole system can be done by adding the number of module of series converter and the number of inputs of MTL converter. The results are shown for the worst conditions of the first FC stack. Therefore, simulation with real-time PEMFC and experiment for the proposed architecture should be validated.

Appendix

Version française de l’introduction

L'énergie fait partie des besoins fondamentaux des personnes. C'est aussi le principal facteur de développement du secteur industriel. De plus, l'augmentation rapide de la population mondiale et la croissance économique contribuent à l'augmentation de la consommation énergétique mondiale [1]. Dans le même temps, les sources d'énergie conventionnelles, présentes en quantité limitée et utilisées depuis longtemps, tendent à décliner régulièrement dans le monde. Ces sources dites non renouvelables, par exemple les combustibles fossiles tels que le charbon, le pétrole et le gaz naturel, formées au cours de centaines de millions d'années à partir de matières organiques en décomposition, ont aujourd’hui de forts impacts sur notre environnement, y compris l'air, la pollution de l'eau, les dommages à la santé publique, la faune et sont responsables du réchauffement climatique. En conséquence, il est proposé d'utiliser l'énergie renouvelable, qui est une énergie propre [2]. Les avantages des énergies renouvelables ont conduit de nombreux pays à y investir. Des chercheurs du monde entier développent des technologies pour des systèmes d'énergie renouvelable plus efficaces afin de réduire les coûts, d'économiser l'énergie, de réduire la pollution et de résoudre le problème environnemental mondial. Bien que les énergies renouvelables soient une solution prometteuse au réchauffement climatique, il existe encore de nombreuses limites. Par exemple, l'énergie solaire et éolienne sont intermittentes ce qui fait que l'équilibre entre l'offre et la demande n'est pas toujours assuré.

Dans ce contexte, l'utilisation de l'hydrogène comme vecteur énergétique apparaît comme une bonne solution. L'hydrogène vert serait produit par électrolyse en utilisant l'excédent d'énergie provenant de sources renouvelables, stocké ou transporté, et serait finalement utilisé dans les industries chimiques ou pour produire de l'énergie électrique. Cela pourrait résoudre simultanément le problème des émissions de CO2 liées à la fois au reformage du gaz naturel pour la production d'hydrogène et aux applications de mobilité, principalement les véhicules lourds. En effet, alors que le développement des petits véhicules électriques a pris son envol, la propulsion électrique pose toujours des problèmes aux camions et aux trains en raison de la quantité d'énergie qu'il faut embarquer. En attendant de nouveaux progrès dans la capacité énergétique des batteries, la combinaison de l'hydrogène et de la pile à combustible (FC) pourrait être une solution.

Parmi les différents types de piles à combustible, la pile à combustible à membrane échangeuse de protons (PEMFC) est bien adaptée aux applications mobiles

Cependant, le déploiement à grande échelle des PEMFC pour des applications commerciales présente encore de nombreux défis. Par exemple, le défaut d’approvisionnement en gaz de la PEMFC est un problème bien connu dans une application où la charge a un comportement fortement transitoire comme dans les applications de mobilité. Ce problème est dû à la réponse lente de l’alimentation en gaz de la pile. Or, le manque de gaz réactionnels entraîne non seulement une chute de la tension de la pile mais peut aussi conduire à des dégradations irréversibles de ses composants. Pour atténuer ce problème, la gestion électrique des piles à combustible est essentielle.

Les piles à combustibles sont généralement incorporées à d'autres stockages d'énergie électrique tels que les batteries et les supercondensateurs pour former une source d'énergie appelée "système hybride". Comme le supercondensateur fournit de l'énergie à la charge plus rapidement que la pile et les batteries, la collaboration entre pile à combustible et supercondensateur permet d'éviter le stress élevé de la pile lorsque le système est exposé à une charge transitoire rapide. Ainsi, les systèmes hybrides sont largement utilisés dans les véhicules électriques.

Source d'énergie basée sur les piles à combustible

La pile à combustible a été découverte il y a plus de 100 ans par Sir William Robert Grove [3], et une pile à combustible à haute densité de puissance a été développée pour la première fois par Sir Francis Bacon en 1933. Cependant, les développements technologiques à cette époque se concentrent principalement sur le moteur à combustion, et par conséquent la pile à combustible ne s'est développée que très lentement. Mais depuis quelques années, en raison de la tendance actuelle à la transition énergétique, les chercheurs se sont à nouveau tournés vers le développement des piles à combustible notamment à hydrogène.

Une pile à combustible est un dispositif électrochimique permettant de convertir l'énergie chimique de l'hydrogène en énergie électrique [4]-[5]. Elles sont constituées de deux électrodes appelées anode et cathode séparées par un électrolyte. Les deux réactions électrochimiques, appelées oxydation et réduction, génèrent de l'électricité, de l'eau et de la chaleur résiduelle.

Il existe de nombreux types de piles à combustible et chacun présente des avantages et des inconvénients. Chaque type est caractérisé par son comportement et ses matériaux typiques. La classification est également donnée par la température de fonctionnement et les ions qui traversent l'électrolyte. Les différents types de pile à combustible sont : la pile à membrane échangeuse de protons (PEMFC), la pile à combustible à acide phosphorique (PAFC), la pile à combustible à oxyde solide (SOFC), la pile à combustible alcaline (AFC), la pile à combustible à méthanol direct (DMFC), et Carbonate fondu (MCFC).

Les caractéristiques récapitulatives des différents types de piles à combustible sont présentées dans le tableau 1 ci-dessous. Il donne l'électrolyte, la plage de température de fonctionnement le rendement moyen de chaque type de pile à combustible. Certaines piles utilisent des carburants à faible coût tels que le gaz naturel, le méthanol et l'essence (PAFC, MOFC et SOFC). Cependant, elles ont des températures de fonctionnement très élevées et émettent également du CO2 qui n'est pas respectueux de l'environnement. La pile de type AFC (qui a été utilisé dans plusieurs engins spatiaux) a une faible efficacité de fonctionnement et nécessite un grand volume pour son électrolyte. Le type DMFC produit de l'électricité par réaction entre le méthanol et l'oxygène. Le méthanol est facile à produire, à stocker et a une densité d'énergie élevée, mais la DMFC a tendance à avoir une efficacité inférieure à celle des PEMFC, un temps de démarrage plus long et produit du CO2. Compte tenu de l'efficacité de chaque catégorie, la technologie de PEMFC qui utilise l'hydrogène et l'oxygène comme carburants, est assez intéressante. Elle est particulièrement adaptée aux applications transport. Le principe de la PEMFC est décrit en détail dans la section suivante.

Fuel cell	Electrolyte	Operating temperature (°C)	Electrical efficiency (%)
Proton exchange membrane fuel cell (PEMFC)	Proton exchange membrane	~80	40-70
Direct methanol fuel cell (DMFC)	Proton exchange membrane	15-130	20-40
Alkaline fuel cell (AFC)	Potassium hydroxide solution	50-100	60
Phosphoric acid fuel cell (PAFC)	Phosphoric acid	150-200	40-50
Solid oxide fuel cell (SOFC)	Oxidant ion conducting ceramic	550-1000	60-65
Molten carbonate fuel cell (MCFC)	Molten mixture of alkali metal carbonates	650	55

Table 1 Principales technologies de pile à combustible.

Pile à combustible à membrane échangeuse de protons (PEMFC)

La structure de base de la pile à combustible PEMFC alimentée en hydrogène et en oxygène, est présentée sur la figure 1. L'entrée d'hydrogène est côté anode et celle de l'oxygène est côté cathode. Les gaz en excès, l'azote si la pile est alimentée avec de l'air et les produits de la réaction (eau et chaleur) quittent la cellule par les sorties. L'anode et la cathode sont séparées par un électrolyte. L'électrolyte est le facteur principal qui classe les piles à combustible et dans le cas de la PEMFC c'est une membrane polymère.

Les deux réactions électrochimiques sont :

$$2H_2 + O_2 \rightarrow 2H_2O \quad (1)$$

$$\frac{1}{2}O_2 + 2H^+ + 2e^- \rightarrow H_2O \quad (2)$$

A l'anode (1), l'hydrogène est oxydé en protons et en électrons. Les protons sont transportés vers la cathode à travers l'électrolyte. Les électrons circulent dans un circuit externe et alimentent la charge électrique. Les protons et les électrons arrivent à la cathode où ils sont combinés avec de l'oxygène pour produire de l'eau (2). Le fonctionnement de la pile est similaire à celui d'une batterie, mais elle peut fonctionner aussi longtemps que du carburant est fourni. Une seule cellule de pile à combustible a une tension égale à1 Volt, et donc pour produire une puissance élevée plusieurs cellules sont assemblées en série pour former un stack.

Une PEMFC présente les avantages d'un rendement et d'une densité de puissance élevés, d'une réponse rapide et d'une température de fonctionnement basse d'environ 80 °C [6]. L'efficacité de la conversion énergétique, c'est-à-dire la conversion de l'énergie de l'hydrogène en électricité est de l'ordre de 40 à 70 %, le complément à 100 % de l'énergie est de l'énergie thermique. Puisque les piles à combustible ne produisent pas de gaz à effet de serre, l'énergie électrique est considérée comme une énergie propre qui contribue à réduire le problème du réchauffement climatique. La pile type PEMFC est une source d'alimentation électrique pour les véhicules car elle présente l'avantage d'un démarrage rapide, d'un fonctionnement à basse température, de bonnes capacités de suivi de charge [7]-[8], un rendement élevé et une modularité aisée. Elle démarre à basse température et elle est petite et compacte. Elle est également considérée comme la source d'énergie utilisable dans les applications portables.

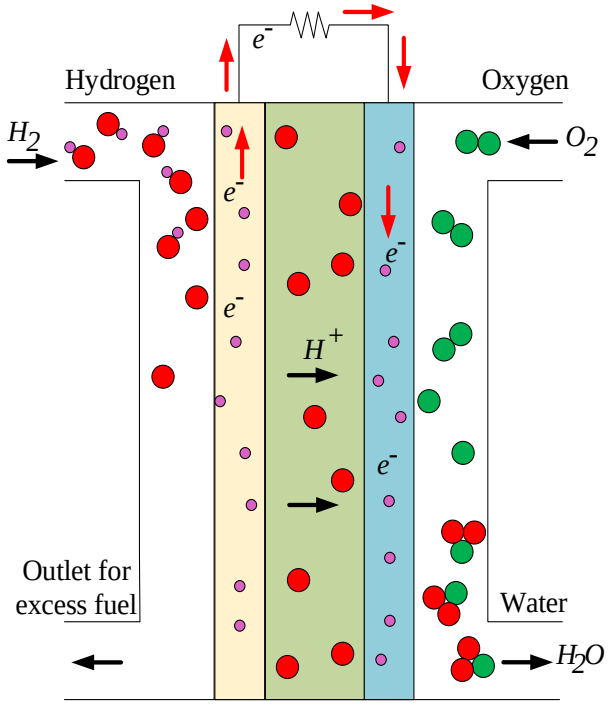

Figure 1. Principe de fonctionnement d'une pile à combustible de type PEM

Les principaux composants d'une PEMFC sont illustrés à la Figure 2. Les deux électrodes séparées l'une de l'autre par une membrane formant l'Assemblage Membrane-Electrode (AME). L'AME est pris en sandwich entre deux matériaux poreux appelés couche de diffusion de gaz (GDL) et deux plaques bipolaires utilisées pour l'approvisionnement en hydrogène et en oxygène et pour l'évacuation des produits de la réaction (eau et énergie thermique) et des gaz en excès ou non actifs (azote).

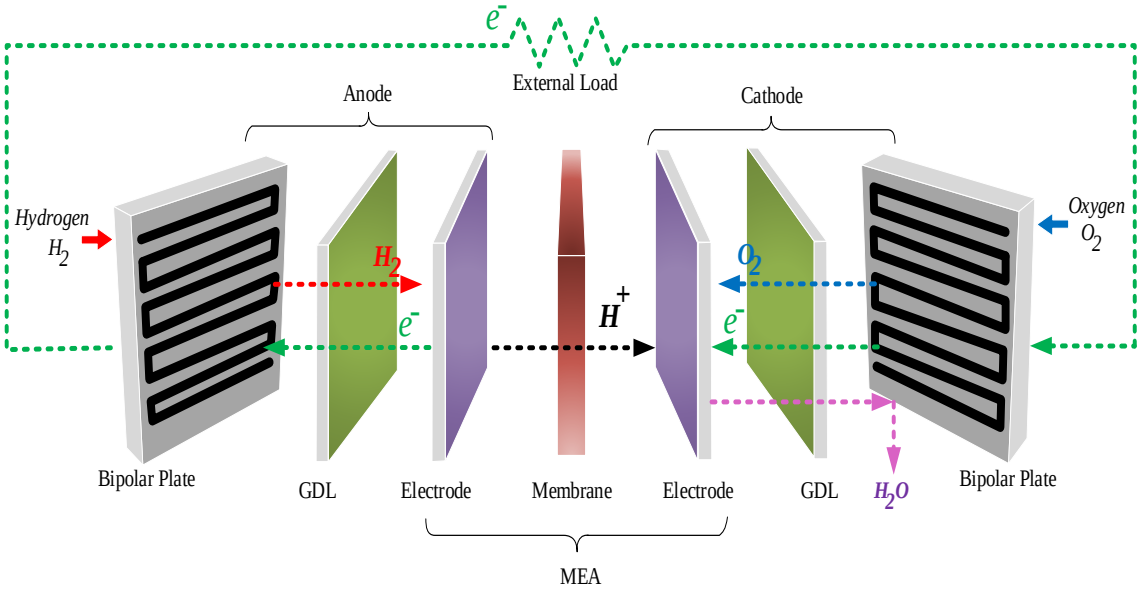

Figure 2 Composants d'une cellule de pile à combustible de type PEMFC.

Membrane

La fonction principale de la membrane est la conduction jusqu'à la cathode des protons produits à l'anode. Elle doit également empêcher la perméation des gaz réactifs tout en permettant le transport de l'eau. La conductivité ionique de la membrane est en effet directement liée à sa teneur en eau, ce qui fait de la gestion de l'eau un problème crucial [9]. Typiquement, les membranes des piles à combustible PEM sont en ionomère de type acide perfluorocarbone-sulfonique (PSA). Il s'agit d'un copolymère de type PTFE (Téflon) et perfluorosulfonates. Le matériau le plus fréquemment utilisé est le Nafion® qui présente l'avantage d'une conductivité protonique très élevée même à température ambiante. La conductivité de la membrane est étroitement liée à son humidité qui doit toujours être maintenue élevée. Pour réduire sa résistance ionique, la membrane doit être la plus fine possible. De plus, la membrane doit être chimiquement stable.

Électrodes

Une électrode de pile à combustible est essentiellement une fine couche composée de catalyseur, de carbone et de ionomère qui est pressée entre la membrane et la couche de diffusion poreuse. C'est l'endroit où se produisent les réactions électrochimiques. Plus précisément, les réactions électrochimiques ont lieu à la surface du catalyseur. Le platine est le catalyseur le plus couramment utilisé dans les PEMFC pour la réduction de l'oxygène et l'oxydation de l'hydrogène [10]- [11]- [12]. Il est important d'avoir de petites particules de platine (4 nm ou moins) avec une grande surface. La minimisation de la perte de potentiel de cellule est liée à la vitesse de transport des protons et à la perméation des gaz réactifs dans la couche de catalyseur [13]. Cependant, la clé pour améliorer les performances de la PEMFC est d'augmenter l'utilisation du platine dans la couche de catalyseur, et non dans la charge de platine. Le platine est sensible à la pureté de l'hydrogène.

Couche de diffusion des gaz (GDL)

La couche de diffusion des gaz (GDL) est située entre les électrodes et les plaques bipolaires. Plusieurs propriétés caractérisent le matériau utilisé comme GDL. Premièrement, il doit être suffisamment poreux pour permettre le transport à la fois des gaz réactifs et de l'eau produite par la réaction électrochimique. Deuxièmement, il doit être à la fois électriquement et thermiquement conducteur [14]. Troisièmement, il doit être suffisamment solide pour renforcer l'AME qui est fragile. Le matériau le plus utilisé pour fabriquer une GDL est le papier en fibre de carbone. Une petite quantité de PTFE (Teflon®) est étalée dans le matériau pour le rendre hydrophobe afin de faciliter l'évacuation de l'eau. Enfin, une fine couche de particules de graphite mélangées à du PTFE pour former la Micro Porous Layer (MPL) est souvent présente à l'interface avec l'électrode. La taille des pores dans le MPL est d'environ 0,1 à 0,5 μm, ce qui est inférieur à la taille des pores du papier en fibre de carbone (20-50 μm) [15, 16, 17].

Plaques bipolaires

Les plaques bipolaires sont utilisées pour l'alimentation en gaz réactifs, pour éliminer la chaleur et l'eau, pour séparer les cellules individuelles dans stack et pour transporter le courant d'une cellule à la cellule voisine jusqu'à atteindre la plaque collectrice à l'extrémité de l'empilement. Le graphite (mélangé à un polymère) et le métal sont deux types de matériaux les plus utilisés pour la fabrication de plaques bipolaires de piles à combustible PEM [18]. D'autres types de matériaux tels que l'aluminium, l'acier, le titane ou le nickel se corroderaient dans l'environnement de la pile à combustible et une couche de corrosion sur la surface de la plaque bipolaire augmenterait la résistance électrique [19]-[20]. Cependant, ce problème peut être résolu en revêtant la plaque d'un matériau non corrosif électriquement conducteur. La caractéristique la plus importante des plaques bipolaires est leur conductivité électrique qui doit être la plus élevée possible [21]-[22].

Caractéristique courant-tension de la pile à combustible

Les performances de la pile à combustible sont généralement données par une courbe de polarisation qui donne la variation de tension aux bornes de la pile avec la densité surfacique de courant. Elle permet une évaluation rapide des performances de la pile. De nombreux facteurs influencent les performances de la PEMFC, parmi lesquels les matériaux, la conception et les conditions de fonctionnement, mais la tension de la cellule est aussi influencée par des facteurs électrochimiques et physiques et elle dépend des conditions de fonctionnement telles que la température, la pression, la composition du gaz et les propriétés du carburant. Ces facteurs induisent une chute de tension lors du passage du courant. Le potentiel théorique de la pile à combustible hydrogène-oxygène est de 1,23 volts par rapport à l'électrode de référence à hydrogène. Cependant, le potentiel de la cellule est inférieur à 1,23 volt car la polarisation des électrodes entraîne une perte de potentiel dans le système. Une courbe de polarisation typique est représentée schématiquement sur la Figure 3. Il existe trois principales sources de perte de potentiel (appelée surtension) dans la cellule :

- La polarisation d'activation est la surtension correspondant à l'énergie d'activation que doit surmonter la réaction électrochimique sur la surface catalytique. Ce type de polarisation s'observe principalement à faible densité de courant [24] et la baisse de tension est d'environ 0,1 à 0,2 volts.

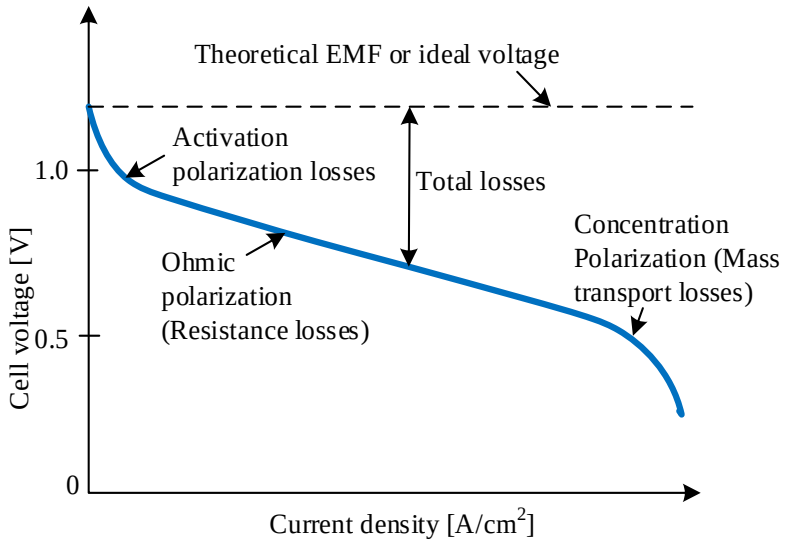

Figure 3 Courbe de polarisation d'une pile de type PEMFC.

- La polarisation ohmique est la perte de tension causée par le transport de charges. Elle comprend la résistance électronique, la résistance ionique de la membrane et les résistances de contact électriques aux interfaces et aux connexions terminales des composants.

- La polarisation de concentration est une perte de tension due à la limitation du transport de matière. Elle apparait surtout à forte densité de courant, lorsque la diffusion ne permet plus d'alimenter correctement les électrodes en gaz actifs, ou lorsque le flux de gaz est faible (coefficient stœchiométrique proche de 1). L'alimentation en gaz des électrodes est l'un des principaux paramètres de fonctionnement, et la gestion de l'eau et la chaleur produites par les réactions électrochimiques en dépend également.

Dégradations des piles à combustible PEMFC

La durée de vie des piles à combustible de type PEM est influencée par les conditions de fonctionnement, la tension de fonctionnement, l'humidité de la température et les oscillations de tension. Le maintien de l'humidité des gaz à des valeurs optimales à l'intérieur de la cellule entraîne des performances optimales de la pile, tandis le séchage de la membrane ou le noyage des électrodes et des GDL les dégradent. De même, une mauvaise alimentation en gaz ou la présence d'impuretés, affectera les performances. Pour améliorer la fiabilité et la durabilité, une gestion appropriée doit être effectuée pour éliminer les défauts et prévenir d'éventuels dommages. Certaines dégradations des performances de la FC sont réversibles car liées à des conditions de fonctionnement adaptables, d'autres sont irréversibles car liées à des modifications physiques des matériaux qui composent une cellule. L'asséchement de la membrane et le noyage des électrodes produisent des pertes de performances réversible alors que le manque de gaz (fuel starvation) engendre le plus souvent des dégradations irréversibles des couches catalytiques (par exemple par oxydation du carbone qui sert de support au catalyseur - Pt).

Périphérique de stockage

Les premières technologies de dispositifs de stockage ont été développées au milieu des années 1800 avec les batteries au plomb proposé par Gaston Planté. Depuis lors, il y a eu de nombreux développements dans le secteur des batteries. Dans les années 1950, les ingénieurs électriciens ont commencé à utiliser des électrodes en carbone poreux pour fabriquer des condensateurs et un condensateur basse tension a été proposé en 1957. Les scientifiques étudient les systèmes de condensateurs électrochimiques avec des électrodes de charbon actif qui sont une propriété fondamentale des supercondensateurs et des batteries. Depuis 1990, l'Institut de recherche Maxwell a introduit les "Boost caps" en tant que supercondensateurs à haute énergie.

Le diagramme de Ragone donne la relation entre la densité de puissance et la densité d'énergie tel que présenté sur la Figure 4. On peut observer que les batteries ont une densité d'énergie plus élevée et que les condensateurs ont une densité de puissance plus élevée. Les supercondensateurs (SC) sont un pont entre les batteries et les condensateurs : la densité d'énergie des SC est meilleure que celle des condensateurs et leur densité de puissance est meilleure que celle des batteries.

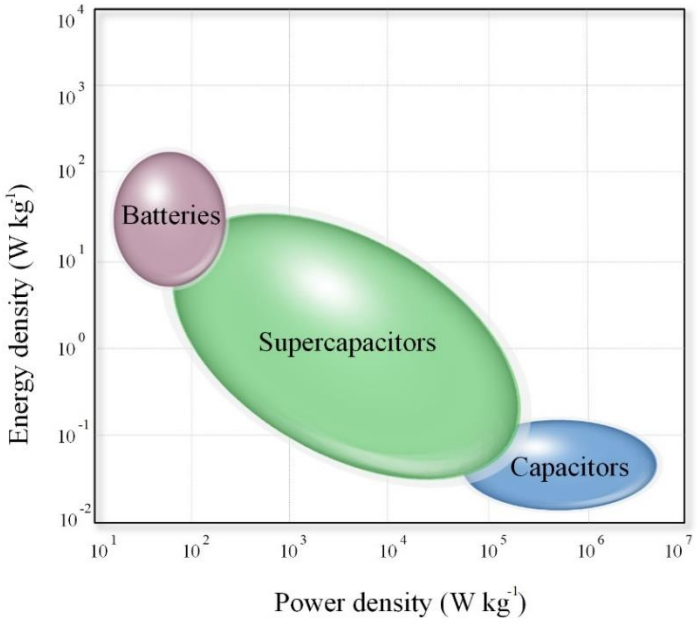

Figure 4. Diagramme de Ragone.

Les batteries sont généralement lourdes, encombrantes et ne peuvent pas être facilement recyclées. Les condensateurs conventionnels fournissent une densité de puissance élevée et ont une longue durée de vie. L'avantage des SC est leur poids plume, leur flexibilité, leur portabilité, leur réponse rapide et leur grande robustesse qui conduisent à de meilleures performances telles qu'une densité d'énergie élevée et une densité de puissance élevée [45].

Supercondensateur

La structure primaire d'un supercondensateur est présentée à la figure 5. Les collecteurs de courant servent à collecter les électrons et à supporter le matériau d'électrode. Leur conductivité et la résistance de contact avec l'électrode affectent directement la densité de puissance et la capacité du SC. Généralement, une électrode est constituée de charbon actif qui est imprégné d'un électrolyte organique ou aqueux. Le courant circule de l'anode à la cathode, puis il passe dans le circuit externe. Un séparateur isole les deux électrodes pour éviter un court-circuit et laisse passer les ions.

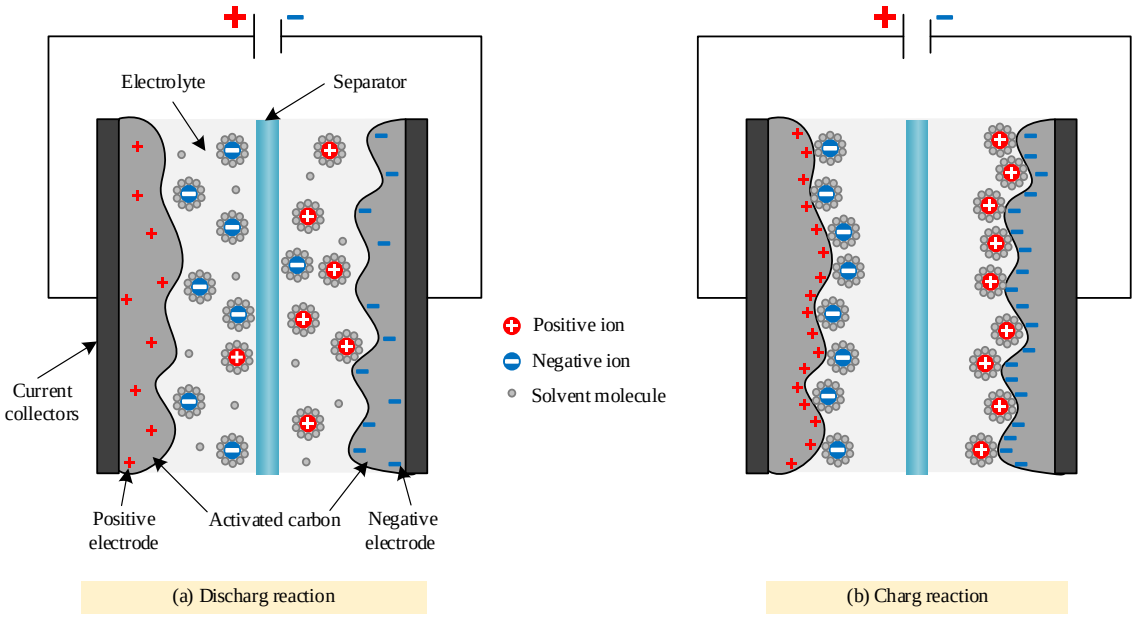

Figure 5. Structure d'un supercondensateur et principe de fonctionnement (a) décharge et (b) charge.

Le stockage d'énergie se fait via les ions qui se répartissent à partir de l'électrolyte autour de la surface des deux électrodes. Il existe plusieurs types de SC qui dépendent des mécanismes de stockage d'énergie : le condensateurs électriques à double couche, le pseudo-condensateur et le condensateur hybride.

Conclusion

Les piles à combustible sont des dispositifs de conversion d'énergie efficaces, car le processus de transformation de l'énergie se fait en une seule étape et il est respectueux de l'environnement car il ne produit que de l'eau. Les piles à combustible peuvent fonctionner en continu tant que le système est alimenté en hydrogène. Il existe plusieurs types de piles à combustible. La plus couramment utilisée pour les applications transport est la pile à combustible à membrane échangeuse de protons (PEMFC). Ce type de pile fonctionne à basse température, est de petite taille et présente une densité de courant élevée. Les principaux composants de la PEMFC sont la membrane, les électrodes (formant l'AME), la couche de diffusion des gaz et les plaques bipolaires. La courbe de polarisation est l'élément essentiel de la performance et de la fonctionnalité de la pile. Cette courbe est influencée par les conditions de fonctionnement telles que la température, la pression, la composition du gaz et les propriétés du combustible. Lorsque ces conditions de fonctionnement changent, elles entraînent une

modification de la courbe de polarisation et certaines conditions comme par exemple, le séchage, le noyage, le manque de gaz actifs, les impuretés conduisent à la dégradation de certains composants. Pour éviter toutes ces dégradations, la gestion de la PEMFC est essentielle. Elle consiste en la gestion de l'eau, la gestion thermique, la gestion de l'humidité, la gestion du carburant et la gestion de l'énergie.

Comme la durabilité de la PEMFC joue un rôle clé dans son déploiement à grande échelle en tant que source d'énergie, l'objectif de la thèse est de développer une source de puissance à base de piles à combustible permettant d'atteindre de meilleures performances et de diminuer les dégradations liées aux opérations dynamiques. La nouvelle architecture d'électronique de puissance développée est basée sur une configuration modulaire dans laquelle la source globale est répartie en plusieurs stacks de plusieurs cellules de pile à combustible. Chaque stack est connecté à son propre convertisseur pour former un système modulaire, et la sortie de plusieurs systèmes modulaires est connectée en série pour fournir de l'énergie à la charge. Cette configuration doit offrir de meilleures performances en termes de fiabilité et de durabilité par rapport aux configurations impliquant un seul convertisseur. Comme la dynamique de puissance de la pile à combustible est faible (liée à l'alimentation en gaz actifs), l'hybridation avec un dispositif de stockage à réponse rapide, tel que le supercondensateur (SC), est nécessaire pour la charge à large bande passante. Les supercondensateurs sont des dispositifs permettant de stocker de l'énergie. Ils peuvent se charger et fournir de l'énergie rapidement. Ils ont également une longue durée de vie. Les types concernés par cette recherche sont les condensateurs électriques à double couche (EDLC). Afin d'augmenter l'efficacité du système global et permettre une utilisation optimale du SC, une topologie série pour l'hybridation est proposée dans cette étude, dans laquelle un convertisseur isolé est placé en série entre la pile à combustible et le SC. Cette hybridation est appliquée au niveau modulaire, le SC étant distribué dans tous les systèmes hybrides modulaires. La tension aux bornes du convertisseur en série doit être contrôlée pour que le transfert d'énergie de la pile à combustible vers le SC se fasse progressivement. Tous les SC fourniront de l'énergie à la charge par l'intermédiaire d'un convertisseur DC/DC adapté, spécialement conçu pour assurer un degré de liberté au flux de puissance ce qui est nécessaire pour la mise en œuvre d'un système de gestion des piles à combustible. Le système proposé est validé par la simulation et les résultats expérimentaux.

List of Publication

International Journals

1. **A. Siangsanoh,** M. Bahrami, W. Kaewmanee, R. Gavagsaz-ghoachani, M. Phattanasak, J.P. Martin, B. Nahid-Mobarakeh, M. Weber, S. Pierfederici, G. Maranzana, S. Didierjean, “Series hybrid fuel cell/supercapacitor power source”, *Mathematics and Computers in Simulation*, 2020.
2. M. Afkar, R. Gavagsaz-Ghoachani, M. Phattanasak, **A. Siangsanoh**, J. -P. Martin and S. Pierfederici, "Generalization of a DC–DC Modular Converter Topology for Fuel Cell Applications," in *IEEE Transactions on Industry Applications*, vol. 58, no. 2, pp. 2255-2267, March-April 2022.

International conferences

1. **A. Siangsanoh**, M. Bahrami, W. Kaewmanee, R. Gavagsaz-Ghoachani, M. Phattanasak, J.P. Martin, B. Nahid-Mobarakeh, M. Weber, S. Pierfederici, G. Maranzana, S. Didierjean, “Series hybrid Fuel cell/Supercapacitor power source”, ELECTRIMACS 2019 – Salerno, Italy, 21st-23rd May 2019, **Best paper award**.
2. **A. Siangsanoh**, M. Bahrami, W. Kaewmanee, R. Gavagsaz-Ghoachani, M. Phattanasak, J.P. Martin, M. Weber, S. Pierfederici, S. Didierjean, “Hybrid Fuel Cell/Supercapacitor using a series converter”, 2019 IEEE Energy Conversion Congress and Exposition (ECCE), Baltimore, MD, USA, September 29 – October 3, 2019.
3. M. Afkar, R. Gavagsaz-Ghoachani, **Apinya Siangsanoh**, M. Phattanasak, J-P. Martin and S. Pierfederici, “A Modular DC-DC Converter Topology Based on A Three-Level DC-DC Converter for Distributed Fuel Cell Architecture”, 2019 IEEE Energy Conversion Congress and Exposition (ECCE), Baltimore, MD, USA, September 29 – October 3, 2019.
4. **A. Siangsanoh** · W. Kaewmanee · R. Gavagsaz-Ghoachani · J.P. Martin · M. Weber · M. Phattanasak · S. Pierfederici · G. Maranzana · S. Didierjean, “An Improved Control of High Efficiency Series Converter for Fuel cell/Supercapacitor Hybrid System”, ELECTRIMACS 2022, Nancy, France, 16-19 May 2022.

References

[1] R. M. Elavarasan et al., "A Comprehensive Review on Renewable Energy Development, Challenges, and Policies of Leading Indian States With an International Perspective," *IEEE Access,* vol. 8, pp. 74432-74457, 2020.

[2] A. Harrouz, D. Belatrache, K. Boulal, I. Colak and K. Kayisli, "Social Acceptance of Renewable Energy dedicated to Electric Production," in *9th International Conference on Renewable Energy Research and Application (ICRERA)*, Glasgow, United Kingdom, 2020.

[3] F. Bacon, Electrochim, 1969.

[4] G. Hoogers, Fuel Cell Technology Handbook, Florida, USA, 2002.

[5] K. Ota, "Fuel cells: Past, present and future," *IEEJ Trans*, vol. 128, pp. 329-332, 2008.

[6] S. V. M. Guaitolini, I. Yahyaoui, J. F. Fardin, L. F. Encarnação and F. Tadeo, "A review of fuel cell and energy cogeneration technologies," in *9th International Renewable Energy Congress (IREC)*, Hammamet, 2018.

[7] B. G. Pollet, S. S. Kocha and I. Staffell, "Current status of automotive fuel cells for sustainable transport," *Current Opinion in Electrochemistry,* vol. 16, pp. 90-95, 2019.

[8] M. M. Whiston, I. L. Azevedo, S. Litster, K. S. Whitefoot, C. Samaras and J. F. Whitacre, "Expert assessments of the cost and expected future performance of proton exchange membrane fuel cells for vehicles," *Proceedings of the National Academy of Sciences,* vol. 116, no. 11, pp. 4899-4904, 2019.

[9] S. Gottesfeld and T. A. Zawodzinski, "Polymer Electrolyte Fuel Cells," in *Advances in Electrochemical Science and Engineering*, New York, USA, Wiley-VCH, 1997.

[10] Y. Yazawa, H. Yoshida and T. Hattori, "The support effect on platinum catalyst under oxidizing atmosphere: improvement in the oxidation-resistance of platinum by the electrophilic property of support materials," *Applied Catalysis A: General,* vol. 237, no. 1-2, pp. 139-148, 2002.

[11] J. Liu, D. Takeshi, K. Sasaki and S. Lyth, "Defective Graphene Foam: A Platinum Catalyst Support for PEMFCs," *Journal of The Electrochemical Society,* vol. 161, pp. 838-844, 2014.

[12] L. Jiang, X. Tao, L. Li, W. Xia and R. Si, "Ceria supported platinum catalyst for CO oxidation reaction: Importance of metallic active species - Commemorating the 100th anniversary of the birth of Academician Guangxian Xu," *Journal of Rare Earths,* vol. 39, no. 5, pp. 495-503, 2021.

[13] H. A. Gasteiger, W. Gu, R. Makharia and M. F. Mathias, "Catalyst utilization and mass transfer limitations in the polymer electrolyte fuel cells," in *Electrochemical Society Meeting*, Orlando, USA, 2003.

[14] N. Zamel, "The catalyst layer and its dimensionality – A look into its ingredients and how to characterize their effects," *Journal of Power Sources,* vol. 309, pp. 141-159, 2016.

[15] J. Roth, J. Fleming and W. Lehnert, "Diffusion media materials and characterization, Fundamentals," *Fuel Cell Technology and Applications,* vol. 3, pp. 517-537, 2003.

[16] A. Alrashidi and H. Liu, "Laser-perforated anode gas diffusion layers for direct methanol fuel cells", International Journal of Hydrogen Energy," *International Journal of Hydrogen Energy,* vol. 45, no. 34, pp. 17886-17896, 2021.

[17] Q. Z. Shu, Z. X. Xia, W. Wei, X. L. Xu, S. L. Wang, H. Zhao and G. Q. Sun, "A novel gas diffusion layer and its application to direct methanol fuel cells, New Carbon Materials," vol. 36, no. 2, pp. 409-419, 2021.

[18] A. Tang, L. Crisci, L. Bonville and J. Jankovic, "An overview of bipolar plates in proton exchange membrane fuel cells," *Journal of Renewable and Sustainable Energy,* vol. 13, no. 2, p. 022701, 2021.

[19] Y. Song, C. Zhang, C. Y. Ling, M. Han, R. Y. Yong, D. Sun and J. Chen, "Review on current research of materials, fabrication and application for bipolar plate in proton exchange membrane fuel cell," *International Journal of Hydrogen Energy,* vol. 45, no. 54, pp. 29832-29847, 2020.

[20] T. Wilberforce, O. Ijaodola, E. Ogungbemi, Z. E. Hassan, J. Thompson and A. G. Olabi, "Effect of Bipolar Plate Materials on Performance of Fuel Cells," *Reference Module in Materials Science and Materials Engineering,* 2018.

[21] W. Liao, F. Jiang, Y. Zhang, X. Zhou and Z. He, "Highly-conductive composite bipolar plate based on ternary carbon materials and its performance in redox flow batteries," *Renewable energy,* vol. 152, pp. 1310-1316, 2020.

[22] H. Dong, S. He, X. Wang, C. Zhang and D. Sun, "Study on conductivity and corrosion resistance of N-doped and Cr/N co-doped DLC films on bipolar plates for PEMFC," *Diamond and Related Materials,* vol. 110, 2020.

[23] F. Barbir, "PEM Fuel Cells," Academic Press, 2005, pp. 33-72.

[24] A. Andronie, L. Stamatin, V. Girleanu, V. Ionescu and N. Buzbuchi, "Simplified Mathematical Model for Polarization Curve Validation and Experimental Performance Evaluation of a PEM Fuel Cell System," *Procedia Manufacturing,* vol. 32, pp. 810-819, 2019.

[25] A. Thomas, G.Maranzana, S. Didierjean, J. Dillet, O. Lottin, "Measurements of Electrode Temperatures, Heat and Water Fluxes in PEMFCs: Conclusions about Transfer Mechanisms," *Journal of the Electrochemical Society,* vol. 160, no. 2, pp. 191-204, 2013.

[26] W. Dai, H. Wang, X. Z. Yuan, J. J. Martin, D. Yang, J. Qiao and J. Ma, "A review on water balance in the membrane electrode assembly of proton exchange membrane fuel cells," *International Journal of Hydrogen Energy,* vol. 34, no. 23, pp. Pages 9461-9478, 2009.

[27] Y. Zhao, Y. Mao, W. Zhang, Y. Tang and P. Wang, "Reviews on the effects of contaminations and research methodologies for PEMFC," *International Journal of Hydrogen Energy,* vol. 45, no. 43, pp. 23174-23200, 2020.

[28] L. Y. Sung, B. J. Hwang, K. L. Hsueh and F. H. Tsau, "Effects of anode air bleeding on the performance of CO-poisoned proton-exchange membrane fuel cells," *Journal of Power Sources,* vol. 195, no. 6, pp. 1630-1639, 2010.

[29] Y. Liu, L. Fan, P. Pei, S. Yao and F. Wang, "Asymptotic analysis for the inlet relative humidity effects on the performance of proton exchange membrane fuel cell," *Applied Energy,* vol. 213, pp. 573-584, 2018.

[30] C. Mittelsteadt, T. Norman, M. Rich and J. Willey, "PEM Electrolyzers and PEM Regenerative Fuel Cells Industrial View," *Electrochemical Energy Storage for Renewable Sources and Grid Balancing,* pp. 159-181, 2015.

[31] X. Xie, C. He, B. Li et al., "Performance enhancement and degradation mechanism identification of a single-atom Co–N–C catalyst for proton exchange membrane fuel cells," *Nature Catalysis,* vol. 3, no. 12, p. 1044–1054, 2020.

[32] X. Chen, J. Xu, Q. Liu, Y. Chen, X. Wang, W. Li, Y. Ding and Z. Wan, "Active disturbance rejection control strategy applied to cathode humidity control in PEMFC system," *Energy Conversion and Management,* vol. 224, p. 113389, 2020.

[33] A. Baroutaji, A. Arjunan, M. Ramadan, J. Robinson, A. Alaswad, M. A. Abdelkareem and A. G. Olabi, "Advancements and prospects of thermal management and waste heat recovery of PEMFC," *International Journal of Thermofluids,* vol. 9, p. 100064, 2021.

[34] M. Gerard, P. Mathias, J. P. Poirot-Crouvezier, D. H. Daniel and M. C. Marion-Péra, "Oxygen starvation analysis during air feeding faults in PEMFC," *International Journal of Hydrogen Energy,* vol. 35, pp. 12295-12307, 2010.

[35] D. Gong, S. Xu and B. Zhang, "Control Strategies for Prevention of PEMFC Oxygen Starvation: A Review," in *SAE International*, United States, 2021.

[36] A. Kolli, A. Gaillard, A. De Bernardinis, O. Bethoux, D. Hissel and Z. Khatir, "A review on DC/DC converter architectures for power fuel cell applications," *Energy Conversion and Management,* vol. 105, pp. 716-730, 2015.

[37] S. Agarwal and V. Boddu, "Maximum Power Extraction From Series-Connected Fuel Cell Stacks by the Current Compensation Technique," *IEEE Transactions on Power Electronics*, vol. 30, no. 2, pp. 582-589, 2015.

[38] N. Marx, J. Cardozo, L. Boulon, F. Gustin, D. Hissel and K. Agbossou, "Comparison of the Series and Parallel Architectures for Hybrid Multi-Stack Fuel Cell - Battery Systems," in *IEEE Vehicle Power and Propulsion Conference (VPPC)*, Montreal, QC, 2015.

[39] J. Cardozo, N. Marx, L. Boulon and D. Hissel, "Comparison of Multi-Stack Fuel Cell System Architectures for Residential Power Generation Applications Including Electrical Vehicle Charging," in *IEEE Vehicle Power and Propulsion Conference (VPPC)*, 1-6, 2015.

[40] L. Enjeti and P. N. Palma, "A Modular Fuel Cell, Modular DC–DC Converter Concept for High Performance and Enhanced Reliability," *IEEE Transactions on Power Electronics*, vol. 24, no. 6, pp. 1437-1443, 2009.

[41] A. De Bernardinis, "Synthesis on power electronics for large fuel cells: From power conditioning to potentiodynamic analysis technique," *Energy Conversion and Management*, vol. 84, pp. 174-185, 2014.

[42] M. Y. Suberu, M. W. Mustafa and N. Bashir, "Energy storage systems for renewable energy power sector integration and mitigation of intermittency," *Renewable and Sustainable Energy Reviews*, vol. 35, pp. 499-514, 2014.

[43] O. Bolufawi, "Renewable Energy Integration with Energy Storage Systems and Safety," in *Special Topics in Renewable Energy Systems*, 2018.

[44] J. Raut, A.S. Parker, C. B. Glass and T. Jeffrey , "A method to obtain a Ragone plot for evaluation of carbon nanotube supercapacitor electrodes," *Journal of Materials Research*, vol. 25, no. 8, pp. 1500-1506, 2010.

[45] A. Chu and P. Braatz, "Comparison of commercial supercapacitors and high-power lithium-ion batteries for power-assist applications in hybrid electric vehicles: I. Initial characterization," *Journal of Power Sources*, vol. 112, no. 1, pp. 236-246, 2002.

[46] M. Young, A. Holder, S.M. George and C. Musgrave, "Mechanism of Pseudocapacitive Charge Storage in MnO2," 2014.

[47] L. L. Tian, Q. C. Zhuang, J. Li, Y. Shi, J. Chen, F. Lu and S. Sun, "Mechanism of intercalation and deintercalation of lithium ions in graphene nanosheets," *Chinese Science Bulletin*, vol. 56, no. 30, pp. 3204-3212, 2011.

[48] W. Kai, R. Baosen, L. Liwei, L. Yuhao, Z. Hongwei and S. Zongqiang, "A review of modeling research on supercapacitor," in *2017 Chinese Automation Congress (CAC)*, Jinan, China, 2017.

[49] Y. Wang, Z. Sun and Z. Chen, "Energy management strategy for battery/supercapacitor/fuel cell hybrid source vehicles based on finite state machine," *Applied Energy,* vol. 254, 2019.

[50] F. Rafik, H. Gualous, R. Gallay, A. Crausaz and A. Berthon, "Frequency, thermal and voltage supercapacitor characterization and modeling," *Journal of Power Sources,* vol. 165, p. 928–934, 2006.

[51] H. Rezk, A. M. Nassef, M. A. Abdelkareem, A. H. Alami and A. Fathy, "Comparison among various energy management strategies for reducing hydrogen consumption in a hybrid fuel cell/supercapacitor/battery system," *International Journal of Hydrogen Energy,* vol. 46, no. 8, pp. 6110-6126, 2021.

[52] H. Moradisizkoohi, N. Elsayad and O. A. Mohammed, "Experimental Verification of a Double-Input Soft-Switched DC–DC Converter for Fuel Cell Electric Vehicle With Hybrid Energy Storage System," *IEEE Transactions on Industry Applications,* vol. 55, no. 6, pp. 6451-6465, 2019.

[53] S. Abbou, J. Dillet, G. Maranzana, S. Didierjean, O. Lottin, "Local potential evolutions during proton exchange membrane fuel cell operation with dead-ended anode – Part I: Impact of water diffusion and nitrogen crossover," *Journal of Power Sources,* vol. 340, pp. 337-346, 2017.

[54] Andrew L. Dicks and David A. J. Rand, Fuel Cell Systems Explained, 2018.

[55] D. B. Murray and J. G. Hayes, "Cycle Testing of Supercapacitors for Long-Life Robust Applications," *IEEE Transactions on Power Electronics,* vol. 30, no. 5, pp. 2505-2516, 2015.

[56] J. L. a. P. V. a. C.-C. R. Sampietro, "Optimal Sizing of Storage Elements for a Vehicle Based on Fuel Cells, Supercapacitors, and Batteries," *Energies,* vol. 12, no. 5, 2019.

[57] B. Allaoua, K. Asnoune and B. Mebarki, "Energy management of PEM fuel cell/ supercapacitor hybrid power sources for an electric vehicle," *International Journal of Hydrogen Energy,* vol. 42, no. 33, pp. 21158-21166, 2017.

[58] C. Turpin, D. Van Laethem, B. Morin, O. Rallières, X. Roboam, O. Verdu, V. Chaudron, "Modelling and analysis of an original direct hybridization of fuel cells and ultracapacitors," *Mathematics and Computers in Simulation,* vol. 131, pp. 76-87, 2017.

[59] M. Garcia-Arregui, C. Turpin and S. Astier, "Direct connection between a fuel cell and ultracapacitors," in *International Conference on Clean Electrical Power,* Capri, 2007.

[60] A. Kolli, A. Gaillard, A. De Bernardinis, O. Bethoux, D. Hissel and Z. Khatir, "A review on DC/DC converter architectures for power fuel cell applications," *Energy Conversion and Management,* vol. 105, pp. 716-730, 2015.

[61] J. R. R. Zientarski, M. L. da Silva Martins, J. R. Pinheiro and H. L. Hey, "Evaluation of Power Processing in Series-Connected Partial-Power Converters," *IEEE Journal of Emerging and Selected Topics in Power Electronics,* vol. 7, no. 1, pp. 343-352, 2019.

[62] M. Kasper, D. Bortis and J. W. Kolar, "Classification and Comparative Evaluation of PV Panel-Integrated DC–DC Converter Concepts," *IEEE Transactions on Power Electronics,* vol. 29, no. 5, pp. 2511-2526, 2014.

[63] N. Allali, Convertisseur haut rendement à dimensionnement réduit pour batterie hybridée puissance/énergie de véhicule électrique : Principe de source de courant controle, Dissertation, Ecole centrale de Lille, 2016.

[64] J. R. R. Zientarski, M. L. d. S. Martins, J. R. Pinheiro and H. L. Hey, "Series-Connected Partial-Power Converters Applied to PV Systems: A Design Approach Based on Step-Up/Down Voltage Regulation Range," *IEEE Transactions on Power Electronics,* vol. 33, no. 9, pp. 7622-7633, 2018.

[65] L. Shu, W. Chen, D. Ma and G. Ning, "Analysis of Strategy for Achieving Zero-Current Switching in Full-Bridge Converters," *IEEE Transactions on Industrial Electronics,* vol. 65, no. 7, pp. 5509-5517, 2018.

[66] T. Liang, M. Cheng, W. Huang and W. Tseng, "Interleaved Half-Bridge Flyback Converter With Zero-Current Switching," *IEEE Transactions on Power Electronics,* vol. 34, no. 4, pp. 3370-3383, 2019.

[67] T. Lagier, P. Dworakowski, L. Chédot, F. Wallart, B. Lefebvre, J. Maneiro, J. Páez, P. Ladoux and C. Buttay, "How Good are the Design Tools in Power Electronics?," in *22nd European Conference on Power Electronics and Applications* , Lyon, France, 2020.

[68] M. Nitzsche, C. Cheshire, M. Fischer, J. Ruthardt and J. Roth-Stielow, "Comprehensive Comparison of a SiC MOSFET and Si IGBT Based Inverter," in *International Exhibition and Conference for Power Electronics*, Nuremberg, Germany, 2019.

[69] Z. Tang et al.,, "Modulation for the AVC-HERIC Inverter to Compensate for Deadtime and Minimum Pulsewidth Limitation Distortions," *IEEE Transactions on Power Electronics,* vol. 35, no. 3, pp. 2571-2584, 2020.

[70] A. Guha and G. Narayanan, "Small-Signal Stability Analysis of an Open-Loop Induction Motor Drive Including the Effect of Inverter Deadtime," *EEE Transactions on Industry Applications,* vol. 52, no. 1, pp. 242-253, 2016.

[71] A. Payman, S. Pierfederici and F. Meibody-Tabar, "Energy Management in a Fuel Cell/Supercapacitor Multisource/Multiload Electrical Hybrid System," *IEEE Transactions on Power Electronics,* vol. 24, no. 12, pp. 2681-2691, 2009.

[72] R. Gavagsaz-Ghoachani, L. Saublet, J. Martin, B. Nahid-Mobarakeh and S. Pierfederici, "Stability Analysis and Active Stabilization of DC Power Systems for Electrified

Transportation Systems, Taking into Account the Load Dynamics," *IEEE Transactions on Transportation Electrification,* vol. 3, no. 1, pp. 3-12, 2017.

[73] P. Magne, "Contribution to the stability analysis and stabilization of DC microgrid with energy storage capability," University of Lorraine, 2012.

[74] W. Hassan, D. Lu and W. Xiao, "Optimal Analysis and Design of DC-DC Converter to Achieve high Voltage Conversion Gain and High Efficiency for Renewable Energy Systems," in *27th International Symposium on Industrial Electronics (ISIE),* Cairns, QLD, 2018.

[75] D. Dell'Isola, M. Urbain, M. Weber, S. Pierfederici and F. Meibody-Tabar, "Optimal Design of a DC–DC Boost Converter in Load Transient Conditions, Including Control Strategy and Stability Constraint," *IEEE Transactions on,* vol. 5, no. 4, pp. 1214-1224, 2019.

[76] M. H. Ahmed, M. Wang, M. A. S. Hassan and I. Ullah, "Power Loss Model and Efficiency Analysis of Three-Phase Inverter Based on SiC MOSFETs for PV Applications," *IEEE Access,* vol. 7, pp. 75768-75781, 2019.

[77] A. Shahin, J. -. Martin, B. Nahid-Mobarakeh and S. Pierfederici, "Optimal efficiency operation of non-isolated DC/DC converter for high voltage ratio applications," in *39th Annual Conference of the IEEE Industrial Electronics Society*, Vienna, 2013.

[78] N. Allali, "Convertisseur haut rendement à dimensionnement réduit pour batterie hybridée puissance/énergie de véhicule électrique : Principe de source de courant contrôlée," 2016.

[79] I. Al-Bahadly, "Portable Multi-Inputs Renewable Energy System for Small Scale Remote Application," *Journal of Power and Energy Engineering,* vol. 6, pp. 59-73, 2018.

[80] R. K. Ahluwalia and X. Wang, "Fuel cell systems for transportation: Status and trends," *Journal of Power Sources,* vol. 177, no. 1, pp. 167-176, 2008.

[81] A. Yilanci, I. Dincer and H.K. Ozturk, "A review on solar-hydrogen/fuel cell hybrid energy systems for stationary applications," *Progress in Energy and Combustion Science,* vol. 35, no. 3, pp. 231-244, 2009.

[82] Q. Wu, Q. Wang, J. Xu, H. Li and L. Xiao, "A High-Efficiency Step-Up Current-Fed Push–Pull Quasi-Resonant Converter With Fewer Components for Fuel Cell Application," *IEEE Transactions on Industrial Electronics,* vol. 64, no. 8, pp. 6639-6648, 2017.

[83] T. Arunkumari and V. Indragandhi, "An overview of high voltage conversion ratio DC-DC converter configurations used in DC micro-grid architectures," *Renewable and Sustainable Energy Reviews,* vol. 77, pp. 670-687, 2017.

[84] H. M. M. Swamy, K. P. Guruswamy and S. P. Singh, "Design, Modeling and Analysis of Two Level Interleaved Boost Converter," in *nternational Conference on Machine Intelligence and Research Advancement*, Katra, India, 2013.

[85] M. Afkar, R. Gavagsaz-Ghoachani, M. Phattanasak, and S. Pierfederici, "Commandable areas of a modular converter for DC voltage imbalance mitigation in fuel cell systems," *Sustainable Energy Technologies and Assessments* , vol. 48, pp. 1-12, December 2021.

[86] M. B. e. al., "Design and Modeling of an Equalizer for Fuel Cell Energy Management Systems," *IEEE Transactions on Power Electronics,* vol. 34, no. 11, pp. 10925-10935, 2019.

[87] M. Daowd, N. Omar, P. Van Den Bossche and J. Van Mierlo, "Passive and active battery balancing comparison based on MATLAB simulation," in *IEEE Vehicle Power and Propulsion Conference*, Chicago, IL, USA, 2011.

[88] K. Zhi-Guo, Z. Chun-Bo, L. Ren-Gui and C. Shu-Kang, "Comparison and evaluation of charge equalization technique for series connected batteries," in *7th IEEE Power Electronics Specialists Conference*, Jeju, Korea (South), 2006.

[89] S. Shili, A. Hijazi, A. Sari, X. Lin-Shi and P. Venet, "Balancing Circuit New Control for Supercapacitor Storage System Lifetime Maximization," *IEEE Transactions on Power Electronics*, vol. 32, no. 6, pp. 4939-4948, 2017.

[90] Y. Shang, F. Lu, B. Xia, C. Zhang, N. Cui and C. Mi, "A switched-coupling-capacitor equalizer for series-connected battery strings," in *IEEE Applied Power Electronics Conference and Exposition (APEC)*, Tampa, FL, USA, 2017.

[91] S. Wang, S. Yang, W. Yang and Y. Wang, "A New Kind of Balancing Circuit With Multiple Equalization Modes for Serially Connected Battery Pack," *IEEE Transactions on Industrial Electronics,* vol. 68, no. 3, pp. 2142-2150, 2021.

[92] A. Khoshkbar Sadigh, V. Dargahi and K. A. Corzine, "Logic-Form-Equation-Based Active Capacitor Voltage Balancing Control Technique for Stacked Multicell Converters," *IEEE Transactions on Industrial Electronics*, vol. 64, no. 5, pp. 3456-3466, 2017.

[93] W. Hong, K. Ng, J. Hu and C. Moo, "Charge equalization of battery power modules in series," in *The 2010 International Power Electronics Conference - ECCE ASIA*, Sapporo, Japan, 2010.

[94] C. Moo, K. S. Ng and Y. Hsieh, "Parallel Operation of Battery Power Modules," *IEEE Transactions on Energy Conversion,* vol. 23, no. 2, pp. 701-707, 2008.

[95] M. T. e. al., "A study and implementation of three-level boost converter with MPPT for PV application," in *IEEE 3rd International Future Energy Electronics Conference and ECCE Asia* , Kaohsiung, Taiwan, 2017.

[96] C. Balakishan, N. Sandeep and M. V. Aware, "Design and Implementation of Three-Level DC-DC Converter with Golden Section Search Based MPPT for the Photovoltaic Applications," *Advances in Power Electronics*, vol. 2015, pp. 1-9, 2015.

[97] M. Afkar, G. Ghochani, M. Phattanasak, A. Siangsanoh, J. Martin and S. Pierfederici, "A Modular DC-DC Converter Topology Based On A Three-Level DC-DC Converter For Distributed Fuel Cell Architecture," in *2019 IEEE Energy Conversion Congress and Exposition (ECCE)*, Baltimore, MD, USA, 2019.

[98] A. Shahin, M. Hinaje, J. Martin, S. Pierfederici, S. Rael and B. Davat, "High Voltage Ratio DC–DC Converter for Fuel-Cell Applications," *IEEE Transactions on Industrial Electronics*, vol. 57, no. 12, pp. 3944-3955, Dec. 2010.

[99] P. Thounthong, "Control of a Three-Level Boost Converter Based on a Differential Flatness Approach for Fuel Cell Vehicle Applications," *IEEE Transactions on Vehicular Technology*, vol. 61, pp. 1467-1472, 2012.

[100] M. Afkar, S. A. Sadat Sakkak, R. Gavagsaz-Ghoachani, M. Phattanasak, S. Pierfederici and P. Sethakul,, "Pulse-width modulation technique for a multi-input dc-dc boost converter," 2021.

[101] M. Afkar, R. Gavagsaz-Ghoachani, M. Phattanasak, J. -P. Martin and S. Pierfederici, "Proposed System Based on a Three-Level Boost Converter to Mitigate Voltage Imbalance in Photovoltaic Power Generation Systems," *IEEE Transactions on Power Electronics*, vol. 37, no. 2, pp. 2264-2282, Feb. 2022.

[102] J. M. Bourgeois, "Circuits for power factor correction with regards to mains filtering," in *SGS-THOMSON Microelectronics*, Geneva, Switzerland, 1997.

[103] A. M. Roldan, A. Barrado, J. Pleite, J. Vazquez, and E. Olias, "Size and cost reduction of the energy storage capacitors," in *Proc. Appl. Power Electron. Conf. Expo*, 2004.

[104] D. L. Loree and J. P. O'Loughlin, "Design optimization of L-C filters," in *Proc. Conf. Rec. 2000 24th Int. Power Modulator Symp*, 2000.

[105] P. Thounthong, V. Chunkag, P. Sethakul, S. Sikkabut, S. Pierfederici and B. Davat., "Energy management of fuel cell/solar cell/supercapacitor hybrid power source," *Journal of Power Sources*, vol. 196, pp. 313-324, 2011.

[106] M. Zandi, A. Payman, J. Martin, S. Pierfederici, B. Davat and F. Meibody-Tabar, "Energy Management of a Fuel Cell/Supercapacitor/Battery Power Source for Electric Vehicular Applications," *IEEE Transactions on Vehicular Technology*, vol. 60, no. 2, pp. 433-443, 2011.

[107] N. Dyantyi, A. Parsons, O. Barron and S. Pasupathi., "State of health of proton exchange membrane fuel cell in aeronautic applications," *Journal of Power Sources*, vol. 451, 2020.

[108] A. El-kharouf, A. Chandan, M. Hattenberger and B. Pollet, "Proton exchange membrane fuel cell degradation and testing: Review," *Journal of the Energy Institute,* vol. 85, pp. 188-200, 2012.

[109] M. Bahrami, J-P Martin, G. Maranzana, S. Pierfederici, M. Weber and S. Didierjean, "Fuel cell management system: An approach to increase its durability," *Applied Energy,* vol. 306, p. 118070, 2022.

[110] C. Zhang, W. Li, M. Hu, X. Cheng, K. He and L. Mao, "A Comparative Study of Using Polarization Curve Models in Proton Exchange Membrane Fuel Cell Degradation Analysis," *Energies,* vol. 13, no. 15, 2020.

[111] A. Andronie, I. Stamatin, V. Girleanu, V. Ionescu and N. Buzbuchi, "Simplified Mathematical Model for Polarization Curve Validation and Experimental Performance Evaluation of a PEM Fuel Cell System," *Procedia Manufacturing,* vol. 32, pp. 810-819, 2019.

[112] D. Hao, J. Shen, Y. Hou, Yi Zhou, Hong Wang, "An Improved Empirical Fuel Cell Polarization Curve Model Based on Review Analysis," *International Journal of Chemical Engineering,* vol. 2016, 2016.

[113] D. Hissel and M.C. Pera,, "Diagnostic & health management of fuel cell systems: Issues and solutions," *Annual Reviews in Control,* vol. 42, pp. 201-211, 2016.

[114] N. Yousfi Steiner, D. Candusso, D. Hissel and P. Moçoteguy, "Model-based diagnosis for proton exchange membrane fuel cells," *Mathematics and Computers in Simulation,* vol. 81, no. 2, pp. 158-170, 2010.

[115] M. Bahrami, J-P Martin, G. Maranzana, S. Pierfederici, M. Weber and S. Didierjean, "Fuel cell management system: An approach to increase its durability," *Applied Energy,* vol. 306, p. 118070, 2022.

[116] D. Bezmalinovic, B. Simic and F. Barbir, "Characterization of PEM fuel cell degradation by polarization change curves," *Journal of Power Sources,* vol. 294, pp. 82-87, 2015.

[117] M. Bahrami, "Contribution to the development of a fuel cell management," 2020.

[118] Zhang, C. Zhang, W. Li, M. Hu, X. Cheng, K. He, and L. Mao, "A Comparative Study of Using Polarization Curve Models in Proton Exchange Membrane Fuel Cell Degradation Analysis.," *Energies,* vol. 13, no. 15, p. 3759, 2020.

[119] M. Salam, M. Habib, P. Arefin, K. Ahmed, M. Uddin, T. Hossain and N. Papri, "Effect of Temperature on the Performance Factors and Durability of Proton Exchange Membrane of Hydrogen Fuel Cell: A Narrative Review," *Material Science Research India,* vol. 17, no. 2, pp. 179-191, 2020.

[120] M. Bahrami, R. Bligny, J. Dillet, S. Didierjean, J. P. Martin, S. Pierfederici and G. Maranzana, "Modeling a Proton Exchange Membrane Fuel Cell Stack Cell by Cell:

Illustration of a Mechanism for the Propagation of Degradations," *Journal of The Electrochemical Society, Volume 168, Number 9,* vol. 168, no. 9, 2021.

[121] T. Gaumont, G. Maranzana, O. Lottin, J. Dillet, L. Guétaz and J. Pauchet, "In Operando and Local Estimation of the Effective Humidity of PEMFC Electrodes and Membranes," *Journal of The Electrochemical Society,* vol. 164, no. 14, 2017.

[122] D. Ramsey, T. Letrouve, A. Bouscayrol and P. Delarue, "Comparison of Energy Recovery Solutions on a Suburban DC Railway System," *IEEE Transactions on Transportation Electrification,* vol. 7, no. 3, pp. 1849-1857, 2021.

Abstract

Design and Control of Fuel Cell management system with distributed supercapacitors storage element

A fuel cell is a device that directly converts the chemical energy of fuel (H_2) to electricity through two electrochemical reactions. It consists of two electrodes (anode and cathode), two bipolar plates, gas diffusion layers, and an electrolyte. For Proton Exchange Membrane Fuel Cell (PEMFC), the electrolyte is a polymer membrane allowing protons transport from the anode to the cathode. It is sandwiched between two catalyst layers to form the Membrane Electrode Assembly (MEA). Gas diffusion layers (GDL) allow the diffusion of hydrogen and oxygen from the channels machined in the bipolar plates to the catalyst layers. At the anode side, hydrogen splits into protons and electrons (hydrogen oxidation). Protons cross the membrane, and the electrons go from the anode to the cathode through the GDL and through an external circuit connected to the load. At the cathode, oxygen molecules react with electrons and protons to produce water (oxygen reduction reaction). Many factors affect the fuel cell performances such as materials, design, and operating conditions. Gas supply to the electrodes is one of the main operating parameters and it is strongly linked to water and thermal managements. Due to its high time response, gas flow also has a major influence on the fuel cell behavior during high frequency power variations, and gas starvation is one of the main mechanisms related to fuel cell degradations.

As durability of PEMFC has a key role in the acceptance of it as a feasible power source, the objective of the thesis is to develop a fuel cell power source in order to reach better performances and to decrease the degradations related to the dynamic operations. The new power electronic architecture is based on a modular configuration in which the global fuel cell source is separated into several stacks each being composed with few cells.
Each stack is connected to its own converter to form a modular system, and the output of several modular systems is connected in series to supply energy to the load. This configuration is expected to give better reliability and durability performance compared with the configurations involving a single converter. Since the power dynamics of the fuel cell is low, hybridization with a rapid power response storage device, such as supercapacitor (SC) is necessary for the high bandwidth load. In order to increase the efficiency of the global system and to allow an optimal utilization of SC, a serial topology for hybridization is proposed in this study, where isolated converter is placed in series between the fuel cell and SC. This hybridization is applied at the modular level, the SC being distributed into all modular hybrid system. The voltage across the series converter has to be controlled so that the energy transfer from the fuel cell to supercapacitor occurs smoothly. All the SC will supply energy to the load through an adapted DC/DC converter specially design to own power flow freedom degree which is a requirement for implementing a Fuel Cell Management system. The proposed system is validated through the simulation and experimental results.

Keywords: Fuel cell, Series converter, Three-level converter, Energy management

Résumé

Une pile à combustible est un dispositif qui convertit directement l'énergie chimique du combustible (H_2) en électricité lors de deux réactions électrochimiques. Elle se compose de deux électrodes (anode et cathode), de deux plaques bipolaires, de couches de diffusion de gaz et d'un électrolyte. Dans une pile à combustible à membrane échangeuse de protons (PEMFC), l'électrolyte est une membrane polymère permettant le transport des protons de l'anode à la cathode. Elle est prise en sandwich entre les deux couches de catalytiques pour former l'Assemblage Membrane-Electrode (AME). Les couches de diffusion des gaz (GDL) permettent la diffusion de l'hydrogène et de l'oxygène depuis les canaux usinés dans les plaques bipolaires vers les couches de catalyseur. Du côté de l'anode, l'hydrogène se décompose en protons et en électrons (oxydation de l'hydrogène). Les protons traversent la membrane, et les électrons vont de l'anode à la cathode en traversant les GDL et un circuit externe relié à la charge. À la cathode, l'oxygène réagit avec les électrons et les protons pour produire de l'eau (réaction de réduction de l'oxygène). De nombreux facteurs affectent les performances des piles à combustible, tels que les matériaux, la conception et les conditions de fonctionnement. L'alimentation en gaz des électrodes est l'un des principaux paramètres de fonctionnement et elle est fortement liée à la gestion de l'eau et à la gestion thermique. En raison de son temps de réponse élevé, le flux de gaz a également une influence majeure sur le comportement de la pile à combustible lors des variations de puissance à haute fréquence, et le manque de gaz est l'un des principaux mécanismes liés à la dégradation des piles à combustible.

Comme la durabilité de la PEMFC joue un rôle clé dans son déploiement à grande échelle en tant que source d'énergie, l'objectif de la thèse est de développer une source de puissance à base de piles à combustible permettant d'atteindre de meilleures performances et de diminuer les dégradations liées aux opérations dynamiques. La nouvelle architecture d'électronique de puissance est basée sur une configuration modulaire dans laquelle la source globale est répartie en plusieurs stacks de plusieurs cellules de pile à combustible. Chaque stack est connecté à son propre convertisseur pour former un système modulaire, et la sortie de plusieurs systèmes modulaires est connectée en série pour fournir de l'énergie à la charge. Cette configuration doit offrir de meilleures performances en termes de fiabilité et de durabilité par rapport aux configurations impliquant un seul convertisseur. Comme la dynamique de puissance de la pile à combustible est faible, l'hybridation avec un dispositif de stockage à réponse rapide, tel que le supercondensateur (SC), est nécessaire pour la charge à large bande passante. Afin d'augmenter l'efficacité du système global et permettre une utilisation optimale des SC, une topologie série pour l'hybridation est proposée dans cette étude, dans laquelle un convertisseur isolé est placé en série entre la pile à combustible et le SC. Cette hybridation est appliquée au niveau modulaire, les SC étant distribués dans tous les systèmes hybrides modulaires. La tension aux bornes du convertisseur en série doit être contrôlée pour que le transfert d'énergie de la pile à combustible vers les SC se fasse progressivement. Tous les SC fourniront de l'énergie à la charge par l'intermédiaire d'un convertisseur DC/DC adapté, spécialement conçu pour assurer un degré de liberté au flux de puissance ce qui est nécessaire pour la mise en œuvre d'un système de gestion des piles à combustible. Le système proposé est validé par simulation et par des résultats expérimentaux.

Mots clés : Pile à combustible, Convertisseurs Série, Convertisseurs 3 niveaux, Gestion de l'énergie